THE UNIVERSITY OF HULL

VUV 157nm F_2 Laser Irradiation of Micro- and Nano-scale Particles

being a Thesis submitted for the Degree of

Doctor of Philosophy (PhD)

in the University of Hull

by

Stephanie Cockcroft, BSc (Hons)

(August 2012)

In the right light, at the right time, everything is extraordinary

Aaron Rose

American Director, Artist and Writer

Dedicated to Grandad

Abstract

Micro- and nanoscale particles have recently become the focus of a great deal of research interest due to their wide-ranging potential in a number of applications.

This thesis concerns the interaction of small particles with the 157nm wavelength vacuum ultraviolet, VUV, emission from a molecular fluorine gas, F_2, laser. The laser system is introduced and an overview of laser ablation of polymers is presented.

Small particles of different materials and sizes, supported on polymeric substrates, are irradiated at a wavelength of 157nm. The silica particles are transparent to the 157nm radiation, which leads to a lens effect. The polystyrene, silicon carbide and silver particles are opaque to the 157nm radiation, leading to a substrate-shielding effect.

The lens effect results in the focussing of the incident laser beam into a hotspot at the interface between the particle and the substrate. The enhancement leads to the removal of substrate material underneath the particle to form a dimple on the surface of the substrate. The substrate-shielding effect leads to the removal of the substrate material around the opaque particle while the underlying material is left behind. This forms a polymeric support structure, with the seeding particle attached to the top. The shape of the seeding particle dictates the shape of the support structure, for example spherical particles seed composite conical structures and cylindrical particles seed linear prismatic structures. The polystyrene and silver particles are seen to undergo shape and size transformations as a result of laser irradiation. This is discussed in terms of mass loss through heating.

Finite Element Method modelling is used to investigate and support the experimental results.

Fluorescent polystyrene particles are also irradiated at a wavelength of 157nm. They retain their fluorescence after irradiation and exhibit Whispering Gallery Mode resonances, ideal for high-sensitivity sensing applications and *Lab-on-a-Chip* microreactors.

Acknowledgements

Thanks must go firstly to my supervisor Dr. Chris Walton for his continued support and guidance throughout my PhD. If you had not given me this opportunity, I would not be the person I am today. I must also thank Professor Peter Dyer for your interest, support and many helpful conversations.

Thank you to all the staff and my fellow PhD students in the Department of Physics for your friendship, support and assistance, in particular Dr. Ali Adawi, Dr. Rozalina Zakaria, Dr. Abi Marchant, John Metheringham, Dr. Steve Myers and Anthony Edwards. Research would not be possible without collaboration, and therefore I must also thank Mustafa Ozmen in the Department of Chemistry, as well as Dr. Frank Voncken and Ms. Fei Gao in the Department of Biology.

This research would not have been possible without excellent technical support, and for that I must thank Mr. David Stavenau, Mr. Graham Randerson and Mr. Gordon Sowersby. Special thanks must go to Mr. Tony Sinclair for the many hours he spent on the SEM, and to Ms Ann Lowry and Mr. Garry Robinson for their expertise on the TEM and the SEM respectively.

I must also thank Professor David Barrow and Mr. Neil Sykes of metaFAB, based at the University of Cardiff, for the use of their VUV 157nm F_2 laser system while ours was out of action.

I would not have achieved everything I have if it weren't for the love and support of my parents, Peter and Christine, and my sister, Jennifer. Thank you for supporting me through my education as a whole and PhD experience in particular, and for showing me that I can achieve anything. I hope I have made you proud.

To all my friends, thank you for your support and friendship, even when you are on the other side of the world!

And most of all, thank you to Gary, for all your love and support even while working on your own PhD.

Table of Contents

Summary of the Thesis

This thesis is concerned with the laser processing of polymeric substrates using different techniques intended for the fabrication of micro- and nanoscale structures. These structures are machined though the interaction of a variety of micro- and nanosized particles with the 157nm wavelength emission from a VUV F_2 laser. The small particles are used to pattern the surface of a polymer, and include transparent and opaque particles of different sizes and geometries. The interaction of the laser radiation with fluorescent polystyrene particles is also investigated, along with the resulting effects of the interation on the light-emitting properties of these particles. Observation and investigation of the effects of the laser interactions with the particles have also taken place, focussing particularly on the shape and size transformations seen once the particles have been subjected to laser irradiation.

Chapter 1 presents a review of the literature available in fields related to this work, looking into laser interactions with materials, electromagnetic theory for light scattering by small particles and plasmonics, as well as the applications of small particles as light emitters and detectors.

Chapter 2 introduces the VUV 157nm F_2 laser system that is used for this work, including the system arrangement and laser properties, such as the laser fluence, that are important factors in carrying out the experiments presented here.

In Chapter 3, the interaction of the radiation from this laser with small transparent spherical particles supported on polymeric substrates is investigated. Silica particles of diameters 500nm and 1μm are irradiated at a wavelength of 157nm in order to demonstrate the light focussing capabilities of these transparent, lens-like particles. This focussing effect causes the fabrication of a dimple in the surface of the polymer substrate, which is characterised by inverse moulding. Finite Element Method modelling is used to help understand the processes that are happening experimentally. The attachment of particles to a substrate and their subsequent removal during laser irradiation is discussed.

For comparison with transparent particles, in Chapter 4 opaque polystyrene spherical particles supported on polymeric substrates are irradiated with 157nm radiation using

the VUV F_2 laser. The presence of the opaque spherical particle results in the formation of a composite conical structure, and the method of fabrication is discussed. The resolution of the laser beam is tested in order to determine its ability to fabricate miniature structures, and the factors affecting the structure fabrication are studied.

The geometry of the fabricated composite structure is dependent on the shape of the seeding particle, so in Chapter 5 opaque cylindrical particles are utilised to fabricate linear prismatic structures that are analogous to the conical structures demonstrated in the previous chapter. Silicon carbide whiskers are used to seed polymeric substrates to form these types of structures.

Spherical and cylindrical silver particles, which are opaque to the 157nm laser radiation, are used in Chapter 6 to form metal-polymer composite conical and linear prismatic structures. Finite Element Method modelling is used to investigate the interaction between the silver particles and the 157nm laser radiation, as well as the interaction at longer wavelengths.

The polystyrene and silver particles irradiated with 157nm radiation as discussed in the previous chapters exhibit size and shape transformations and this is studied further in Chapter 7. Laser-induced transformations by heating are suggested as the cause, and melting models are presented. The temperature of the small particles during laser irradiation is determined using a heating model in order to determine if the energy generated by the laser beam is sufficient to raise the temperature of the particles and initiate melting. The silicon carbide whiskers do not appear to undergo a shape or size change, and the heating model is used to determine the reason for this.

In Chapter 8, fluorescent polystyrene particles are irradiated with the 157nm wavelength emission from the VUV F_2 laser to fabricate supported fluorescent structures, and the emission from the particles is measured to determine the effect of the laser radiation on the emissive properties of the particles. Silver-polystyrene core-shell particles are fabricated and incorporated into an active medium to investigate the effect of the presence of the particles on the emission from the active medium. The results in this chapter are concerned with the application of the types of structures that may be fabricated using the interaction of the VUV F_2 laser with small particles.

Directions for future work are discussed in Chapter 9, relating to the results presented in the previous experimental chapters.

Chapter 1: Introduction

Section 1.1 - Emission of Radiation from Molecules

Since lasers were first introduced in 1960 with the development of the ruby crystal laser, researchers have become spoiled by the wide variety of wavelengths on offer from many different media, including crystals, semiconductors and gases.

The name *laser* originates from the process by which light is produced – Light Amplification by Stimulated Emission of Radiation. Atoms, molecules and other matter exist in discrete, quantised states, and are characterised by the electrons that exist in these quantised states. If these electrons interact or collide with photons, for example, and receive energy, they are transferred to an excited state. This process is known as *absorption* and is shown schematically in Figure 1.1, where the electron is shown traversing the energy gap between the ground state, E_1, and the excited state, E_2, due to the energy received from the incident photon, denoted by the photon's characteristic energy hν. The transferred energy must be greater than the energy gap in order for this process to occur.

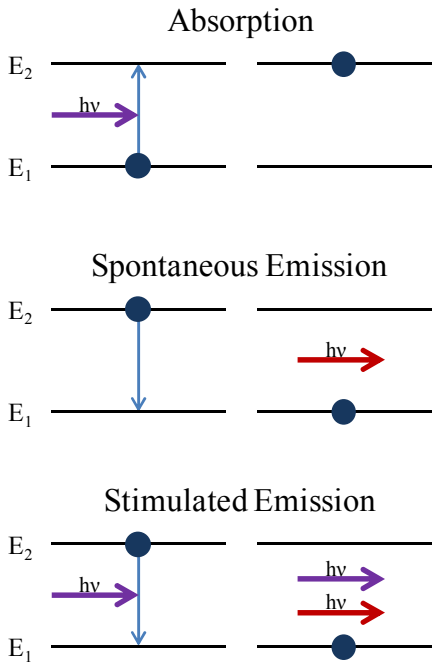

Figure 1.1: Absorption, Spontaneous Emission and Stimulated Emission of radiation. The blue dot represents an electron, the purple arrow an incident photon and the red arrow a photon generated by the emitted energy resulting from an electron dropping down from the excited state E_2 to the ground state E_1.

If the electron is raised by the absorption of energy to the excited state E_2 for a short time before returning to the ground state E_1, the absorbed energy may be emitted as a photon with energy given by [1]

$$\Delta E = E_2 - E_1 = h\nu$$

Equation 1.1

This process is known as *spontaneous emission*, as shown schematically in Figure 1.1 where the electron returns back to ground state E_1, accompanied by the emission of a photon.

In contrast, if an incident photon drives the electron to the lower ground state E_1 and an additional photon is emitted, as long as the frequency of the incident photon matches the excitation energy hν, the emission process is known as *stimulated emission*, shown schematically in Figure 1.1. The emitted photon matches the stimulating photon in both direction and phase, resulting in the amplification of the light emitted from the system.

For the process of stimulated emission, and hence light amplification to occur the distribution of the electrons in the ground and excited energy states must be inverted – a process known as *population inversion*. In a normal system the electrons drop to the ground state, and the distribution of the electrons can be described using the Boltzmann distribution [1]

$$\frac{N_2}{N_1} = e^{-\Delta E/\mathrm{kT}} = e^{-h\upsilon/kT}$$

Equation 1.2

where N_1 and N_2 are the number of atoms in the ground state and the excited state respectively, k = $1.38\times10^{-23}\mathrm{m^2kgs^{-2}K^{-1}}$ is Boltzmann's constant [2] and T is the temperature in Kelvin.

The temperature of the system must be positive, as it is in thermal equilibrium, and so N_2/N_1 will be less than or equal to 1. This means that there is a greater probability of the stimulating photon being absorbed instead of stimulating the emission of a photon, therefore spontaneous emission is the dominant process and there is no light amplification.

For population inversion to occur, i.e. $N_2 > N_1$, the laser medium must be excited, or *pumped*, by passing an electrical current through the laser medium or by the

dissociation of a donor atom followed by recombination. As a result, stimulated emission becomes the dominant process and light amplification can take place.

This process of stimulated emission and hence light amplification can occur in numerous gas molecules, meaning that a number of gases may be used to create a laser system. One such example is the molecular fluorine gas, F_2, laser.

Lasers find application in a wide variety of situations and industrial processes, including communications, medicine, barcode-reading, laser printing, materials processing e.g. cutting, drilling, welding, lithography and material removal through ablation processes [3].

Section 1.2 - Laser Ablation of Polymers

Since the early 1980's when Srinivasan et al. reported on the ablation of polymeric materials with the 193nm ArF laser [4-7], naming the process *ablative photodecomposition*, many groups have expanded on this work by using other lasers of various wavelengths and other polymers, until a detailed understanding of the mechanisms behind the process was achieved.

Laser emission in the near ultraviolet was first reported in 1963 by Heard [8], and achieved by exciting nitrogen gas, N_2, with a high voltage electrical pulse. The emission was observed over the wavelength range 300-400nm, with the strongest emission line at 337.1nm, with a pulse duration of 20ns [8]. Laser emission in the vacuum ultraviolet at a wavelength of 157.5nm using electron beam pumped fluorine gas, F_2, was first reported in 1977 by Rice et al. [8].

The ablation of polymers with ultraviolet (UV) and vacuum ultraviolet (VUV) excimer lasers has numerous applications thanks to the advantages these lasers hold over others, for example CO_2 or Nd:YAG lasers. These include better feature definition, a smaller heat-affected region and strong optical absorption in most materials due to the high photon energy – 7.9eV for the VUV 157nm F_2 laser. In addition, shorter wavelengths are diffracted to a lesser extent, allowing smaller features to be produced.

An important property to know when wanting to ablate a polymer is the *ablation threshold fluence*. This is a distinct laser fluence, or laser energy per unit area, typically presented in units of Jcm^{-2}, that must be exceeded in order for significant material removal, or *ablation*, to occur. This is not a process that occurs solely in the UV and VUV regimes, indeed the occurrence of an ablation threshold fluence spans the entire

laser wavelength range. However, in UV and VUV laser ablation, the ablation threshold fluence can be very low, typically in the range 20-200mJcm^{-2} [6]. Some removal of material can occur below this threshold fluence, although it is not deemed significant - more like "tickling" the surface than removing material. For example, exposure to a large number of laser pulses at a fluence that is below the threshold does not result in the same quantity of material removal as a single pulse above the threshold fluence. Experiments using pyroelectric calorimetric techniques to monitor samples during irradiation at sub-threshold fluences show that all absorbed laser energy propagates as heat [7, 9]. The typically short pulse duration of UV and VUV lasers (usually ~10ns) is also beneficial in polymer ablation as this restricts heat transfer, limiting any change or damage to the remaining material.

A well established method for characterising the ablation of a polymer is to measure the etch rate per pulse. This is the depth of material removed by each individual laser pulse from the surface of the polymer at a given fluence, x. It is usually an average value that is derived by measuring the depth, h, of an ablation site exposed to n pulses [6]

$$x = \frac{h}{n}$$

Equation 1.3

The ablation threshold fluence and etch rate per pulse can be used to determine another material property of the polymer - the effective absorption coefficient, α, which is generally expressed in units of cm^{-1}. This is a measure of the absorption capabilities of the material, and is inversely proportional to the beam penetration depth. A high absorption coefficient is beneficial as the etch rate varies with beam penetration depth, meaning that greater spatial depth resolution can be obtained and the depth of the material removed can be more finely controlled. Also, a higher absorption coefficient means the ablation threshold fluence, and subsequently the thermal loading of the material is reduced.

Through experiments, it has been found that the relationship between laser fluence, etch rate and effective absorption coefficient is not strictly linear, as the material that is removed from the surface by laser ablation forms a *plume* - a thin cloud of material that forms between the incident laser beam and the material. Subsequent laser pulses must pass through this plume in order to ablate more material away, which attenuates the laser beam. The plume is typically composed of a complex mixture of high-temperature

species which leave the surface of the ablated material at high speeds (of order 10^5-10^6cms^{-1})[7]. If the absorption coefficient of the plume differs to that of the solid material, the relationship between laser fluence and etch rate is defined by [7]

$$d = \frac{1}{\alpha_p} ln\left(\frac{\alpha_p F}{\alpha F_T} - \frac{\alpha_p}{\alpha} + 1\right)$$

Equation 1.4

where d is the etch depth per pulse, F is the laser fluence, F_T is the ablation threshold fluence, and α_p and α are the effective absorption coefficients of the plume and the bulk material respectively.

When $\alpha_p = \alpha$, Equation 1.4 reduces to Equation 1.5, and it is this linear form that is most commonly used to relate etch rate, laser fluence and effective absorption coefficient [10]

$$d = \frac{1}{\alpha} ln\frac{F}{F_T}$$

Equation 1.5

From Equation 1.5, if the etch depth per pulse is plotted as a function of the natural logarithm of the laser fluence, the gradient is equal to the reciprocal of the effective absorption coefficient. Shown below in Figure 1.2 is an example of a simplified graph for an etch rate experiment where Equation 1.5, a form of Beer's Law, is applied. The threshold fluence is also indicated.

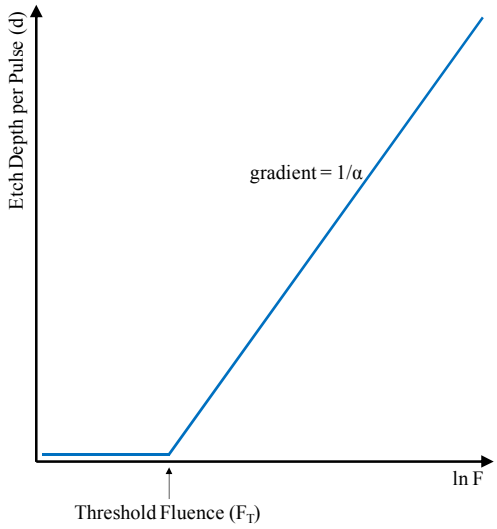

Figure 1.2: Etch depth per pulse as a function of the natural logarithm of fluence, indicating the ablation threshold fluence and the inverse of the effective absorption coefficient. Adapted from [7].

Another process to consider when discussing laser ablation of polymers is *incubation*. This occurs when ablation of material does not start on the first laser pulse and does not commence until the absorption of the polymer has been increased by photochemical modification by exposure to a sufficient number of pulses.

When discussing laser ablation it is important to look into the mechanism by which material is removed as a result of the incident laser pulse. The lack of significant thermal damage in laser irradiated polymers suggests that the energy from the laser beam is sufficiently high to cause a chemical breakdown of the main chain bonds in the polymer's molecules - this is what gives the F_2 laser an advantage over many other lasers as the photon energy is 7.9eV, compared with, say, 4.9eV (248nm) for the KrF laser. The material is ejected due to the bond breaking and an accompanying rise in pressure. Kuper et al. [11], when irradiating polyimide at a wavelength of 193nm around the ablation threshold fluence obtained results for the etch rate that were consistent with a thermal ablation model, and investigations into the surface temperature of the sample being irradiated suggested a drastic increase, implying that *photochemical ablation* occurs on a hot surface.

It seems likely that both chemical and thermal processes play a role in laser ablation of polymers in the VUV regime, and the general consensus seems to be that at shorter wavelengths the photochemical component has the greatest influence on ablation.

Applications of polymer ablation using UV and VUV lasers include micromachining and patterning, drilling, cutting, lithography, cleaning and surface modification.

VUV lasers are particularly useful for lithography and micro-machining as they have been shown to produces feature sizes as small as 0.2μm [7]. An excellent study on the high-resolution capabilities of using a 157nm wavelength has been carried out by Gruenewald et al. [12], by using this laser to pattern polymers and photo-resists.

Three-dimensional microstructures have been fabricated in wide-band-gap materials, such as fused silica and calcium fluoride (CaF_2), and organic materials such as PTFE, using a 157nm wavelength laser [13]. Fused silica substrates have been ablated at a wavelength of 157nm with the F_2 laser, and then nano-patterned by a Focussed Ion Beam, FIB, for use as Nano Imprint Lithography, NIL, templates [14].

Some examples of the modifications that can be made to polymeric surfaces include alterations to wetability, adhesion, biocompatibility and optical properties [7, 15, 16].

Another example of a modification that can be made to the surface of a material by laser ablation is the production of micro- and nano-sized structures due to the presence of a particulate inclusion. This can be present due to defects or impurities in a substrate material, redeposited ablation debris or deliberately added foreign particles.

It is well known that irradiation of an opaque spherical particle adjacent to a polymeric substrate results in the formation of a conical type structure [6, 7, 10, 17-21]. This occurs as the presence of the particle shields the material directly underneath it while the substrate material surrounding the particle is ablated away.

The conical structures exhibit a fringe pattern around the base of the structure. This pattern is produced by interference between the incident laser beam and the reflections from the walls of the conical structure, which continues to increase in height with each incident laser pulse. The period of the fringe pattern, Λ, is dependent on the laser wavelength, λ, and the cone apex half angle, θ_t, and is given by [10]

$$\Lambda = \frac{\lambda}{sin2\theta_t}$$

Equation 1.6

The nature of the interference fringe pattern has been investigated, taking into account the interactions between the incident beam and the reflections from the wall of the conical structure [10]. Figure 1.3 shows a schematic representation of the formation of a conical structure through the interaction of incident and reflected beams of laser radiation with a seeding particle (not shown) and the sloping walls of the fabricated conical structure. The conical structure apex angle, θ_t, can be altered by changing the fluence of the incident radiation and the height of the structure can be increased by increasing the number of applied laser pulses.

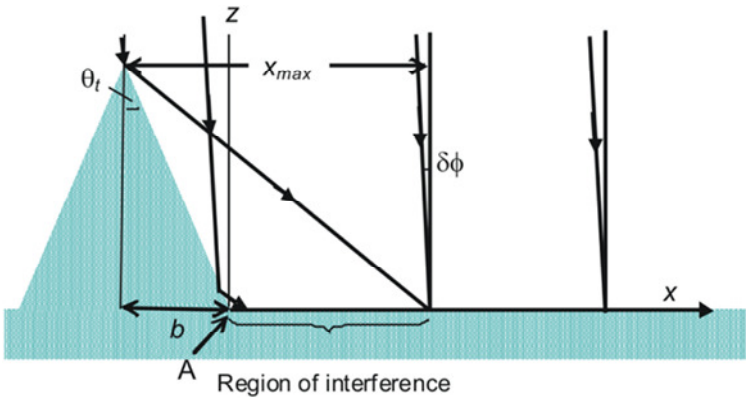

Figure 1.3: Schematic representation of conical structure fabrication, showing the region of interference of the incident beam and the reflected beams. From [10].

Photoablation and cone formation has been investigated using a variety of excimer lasers and both seeded and unseeded polymers, including but not limited to, 193nm and 308nm irradiation of polyimide and poly(ethylene terephtalate), PET [22], 248nm irradiation of polyimide [19], 248nm and 532nm irradiation of an elastomer/carbon composite [20], and 157nm irradiation of polycarbonate [10].

As well as laser ablation, lasers also find applications in material modification through a process known as *optical lithography*.

Section 1.3 - Optical Lithography by Laser Irradiation of Small Transparent Particles

Optical lithography is becoming one of the most useful processes in industry for the fabrication of miniature devices. The main factor involved is decreasing the feature size in order to increase data capacity while decreasing the overall device size. However, the smallest available feature size is limited by the wavelength of the light, making shorter wavelength lasers, such as the VUV 157nm F_2 excimer laser and the EUV 13nm laser source highly desirable for these purposes. Laser surface nanopatterning holds many advantages over other techniques, for example electron beam and focussed ion beam lithography, including simple setup, faster speeds and large area processing [23].

Optical techniques are limited in resolution by the light diffraction limit, hence why shorter wavelength light sources are more desirable. In recent years, a technique has been able to break through this diffraction limit, and increase the resolution of optical systems. This is *Nanosphere Lithography* [24, 25]. Small particles that are transparent to the incident wavelength of light are deposited on a surface and used as a mask to pattern the underlying surface. The small particle acts like a lens, focussing the incident light to a small point and concentrating all the energy at the base of the particle, as shown below in Figure 1.4. A particle lens array can increase processing efficiency, as it can convert a single laser beam into a number of enhanced optical spots.

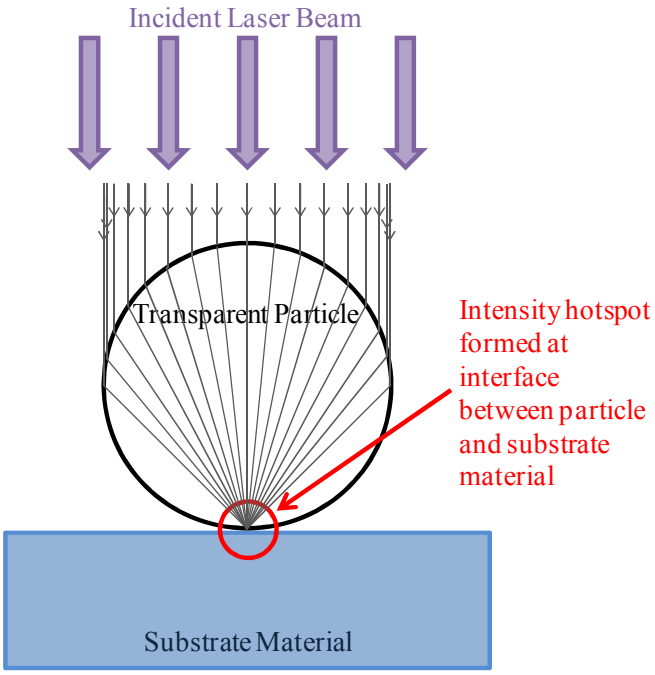

Figure 1.4: Schematic diagram of the Nanosphere Lithography technique using the focussing effect of small, transparent particles adjacent to a substrate.

Laser surface patterning using small particles as lenses has been shown to be an effective method for patterning a variety of substrate materials, including metals and magnetic media. Hong et al. [23] have reported the use of a 248nm KrF laser to pattern aluminium using 0.95µm silica (SiO_2) particles to form 200nm pits, as well as 140nm particles to mask a magnetic media surface, resulting in pits 20nm in size, i.e. an order of magnitude below the laser wavelength.

The fabrication of sub-wavelength hole arrays using laser-irradiated silica particles has also been demonstrated on silicon surfaces [26]. Silica particles hold an advantage over many other materials, as silica can exhibit high transmission over a wide range of wavelengths. In work demonstrated by Zhou et al. [26], 1µm diameter silica particles were self-assembled into an array, and irradiated by a single pulse from an 800nm wavelength 150fs femtosecond laser, fabricating a hole array. Irradiation of the silica particles was shown to result in the formation of *nanorings* when the particles were both isolated from each other and arranged in arrays when supported on glass substrates. A typical nanoring had a diameter of 900nm and a height of 90nm, and the dimple in the centre had a 400nm diameter [26].

As well as producing modifications on the surface of a substrate, particle lens arrays have been shown to produce micro-voids inside glasses. This is made possible by shifting the intensity hotspot from the outside edge of the particle to a location further

away from the particle, by altering the environment of the particle. For example, changing the environment from air to water has been shown to drastically move the hotspot of a 5μm silica particle into the glass substrate [27].

The irradiation of these 5μm silica particles by a femtosecond laser operating at 800nm in a water medium results in the formation of rings on the surface of the glass substrate at lower fluences, and taller convex bumps when irradiated at higher fluences. The modelling that was carried out suggested that the focus of the particle lens would be inside the glass substrate, hence resulting in a micro-void inside the glass. This was confirmed by optical microscopy which showed a hexagonal array of patterns inside the glass [27]. The bump structures are formed on the surface of the glass as a result of the material being pushed out of the glass in order to form the micro-void.

For efficient surface patterning in air, the particle must be kept in contact with the substrate. However, the particle tends to be removed after single pulse irradiation, due to the proximity of the intensity hotspot to the base of the particle. When the irradiation is carried out in water the focus is moved dramatically and in this case, the particle lens array tends to remain on the substrate surface even after multiple laser shots [27]. The field enhancement can been seen to decay much more slowly in water than in air, resulting in a significantly longer focal region, which could be beneficial for using multiple laser shots to fabricate higher aspect ratio structures.

The lens effect has also been observed in polystyrene (PS) particles at a laser wavelength of 800nm [28]. Polystyrene particles of 800nm diameter and 450nm diameter on a silicon substrate were irradiated using a single shot from an 800nm 150fs pulse duration laser. Irradiation at 124mJcm^{-2} and 198mJcm^{-2} resulted in elliptical-shaped dimples of diameters 246nm and 352nm respectively [28]. It is of interest to note that at this wavelength the ablation threshold of bulk silicon is ~200mJcm^{-2} [28], indicating that the focussing of the laser beam by the particle increases the energy of the incident laser beam sufficiently to raise it above the irradiating fluence and ablate the underlying material.

This work by Sakai et al. [28] also investigated the boundary between the lens effect and Mie Scattering and its dependence on particle radius, defined by the size parameter, a [28]

$$a = \frac{2\pi r}{\lambda}$$

Equation 1.7

where r is the radius of the particle and λ is the laser wavelength.

It has been shown that when the particle size parameter lies in the range $10 < a < 100$, resonance modes and heat effects are caused by the enhanced electric field that occurs as a result of the particle acting like a lens. It has been shown that the size of the features fabricated by the lens effect can be reduced by decreasing the size of the particle, and hence the size parameter. It can also be noted that as the size parameter is decreased, particularly when the particle size is equal to or less than the wavelength (i.e. $a \leq 3$), the effect of Mie Scattering becomes dominant over the lens effect.

Section 1.4 - Electromagnetic Theory for the Scattering of Light by Small Particles

The scattering of light by small particles forms the basis of many natural phenomena, including rainbows and even the colour of the sky. This important phenomenon also plays a role in the laboratory in such techniques as the sizing of small particles.

Two processes are used to describe the scattering of light by spherical particles – *Rayleigh Scattering* and *Mie Scattering* [29]. Rayleigh Scattering is applied to particles that are smaller than the wavelength of the incident radiation, and the degree of scattering is highly dependent on both wavelength and particle size. Mie Theory is used to describe the scattering of light by particles of dimensions larger than the wavelength of the incident light. Mie Theory is wavelength independent, and assumes that the scattering particle is isolated from any others and is homogenous. Mie Theory provides an analytical solution to Maxwell's Equations.

Within the particle system, Mie Theory uses three separate regions – the incident region, the particle, and the scattered region, as shown in Figure 1.5 below.

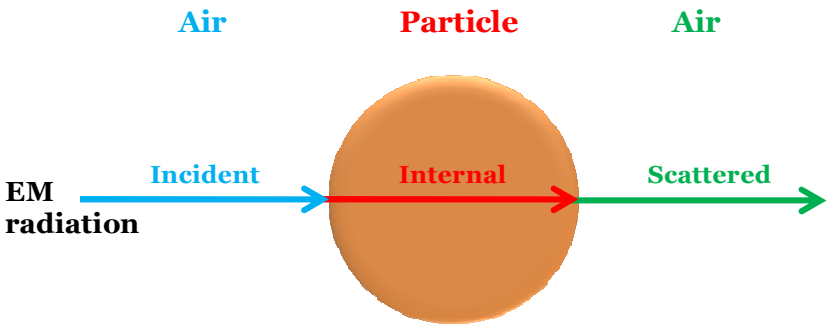

Figure 1.5: The Mie Theory of Scattering breaks the particle system into three separate regions.

Different equations, incorporating the spherical polar coordinates (r, θ, ϕ), are used to describe the scattering of the electric field component of the electromagnetic radiation in each region, and these may be found in [30].

These equations are complex and can be tricky to solve. As an alternative, solutions can be constructed numerically using a computational technique known as the *Finite Element Method*.

Section 1.5 - Finite Element Method Computational Techniques for Electromagnetic Modelling

The Finite Element Method (FEM) is a useful technique in computational modelling, with wide ranging applications in the car industry and aerospace industries, to name just a couple of examples. Since the introduction of the technique in the 1950's [31], and with the growth and development in computer technology over recent decades, the technique has become even more widely used with the ability to analyse larger and more complex problems as technology has improved.

The key feature of the FEM technique is the method of analysis. The area to be analysed is broken down by a process known as *meshing*, into a number of sub-divisions called *elements* which are connected at joints known as *nodes*. The variable then acts over each element, and the model equations are solved for each element.

COMSOL Multiphysics is a commercially available FEM software package that can be used for a wide variety of modelling activities. To assist with defining models within different fields it is made of up a number of modules, for example Acoustics, Heat Transfer and Structural Mechanics. The RF module is optimised for the analysis of electromagnetic waves in fields such as RF and microwave applications, optics and photonics [32].

Solving a model with the Finite Element Method using the RF module of COMSOL Multiphysics consists of several steps [32]:

- Choose the type of analysis e.g. plane waves, TE or TM polarisation, number of dimensions,
- Create the model geometry,
- Set the appropriate boundary conditions,
- Apply the appropriate properties to each subdomain e.g. optical properties,
- Apply the appropriate scalar variables to the model e.g. wavelength,

- Generate the mesh,
- Compute the solution,
- Visualise and postprocess the results.

Finite Element Method software is able to solve models in 1-dimensional, 2-dimensional and 3-dimensional space. In-plane waves and perpendicular waves can be used, and transverse electric (TE) or transverse magnetic (TM) waves can be selected.

The geometry of the model can be drawn using a number of shape and free-hand tools. Depending on the type of model, *Perfectly Matched Layers* (PMLs) may be used. Perfectly Matched Layers are subdomains around the actual model subject that restrict the region being solved over and are used to absorb the energy scattered away by the subject with no reflections.

Boundary conditions are used to define the interface between the model geometry and the surroundings. Boundaries can be *external* or *internal* – an exterior boundary separates the model subject from the surroundings, an interior boundary divides two or more subdomains within the model subject itself. A number of different boundary conditions can be applied, including continuity and absorbing boundary conditions.

Each region of the model, known as a *subdomain*, can then be applied with the appropriate material properties. The PMLs can be set to absorb radiation in particular directions, and the subdomains of the model geometry can be defined using the refractive index (real or complex) or permittivity and permeability data for the material being investigated. Appropriate scalar variables, such as the wavelength of the radiation incident on the model geometry can be set, to coincide with the material properties if necessary.

After the model has been drawn and the appropriate settings applied, the mesh can be initiated. Either a default setting can be used, or the mesh size can be defined manually. Also, adaptive meshing can be used if finer resolution is needed in certain areas, for example in smaller regions or at boundaries. The standard mesh for FEM modelling is a triangular mesh, as shown in Figure 1.6, which also indicates the features known as elements and nodes.

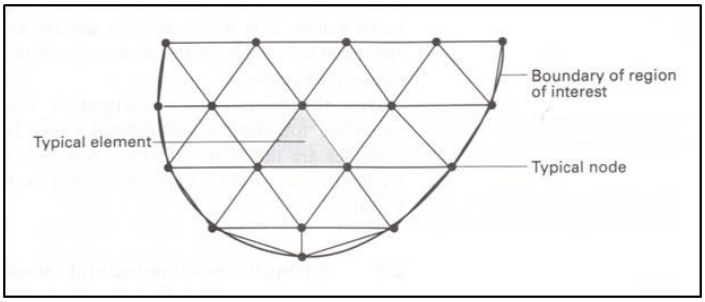

Figure 1.6: Meshing of a region into a number of elements connected by nodes – from [31].

After the model has been set up, the solution can be calculated. For electromagnetic analysis, Maxwell's equations are solved, subject to the applied mesh, subdomain and boundary conditions. The solution can then be visualised, and processed in different ways, for example cross-sections of energy and different outcomes of the modelling.

COMSOL Multiphysics is FEM software that has found a wide range of applications in the field of plasmonics, and is an efficient method for predicting experimental results, for example when working with plasmonic sensor devices.

A directly adjacent dielectric medium is known to alter the plasmonic properties of a metallic nanoparticle [33], which has a significant effect on the development of ultrasensitive LSPR sensor devices. Therefore, it is very important to examine the effect on the plasmonic properties of a nanoparticle on the surface of a dielectric substrate. Knight et al. have compared experimental and modelling data using gold-silica core-shell nanoparticles and gold nanospheres on glass, sapphire and zinc selenide substrates [33].

Dmitriev et al. [34] have been able to experimentally and theoretically double the refractive index sensitivity of surface-supported nanoplasmonic sensors by raising the metallic nanoparticle above the substrate on dielectric nanopillars, shown in Figure 1.7.

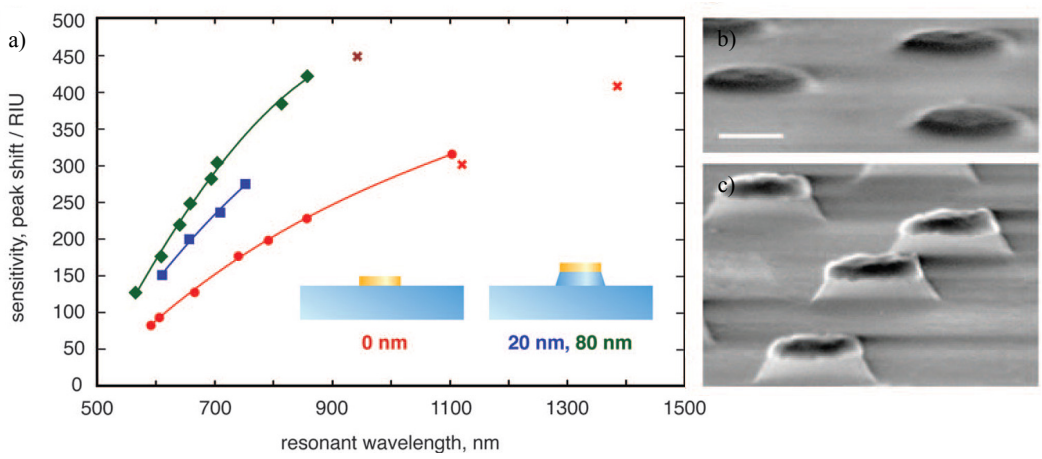

Figure 1.7: Enhancement of the refractive index sensitivity of gold nanodisks directly on a SiO_2 substrate (red circles), supported on 20nm SiO_2 pillar (blue squares) and supported on 80nm SiO_2 pillar (green diamonds) - a) schematics of structures, b) SEM of gold nanodisks directly on SiO_2 surface and c) SEM of gold nanodisks supported on SiO_2 pillars. Scale bar indicates 100nm and applies to both SEMs. From [34].

Core-shell nanoparticles have the potential for use in plasmonic sensor applications. The field enhancement around a dielectric shell coated gold nanosphere has been studied using FEM modelling, paying particular attention to the location around the core-shell particle and the effect on the plasmonic resonance with varying shell thickness and dielectric constant [35].

Vo-Dinh et al. have investigated silver particle dimers, or pairs of particles, particularly nanoshells, for applications in Surface Enhanced Raman Scattering (SERS) [36]. COMSOL Multiphysics version 3.5a FEM software was used to analyse the hotspot effect seen in close-packed metallic plasmonic particles in the air gap between two 20nm diameter hollow silver nanoshells.

Nanoshell dimers are of interest because of the huge electric field enhancements these pairs of plasmonic particles have to offer in the gap that separates them. Finite Element Modelling based on 3D geometries has been used to model silver and gold nanoshell pairs [37]. Nanoshells are particularly versatile as their plasmon resonance wavelength can be tuned by altering the shell size and/or thickness. Finite Element Method modelling is an excellent tool for plasmonics, as results can be generated quickly and easily (depending on the computational capabilities available). Modelling of silica-silver core-shell particles shows that as the particle size increases there is a red-shift of the plasmon resonance wavelength as well as a broadening of the resonance peak [38].

In order to produce useable, sensitive devices, ordered arrays of particles may be needed, and there are a number of methods that can be used to achieve this.

Section 1.6 - Methods of Fabricating Ordered Arrays of Small Particles

One method of particle alignment is *Dielectrophoresis* [39-42]. Dielectrophoresis, or DEP, is the movement and alignment of particles using an electric field. The electric field is applied via electrodes, which are separated by a gap, and the nanoparticles, dispersed in a liquid, are aligned in the gap.

Another method for aligning nano- or microparticles is *Optical Trapping,* or *Optical Tweezing* [43-45]. Optical tweezing involves the trapping and manipulation of small spherical particles using a highly focussed beam of light. Focussing a Gaussian beam creates an intense spot of light, and when this light interacts with a particle, it is reflected and refracted. The forces from the light on the bead can be described by two components – the scattering force and the gradient force. The gradient force acts as a restoring force, returning the particle to the centre of the optical trap when it is displaced, for example by Brownian motion. There is no mechanical contact with the particles, and arrays of particles can be readily assembled. The first recorded experimental use of optical tweezers, then called a *single-beam gradient force radiation pressure particle trap*, was by Ashkin et al. in 1986 [43], manipulating dielectric particles over a size range of ~25nm-10μm in water. Metallic spheres in water can also be manipulated, although the particles ability to support surface plasmon resonances needs to be taken into account.

Another method of particle arrangement and alignment is *Dip-Pen Nanolithography* [46, 47]. Dip-Pen Nanolithography, or DPN, involves depositing materials on a surface using a sharp tip, usually a modified Atomic Force Microscope (AFM) tip. The particles are transferred from the tip to the substrate in solution (the "ink"), and can be arranged with high precision and accuracy.

Arrays of silver nanowires with a 35nm periodicity have been fabricated [48], while functionalising the surface of the nanoparticles with molecules that are attracted to specific locations on a patterned substrate has also been suggested as a possible method of arranging regular arrays of particles [49].

Micro- and nanosized particles, particularly those in ordered arrays, have found many applications but none more relevant in today's world of "miniature devices" as nanolasers and optical antennas. Small particles, including core-shell particles, have also been successfully used in medicine and as sensor devices.

Section 1.7 - Applications of Small Particles in Medicine and as Sensor Devices, Light Emitters and Optical Antennas (Detectors)

Core-shell nanoparticles have generated a great deal of interest in recent years. Core-shell particles consist of a spherical core surrounded by an outer uniform layer of a different material, and have been made from a variety of combinations of materials such as silver-polypyrrole [50], silver-silica [51], gold-silica [52] and silica-silver [38].

The uses of this type of particle can be increased by altering the geometry slightly. Examples of interest include *nanoeggs* [52], where the core is offset within the shell and *nanocups* [52], where the core protrudes though the shell. Nanoeggs have been shown to behave analogously to optical lenses, in that they can focus light into a hotspot which holds the potential for illuminating single or multiple molecules for surface-enhanced spectroscopy [52]remove. Hollow nanoshells may be fabricated by excavating the core from a core-shell particle.

Both solid and hollow nanospheres and core-shell particles have potential applications in many fields, including Surface Enhanced Raman Spectroscopy (SERS), chemical sensing and in medicine and pharmaceuticals, for example as drug delivery systems and in photothermal cancer therapy.

Metallic particles have been proven to be highly effective in the treatment of cancerous tumours, and these minimally invasive photothermal cancer therapies hold many advantages over traditional, highly invasive, surgical methods.

Metallic particles engaged as sensors have high sensitivity, and as such have the potential for detecting small quantities of, for example, bio-toxins or cancerous tissue. Peng et al. have recently presented some highly promising results using an array of sensors based on gold nanoparticles that can rapidly distinguish between the breath of healthy test subjects and the breath of patients with lung cancer [53]. An LSPR sensor using triangular silver nanoparticles has been shown to be sensitive enough to provide a diagnosis of Alzheimer's Disease in both synthetic and clinical samples [54].

Gold spherical particles and gold nanorods have been shown to be effective in the treatment of cancer cells [55]. Particles injected into the cancerous tissue and irradiated at a wavelength appropriate to excite a plasmon resonance cause a localised temperature increase in the tumour that is sufficient to kill the malignant cells. Gold particles can also be easily functionalised for selective delivery through the body to one or more cancerous tumours.

Silica-gold core-shell nanoparticles injected into cancerous tissue in both *in vitro* and *in vivo* tests have also displayed highly promising results. The nanoshells were tuned to a resonance wavelength in the near-infrared, where transmission through human tissue is very high with no observable damage, and irradiated *in situ* with low doses of laser radiation. This increased the local temperature by nearly 40°C, which is sufficient to kill cancerous cells while nearby healthy tissue that was not injected with particles experienced a temperature increase of less than 10°C which caused no damage to the healthy cells [56-58].

Silver nanosphere-nanowire pairs have demonstrated the emission of light as a result of plasmonic coupling between the particles. The nanosphere acts as an antenna which couples incident light into the nanowire by interacting plasmonic resonances. The nanowire surface propagating plasmons are converted back to photons at the nanosphere-nanowire junction and at the ends of the nanowire [59].

One problem with metallic particle devices is that the plasmonic fields that are generated are not coherent. A solution is to combine a plasmonic medium with an active gain medium in order to stimulate coherent emission of surface plasmons. This type of device has become known as a *spaser*, named for the process it carries out - Surface Plasmon Amplification by Stimulated Emission of Radiation.

The smallest spaser to be presented uses luminescent core-shell nanoparticles [60]. These particles are also the first to emit at visible wavelengths. They are comprised of a gold core particle, ~14nm in diameter, surrounded by a silica shell, ~15nm in diameter, that has been doped with Oregon Green 488 dye. The surface plasmon wavelength, ~520nm, overlaps both the excitation and emission bands of the dye and these particles have demonstrated laser-like emission at a wavelength of 531nm when pumped at a wavelength of 488nm.

Thermal light sources are a highly promising emerging technology, particularly in the infrared where certain constraints restrict the use of some semiconductor materials. Silicon carbide is an ideal infrared optical antenna thermal emitter. Silicon carbide exhibits a transverse optical phonon resonance at a wavelength of 12.5μm [61, 62]. Below this resonance wavelength, the dielectric permittivity of silicon carbide is large and positive. Above this phonon resonance wavelength, the relative permittivity becomes negative, leading to some interesting properties such as a negative refractive

index. Silicon carbide whiskers exhibit a number of resonant modes, which result in the radiation of infrared light in a discrete manner when they are heated [61].

Room-temperature nanolasers in the ultraviolet have also been demonstrated using zinc oxide nanowires of diameters 20-150nm and lengths ≤10μm [63]. When excited at a wavelength of 266nm, numerous emission peaks in the wavelength range 370-400nm are observed.

A variety of nanolaser devices have emerged in recent years that are capable of emitting at wavelengths across the electromagnetic spectrum. These include gallium nitride, GaN, nanowires that emit in the UV-blue region at a wavelength of ~375nm [64], an InGaAsP disc surrounded by an aluminium/silica shield that lases at a wavelength of 1.43μm [65] and nanopillars comprised of an InGaAs core with a GaAs shell emitting at ~950nm [66]. Nanolasers that exploit metallic plasmon resonances are also being developed, including a nanolaser emitting at a wavelength of ~489nm made from a cadmium sulphide nanowire in close proximity to a silver surface [67].

Active, or fluorescent, materials can be employed along with micro- and nanoscale particles to broaden the applications of these miniature devices.

Fluorescent materials are essential for many applications in nanotechnology, particularly in biological fields. Excellent spatial and temporal resolution make fluorescent materials ideal for nanoscale exploration. A large number of materials are currently in use as both emitters and detectors, including organic and metallo-organic dye molecules, semiconductor quantum dots (QDs) and polymer-dye and silica-dye hybrid micro- and nano-scale particles [56].

Dye molecules alone tend to be the smallest architectures, but they are also generally the dimmest and the least stable emitters. Dyed polymer and silica particles are generally the largest architectures, with dimensions of tens of nanometres up to millimetres. A dye molecule is usually either attached to the outside of the polymeric or silica particle or is absorbed and trapped by the particle itself. While these approaches make highly useful fluorescent particles, there are still problems attached to this method. The polymer particle can offer little protection to the dye molecules, making them prone to dye leaching and also quenching and bleaching when exposed to radiation. Dye doped silica particles do hold some advantages over polymeric particles, such as polystyrene - the silica particles are more mechanically and chemically robust, which protects the encapsulated dye molecules more effectively. Various methods exist

that enable plain particles to later be doped with fluorescent dyes, including the liquid two-phase system and the gradual solvent evaporation method.

Close-packed arrays of dye-doped polystyrene microspheres have been shown to be emissive at increasing angles of irradiation up to 50° [68].

Polystyrene and silica micro- and nanoparticles can also be doped with quantum dots using the liquid two-phase system and the gradual solvent evaporation method [69, 70]. Quantum dots (QDs) are highly effective as they are stable against photobleaching, their emission wavelengths can be tuned by changing the QD size while being excited at a single wavelength, and single quantum dots can be ~20× more intense than organic dyes [70].

Core-shell particle architectures are highly useful for applications involving fluorescence. Fluorescent core-shell nanoparticles with high brightness and photostability have been demonstrated by Burns et al., where fluorescent dye molecules constitute a core and are contained within a silica shell [56]. Core-shell particles of this design are highly adaptable in terms of the dimensions of both core and shell and in emission - the presence of the silica shell prevents the fluorescent cores from quenching each other and reducing the emission intensity.

A similar core-shell construction of interest is the addition of a metallic layer to the exterior of a dye-silica core-shell particle [56]. The metal outer shell exhibits a plasmon resonance at a particular wavelength, absorbing light much more strongly at this wavelength. This absorption wavelength is also tuneable by altering the metal shell thickness. The emission properties of a fluorescent molecule, or *fluorophore*, can be changed dramatically by interactions with electron-dense materials, i.e. metals [56, 71]. For certain fluorescent polymeric particle diameters with certain thickness silver shells, fluorescence intensity compared with un-coated fluorescent particles increased by ~20× in spite of absorption by the metal shell [71]. Fluorescent silica particles of this type are highly promising for biological and chemical sensing applications as *Lab-on-a-Particle* devices and for incorporation into *Lab-on-a-Chip* devices.

Chapter 2: The VUV 157nm F_2 Laser System

Section 2.1 - Introduction

The F_2 molecular fluorine gas laser emits at a wavelength of 157nm, in the vacuum ultraviolet (VUV) region of the electromagnetic spectrum.

In the case of the fluorine gas (F_2) laser, the fluorine molecule is dissociated by impact with an electron into F^- and F. A buffer gas is incorporated in the laser system to result in *ion-ion recombination*, i.e. a charge transfer from, say, He_2^+ to F^-, as described below [72]

$F_2 + e \rightarrow F^- + F,$

$He_2^+ + F^- \rightarrow F^*(3p) + 2He.$

Each energy state consists of a number of energy levels. When the electrons are excited they may occupy any of the energy levels in the excited state, as long as they obey Pauli's Exclusion Principle, and so during stimulated emission electrons may fall back to the ground state from various excited levels, as demonstrated schematically in Figure 2.1. This results in the emitted photons possessing slightly different energies, and so the radiation (light) emitted from the laser is comprised of a number of wavelengths over a small range.

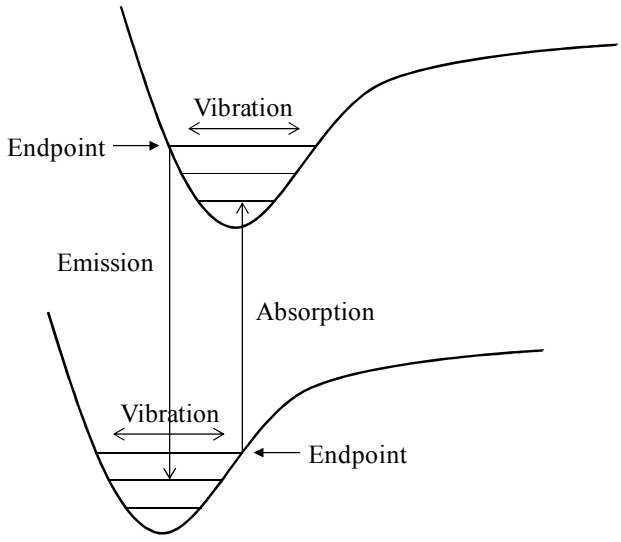

Figure 2.1: Absorption and emission originate primarily at endpoints of individual vibrational levels of two electronic states of a molecule. The Franck-Condon Principle places certain restrictions on which energy levels, and sub-levels, may be involved in the transitions.

By this process the F_2 laser is allowed six transitions that results in six emitted vacuum ultraviolet (VUV) wavelengths, shown in Table 2.1 below.

Transition Number	Emitted Wavelength (nm)
1	157.63094
2	157.52433
3	157.40231
4	156.73519
5	157.52988
6	157.5970

Table 2.1: F_2 laser VUV wavelengths, data from [73].

The dominant transition is that which results in a wavelength of 157.63094nm [73]. The F_2 transitions also allow for a small quantity of red emission, roughly 3-5% of the total beam energy [74], which is of wavelengths in the range 620-780nm [75]. The buffer gas is usually helium or neon; neon being the preferred gas as it suppresses this red emission.

Section 2.2 - Experimental Results & Discussion

Section 2.2.1 - Laser System Set-up

The main laser used for this work is the Lambda Physik LPF202, a molecular fluorine gas (F_2) laser emitting at a Vacuum Ultraviolet (VUV) wavelength of 157nm. This laser produces a maximum output energy of up to 35mJ per pulse at a charging voltage of 26kV, with a pulse duration of ~11ns at full width at half maximum (FWHM) at a pulse repetition rate of ≤20Hz.

The charging voltage of the laser can be varied in 1kV steps from 21kV to 26kV, enabling the laser energy and hence the fluence at the sample to be varied.

This laser outputs a Hermite-Gaussian beam, and the full-angle beam divergence of the output beam is ~8mrad in its long dimension and ~3mrad in its narrower dimension.

The laser system is shown in Figure 2.2 below. The output beam from the laser travels down the sealed beam tube, passing through an aperture to extract a region of quasi-uniform fluence. The reduced beam then passes through a calcium fluoride, CaF_2, lens of focal length $f \approx 76.4$mm at $\lambda = 157$nm (radius of curvature = 46.4mm, refractive index = 1.607 at 7.725eV [76], located at the intersection between the beam tube and the sample chamber. The laser system was arranged for $1/10\times$ magnification, increasing the fluence at the sample. The system magnification was arranged using [77]

$$M = -\frac{S_1}{S_0}$$

Equation 2.1

where M is the magnification, S_1 is the image-lens distance and S_0 is the aperture-lens distance.

The laser beam then passes into the sample chamber, where the sample stage is located. The stage is motorised and under computer control. It can travel in the x, y and z planes and can move in increments from 1µm to 1mm in all directions.

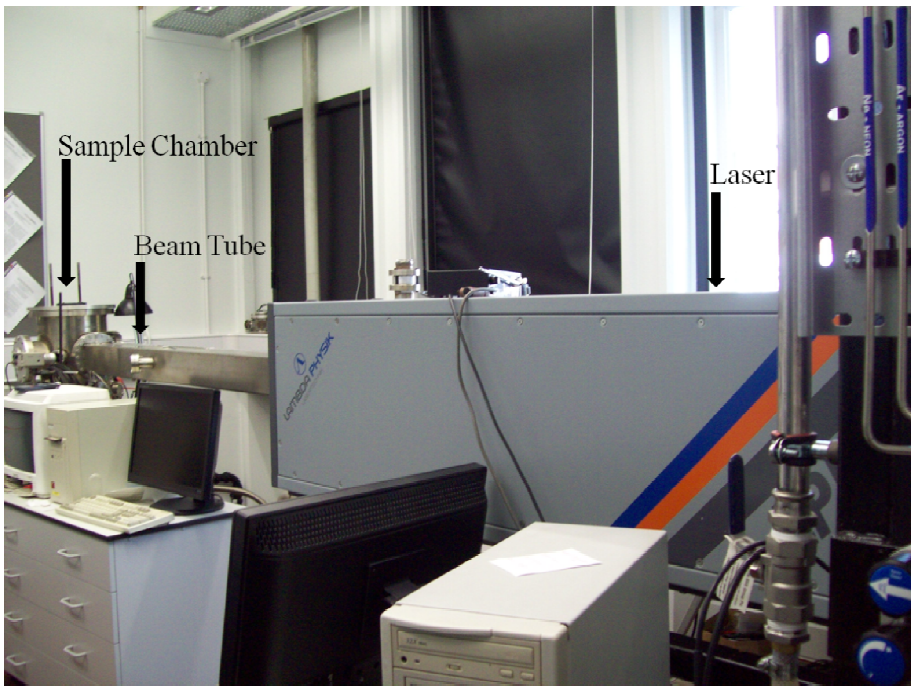

Figure 2.2: The VUV 157nm F_2 laser system.

The laser system arrangement is shown schematically in Figure 2.3.

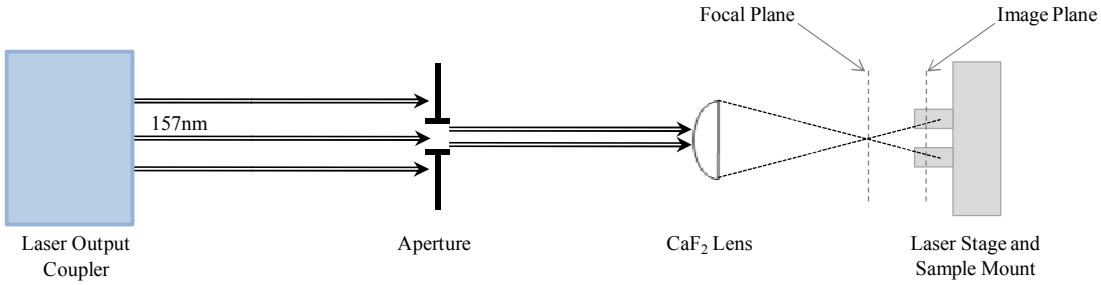

Figure 2.3: Schematic of Lambda Physik LPF202 F_2 laser system.

A joulemeter, with a calibration factor of 29.5V/J, could be placed behind the lens and in front of the sample in order to measure the laser pulse energy. The joulemeter was

coupled to an oscilloscope (Hewlett Packard Infinium), which enabled the laser fluence (units $mJcm^{-2}$) to be calculated from

$$Fluence = \frac{laser\ pulse\ voltage/29.5}{area\ of\ ablation\ site}$$

Equation 2.2

It was important to know the position of the image plane for the system set up, and this was carried out by ablating a piece of polyimide film at various distances from the lens. Polyimide has a low ablation threshold fluence of ~$36mJcm^{-2}$ at a wavelength of 157nm [9]. The ablation sites were viewed using an optical microscope (Leica DMLM), and the cleanest, sharpest site with appropriate dimensions was chosen to best define the image plane location.

The photons within the laser pulses are easily absorbed by oxygen and water vapour, among other molecules, due to the short wavelength of the beam, and so the beam path can either be purged with argon, nitrogen or helium, or evacuated. The experiments presented here have been carried out in vacuum at a pressure of ~10^{-3}-10^{-4}mbar.

For some experiments, an alternative 157nm VUV F_2 laser was used. This laser, a Lambda Physik LPF220 produces a pulse energy of up to 50mJ per pulse, with a pulse duration of ~26ns FWHM at a pulse repetition rate of ≤200Hz. In this laser system, the output beam from the laser is passed through a flies eye homogeniser and reduced in size by $1/25\times$ magnification.

These laser arrangements are for non-contact image projection, in which the aperture is imaged and demagnified onto the surface to be ablated, and allow for laser ablation of polymeric substrates seeded with micro- and nano-sized particles.

Section 2.2.2 - Substrate Material Properties

The substrate materials used in this work were CR-39 polymer (Page Mouldings Ltd, Pershore, UK) and Polycarbonate (Goodfellow Cambridge Ltd, UK).

CR-39 polymer, also known as (poly) allyl diglycol carbonate, or PADC, and polycarbonate are used for their excellent optical properties, including good transparency in the visible region. Both materials have been widely used in research for the detection of alpha particle radiation by a process known as track etching [78-83]. The ablation of polycarbonate has proved of great interest due to its high optical quality

for use in fabricating micro-lenses and large area lens arrays as well as *Lab-on-a-Chip* microreactors.

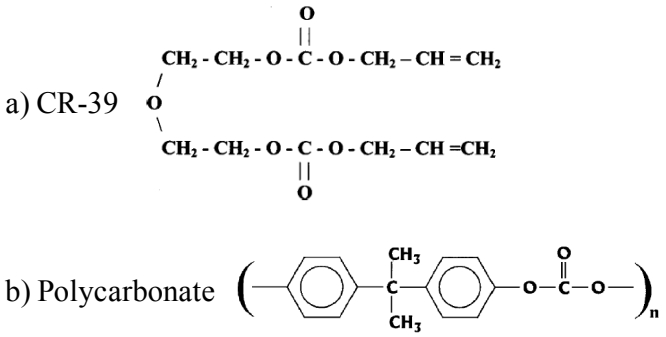

Figure 2.4: Chemical structures of a) CR-39 polymer, from [83] and polycarbonate [80].

In order to carry out laser ablation experiments on these materials, it is necessary to know the laser ablation threshold fluence, or the minimum laser fluence required for significant material removal.

One way to determine this is to measure the etch rate, or etch depth per pulse, of the material when irradiated at a wavelength of 157nm. A clean piece of polycarbonate and CR-39 polymer were each exposed to a known number of pulses at various fluences. The depth of each ablation site was measured using a white light interferometer (Veeco WYKO NT1100), allowing the etch depth per pulse to be obtained. The ablation threshold fluence can then be determined using [10]

$$d = \frac{1}{\alpha} \ln \frac{F}{F_T}$$

Equation 2.3

where d is the etch depth per pulse, F is the laser fluence, and α and F_T are the effective absorption coefficient and ablation threshold fluence respectively.

The graphs in Figure 2.5a) and Figure 2.5b) show the etch rate data for polycarbonate and CR-39 polymer respectively. Using this data, ablation threshold fluences of ~14mJcm^{-2} for polycarbonate and ~55mJcm^{-2} for CR-39 polymer were obtained. Using this data, and Equation 2.3, effective absorption coefficients of 2.8×10^{5}cm^{-1} and 1.4×10^{5}cm^{-1} were calculated for polycarbonate and CR-39 polymer respectively.

The optical absorption depth is the distance to which the incident light is absorbed, and is the inverse of the effective absorption coefficient, i.e. [6]

$$Optical\ Absorption\ Depth = \frac{1}{\alpha}$$

Equation 2.4

These values for the effective absorption coefficients of polycarbonate and CR-39 polymer correspond to optical absorption depths of ~35.7nm and ~71.4nm into each polymer respectively.

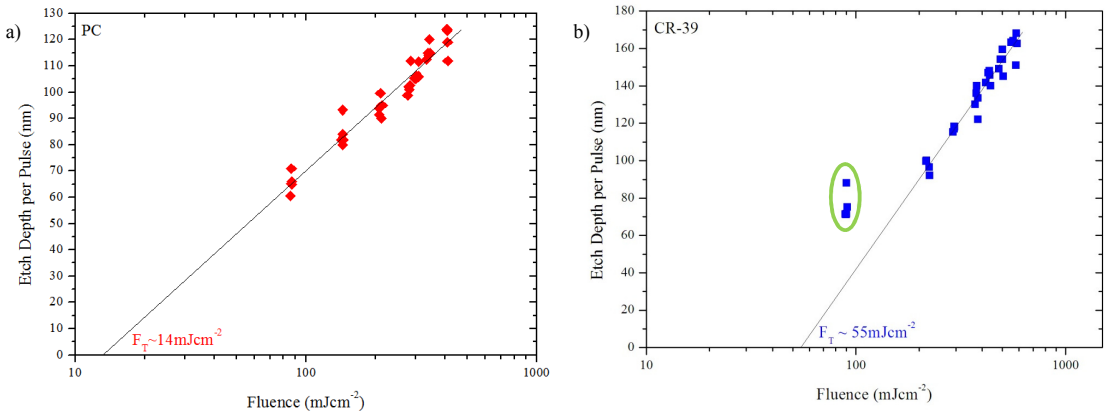

Figure 2.5: Etch rate and threshold fluence data for a) polycarbonate and b) CR-39 polymer. Note: the indicatated points in b) have not been taken into account during the analysis as they do not fit the trend of the other points.

Dyer et al. have previously determined the ablation threshold fluence for polycarbonate to be ~11mJcm^{-2}, with an effective absorption coefficient of 3.0×10^{5}cm^{-1} determined experimentally and 1.14×10^{5}cm^{-1} calculated from theory [10].

Section 2.3 - Conclusions

The VUV 157nm F_2 laser is a highly useful tool in the modification of many materials due to its high photon energy of 7.9eV. It is particularly useful for the ablation of polymeric substrates due to the low energy per unit area, or fluence, required to induce some combination of photochemical and photothermal breakdown of the material molecules.

Short optical absorption depths at 157nm in polycarbonate and CR-39 polymer respectively mean that precise control of the material removal depth can be achieved using the F_2 laser. The ablation threshold fluence of a material is an important quantity to know when ablating materials, and the low threshold fluences of polycarbonate at ~14mJcm^{-2} and CR-39 polymer at ~55mJcm^{-2} mean that these materials can be ablated easily, using low energies from the laser.

Both polycarbonate and CR-39 polymer exhibit clean ablation with little redeposited debris. This indicates that when they are ablated the constituent materials break down into groups of lighter and heavier particles where the lighter particles are able to escape and form a shock wave, or plume, which does not impede the heavier particles' escape from the substrate [84]. This reduces the quantity of heavier particles likely to be deposited back onto the substrate surface as debris, which can be minimised further by performing ablation experiments in a vacuum.

Chapter 3: VUV 157nm F_2 Laser Irradiation of Transparent Particles

Section 3.1 - Introduction

In the previous chapter, the VUV 157nm F_2 laser that is used for the experiments presented throughout this work was introduced. The effect of irradiating small particles that are of a material that is transparent to this 157nm laser radiation is investigated. It is well known that particles made from silica, SiO_2, of certain sizes are transparent at this wavelength, so particles of this material were used to exhibit the lens effect and fabricate dimples on the surface of a polymeric substrate. Silica has an extinction coefficient of $k = 4.7\times10^{-6}$ at a wavelength of 157nm (taken at 7.8eV) [85], corresponding to an optical penetration depth of ~2.7mm.

In order to gain a better understanding of the mechanisms involved in the scattering of light by small particles and in the formation of the composite dielectric structures, computer models using the Finite Element Method (FEM) have been developed. The software used was a commercially available package, COMSOL Multiphysics version 3.5a. This software uses the finite element method to solve partial differential equations in order to provide a numerical solution to the model, based mainly upon the relevant material properties. COMSOL Multiphysics offers a number of application-specific modules which use terminology and solution methods that are specific to certain disciplines. The RF Module has been used in this work for the analysis of electromagnetic waves. Perfectly Matched Layers (PMLs) have been used in these models to absorb the scattered radiation rather than it reflect back towards the scattering particle.

Finite Element Method modelling was utilised in order to best determine what size of particle would exhibit the desired effect experimentally. Following on from this, two different sizes of silica particles were deposited on a polymeric substrate and irradiated at a wavelength of 157nm using the F_2 laser.

As the small transparent particles act to focus the incident laser beam (in a way similar to a lens), the light is focused into a small, high intensity region, which has an ablative effect on the underlying substrate material. This results in the removal of both the particle and material from the substrate, creating a dimple on the surface of the

substrate. These fabricated dimples were then inverse moulded using Polydimethylsiloxane, PDMS, in order to investigate the profile of the dimples.

Following on from this, methods of particle adhesion and removal are discussed, looking particularly at the force of attraction between the particle and the substrate.

Finally, the potential methods for altering both the size and location of the focal region of small transparent particles are investigated, including changing the wavelength of the laser and the particle material.

The lens effect of small transparent particles is well known at longer wavelengths (248nm and longer) [23, 26-28, 30, 86, 87] but does not appear to have been reported for a laser wavelength of 157nm.

Section 3.2 - Experimental Results & Discussion

Section 3.2.1 - FEM Modelling and Laser Irradiation of Transparent Particles

Silica is known to be transparent at a wavelength of 157nm under certain geometrical conditions, so for the lens effect to occur, the dominant factor is the size of the spherical particle needed. Finite Element Method modelling using COMSOL Multiphysics version 3.5a was utilised to determine the optimum silica particle size to experimentally achieve the lens effect, and hence pattern a polymeric substrate.

A number of silica particles with diameters in the range from 100nm to 5μm were modelled at 157nm irradiation, and it was determined that particles with a diameter ≤1μm show the best lens effect, as evidenced by a *hotspot* effect in the model. In agreement with the literature [28], the size parameters for a 500nm diameter particle and a 1μm diameter particle using Equation 1.7 are a = 10 and a = 20 respectively, indicating that the lens effect is predominant over Mie Scattering for these sizes of particles. The refractive index of silica used in these models is N = 1.676+0.0000047i (at 7.8eV) [85]. This hotspot appears at the back, or exit side, of the particle, as shown in Figure 3.1 below.

Figure 3.1 shows a silica particle of 500nm diameter, irradiated at a wavelength of 157nm from the left. A particle of this size exhibits a hotspot inside the particle itself, indicating that if a polymeric substrate were to be placed on the exit side of the particle (i.e. the particle is sitting on a substrate and irradiated normal to the substrate) then the

polymer substrate would be predominantly affected by the "tail" of the hotspot, rather than the most intense part of the focussed beam.

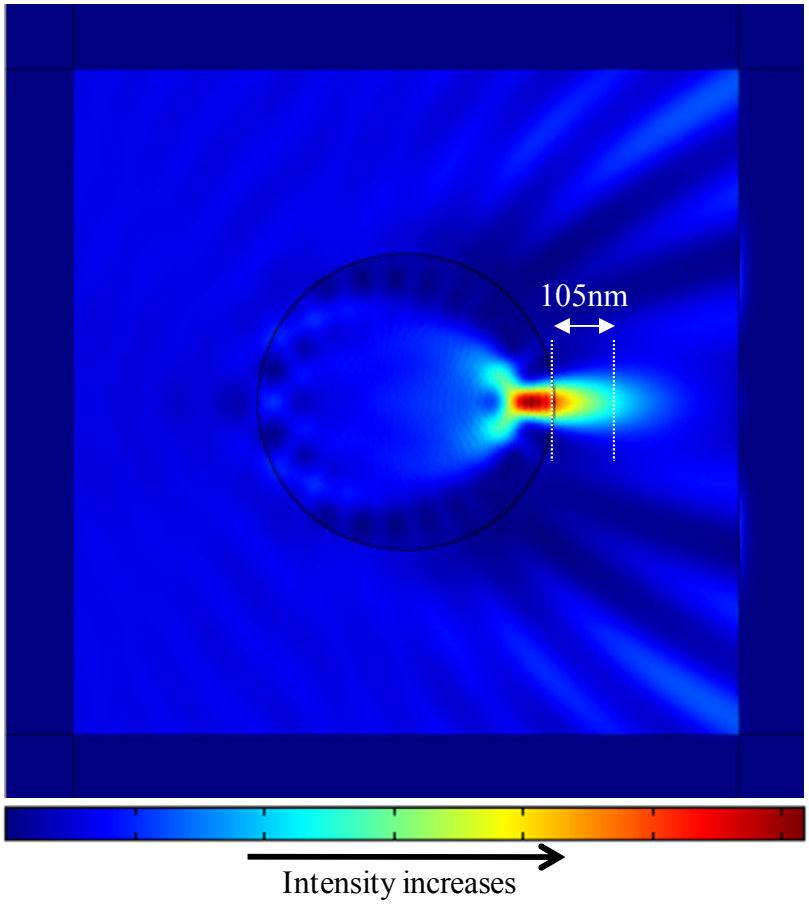

Figure 3.1: Two-dimensional FEM analysis of the intensity around a 500nm diameter silica particle irradiated at 157nm with TM polarised radiation (from the left).

In the case of the 500nm diameter silica particle shown above, the focussed field protrudes outside the particle. The intensity profile through the particle is shown in Figure 3.2a). From this model, the focussed field protrudes ~105nm from the exit side of the particle. The full width at half maximum, FWHM, of the focus at the base of the particle is 60nm, as shown in the intensity profile in Figure 3.2b).

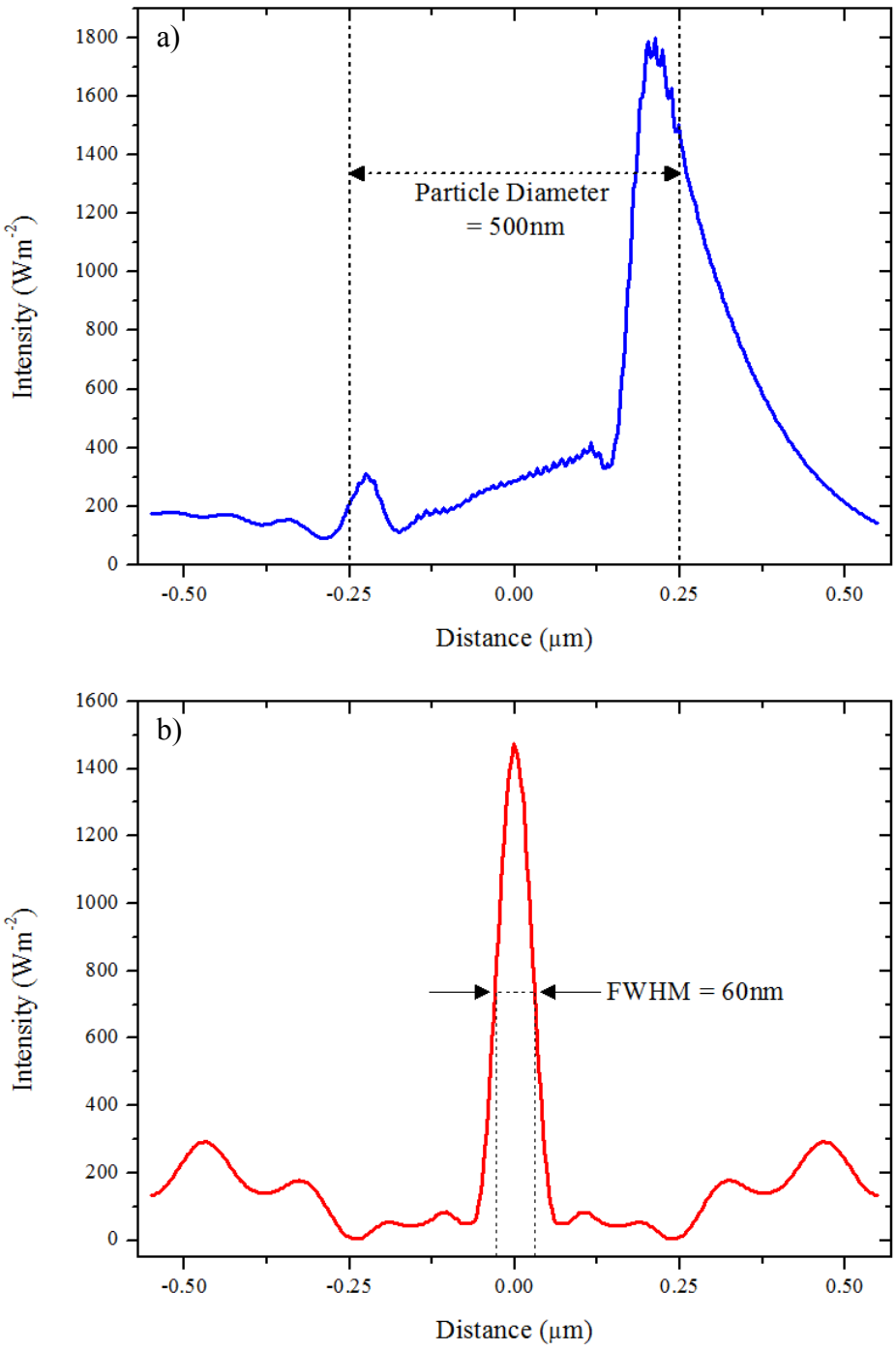

Figure 3.2: Intensity profile of a 500nm diameter silica particle irradiated at 157nm – a) following the direction of the beam from left to right through the particle and b) from bottom to top at the base of the particle.

The model for a 1μm diameter particle, shown below in Figure 3.3, shows that a silica particle of this size also exhibits the lens effect. The intensity hotspot is located inside the particle at the boundary at the exit side of the particle (in this case on the right hand side of the particle as the irradiation is incident from the left).

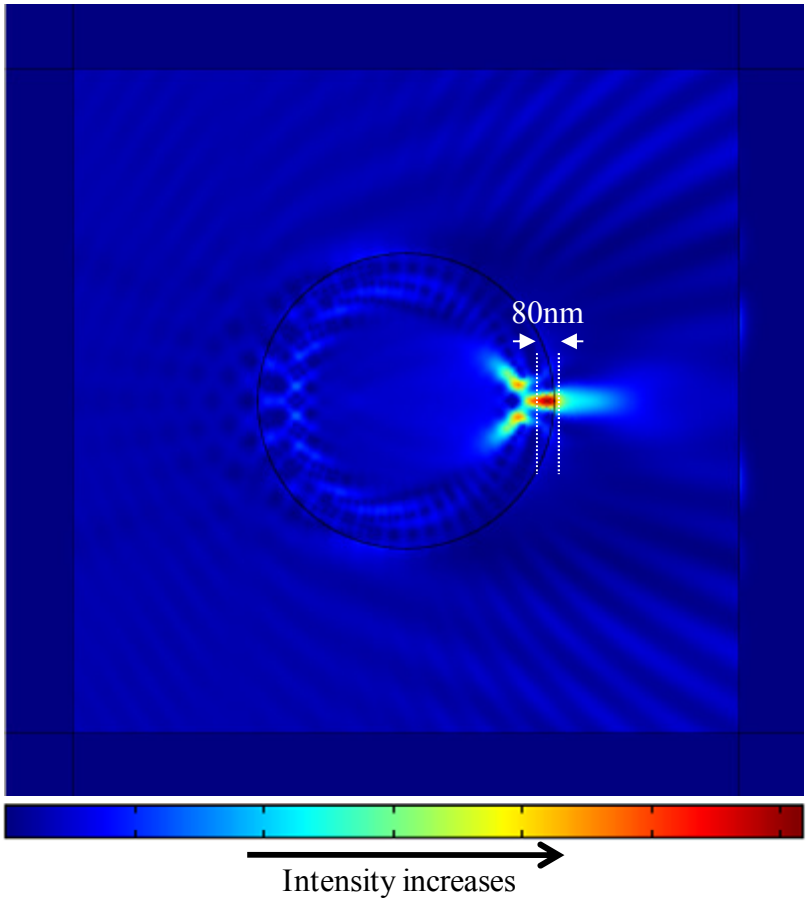

Figure 3.3: Two-dimensional FEM analysis of the intensity around a 1µm diameter silica particle irradiated at 157nm with TM polarised radiation (from the left).

In the case of the 1µm diameter silica particle, the hotspot is at the boundary of the particle, and the focussed field protrudes outside the particle, which would affect a substrate placed adjacent to this particle. The substrate would be influenced by the tail of the focussed beam, as shown by the intensity profile shown in Figure 3.4a), which protrudes ~80nm outside the particle. The FWHM of the focussed field at the base of the particle is 63nm, as shown in the intensity profile in Figure 3.4b).

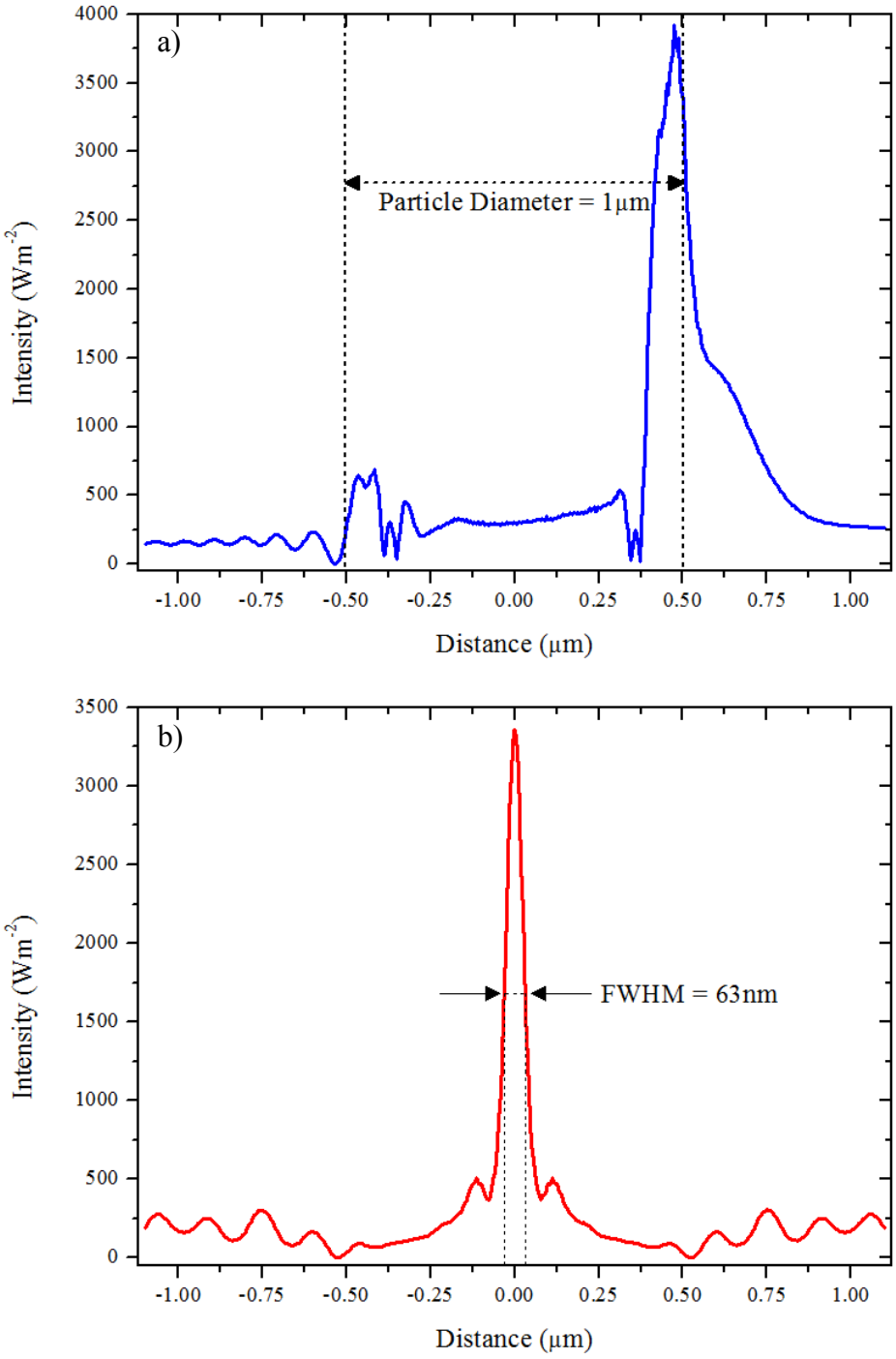

Figure 3.4: Intensity profile of a 1µm diameter silica particle irradiated at 157nm from the left – a) following the beam direction from left to right through the particle and b) from bottom to top at the base of the particle.

In order to observe this lens effect experimentally, 500nm diameter and 1µm diameter silica particles were dispersed onto a CR-39 polymeric substrate by drop-casting. The particles (Kisker Biotech, Germany), purchased in aqueous solution, were diluted further in de-ionised water to a solution of low particle concentration, ~2%. A small amount of each dilute solution was dropped onto a CR-39 polymer substrate that had been cleaned by sonication in isopropanol and blown dry with nitrogen, N_2, gas, and left for the solvent to evaporate completely. This method results in a largely single layer of

particles, as shown in the Scanning Electron Micrographs (SEMs) in Figure 3.5 below. As shown in the SEMs, there are also regions on the substrate where there are no particles and regions with multiple layers of particles.

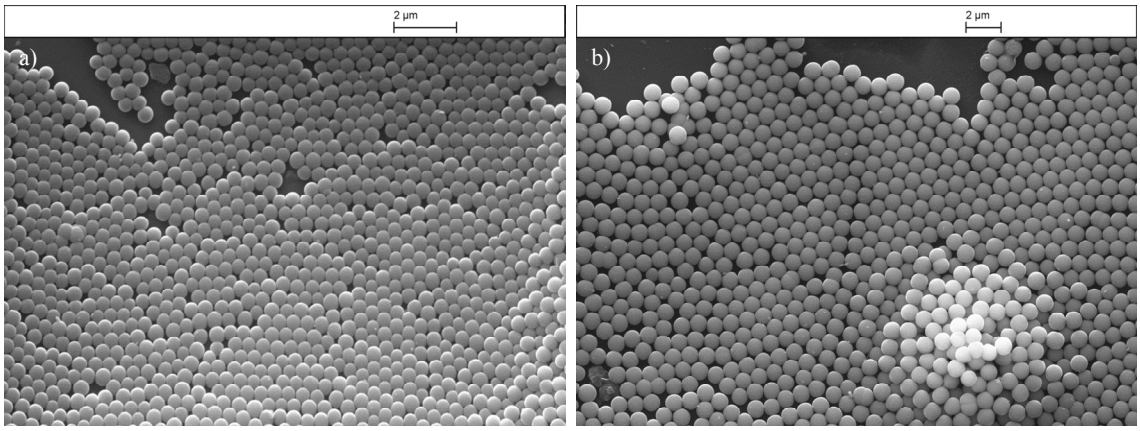

Figure 3.5: Scanning Electron Micrographs of drop-cast silica particles on CR-39 polymer substrate – a) 500nm diameter particles and b) 1µm diameter particles. Both SEMs viewed at normal incidence.

These samples were irradiated at a wavelength of 157nm, with a single pulse at known fluences.

The SEM images in Figure 3.6 below show the result of irradiating 500nm diameter silica particles with 157nm laser radiation with 1 laser pulse at fluences of 325mJcm^{-2} (Figure 3.6a) and b)) and 545mJcm^{-2} (Figure 3.6c) and d)). In both instances, the particles have been removed from the substrate surface, exposing the effect of the light focusing properties of the silica particles on the underlying substrate. Left behind after the particles have been removed is a pattern of dimples, or craters, where the particles were once located. As shown in the higher magnification images, Figure 3.6b) and Figure 3.6d), these dimples are not particularly circular. This may be as a result of the hotspot of the particle-focused light being inside the particle, so the light that actually interacts with the substrate is not highly focussed or intense.

The dimples shown in Figure 3.6 have a diameter of ~150-180nm, which is roughly the same as the wavelength of the incident laser beam. A hexagonal pattern can be seen in the arrangement of the dimples, similar to the hexagonal packing arrangement shown by the 500nm diameter particles in Figure 3.5a). The length of the sides of the hexagons are on average ~450nm.

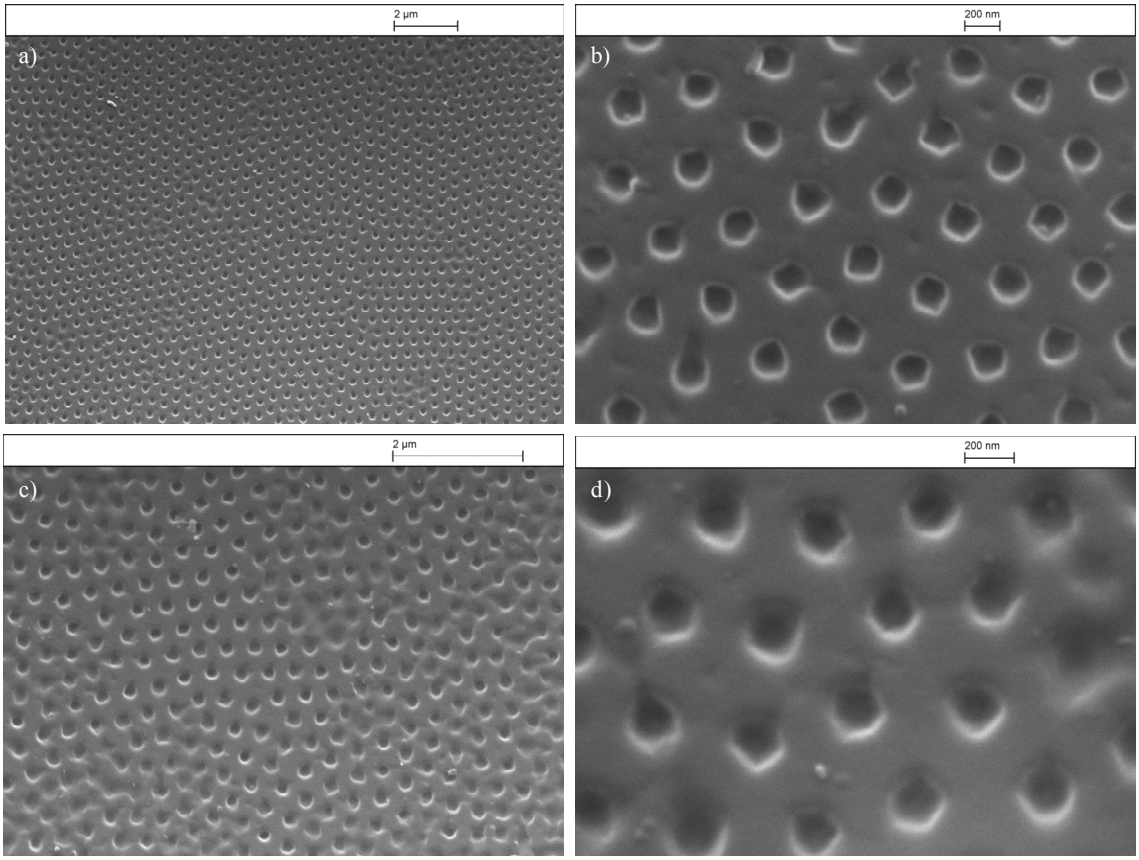

Figure 3.6: VUV 157nm F_2 laser ablation of 500nm diameter silica particles – a) 1 pulse at fluence of 325mJcm^{-2}, c) 1 pulse at fluence of 545mJcm^{-2}. Note: b) and d) are magnified images of a) and c) respectively. All SEMs viewed at normal incidence.

The results of irradiating 1µm diameter silica particles with 157nm laser radiation with 1 laser pulse at fluences of 325mJcm^{-2} (Figure 3.7a), b) and c)) and 530mJcm^{-2} (Figure 3.7d)) are shown below. As with the irradiation of the 500nm diameter particles, the 1µm diameter particles have been removed from the substrate surface, exposing the dimples left behind on the underlying substrate. Unlike the dimples left behind by the 500nm diameter particles, these dimples are much more circular, as shown in the higher magnification image in Figure 3.7b). This is likely due to the fact that, as shown in the FEM model in Figure 3.3, the hotspot is located at the edge of the silica particle, and hence the part of the focussed beam that interacts with the underlying polymeric substrate is fairly intense and focussed.

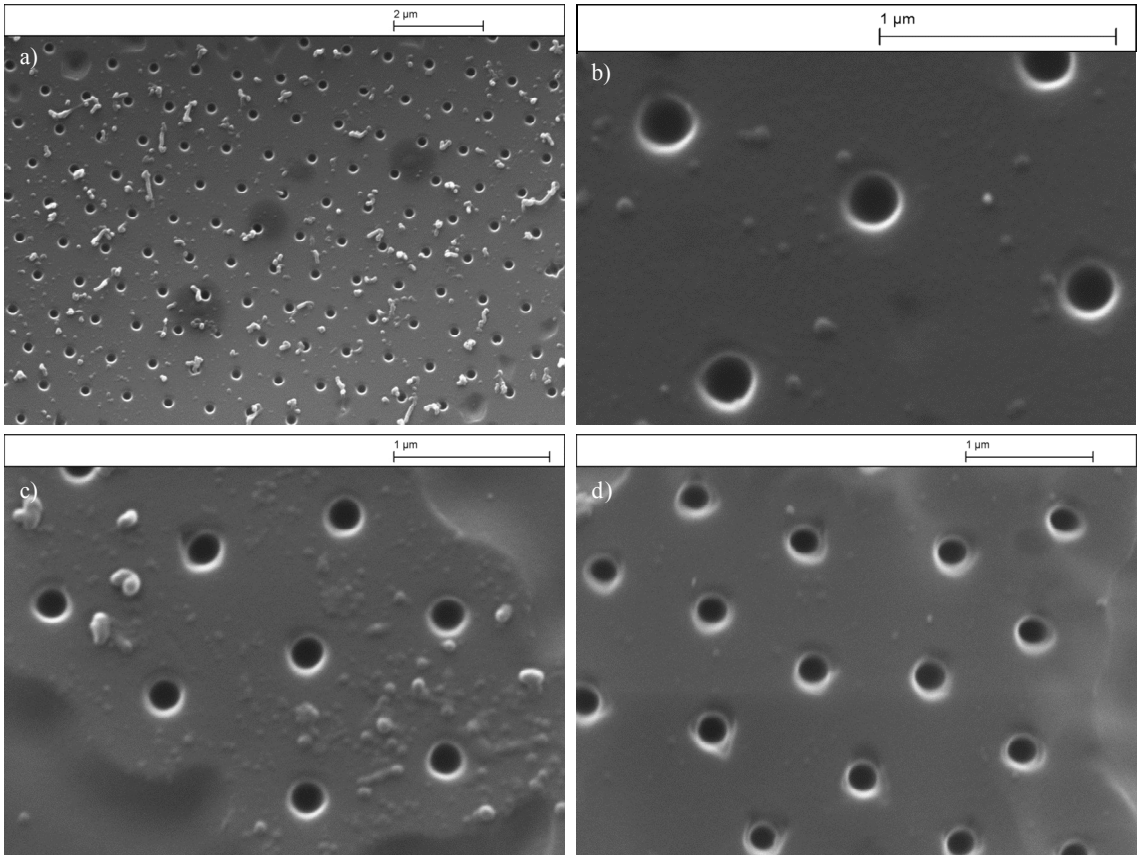

Figure 3.7: VUV 157nm F_2 laser ablation of 1µm diameter silica particles – a) 1 pulse at fluence of 325mJcm^{-2}, c) 1 pulse at fluence of 325mJcm^{-2}, d) 1 pulse at fluence of 530mJcm^{-2}. Note: b) is a magnified image of a). All SEMs viewed at normal incidence.

The dimples shown in Figure 3.7 have a diameter of ~200-220nm, which is comparable to the wavelength of the incident laser beam. Similarly to the 500nm diameter silica particles and their fabricated dimples, the 1µm diameter silica particles, shown in Figure 3.5b), form a hexagonal packing arrangement, which results in the dimples again exhibiting a hexagonal pattern. The length of the sides of these hexagons, fabricated using 1µm diameter particles, are on average ~960nm – over double the size of the hexagons formed by the irradiation of the 500nm diameter particles.

The hexagonal arrangement shown by the laser-fabricated dimples for the 500nm and 1µm diameter silica particles are demonstrated more clearly in Figure 3.8.

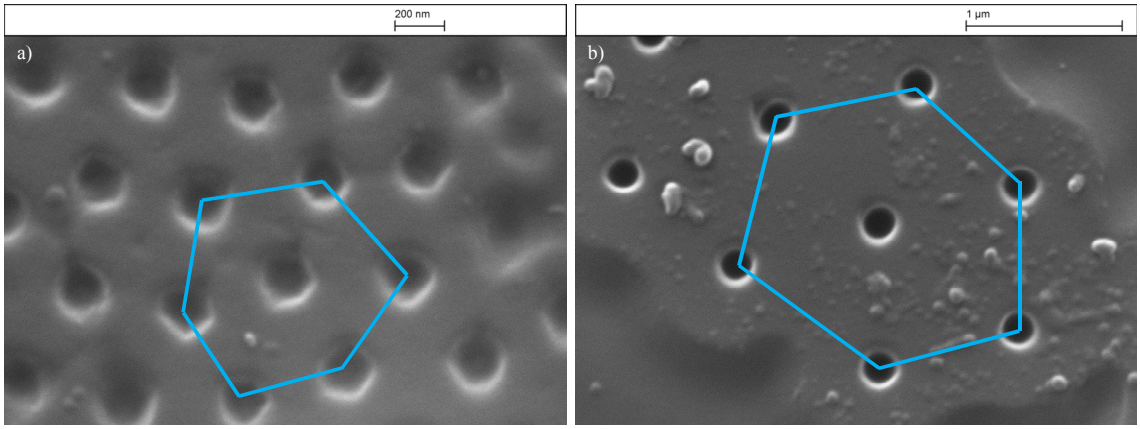

Figure 3.8: Hexagonal arrangement of dimples fabricated by irradiation at 157nm of a) 500nm diameter silica spherical particles and b) 1µm diameter silica spherical particles.

The length of the side of a hexagon in a packing arrangement can be calculated using [88]

$$l = 2r$$

Equation 3.1

where l is the hexagon side length and r is the radius of the particle. Using this equation the hexagon side lengths should be roughly equal to the diameter of the particles, which corresponds well with the measurements taken from Figure 3.6 and Figure 3.7.

The 500nm diameter and 1µm diameter silica particles were also irradiated at these fluences with 5 and 10 laser pulses. At these higher pulse numbers, the dimple effect seen above is smoothed off until the polymer is flat.

What cannot be determined from the SEM images shown in Figure 3.6 and Figure 3.7, is how far the dimples extend into the substrate, and the shape of the bottom, i.e. if it is rounded or if the dimple comes to a sharp tip etc. The shape of the "tail" of the hotspot in the FEM models shown in Figure 3.1 and Figure 3.3 would potentially suggest that the bottoms of the dimples are rounded, however substrate material melting dynamics may also influence the shape of the dimples.

Section 3.2.2 - Inverse Moulding of Dimples

One method of determining the depth and profile of the dimples fabricated by VUV 157nm F_2 laser irradiation of transparent particles is by inverse moulding the substrate using PDMS. This method has previously been used to observe the profile of laser-irradiated N-BK7 glass, where it demonstrated an ability to resolve sub-micron features [89].

PDMS base was mixed with the curing agent in a ratio of 10:1 and applied to the laser-irradiated CR-39 polymer substrates that had previously been covered with 500nm and 1μm diameter silica particles and were exposed to 1 pulse of 157nm laser radiation. The sample was placed in a vacuum chamber to remove any air bubbles and was then left overnight in an oven at ~60°C to cure fully, before being carefully separated from the CR-39 polymer substrate.

The PDMS filled the dimples created by the irradiation of 500nm diameter silica particles on CR-39 polymer, and created the nanobumps shown below in Figure 3.9. The dimples, shown in Figure 3.6c) and d), which were moulded in order to form these bumps, were fabricated by the irradiation of 500nm diameter silica particles with a single laser pulse at 545mJcm^{-2}.

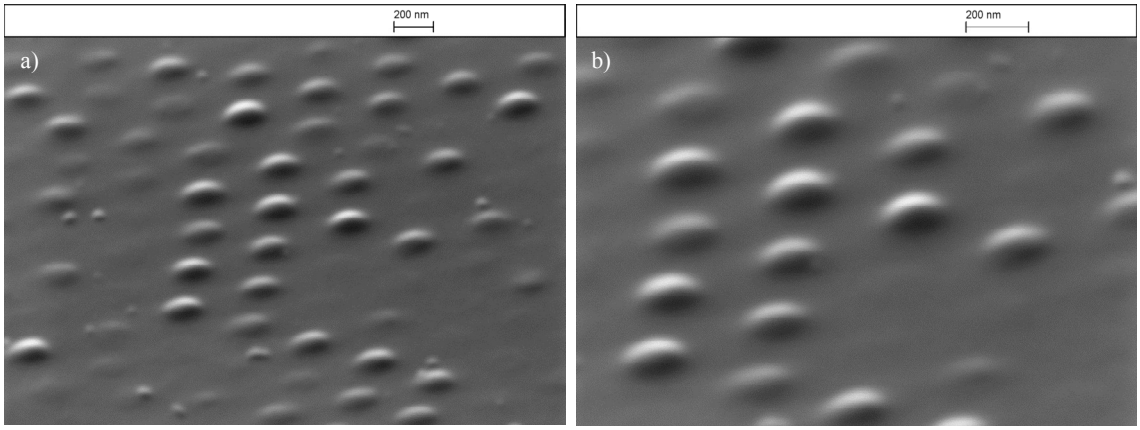

Figure 3.9: Nanobumps created by PDMS inverse moulding of dimples created by the irradiation of 500nm diameter silica particles with a single laser pulse at 545mJcm^{-2}. Both SEMs viewed at 60°.

These nanobumps have diameters ~205 ± 15nm. The diameters of the original dimples were in the range ~150-180nm, and as they do not have sharp edges, this would suggest the dimples would have a larger footprint – agreeing with the nanobump diameter. The nanobumps are ~80nm in height. The FEM modelling suggested a hotspot length, and hence dimple depth of ~105nm. The FEM modelling of the irradiation of the 500nm diameter silica particles, shown in Figure 3.1, seemed to suggest that the dimples would have rounded bottoms, and the profile of these nanobumps appears rounded, suggesting good agreement between modelling and experiment. The nanobumps exhibit the same hexagonal arrangement shown by the non-irradiated silica particles and the laser ablated dimples.

Section 3.2.3 - Removal of Particles from a Substrate by Laser Irradiation

It is worth noting that during irradiation, the particles are ejected from the surface of the substrate material. This process has been widely studied in the literature [30, 86, 87, 90, 91].

The main mechanisms that influence the removal of the particles are the focussing effect of the particle itself, and thermal expansion of the substrate material. The focussing effect of the small particle, much like a lens, results in high intensities in the near-field region and leads to the formation of a hotspot. If sufficient laser intensity is applied to the substrate surface, i.e. above the ablation threshold for the substrate material, the material is broken down and ejected from the bulk of the substrate. This acceleration of material, as well as the thermal expansion of the masking particle and/or substrate, is sufficient to remove the masking particle as well.

For dimple fabrication, the field enhancement is needed underneath the particle, at the interface with the substrate material. Evidently, this hotspot effect has some influence on the removal of the particle from the surface and is also responsible for the patterning of the surface, whether by the formation of a dimple, a nanoring or a nanobump.

A number of different factors influence the laser cleaning efficiency, including particle size, particle and substrate material properties, laser fluence and laser wavelength. Substrate surface roughness and the angle of laser beam incidence have also been shown to have an effect on the cleaning efficiency [86].

In order for the particle to be removed, the laser beam must overcome the adhesion force between the particle and the substrate. This adhesion force occurs due to the dipole interactions inducing an attractive van der Waals force between the particle and the substrate. In 1937, Hamaker determined that the attractive force, F, between a spherical particle and a substrate is given by [86, 92]

$$F = \frac{\langle \hbar\omega \rangle R}{8\pi h^2} + \frac{\langle \hbar\omega \rangle a^2}{8\pi h^3}$$

Equation 3.2

where R is the particle radius, a is the radius of contact, and h is the separation distance between the particle and the substrate - this is typically taken to be 4Å [86]. The radius of contact, a, for a spherical particle on a substrate is [86]

$$a^3 = \frac{3}{4}\frac{P_l R}{E^*}$$

Equation 3.3

where

$$\frac{1}{E^*} = \frac{1-\sigma_p^2}{E_p} + \frac{1-\sigma_s^2}{E_s}$$

Equation 3.4

and the loading force

$$P_l = \frac{\langle \hbar\omega \rangle}{8\pi}$$

Equation 3.5

These equations take into account the particle and substrate material properties, where σ_p and σ_s are the Poisson coefficients and E_p and E_s are the Young's Moduli for the particle and substrate respectively.

The Lifshitz constant, $\langle \hbar\omega \rangle$, is related to the Hamaker Constant, A, by [86]

$$A = \frac{3}{4\pi}\langle \hbar\omega \rangle$$

Equation 3.6

The Hamaker constant is dependent on both the materials, i.e. the particle and the substrate, and the individual Hamaker constants for each material are combined as follows [93]

$$A = \sqrt{A_p A_s}$$

Equation 3.7

where $A_{p,s}$ are the Hamaker constants of the particle and substrate respectively.

In the case of the irradiation of silica particles on a polycarbonate substrate, A_{SiO2} = 68.5×10^{-21}J [94] and A_{PC} = 7×10^{-20}J [95], so from Equation 3.7 the combined Hamaker constant A = 6.93×10^{-20}J. The relationship between particle radius, R, and the attraction force, F, for a silica particle, diameter 50nm-10μm, on a polycarbonate substrate can be seen in Figure 3.10 below. The attraction forces for polystyrene and silver particles are also shown in Figure 3.10 for comparison. The individual Hamaker

constants for polystyrene and silver are A_{PS} = 7.9×10^{-20}J [96] and A_{Ag} = 3.496×10^{-19}J [97], and the incorporation of a polycarbonate substrate gives combined Hamaker constants of A_{PS-PC} = 7.436×10^{-20}J and A_{PS-PC} = 1.564×10^{-19}J respectively.

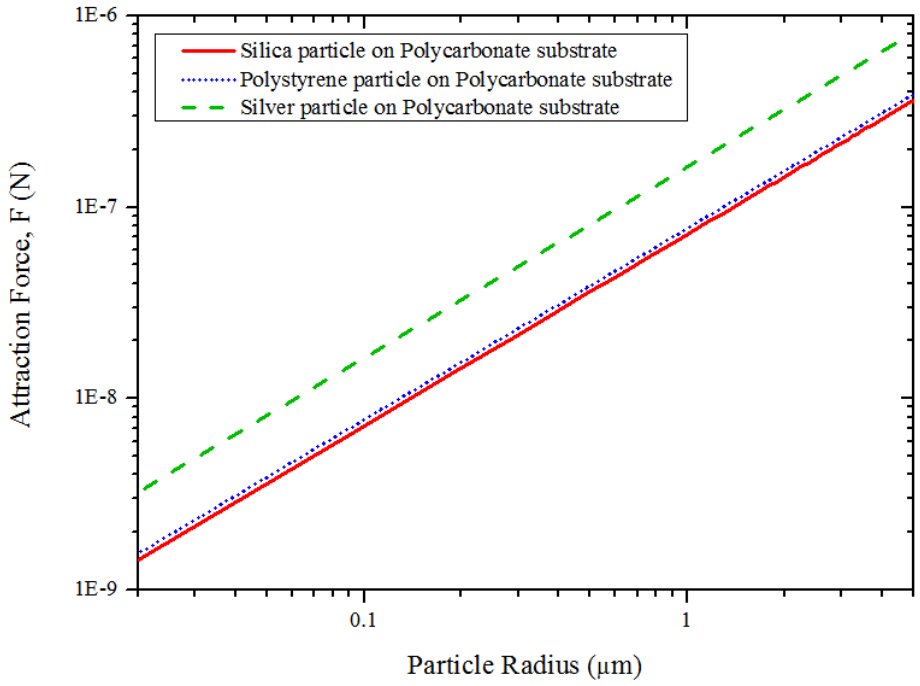

Figure 3.10: Attraction force vs particle radius for silica (solid red line), polystyrene (dotted blue line) and silver (dashed green line) particles on polycarbonate substrate.

When irradiated using a laser, this large attractive force between the particle and the substrate must be overcome by the force induced by the laser beam in order for the particle to be removed.

It is worth noting that the fluence at the base of the particle, i.e. at the interface between the particle and the polymeric substrate, is greatly increased from the initial irradiating fluence by the lens effect of the particle. Although in this case the initial fluences are much greater than the ablation threshold of CR-39 polymer (see section 2.2.2 for material properties), the lens effect increases the incident fluence even higher so that significant material removal can occur.

It has been shown the presence of a transparent spherical particle changes the intensity distribution underneath the particle at the particle-substrate interface. When the particle is larger than the incident wavelength a geometric approximation can be used to quantify this in terms of the size parameter $a = 2\pi r/\lambda$ (Equation 1.7) where r is the particle radius and λ is the radiation wavelength. Spherical particles of diameters 500nm and 1µm correspond to size parameters of a = 10 and a = 20 respectively, and the

intensity underneath the particle can be approximated using a ray tracing approach using Snell's law. If the intensity within the caustic (or focus) underneath the particle is assumed to be homogeneous from imperfections inside the spherical particle and also by reflections from the substrate, the intensity enhancement underneath the particle can be estimated using [87]

$$\frac{I_m}{I_0} = \frac{r^2}{\omega^2} = \frac{27n^4}{(4-n^2)^3}$$

Equation 3.8

where r is the particle diameter, ω is the intensity hotspot size, n is the refractive index of the particle and I_m and I_0 are the maximum and incident light intensities respectively. Using Equation 3.8 above, the intensity enhancement factor for 500nm and 1μm diameter silica particles is ~126 and hence there is a concommitant increase in the laser fluence at this spot.

It is of interest to note that the intensity enhancement is identical for both sizes of spherical particles as there is a concomitant change in the spot size, ω, which can be approximated from the caustic produced underneath the particle using [87]

$$\omega = r\sqrt{\frac{(4-n^2)^3}{27n^4}}$$

Equation 3.9

Equation 3.9 results in a spot size of ~40nm and ~44nm for spheres of diameter 500nm and 1μm respectively.

As a consequence of the intensity enhancement there is increased energy loading beneath the particle and hence an increase in the substrate temperature. This leads to thermal expansion of the substrate and increased deformation and stresses. The temperature rise of the substrate can be analytically solved using Green's function and the linear heat equation, and for simplicity the material properties can be kept constant. The calculations can be used to determine the processes that occur during the interaction with the 157nm laser radiation. Although in the experiments CR-39 polymer was used as the substrate, due to the lack of data for this material at a wavelength of 157nm, the calculations will assume polycarbonate is the substrate material.

The temporal intensity profile of the 157nm laser pulse can be simulated using [30]

$$I(t) = \frac{Ft}{\tau_L^2} exp\left[-\frac{t}{\tau_L}\right]$$

Equation 3.10

where F is the laser fluence, $\tau_L = 0.408\tau$ is the laser pulse parameter, τ = 11ns is the laser pulse duration at FWHM and t is the time. Using Equation 3.10 the laser pulse profile can be plotted, as shown in Figure 3.11 .

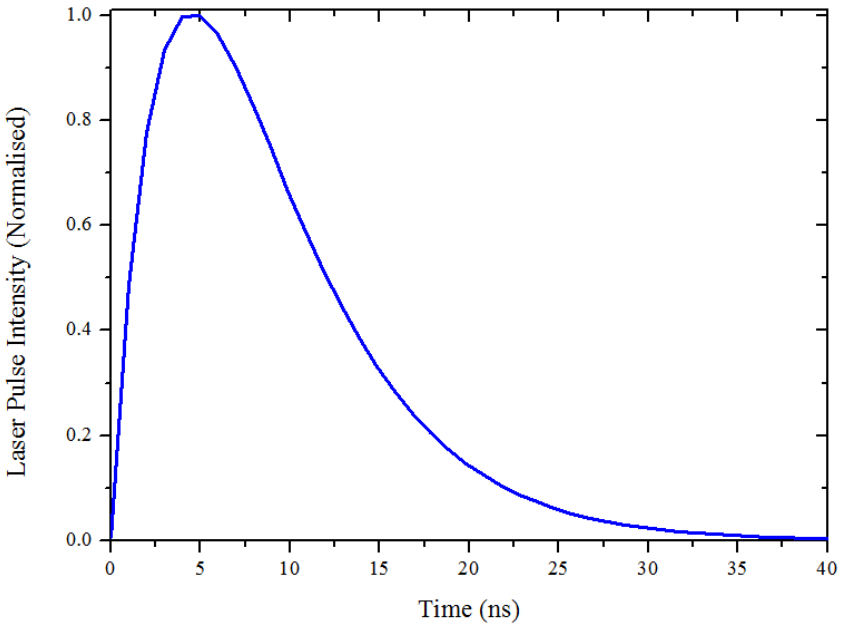

Figure 3.11: Temporal intensity profile of a pulse from the VUV F_2 laser. The laser pulse duration at FWHM is ~11ns.

For simplicity, the intensity distribution of the z component in the x-y plane underneath the particle is approximated by a Gaussian function $S(x,y) = S_0 \exp(-r^2/r_0^2)$ where r is the radial coordinate. With this assumption, the solution to the linear heat equation can be used to calculate the temperature in the substrate using [87]

$$T(r,z,t) = S_0 \frac{A_0\,\alpha}{c_s\,\rho} \int_0^t I_0(t-t_1)\, \frac{exp\left(-\frac{r^2}{\omega^2 + 4\chi t_1}\right)}{1 + 4\chi \frac{t_1}{\omega^2}} F(z,t_1)dt_1$$

Equation 3.11

where S_0=126 is the enhancement factor using Equation 3.8, A_0 is the absorptivity, α = 2.8×10^{5}cm^{-1} is the absorption coefficient, c_s = 1.2Jg^{-1}K^{-1} [supplier] is the specific heat capacity, ρ = 1.2gcm^{-3} [98] is the density, ω is the spot size using Equation 3.9 and χ is the thermal diffusivity and $F(z,t_1)$ is given by [30]

$$\chi = \frac{k}{c_s \rho}$$

$$F(z,t_1) = \frac{1}{2}\exp(\alpha^2 \chi\, t)\left\{\exp(\alpha^2 z)\, erfc\left[\alpha\sqrt{\chi t} + \frac{z}{2\sqrt{\chi t}}\right] + \exp(-\alpha z)\, erfc\left[\alpha\sqrt{\chi t} - \frac{z}{2\sqrt{\chi t}}\right]\right\}$$

Equation 3.12

where k = 0.00192Js^{-1}cm^{-1}K^{-1} [98] is the thermal conductivity of the substrate.

The incident energy, and subsequent temperature increase, is focussed in a small area beneath the transparent particle, as shown in Figure 3.12 below.

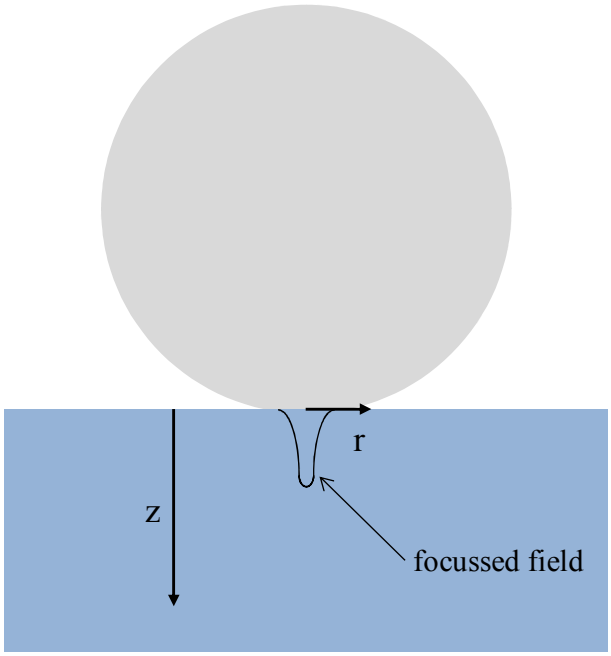

Figure 3.12: Schematic showing the radial, *r*, and depth, *z*, components for the temperature calculations.

The theory suggests that the temperature increase is sufficient to induce melting of the polycarbonate substrate. While this model calculates a maximum temperature of nearly 2.5×10^{5}K, this is clearly not experimentally possible. This figure occurs as Equation 3.11 and Equation 3.12 assume that the thermal conductivity of the substrate is temperature independent, which is not true in practice. These calculations assumed an incident laser fluence of F=325mJcm^{-2} (the energy loss through the particle is negligible).

The graph for the predicted temperature against time, shown in Figure 3.13, indicates that the temperature is highest directly underneath the particle, i.e. at r=0nm. At this point, the temperature drops back to its initial temperature over a period of approximately 100ns. A similar process occurs at the surface further away from the contact point, i.e. where r=50nm and r=100nm, although the temperature increase due to the incident energy is not as elevated.

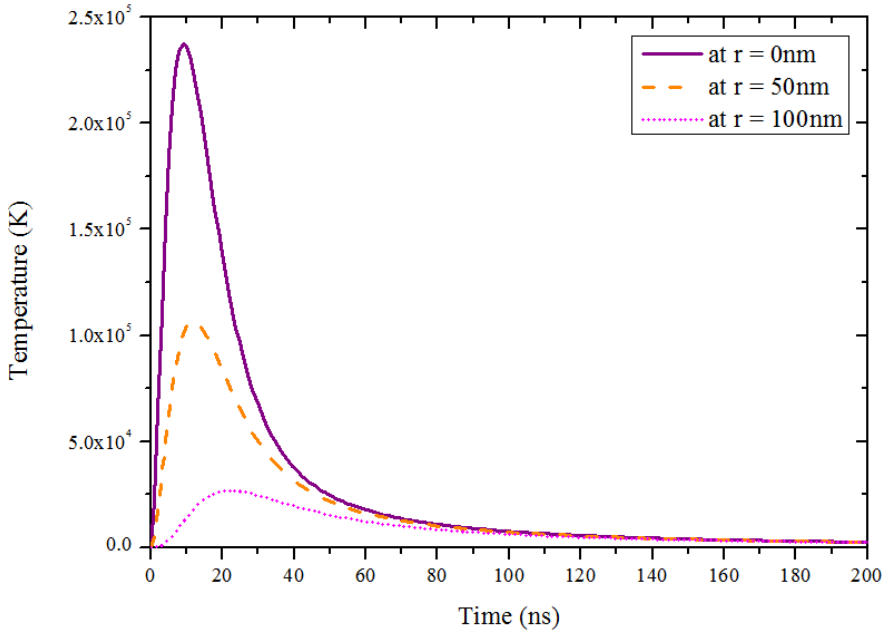

Figure 3.13: Predicted temperature against time for different radial positions across the surface of the substrate.

Similarly, Figure 3.14 shows the temperature against the distance into the substrate material directly underneath the particle, i.e. at r=0nm. The graph shows that as the distance into the substrate material increases the temperature of the material decreases. This is true for three different times after the application of the laser pulse, denoted by 1τ, 2τ and 3τ. The graph shows that at a depth of approximately 200nm the temperature remains unchanged, which indicates that the energy from the incident laser beam that is focussed by the transparent, lens-like particle does not propagate to this distance into the substrate material.

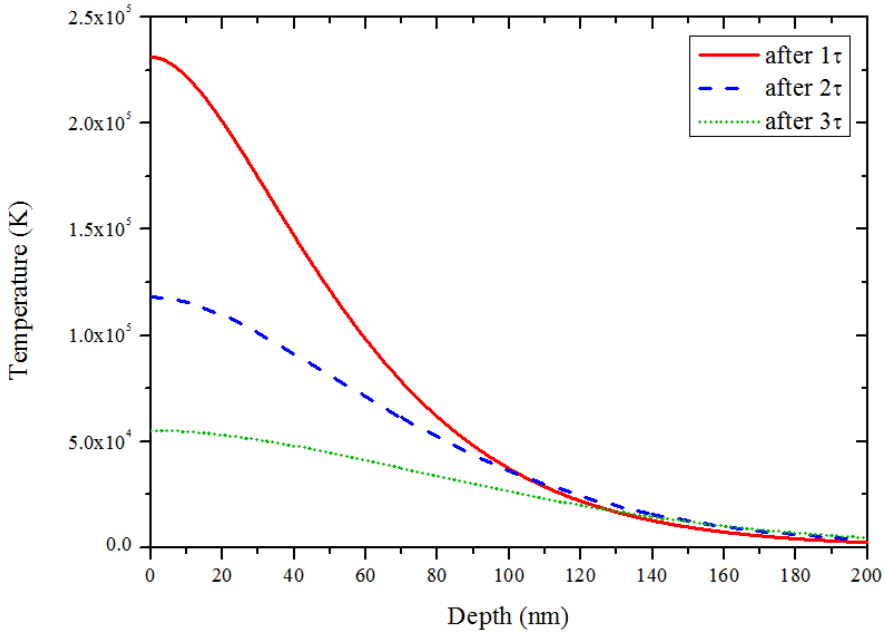

Figure 3.14: Predicted temperature against depth into the substrate after different lengths of time.

The temperature of the substrate is the same for both sizes of particle, as the loss of energy through the particles is negligible due to their high transmission capabilities.

The energy absorbed by the substrate will not only induce a temperature increase but also induce thermal stresses and acceleration of the underlying substrate. This, combined with expulsion of the ablation products, will assist in the ejection of the silica particle from the substrate. The experimental results suggest that the spherical particle is ejected from the substrate after a single laser pulse. Recent results have reported the prevention of the spherical particles from being ejected from the underlying substrate by carrying out laser ablation in water [27]. This method allows multiple laser pulses to be applied to fabricate higher aspect ratio holes than when using single laser pulses. However, this technique may not be applicable at a wavelength of 157nm due to poor transmission in water.

Section 3.2.4 - Adjusting the Lens Effect of Small Transparent Particles

One method for altering the focal region of a small particle, and hence the size of the fabricated dimples, would be to change the wavelength of the laser that is used to irradiate the silica particles. The FWHM of the hotspot at the exit side can be used as an estimate of the size of the dimple.

Table 3.1 shows the FWHM at the exit side of a 500nm diameter silica particle at a number of different wavelengths, calculated using the FEM software.

Laser Wavelength (nm)	Refractive Index; real part		FWHM (nm)
157	1.676	(at 7.8eV)	70
193	1.567	(at 6.5eV)	78
266	1.50004	(at 4.075eV)	94
308	1.48719	(at 4.1034eV)	106
532	1.46008	(at 2.2705eV)	190
1064	1.44949	(at 1.1449eV)	550

Table 3.1: FWHM of hotspot at base of 500nm diameter silica particle irradiated at different wavelengths. Refractive index data from [85].

From this data, it can be seen that shorter wavelength lasers are much more effective for fabricating smaller diameter dimples.

The profiles of these hotspot regions can be seen in Figure 3.15 below. This graph shows that as the wavelength increases, the focussing effect of the 500nm diameter silica particle becomes reduced. This is confirmed by the broadening of the intensity peak and associated increase in the FWHM measurements shown in Table 3.1. The images from the FEM analysis also corroborate these results - when the particle is irradiated at a wavelength of 193nm as shown in Figure 3.15b), the intensity hotspot is very small at the exit side of the particle. However, when the particle is irradiated at a wavelength of 1064nm as shown in Figure 3.15c) the incident beam is no longer highly focussed by the particle and the hotspot at the exit side of the particle is almost as broad as the particle itself.

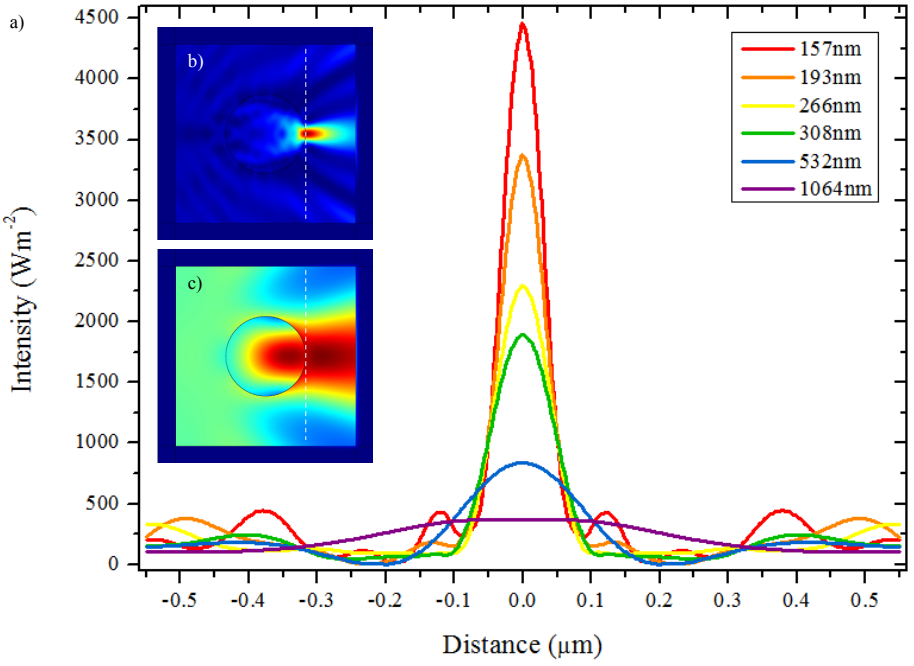

Figure 3.15: a) Predicted profiles of the intensity hotspot at the exit side of a 500nm diameter silica particle, irradiated at 157nm (red line), 193nm (orange line), 266nm (yellow line), 308nm (green line), 532nm (blue line) and 1064nm (purple line) wavelengths from the left; insets - b) irradiated at 193nm and c) irradiated at 1064nm. White dashed lines indicate the point at which the profile is taken.

It is also possible to adjust the focal region of the lens-like particle, and hence the dimple effect by changing the material the particle is made from. Table 3.2 below shows the real part of the refractive index for 5 different materials, and the FWHM of the focal region when a 1µm diameter particle of these materials is irradiated at a wavelength of 157nm.

Material (particle diameter 1µm)	Refractive Index; real part			FWHM (nm)
Water	1.311	(at 8.0057eV)	[76]	89
Magnesium Fluoride, MgF_2	1.478	(at 7.749eV)	[76]	72
Calcium Fluoride, CaF_2	1.607	(at 7.725eV)	[76]	58
Silica, SiO_2	1.702	(at 8eV)	[85]	60
Alumina	2.102	(at 7.932eV)	[99]	44

Table 3.2: FWHM for 1µm diameter particles of different materials and refractive indices.

Finite Element Method modelling was used to investigate the effect of irradiating these particles, and the intensity profiles through the particles are shown in Figure 3.16.

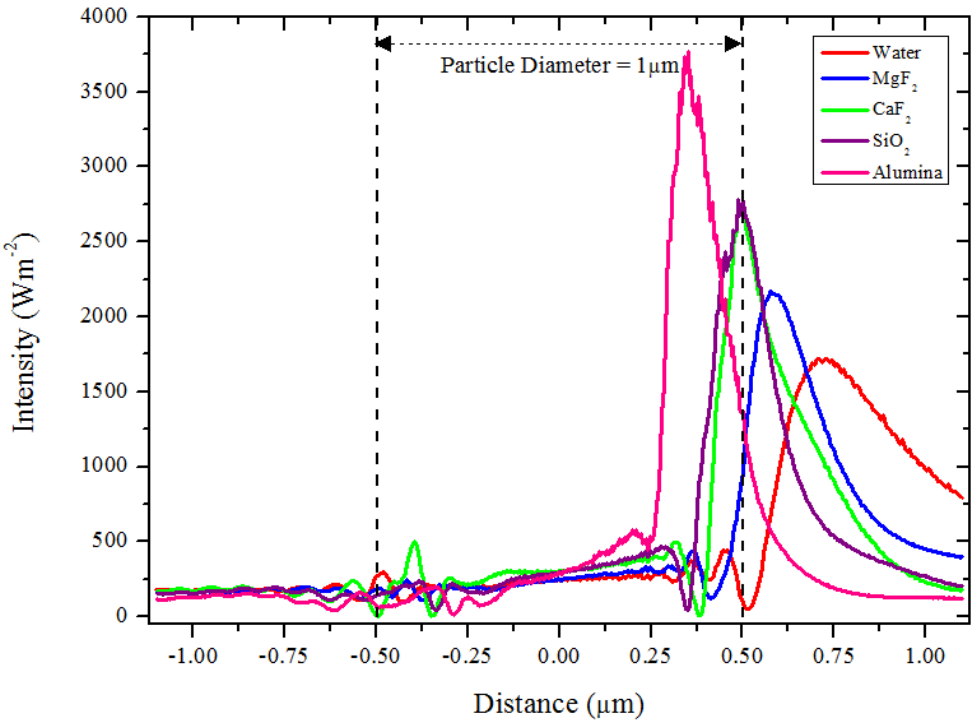

Figure 3.16: Predicted intensity profiles through 1µm diameter particles made from materials of different refractive index irradiated at 157nm using FEM software.

The point of highest optical intensity is located at the focal point of the particle, as shown by the graph in Figure 3.16. When the refractive index is low, for example water, $n_{water} = 1.311$, and MgF_2, $n_{MgF2} = 1.478$, the focal point is outside the particle. When the refractive index is close to that of glass, e.g. calcium fluoride, $n_{CaF2} = 1.607$, and silica, $n_{SiO2} = 1.702$, the hotspot is located at the edge of the particle, and as the refractive index increases, e.g. alumina, $n_{alumina} = 2.210$, the focal point moves towards the centre

of the particle. From Table 3.2 it can also be noted that as the refractive index increases, the FWHM of the focal point decreases, indicating that the light is being more highly focussed by the higher index materials than the lower index materials.

If a particle made of the higher refractive index materials, such as alumina, were to be irradiated at a wavelength of 157nm in order to fabricate dimples on the surface of an adjacent polymeric substrate, the dimples would likely be relatively non-spherical, similar to those seen in Figure 3.6: the portion of the focussed beam that interacts with the substrate would not be highly focussesd, as the focal point is further inside the particle than when using the silica particles. If particles made from the lower index materials, such as water and magnesium fluoride, were to irradiated at a wavelength of 157nm, the fabricated dimples would potentially be deeper than those seen here as the focal point of the particle is located outside the particle, i.e. beneath the surface of the substrate material. This may also result in the formation of voids just below the surface, pushing material upwards and forming a bump on the substrate surface instead of a dimple.

Section 3.3 - Conclusions

In this chapter, the interaction between the light from a VUV 157nm F_2 laser and small transparent particles has been investigated.

Silica is known to be transparent to 157nm radiation, subject to certain geometric conditions, and hence this material was used. The lens effect is known to occur in small transparent particles. Finite Element Method modelling was used to determine the optimum size silica particle to focus the 157nm radiation into a hotspot on the exit side of the particle, in order to influence and pattern an underlying polymeric substrate.

Silica particles of 500nm and 1μm diameter were chosen, and deposited on a CR-39 polymer substrate by drop-casting in order to fabricate a predominantly monolayer of particles. The particles were then irradiated with a single pulse from the 157nm laser, causing the fabrication of small dimples, or craters, on the surface of the polymeric substrate.

During the single pulse laser irradiation, the silica particle is ejected from the substrate surface. This process is known as laser cleaning, and the force induced by the laser beam is sufficient to overcome the attraction force between the particle and the substrate.

The dimples that were fabricated by the irradiation of the 500nm diameter silica particles were inverse moulded using PDMS to replicate the profile of the dimples. As shown by the PDMS nanobumps, the dimples have a rounded profile and are ~80nm deep. This measurement is comparable to the distance the focussed field is calculated to protrude from the particles in the FEM models for the two different sized particles.

Using FEM modelling, it has been shown that it is possible to adjust both the size and position of the focal point of the particle caused by the lens effect by changing the wavelength of the laser or by changing the material the particle is made from.

In this chapter, transparent particles supported on a polymeric substrate were irradiated with the VUV 157nm F_2 laser, creating dimples on the surface of the substrate. In the next chapter, the interaction with opaque particles on a polymeric substrate will be investigated.

Chapter 4: VUV 157nm F_2 Laser Irradiation of Opaque Spherical Particles

Section 4.1 - Introduction

In contrast to the previous chapter where transparent spherical particles were irradiated at a wavelength of 157nm, in this chapter particles that are opaque to 157nm radiation are used.

Instead of acting like a lens and focussing the incident laser beam as transparent particles do, opaque particles shield the underlying polymer from the laser beam while the substrate material surrounding the particle is ablated. This results in the formation of a composite conical structure, as the shielding particle remains attached to the substrate material. Interactions between the incident laser beam, the particle, substrate and structure wall result in the formation of a fringe pattern surrounding the base of the structure.

Polymeric substrate materials have been chosen due to their low ablation threshold fluences and good surface quality following ablation.

Following sample preparation by spin-coating, the opaque particles - in this case spherical polystyrene particles - will be irradiated both normal to and at 45° to the direction of laser beam propagation. When irradiated normal to the laser beam propagation direction, upright conical structures are formed, with the seeding polystyrene particle attached to the tip. When irradiated at an angle of 45° to the laser beam propagation direction, oblique conical structures are formed, again with the polystyrene particle attached to the tip.

Polystyrene particles of decreasing size will be used in order to determine the smallest seeding particle the laser can resolve, and hence the smallest footprint a conical structure could have on a substrate.

The effects of the incident laser fluence and number of pulses are also investigated with regards to their effect on the height of the fabricated composite conical structures.

Some materials are opaque at a wavelength of 157nm, including polystyrene, which has an extinction coefficient of 0.17 [100], corresponding to an optical absorption depth of ~73nm. As these materials are opaque to this wavelength, when irradiated with the 157nm laser the use of a seeding particle on a polymeric substrate results in the formation of a micro- or nano-sized composite structure comprised of the seeding particle and a support structure made from the substrate material.

Even the quickest survey of the literature shows that the ablation of both unseeded polymer substrates and polymer substrates seeded with opaque spherical particles is routinely carried out, and has been since the 1980's [7, 17-20], and more recently [10].

The presence of the opaque spherical seeding particle causes the formation of a conical structure when irradiated with the VUV 157nm F_2 laser. The particle shields the underlying substrate material, while that surrounding it is removed by ablation, shown schematically in Figure 4.1. The height and apex angle of the conical structure can be controlled by adjusting the laser fluence and number of applied pulses. Interactions between the incident laser beam and the growing structure, such as reflections from the particle and structure wall, cause an interference pattern to be ablated in the polymer substrate, around the base of the structure.

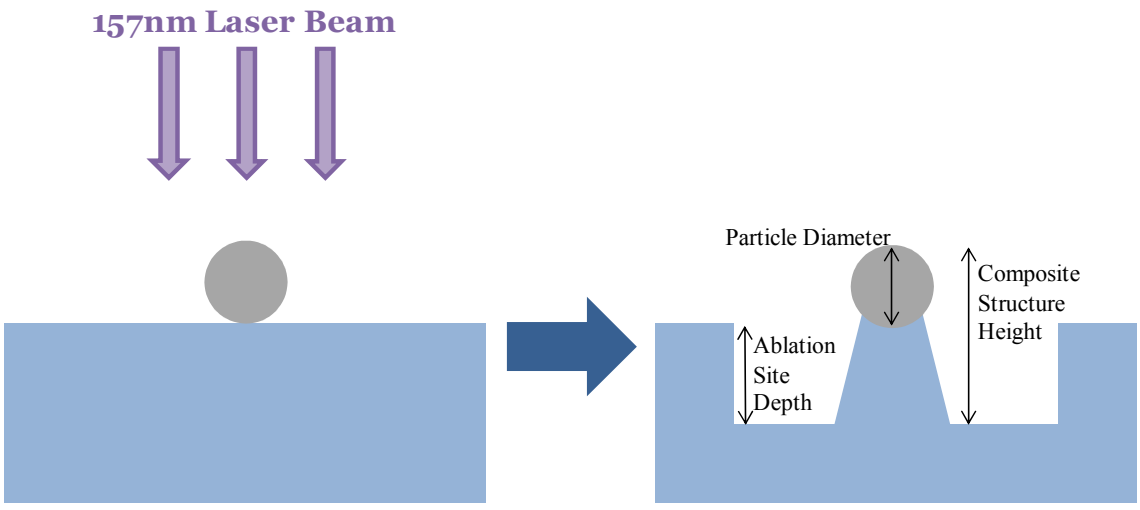

Figure 4.1: Process of the ablation of a spherical seeding particle on a substrate for the fabrication of a composite conical structure.

Section 4.2.1 - Sample Preparation

Prior to the experiments presented here, the substrates were sonically cleaned in isopropanol and in ultra pure water, and were then blown dry using nitrogen gas, N_2. This process was carried out to ensure that the substrates were as clean and free of

debris as possible, so that there was minimal or no contamination during the seeded ablation experiments.

The polystyrene particles of various sizes (Bangs Laboratories Inc, Fishers IN, USA and Kisker Biotech GmbH & Co, Steinfurt, Germany) were deposited on the CR-39 polymer and polycarbonate substrates by spin coating. Spin coating is a process used to apply thin uniform films to substrates by rotating the substrate at high speed (typically ≤6000rpm), thereby allowing the centrifugal force to spread the solution across the surface of the substrate. The thickness of the resulting film is dependent on the concentration of the solution and the speed at which the substrate is spun. Spin coating is traditionally used to apply thin films of polymers or photoresists, for example for use in solar cell fabrication. In the experiments presented here, the micro- and nanoparticles were dispersed in deionised (DI) water for spin coating. A small, known quantity of each particle solution was deposited onto the polycarbonate or CR-39 substrate, and the samples were spun for a certain length of time at a known speed to allow most or all of the solvent, in this case D.I. water, to evaporate. The spin-coated samples are shown in Figure 4.2. If some of the water had not evaporated during the spinning process, the samples were left to completely dry before being mounted into the F_2 laser sample holder, and irradiated at a wavelength of 157nm over a known fluence range with a known number of pulses per ablation site.

After ablation, the samples were characterised using an optical microscope (OM, Leica DMLM), a white light interferometer (Veeco WYKO NT1100 Optical Profiling System) and a Scanning Electron Microscope (SEM, Zeiss Evo 60).

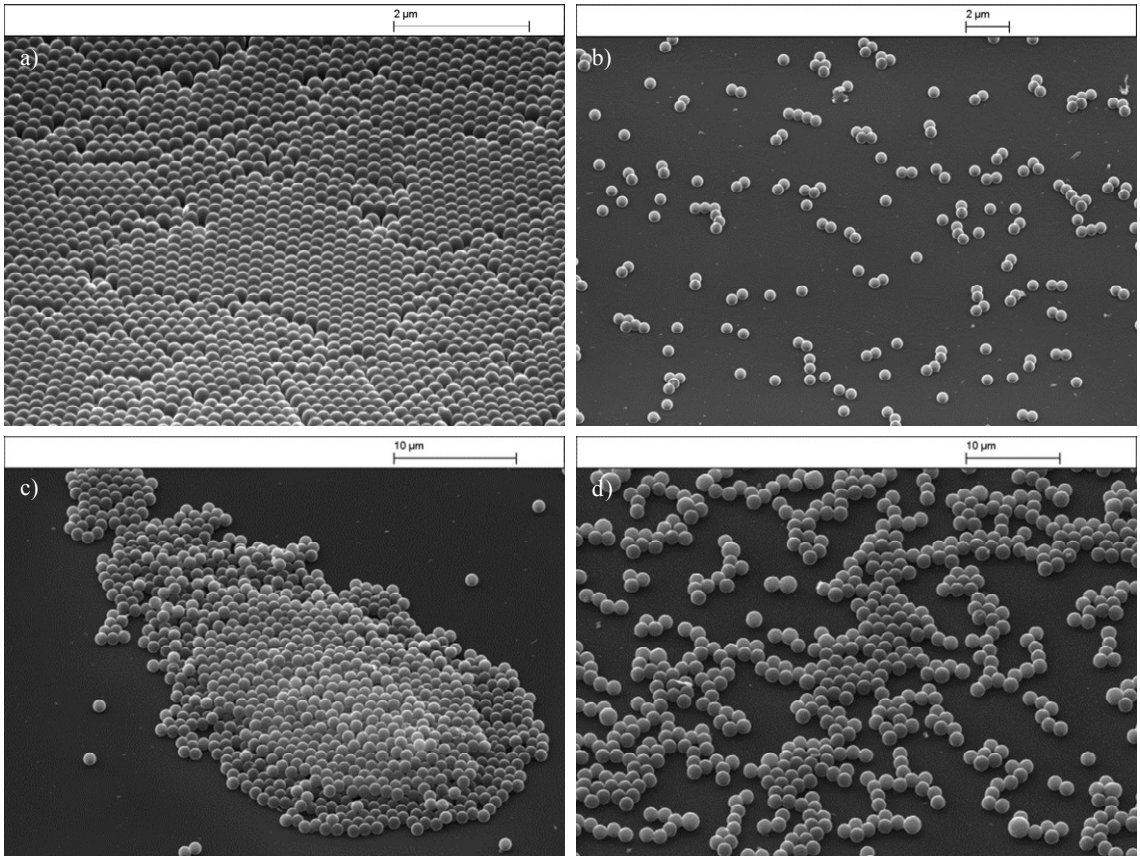

Figure 4.2: SEMs of non-irradiated polystyrene particles on polymer substrate, diameters - a) 210nm, b) 490nm, c) 1µm and d) 1.58µm.

Section 4.2.2 - Irradiation of Polystyrene Spherical Particles Normal to the Substrate

Composite conical structures all exhibit similar characteristics. They have an interference fringe pattern surrounding the base of the structure, and the seeding particle remains attached to the top of the structure. This results from either the particle and/or the substrate material melting and fusing together or by the attractive attachment force between the particle and substrate not being overcome by the force generated by the laser beam.

The conical structures have smooth, slightly curved walls, the angle of which is controlled by the ratio of F/F_T - the irradiating fluence over the threshold fluence. The sloping wall exists as a result of local diffraction effects, and this wall cannot be ablated as the local fluence falls below the ablation threshold fluence.

Using Equation 3.2, the attraction force between a polystyrene particle and polycarbonate substrate can be calculated using a combined Hamaker constant of $A = 7.44\times10^{-20}$J from Equation 3.7.

The forces of attraction for different size polystyrene particles are shown in Table 4.1 below.

Particle Diameter	Attraction Force (N)
50nm	1.94×10^{-9}
210nm	8.13×10^{-9}
490nm	1.90×10^{-8}
1μm	3.87×10^{-8}
1.58μm	6.12×10^{-8}

Table 4.1: Force of attraction between polystyrene particles of various sizes and a polycarbonate substrate.

The height of the polymeric structure supporting the particle can be finely controlled using the number of laser pulses and the laser fluence, and can range anywhere from a small "plinth" a few tens of nanometres high to a protruding structure several microns high. The Scanning Electron Micrographs (SEMs) in Figure 4.4, Figure 4.5 and Figure 4.6 below show a few examples of the types of structures that can be fabricated.

In all of these examples, the particles and substrates have been irradiated using the VUV F_2 laser with the sample orientated perpendicular to the direction of the laser beam, as shown in Figure 4.3.

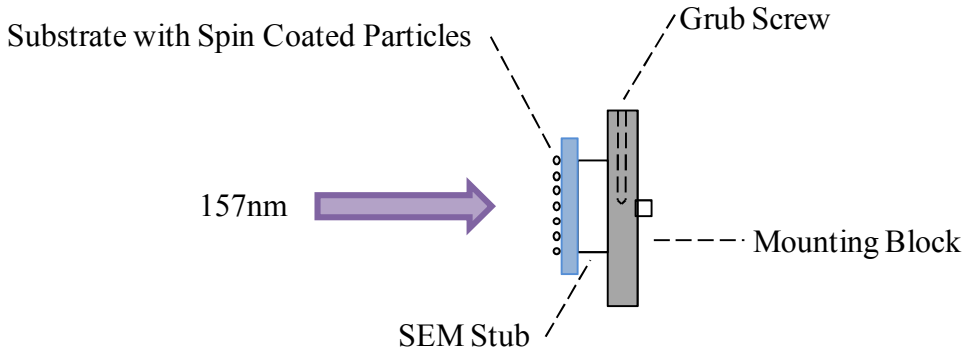

Figure 4.3: F_2 laser sample mounting arrangement for perpendicular laser beam incidence experiments.

The SEMs in Figure 4.4 show 490nm diameter polystyrene particles (Bangs Laboratories Inc, Fishers IN, USA) on a CR-39 polymer substrate that have been irradiated at a wavelength of 157nm using the F_2 laser under different laser conditions.

The structures shown in Figure 4.4a) were fabricated by irradiation of the 490nm diameter polystyrene particles with 2 laser pulses at 1Hz pulse repetition rate, at a laser fluence of 465mJcm^{-2}. The ablation site is ~210nm deep, resulting in a plinth height of ~210nm, and a total composite structure height of ~700nm. The particles do however seem to be slightly embedded within the CR-39 polymer substrate. This is most likely due to either some surface melting of either the particle and/or the substrate, or the attraction force between the particle and the substrate causing the surface of the substrate to relax. The collection of three adjacent particles towards the top of the micrograph appear to have suffered some degree of surface or bulk melting from the

heating effect of the laser pulses and have fused together. The initiation of the fringe pattern around the base of the structures can be seen. The fringe pattern is caused by ablation of substrate material as the incident laser beam interacts with the seeding particle and with the sloped walls of the support structure as it grows with the application of each laser pulse.

The structure shown in Figure 4.4b) was fabricated by the irradiation of an isolated 490nm diameter polystyrene spherical particle with 100 pulses at 5Hz pulse repetition rate, at a fluence of 150mJcm^{-2}. The depth of the ablation site, and hence the supporting structure height, is ~8.6µm, resulting in a total composite structure height of ~9.1µm. The interference fringe pattern can clearly be seen around the base of the composite structure, and the fringe period is ~270nm.

Clearly seen in Figure 4.4b) is the considerable indentation at the base of the composite structure, where the etch depth is greater than that of the open surface.

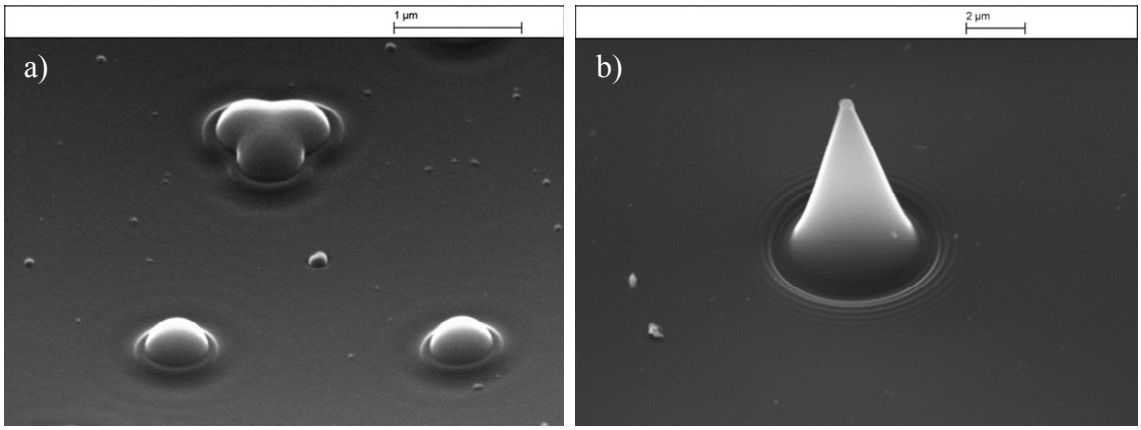

Figure 4.4: VUV 157nm F_2 laser irradiation of 490nm diameter polystyrene particles on CR-39 polymer substrate - a) laser fluence 465mJcm^{-2}, 2 laser pulses at 1Hz pulse repetition rate, composite structure height ~700nm, b) laser fluence 150mJcm^{-2}, 100 laser pulses at 5Hz pulse repetition rate, composite structure height ~9.1µm. Both SEMs viewed at 45°.

The SEMs in Figure 4.5 show the irradiation of 1µm diameter polystyrene particles (Kisker Biotech GmbH & Co, Steinfurt, Germany) on a CR-39 polymer substrate. The particle shown in Figure 4.5a) was irradiated with only one pulse at a laser fluence of 280mJcm^{-2}. These laser conditions have resulted in a site depth, and hence plinth height, of only 57nm, implying that the 1µm diameter particle is sitting just above the surface of the substrate. The interference fringe pattern surrounding the base of the structure is clearly visible. The particles shown in Figure 4.5b) have been irradiated at a laser fluence of 500mJcm^{-2} with 2 laser pulses at a pulse repetition rate of 1Hz. The height of the supporting structures are ~200nm, and so the total composite structure height is ~1.2µm. However these, and other, particles do appear to be slightly embedded within

the substrate material - this effect may also result from the length of time that passed between the fabrication of the sample, the laser irradiation experiment and the SEM investigation [101].

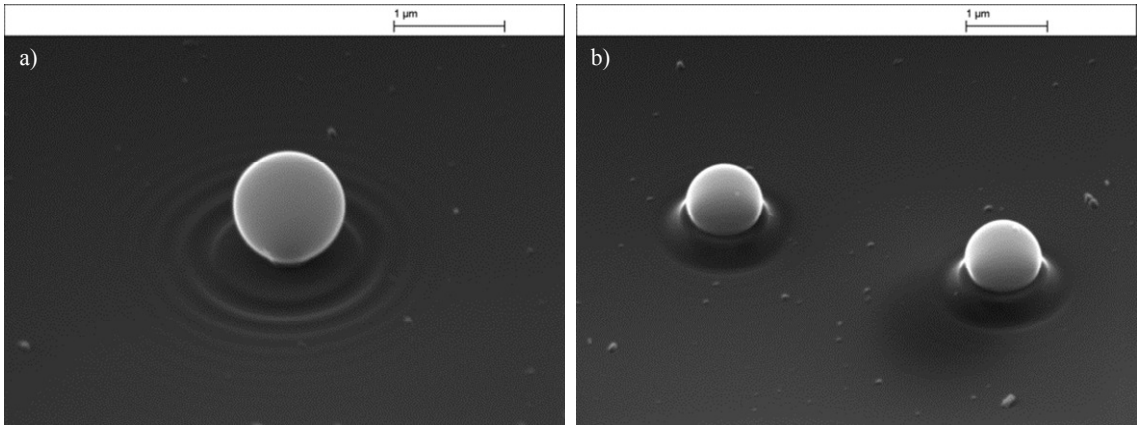

Figure 4.5: VUV 157nm F_2 laser irradiation of 1µm diameter polystyrene particles on CR-39 polymer substrate - a) laser fluence 280mJcm^{-2}, 1 laser pulse at 1Hz pulse repetition rate, composite structure height ~1.057µm, b) laser fluence 500mJcm^{-2}, 2 laser pulses at 1Hz pulse repetition rate, composite structure height ~1.2µm. Both SEMs viewed at 45°.

The effects of irradiating 1.58µm diameter polystyrene particles (Bangs Laboratories Inc, Fishers IN) on a CR-39 polymer substrate are shown in Figure 4.6 below. The structure in Figure 4.6a) shows four polystyrene particles fused together, at an early stage of cone formation having been irradiated with only 10 laser pulses at 1Hz pulse repetition rate at a laser fluence of 160mJcm^{-2}. Figure 4.6b) shows two particles that have been irradiated at a fluence of 275mJcm^{-2} with 5 laser pulses at a pulse repetition rate of 2Hz. The close proximity of these particles means that the interference patterns surrounding the bases of the structures overlap. The influence of a greater number of laser pulses is shown in Figure 4.6c) and d). The large group of composite conical structures in Figure 4.6c) was fabricated by irradiating the polystyrene particles with 100 laser pulses at 2Hz pulse repetition rate at a laser fluence of 250mJcm^{-2}. This SEM shows the consistent nature of the cone fabrication process as the majority of the cones are of a similar shape and size and they exhibit the interference fringe pattern around their bases. Figure 4.6d) shows a group of cones that have formed at the edge of an ablation site. The particles that seeded these structures were also irradiated using the 157nm laser, at a fluence of 250mJcm^{-2}, but this time with 1000 laser pulses at a pulse repetition rate of 2Hz. The polystyrene particles that seeded the structures in Figure 4.6a), c) and d) appear to be similar to the non-irradiated particles shown in Figure 4.2d), however the particles irradiated at the higher fluence, shown in Figure 4.6b), appear to have suffered some degree of surface melting caused by the transfer of energy from the laser photons. This will be discussed later in Chapter 7.

When the particles are irradiated at higher pulse numbers, such as 1000 pulses as in Figure 4.6d), the fringe pattern is no longer visible. This is as a result of the fringe system moving as each laser pulse is applied as both the cone height and base diameter increase.

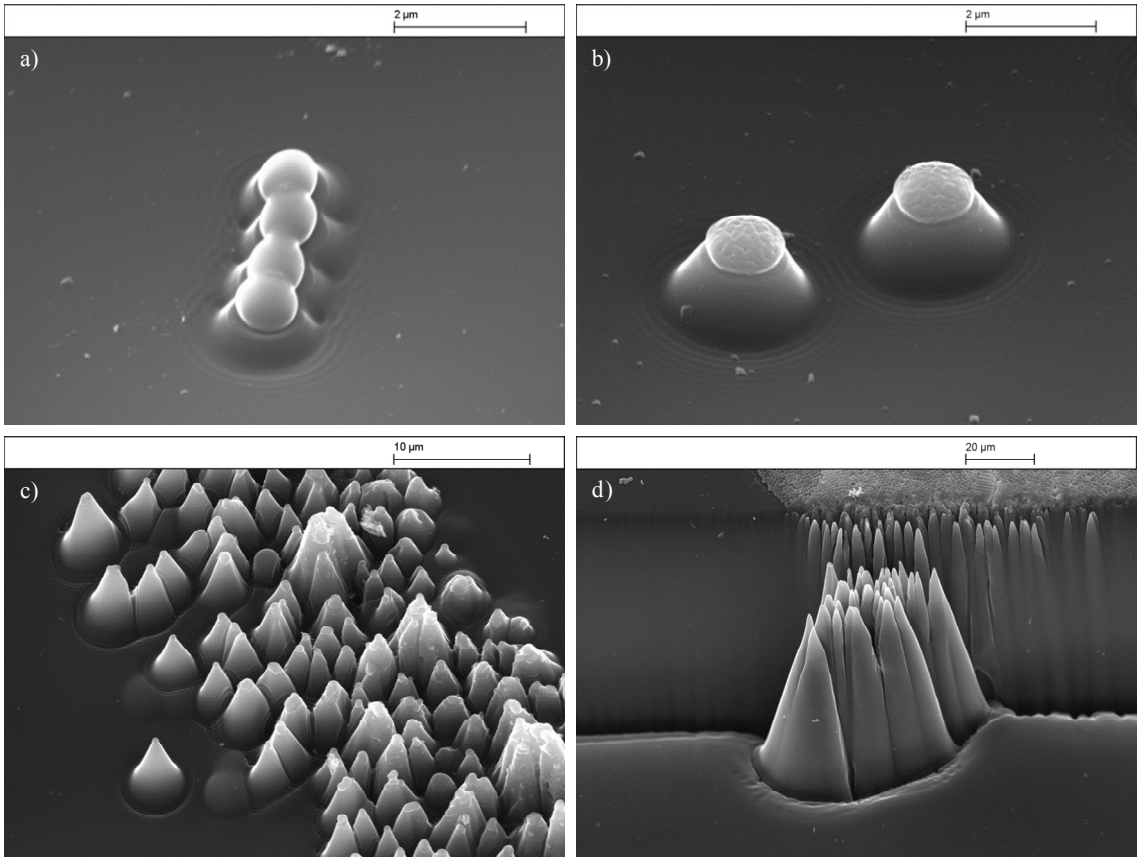

Figure 4.6: VUV 157nm F_2 laser irradiation of 1.58µm diameter polystyrene particles on CR-39 polymer substrate - a) laser fluence 160mJcm^{-2}, 10 laser pulses at 1Hz pulse repetition rate, b) laser fluence 275mJcm^{-2}, 5 laser pulses at 2Hz pulse repetition rate, composite structure height ~1.96µm, c) laser fluence 250mJcm^{-2}, 100 laser pulses at 2Hz pulse repetition rate, and d) laser fluence 250mJcm^{-2}, 1000 laser pulses at 2Hz pulse repetition rate. SEMs viewed at - a) and b) 45°, c) and d) 30°.

When the composite structures have been fabricated, they appear to be stable, with the seeding particle remaining firmly attached to the top of the structure, although no direct force measurement tests have been carried out to determine their stability.

It should be noted that at higher fluences and pulse numbers, the seeding particles tend to be removed from the substrate surface, most likely by laser cleaning or melting and/or evaporation of the particle.

It can also be observed that in all the SEM images presented here, the surface well away from the composite conical structures is very smooth and relatively free of debris. This indicates that good surface quality can be achieved when ablating CR-39 polymer using the VUV 157nm F_2 laser.

Section 4.2.3 - Irradiation of Polystyrene Particles at 45° to the Substrate

In order to irradiate the opaque particles at a laser beam incidence of 45º, the normal mounting arrangement had to be modified, as shown below in Figure 4.7. The sample was angled relative to the laser beam by means of an angled mounting block.

The samples for these experiments were prepared as detailed previously.

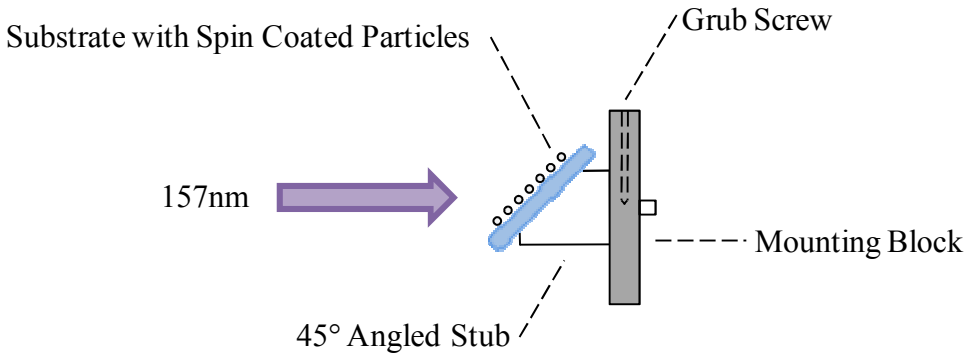

Figure 4.7: F_2 laser sample mounting arrangement for 45° laser beam incidence experiments.

Irradiating the polystyrene spherical particles at a 45° angle results in the formation of oblique composite conical structures, such as those shown in Figure 4.8. A similar, comet-like, ring pattern has been observed when irradiating transparent particles at angles of 45° and 60° [102].

These structures were fabricated by the irradiation of 1.58µm diameter polystyrene particles on a CR-39 polymer substrate. When irradiated at an angle of 45° to the laser beam propagation direction, the supporting polymeric structure is elongated in the direction of the beam propagation, with the seeding particle attached to the tip. The interference fringe pattern is more clearly seen at the back of the structure than at the front, and extends for quite a distance.

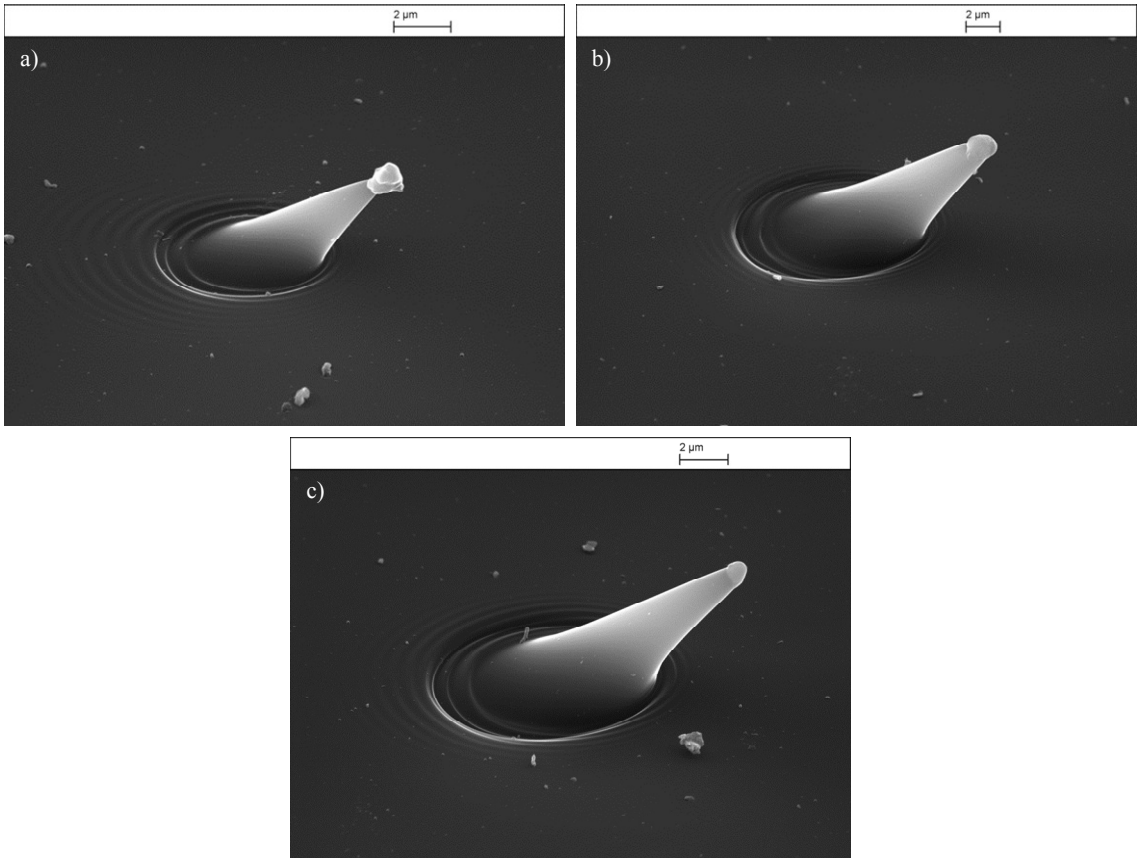

Figure 4.8: VUV 157nm F_2 laser irradiation of 1.58µm diameter polystyrene particles on CR-39 polymer substrate - a) laser fluence 180mJcm^{-2}, 10 laser pulses at 1Hz pulse repetition rate, composite structure vertical height ~5.1µm, b) laser fluence 175mJcm^{-2}, 50 laser pulses at 5Hz pulse repetition rate, composite structure vertical height ~8.3µm, c) laser fluence 185mJcm^{-2}, 50 laser pulses at 5Hz pulse repetition rate, composite structure vertical height ~8µm. All SEMs viewed at 45°.

When irradiating normal to the substrate, laser cleaning results in the removal of a large number of the seeding particles. When ablated at an increasing angle, it has been shown that the laser cleaning efficiency decreases, and drops to zero when the substrate is irradiated oriented at an angle of laser beam incidence above 15° [86].

The formation of cones as a result of particle-seeding with normal-incidence laser irradiation has been well documented since the 1980's, and previous work has also included cone formation in seeded polyimide irradiated at 50° to the normal [7] and unseeded polyimide at 45° to the normal [19].

Section 4.2.4 - Testing the Resolution of the Laser for the Fabrication of Miniature Composite Structures

In order to fabricate smaller structures for use in devices such as *Lab-on-a-Chip* microreactors, it was decided to test the resolution of the VUV 157nm F_2 laser and determine its ability to optically resolve small seeding particles and hence fabricate composite structures. Polystyrene particles of certain sizes in the range 50nm-1.58µm were dispersed on separate CR-39 polymer substrates, and irradiated at a wavelength of

157nm. The fabricated structures, shown in Figure 4.9 were investigated using the SEM.

Figure 4.9a) shows the irradiation of 1.58μm diameter polystyrene particles. The laser irradiation has clearly fabricated composite structures using the particles to seed the growth of the structures. The 1μm diameter and 490nm diameter polystyrene particles, shown in Figure 4.9b) and Figure 4.9c) respectively, have also interacted with the laser beam, even when irradiated with only 1 laser pulse, as evidenced by the initiation of an interference pattern around the particles.

The experiments presented previously show that the 157nm wavelength laser photons can easily interact with particles of a diameter of 490nm and greater. Therefore it was decided to investigate the interaction of the laser beam with polystyrene particles of a diameter smaller than these. Spherical polystyrene particles of diameter 210nm (Bangs Laboratories Inc, Fishers IN, USA) were also irradiated at a wavelength of 157nm, as shown in Figure 4.9d). When irradiated at a fluence of 305mJcm^{-2} using 5 laser pulses at 1Hz pulse repetition rate, a composite structure of height ~480nm is formed. This structure was seeded by the 210nm diameter particle, indicating that the 157nm wavelength laser beam is able to resolve particles of this size on a planar substrate.

In order to test the resolution of the laser even further, 50nm diameter polystyrene spherical particles (Bangs Laboratories Inc, Fishers IN, USA) were deposited on a CR-39 polymer substrate and irradiated using at a wavelength of 157nm. The conical structure shown in Figure 4.9e) was seeded by a ~100nm diameter particle, however it is unclear if this is a pre-existing particle or if a 50nm diameter particle has expanded under the heat from the laser beam. It can be seen that this laser is able to distinguish particles of this size on a planar substrate, and use them to seed the growth of a composite conical structure. This particular particle was irradiated with 2 laser pulses (1Hz pulse repetition rate) at a fluence of 280mJcm^{-2}. The resulting composite structure is ~176nm in height, with a base diameter of ~200nm.

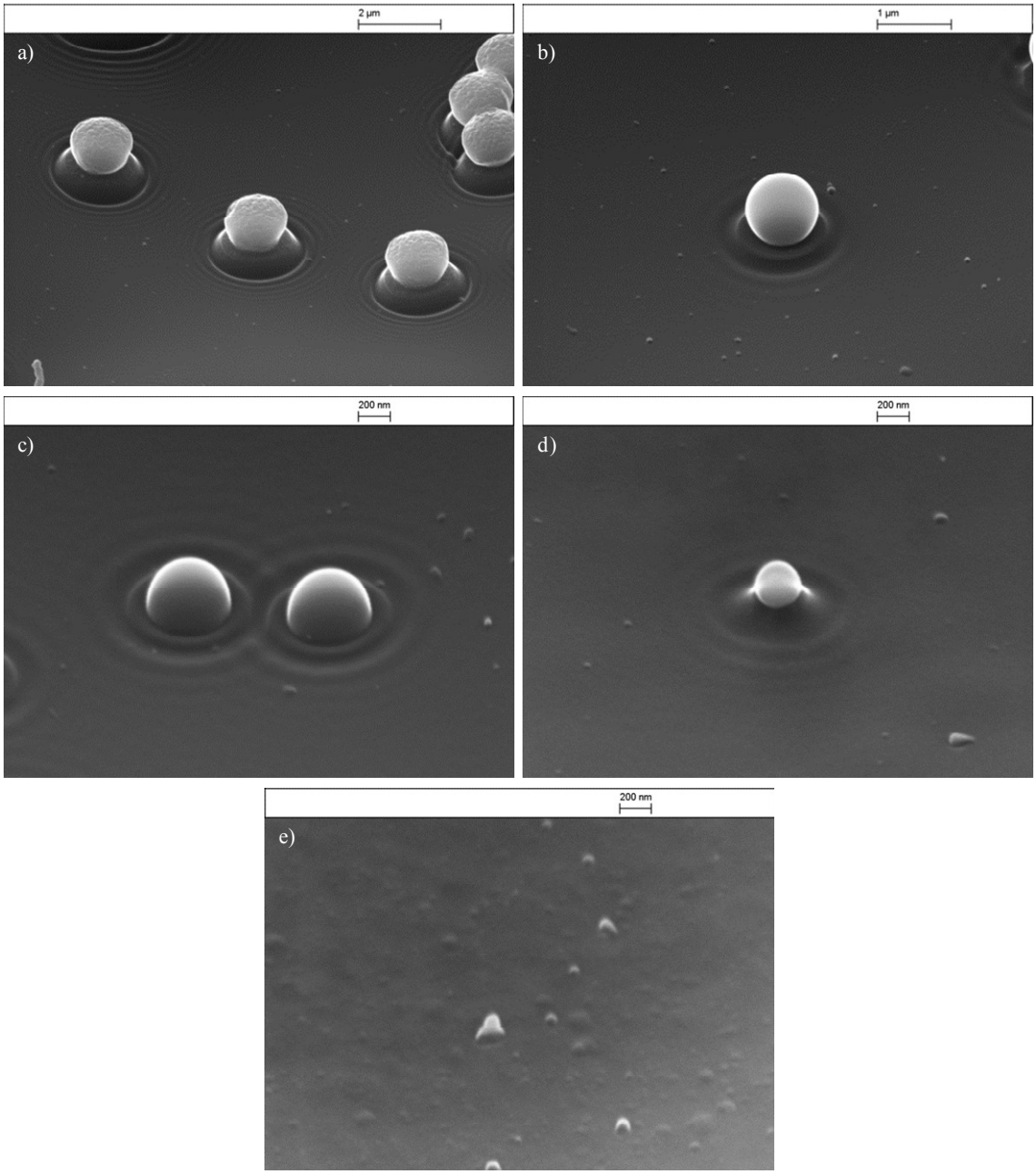

Figure 4.9: Resolution test for VUV 157nm F_2 laser using polystyrene particles on CR-39 polymer substrate - a) 1.58µm diameter particles, laser fluence 160mJcm^{-2}, 10 laser pulses at 1Hz pulse repetition rate, composite structure height ~1.9µm, b) 1µm diameter particles, laser fluence 500mJcm^{-2}, 1 laser pulse, composite structure height ~1.1µm, c) 490nm diameter particles, laser fluence 165mJcm^{-2}, 1 laser pulse, composite structure height ~550nm, d) 210nm diameter particle, laser fluence 305mJcm^{-2}, 5 laser pulses at 1Hz pulse repetition rate, composite structure height ~480nm, e) 50nm diameter particles, laser fluence 280mJcm^{-2}, 2 laser pulses at 1Hz pulse repetition rate, composite structure height ~176nm. All SEMs viewed at 45°.

It was decided not to test particles smaller than 50nm diameter, as a limiting factor in being able to determine if the laser has interacted with the seeding particle is the resolution of the SEM. Even though the laser may be able to resolve smaller particles, a measuring device with even higher depth and lateral resolution than the SEM would be required in order to see the fabricated structures.

Section 4.2.5 - Study on the Factors Affecting Composite Structure Fabrication

The main factors that contribute to the dimensions of the composite structure when irradiating small particles at a wavelength of 157nm are the size of the seeding particle, the laser fluence and the number of laser pulses.

As shown by the SEM images discussed previously, larger sized seeding particles result in the formation of composite structures with a larger footprint, so in this section the focus will be on the influence of the laser properties on the fabrication of composite structures.

Section 4.2.5.1 - Effect of Laser Fluence

All of the structures shown in Figure 4.11 were fabricated using 5 laser pulses at 1Hz pulse repetition rate, while the laser fluence was altered.

The effect of decreasing the fluence while maintaining the number of pulses can be determined by measuring the heights of the fabricated structures, shown in Figure 4.10.

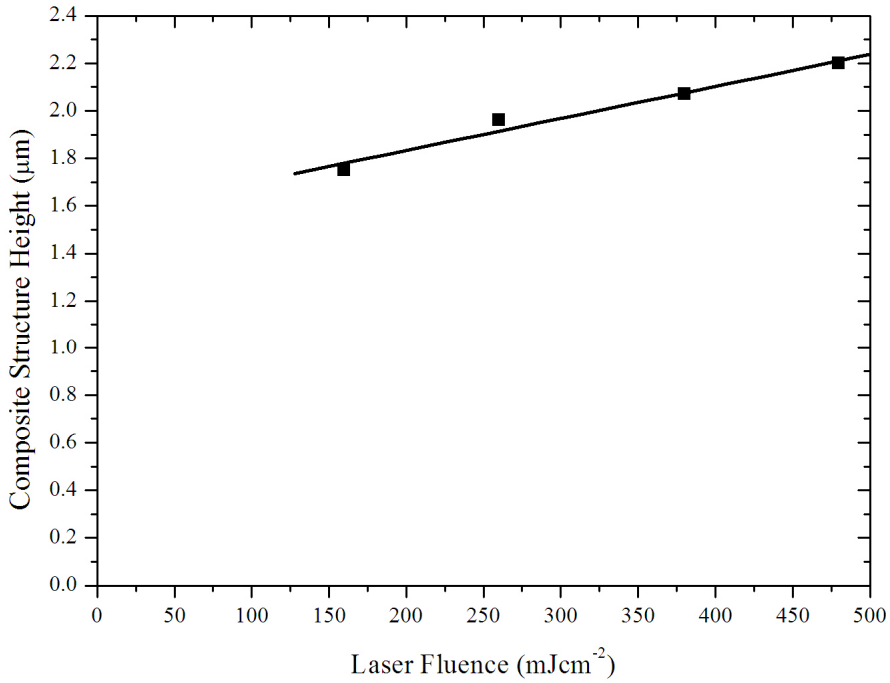

Figure 4.10: Effect of laser fluence on composite structure height (polymeric support structure + particle diameter) for the structures shown in Figure 4.11.

All of the particles appear to have been affected by the heat generated by the incident laser energy, as shown in Figure 4.11. At higher fluences, such as 480mJcm^{-2} in Figure 4.11a), the particles appear to have suffered a high degree of damage due to the higher incident energy. The particles have clearly fused together and appear more flat-topped than those exposed to lower fluences. This is likely due to melting or ablation of the

particle material. As the incident laser fluence decreases, for example to 160mJcm^{-2} in Figure 4.11d), the particles appear to be less affected by the energy from the incident laser beam. This is seen by the texturing on the tops of the particles.

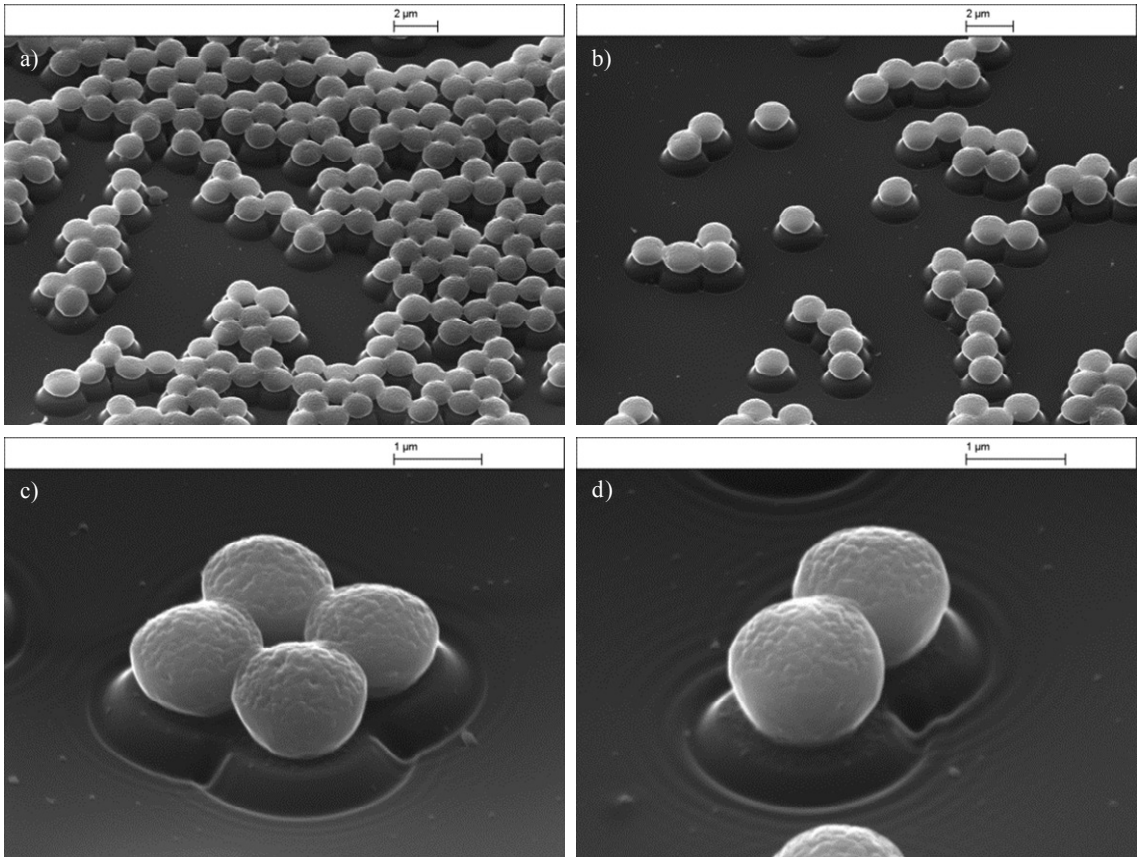

Figure 4.11: VUV 157nm F_2 laser irradiation of 1.58µm diameter polystyrene particles on CR-39 polymer substrate - all irradiated with 5 laser pulses at pulse repetition rate of 1Hz, at fluences of a) 480mJcm^{-2}, b) 380mJcm^{-2}, c) 260mJcm^{-2} and d) 160mJcm^{-2}. All SEMs viewed at 45°.

Section 4.2.5.2 - Effect of Pulse Number

Even when changing the number of laser pulses incident on the particles, the laser fluence still has an effect on the seeding particles and the structures that are fabricated.

The structures shown in Figure 4.13 were seeded using 1µm diameter polystyrene particles and irradiated at a fluence of 335mJcm^{-2} with increasing pulse number. While the site depth increases with increasing pulse number, as shown in Figure 4.12, the composite structures do not correlate with this pattern, as described below.

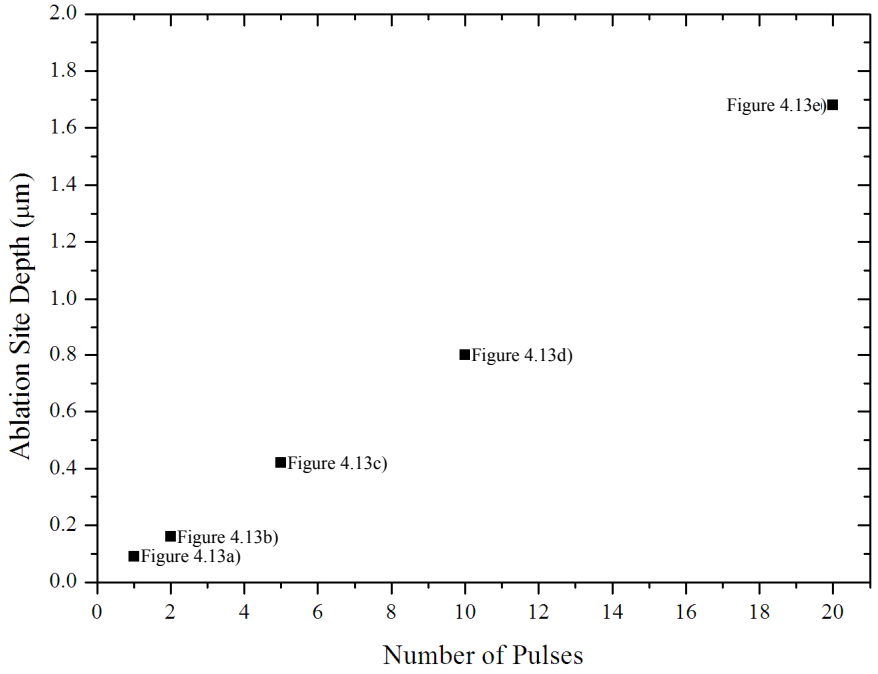

Figure 4.12: Ablation site depths, measured using a White Light Interferometer, for 1μm diameter polystyrene particles irradiated at 335mJcm^{-2} with increasing pulse number, shown in Figure 4.13.

At this higher fluence, the excess heat generated by the laser beam as the number of pulses increases causes the polystyrene particle to melt. In Figure 4.13a), the particles have been irradiated with only one pulse, and appear to be relatively unchanged from their non-irradiated state. When irradiated with 2 laser pulses, as in Figure 4.13b), the particles have undergone some surface melting and have fused together. Increasing the number of pulses to 5, as in Figure 4.13c), appears to result in bulk melting of the particles, so the supporting structure is capped by a melted piece of polystyrene. The effect of increasing the number of pulses to 10 and 20, as in Figure 4.13d) and Figure 4.13e) respectively, shows that the conical type structure has become more of a mound on the surface of the polymer substrate due to the complete removal of the polystyrene seeding material, and subsequent ablation of the supporting structure.

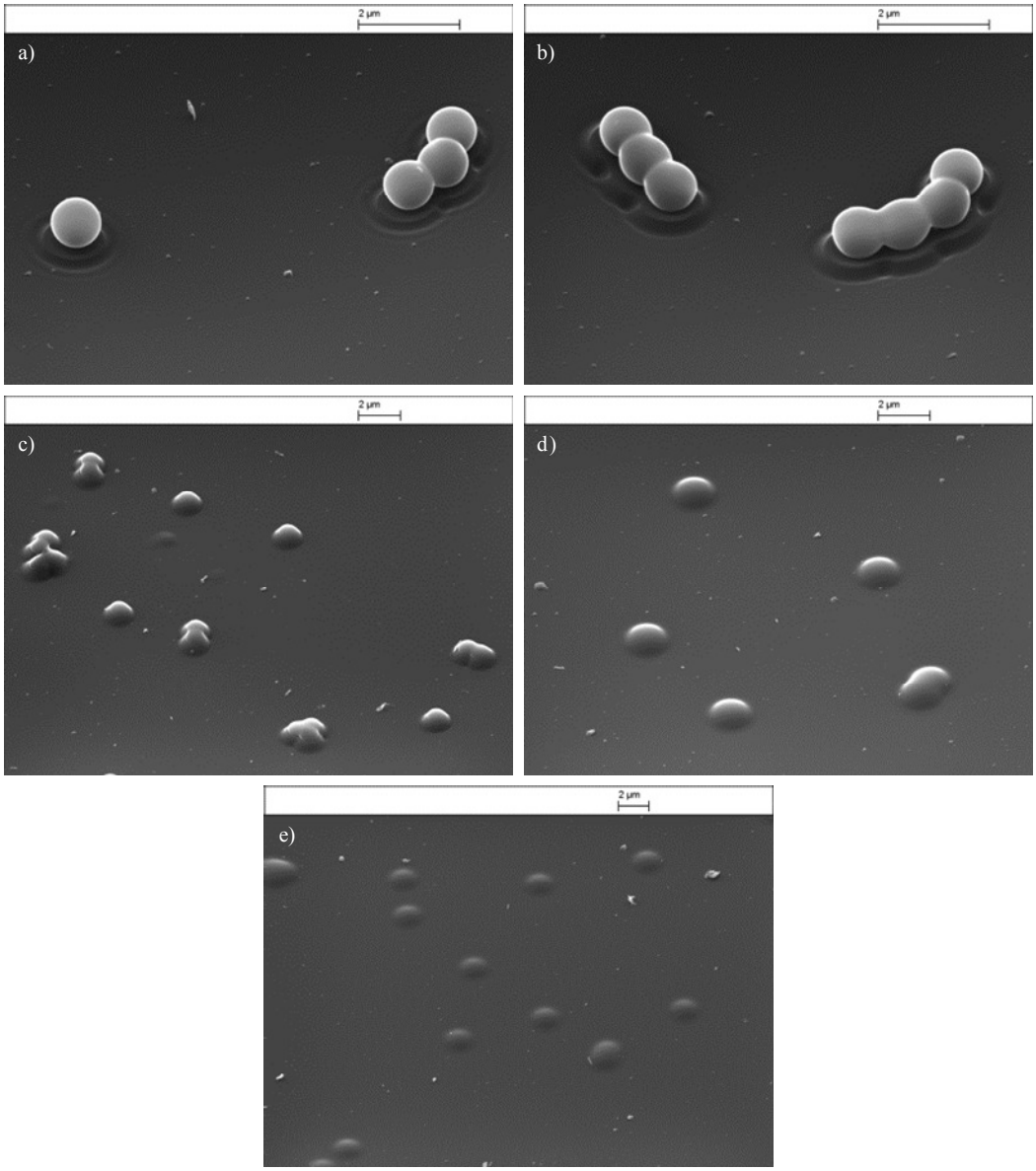

Figure 4.13: VUV 157nm F_2 laser irradiation of 1µm diameter polystyrene particles on CR-39 polymer substrate - all irradiated at fluence 335mJcm^{-2}, with a) 1 pulse, b) 2 pulses, c) 5 pulses, d) 10 pulses and e) 20 pulses, all at a pulse repetition rate of 1Hz. All SEMs viewed at 45°.

A similar effect can be seen when the fluence is decreased to 150mJcm^{-2}, as in Figure 4.15. The depths of the ablation sites are greatly reduced from before, even when using the same number of laser pulses, as shown in Figure 4.14.

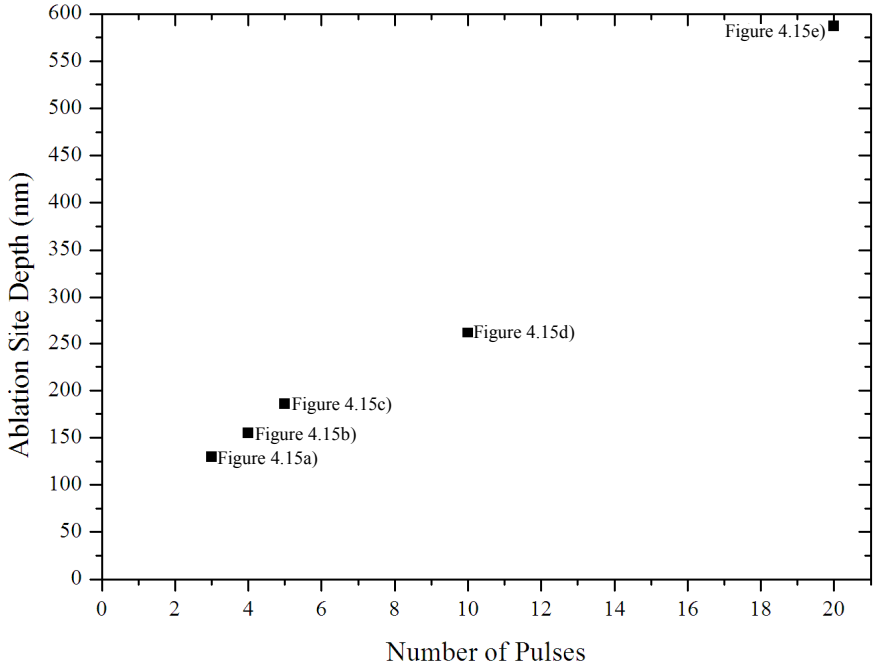

Figure 4.14: Ablation site depths, measured using a White Light Interferometer, for 1µm diameter polystyrene particles irradiated at 150mJcm^{-2} with increasing pulse number, shown in Figure 4.15.

At this fluence, the 1µm diameter particles remain in their spherical shape until 20 pulses are applied, shown in Figure 4.15, when it can be seen that the particle has been removed, either by laser cleaning or by melting and/or evaporation of the polystyrene.

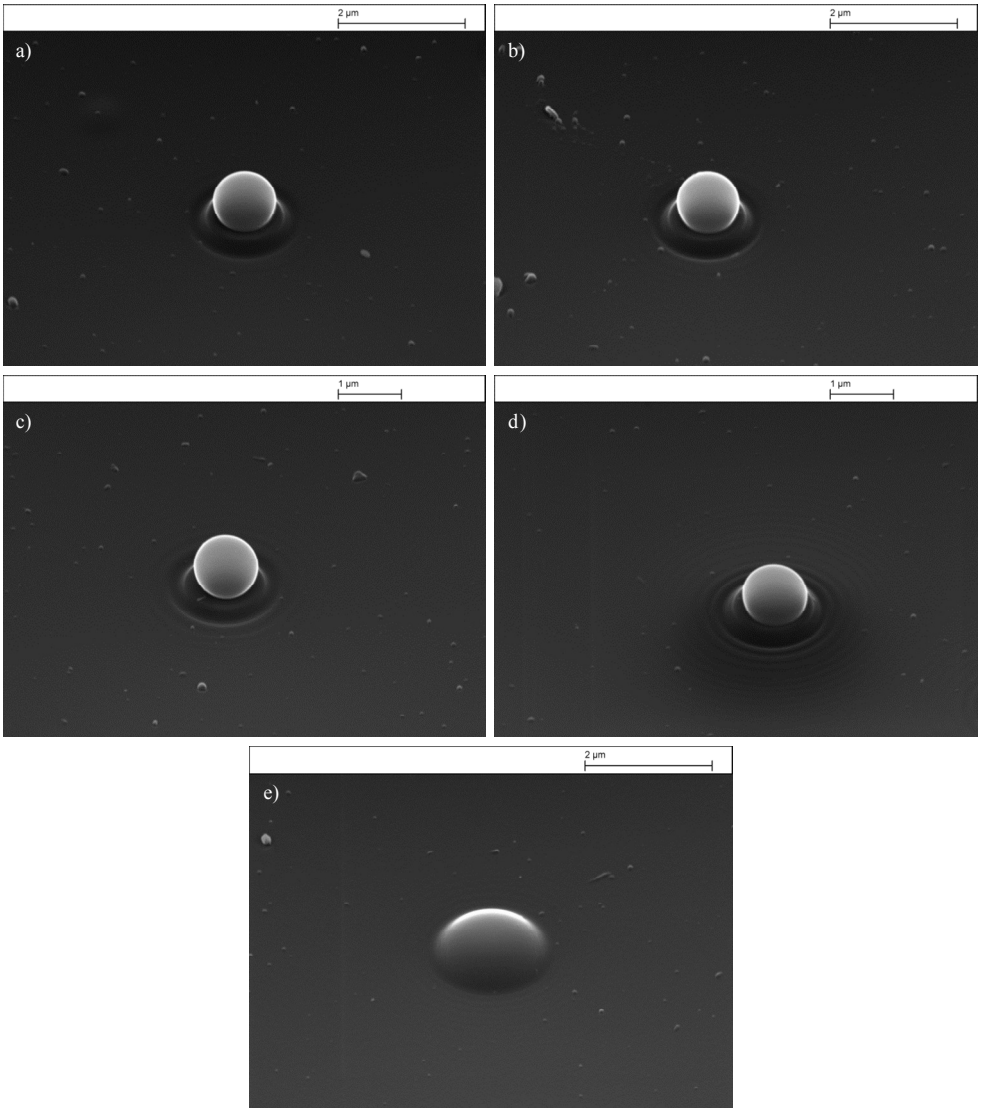

Figure 4.15: VUV 157nm F_2 laser irradiation of 1µm diameter polystyrene particles on CR-39 polymer substrate - all irradiated at fluence 150mJcm^{-2}, with a) 3 pulses, b) 4 pulses, c) 5 pulses, d) 10 pulses and e) 20 pulses, all at a pulse repetition rate of 2Hz. All SEMs viewed at 45°.

The graphs below, in Figure 4.16, show the relationship between ablation site depth and laser fluence (Figure 4.16a)) and ablation site depth and the number of laser pulses (Figure 4.16b)) when 1µm diameter polystyrene particles are irradiated with the VUV 157nm F_2 laser. In order to relate this data to the composite structure height, the diameter of the particle must be added to the site depth. However, the removal of the particle at higher fluences and pulse numbers should be taken into account when doing this.

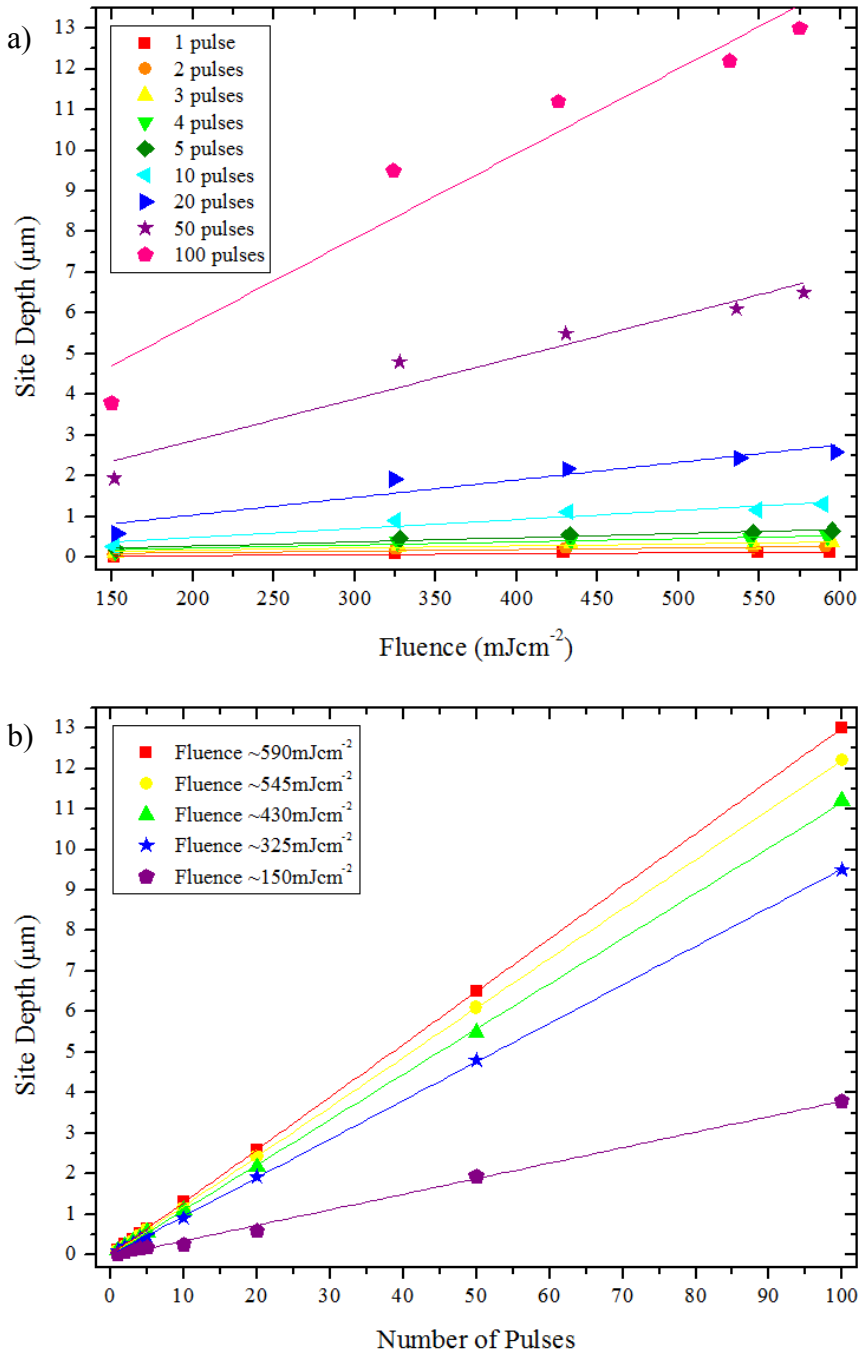

Figure 4.16: Influence of a) laser fluence and b) number of pulses on the ablation site depth, and hence composite structure height for 1µm diameter polystyrene particles, dependent on particle removal.

Section 4.3 - Conclusions

In this chapter, small opaque spherical particles have been irradiated using a VUV 157nm F_2 laser.

Polystyrene is opaque to 157nm radiation, and hence spherical particles of this material were used. The optical absorption depth of polystyrene is ~73nm when irradiated at a wavelength of 157nm.

Opaque particles have the opposite effect to transparent particles in that instead of focussing the radiation and fabricating a dimple in an underlying substrate, the opaque particle shields the underlying substrate, seeding the growth of a free-standing conical structure. Due to the attraction force between the particle and the substrate, and potentially some degree of surface melting, the particle remains attached to the top of the conical structure.

The composite conical structure is formed by the ablation of the substrate material surrounding the particle, while the material directly underneath the particle is shielded. The conical structures have smooth, fairly straight walls and an interference fringe pattern surrounding the base of the structure due to interactions between the incident laser beam, the particle and the substrate. The period of the fringe pattern is of the order of the wavelength of the laser beam.

Polymeric substrates are ideal for this application as they typically have very low laser ablation threshold fluences, particularly in the VUV region. The polymers used here - polycarbonate and CR-39 polymer - were determined to have ablation threshold fluences of ~14mJcm^{-2} and ~55mJcm^{-2} respectively. After ablation, they also exhibit good surface quality with little re-deposited material.

The polystyrene particles of various sizes were deposited on the polymeric substrate by spin-coating, and irradiated both normal to and at 45° to the direction of the laser beam propagation.

Irradiating a spherical polystyrene particle normal to the laser beam propagation direction results in the fabrication of an upright composite conical structure. Irradiation at 45° to the laser beam direction fabricates an oblique conical structure. In both cases, the seeding particle generally remains attached to the tip of the structure.

The ability of the laser beam to resolve the small particles is very important, and potentially very useful in the fabrication of a small footprint structure. It was found that, limited by certain other factors, the smallest diameter polystyrene particle the laser beam could resolve and use to fabricate a composite conical structure was ~100nm, which is smaller than the laser wavelength.

The height of the conical structure can be tailored by varying the laser fluence and/or the number of laser pulses. The height can vary from a few tens of nanometres to several tens of microns, and can be very finely controlled.

A spherical seeding particle results in the formation of a conical structure, however the shape of the supporting structure can be altered by changing the shape of the seeding particle. This will be investigated in the next chapter.

Chapter 5: VUV 157nm F_2 Laser Irradiation of Opaque Cylindrical Particles

Section 5.1 - Introduction

While the use of opaque spherical particles to seed the formation of conical structures on polymers by the ablation of the underlying material has been widely reported (see references in Chapter 4 for just a few examples), to the author's knowledge the available literature shows no evidence for the use of cylindrical particles (also known as rods, whiskers and wires) to seed analogous linear prismatic composite structures.

Cylindrical particles that are opaque to 157nm radiation act in the same manner as opaque spherical particles and prevent the underlying polymeric substrate material from being ablated when irradiated at a wavelength of 157nm. As the polymeric material surrounding the particle is removed, a cylindrical particle will seed the formation of a linear prismatic composite structure, with the particle remaining attached to the top of the structure. As with spherical seeding particles, an interference fringe pattern forms around the base of the linear prismatic structures.

The samples are prepared by spin-coating, and then the opaque particles - in this case silicon carbide whiskers - are irradiated both normal to and at 45° to the direction of laser beam propagation. Irradiation normal to the laser beam direction of propagation fabricates upright linear prismatic structures, where the seeding silicon carbide particle remains attached to the tip. Irradiation at 45° to the laser beam direction results in the formation of oblique linear prismatic structures, again with the silicon carbide whisker attached to the tip.

Section 5.2 - Experimental Results & Discussion

As a spherical seeding particle forms a conical structure, it stands to reason that any shape seeding particle will form an analogous composite micro- or nanostructure. This can be shown by using cylindrical particles, also commonly known as whiskers, wires or rods, to seed the growth of a structure.

Silicon carbide, SiC, is opaque to 157nm radiation, and can be calculated to have an optical absorption depth of ~11nm. Silicon carbide whiskers (Alfa Aesar, Heysham,

UK) have been irradiated in a similar manner to the spherical polystyrene particles in the previous chapter.

Silicon carbide can be an interesting alternative to metallic materials. In the mid-infrared region of the electromagnetic spectrum, around 12.5µm [61, 62], the relative permittivity exhibits a sharp resonance. This is due to the excitation of transverse optical phonons, also known as localised surface phonon polaritions. This resonance is analogous to the localised surface plasmon resonance (LSPR) response shown by metals at a certain frequency. At frequencies higher than this resonance, the dielectric function of silicon carbide is negative, enabling structures made from silicon carbide to be used in sensor devices and metamaterials. A metamaterial based on a perforated silicon carbide membrane has been demonstrated experimentally, with potential applications in circuits and thermal radiation sources [103].

Section 5.2.1 - Sample Preparation

The samples used in these experiments were prepared in a similar manner to those presented for the spherical particle experiments in the previous chapter. The silicon carbide whiskers were dispersed in DI water, and then a small quantity deposited onto polycarbonate and CR-39 polymer substrates. The substrates were then spun for a certain length of time using a spin-coater to deposit the whiskers across the surface, as shown in the optical micrographs in Figure 5.1 below. The samples were left after spinning if all of the solvent had not evaporated during the spinning process to allow them to dry.

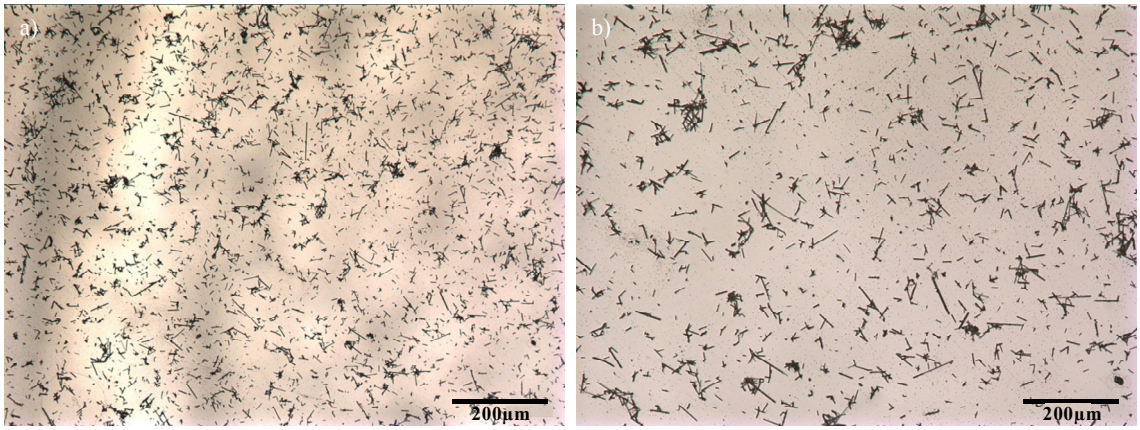

Figure 5.1: Optical micrographs of silicon carbide whiskers spin coated on polycarbonate, at a) 50× magnification, and b) 100× magnification.

A collection of silicon carbide whiskers is shown in Figure 5.2a).

This shows that there is quite a large spread in the dimensions of the particles, which are specified as average diameter = 1.5µm and length = 18µm. The SEMs (Cambridge Instruments Stereoscan 360) shown in Figure 5.2b), c) and d) show three typical whiskers with diameters ~ 1µm, 833nm, 542nm and lengths ~ 56.7µm, 23.8µm, 18µm respectively.

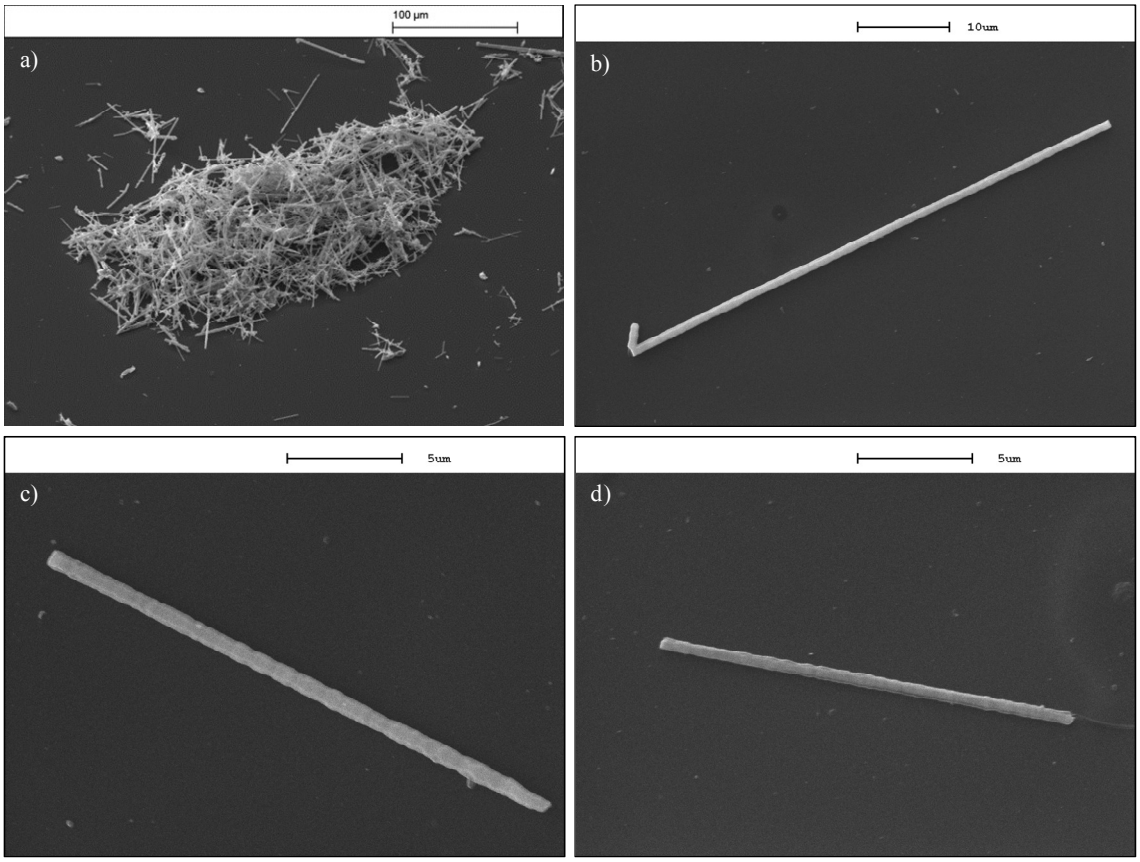

Figure 5.2: Scanning electron micrographs of silicon carbide whiskers - a) collection of particles, b) diameter ~1µm, length ~56.7µm, c) diameter ~833nm, length ~23.8µm, and d) diameter ~542nm, length ~18µm.

Each sample was then irradiated using the 157nm wavelength F_2 laser at known fluences, with a known number of laser pulses. The resulting ablation sites and linear prismatic composite structures were analysed using the optical microscope, a white light interferometer and a scanning electron microscope.

The mounting arrangements presented previously in Figure 4.3 and Figure 4.7 were utilised for the normal and 45° laser irradiation experiments respectively.

Section 5.2.2 - Irradiation of Silicon Carbide Whiskers Normal to the Substrate

The irradiation of cylindrical particles (also known as whiskers, wires and rods) is analogous to the irradiation of spherical particles - a spherical particle seeds the growth of a conical structure, and a cylindrical particle seeds the growth of a linear prismatic structure.

The linear prismatic structures exhibit similar features to the conical structures presented previously. They have smooth, fairly straight walls and an interference fringe pattern surrounding the base of the structure. There is also enhanced scalloping directly at the base of the structure.

Figure 5.3 shows the irradiation of silicon carbide whiskers deposited on a polycarbonate substrate, and the subsequent ablation of material. Figure 5.3a) shows an optical micrograph of an ablation site that has been irradiated at a fluence of 330mJcm^{-2} with 100 laser pulses at 2Hz repetition rate. The coloured region surrounding the ablation site shows the area of the heat damage caused by the incident laser beam. The linear prismatic structures that have formed by ablation of the polymeric substrate around the silicon carbide whiskers can be seen inside the ablation site, characterised by a slight "shadowing" effect. The SEM in Figure 5.3b) shows one of the linear prismatic structures formed within this ablation site, by irradiation of a ~1µm diameter whisker. This micrograph also shows the high surface quality and minimal debris attained by ablation of the polycarbonate substrate.

Irradiation at a fluence of 330mJcm^{-2} with 100 laser pulses at a pulse repetition rate of 2Hz, has resulted in an ablation site depth of ~8.7µm, meaning that this particular composite structure is ~9.7µm in height.

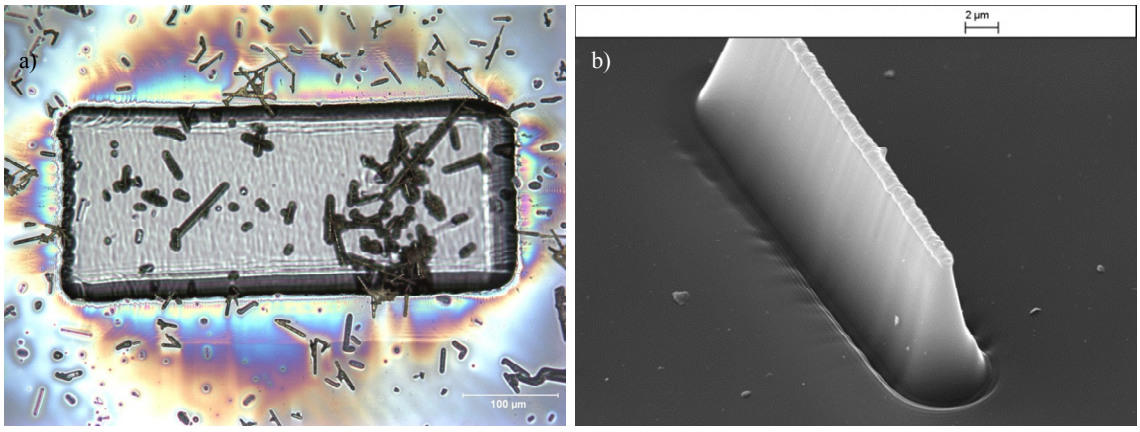

Figure 5.3: VUV 157nm F_2 laser ablation of silicon carbide whiskers on polycarbonate at laser fluence 330mJcm^{-2} with 100 laser pulses at 2Hz pulse repetition rate – a) optical micrograph at 200× magnification and b) particle diameter ~1µm, composite structure height ~9.7µm. SEM viewed at 45°.

Figure 5.4 shows a number of linear prismatic structures, formed by the irradiation of silicon carbide whiskers on a CR-39 polymer substrate with different laser conditions. The whiskers in Figure 5.4a) have been irradiated at a fluence of 85mJcm^{-2} with 100 laser pulses at a pulse repetition rate of 2Hz. Shown by the whisker that is raised from the surface on top of a number of other particles, these laser conditions have only

appeared to "outline" the shape of the whiskers on the CR-39 polymer substrate. The structure in Figure 5.4b) shows the initiation of the formation of a linear prismatic structure. This site was irradiated with 10 laser pulses at a pulse repetition rate of 1Hz at a fluence of 145mJcm^{-2}. The seeding whisker is ~1µm in diameter. The micrographs in Figure 5.4c) and d) show the effect of irradiating the silicon carbide whiskers with a greater number of pulses. The linear prismatic composite structure shown in Figure 5.4c) is ~4µm in height as a result of irradiation at a fluence of 115mJcm^{-2} with 100 laser pulses at 2Hz pulse repetition rate. The seeding particle is ~424nm in diameter. The structure shown in Figure 5.4d) has been fabricated by the irradiation of a silicon carbide whisker, ~435nm diameter, at a fluence of 145mJcm^{-2} with 100 laser pulses at 2Hz pulse repetition rate. The structure is ~6.2m in height and has an apex half angle of ~13°.

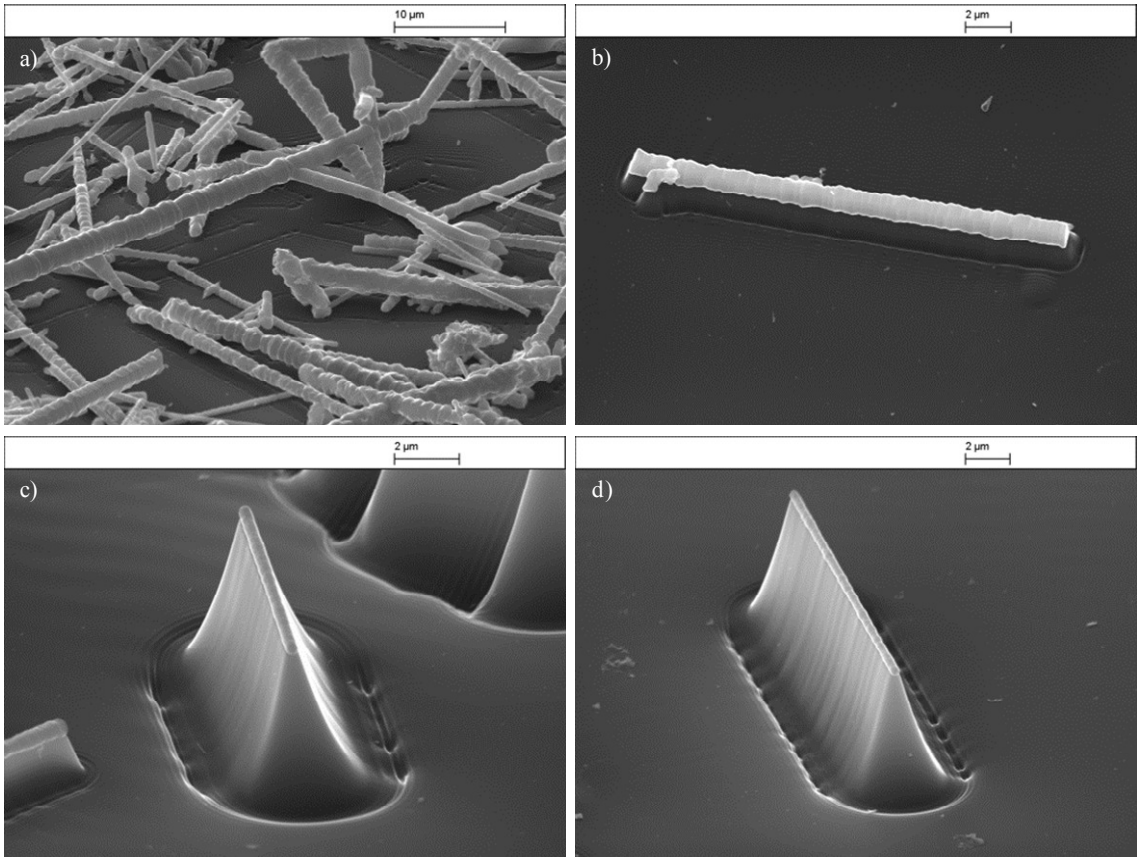

Figure 5.4: VUV 157nm F_2 laser irradiation of silicon carbide whiskers on CR-39 polymer substrate - a) laser fluence 85mJcm^{-2}, 100 laser pulses at 2Hz pulse repetition rate, b) laser fluence 145mJcm^{-2}, 10 laser pulses at 1Hz pulse repetition rate, whisker diameter ~1µm, c) laser fluence 115mJcm^{-2}, 100 laser pulses at 2Hz pulse repetition rate, whisker diameter ~424nm, composite structure height ~4µm, d) laser fluence 145mJcm^{-2}, 100 laser pulses at 2Hz pulse repetition rate, whisker diameter ~435nm, composite structure height ~6.2µm, apex half angle ~13°. All SEMs viewed at 30°.

The two silicon carbide whiskers, and their underlying linear prismatic structures, shown in Figure 5.5a) and b) below, have lined up almost parallel to each other as a result of the spinning process and self-assembly. The whiskers, diameters ~890nm and

~710nm, and lengths ~15.2µm and ~9.6µm, were irradiated on CR-39 polymer at a fluence of 145mJcm^{-2} with 100 laser pulses at 2Hz pulse repetition rate. The image in Figure 5.5c) was taken using a white light interferometer, and this pair of linear prismatic structure can be seen in the top left-hand corner. The profiles of the two linear prismatic structure, shown in Figure 5.5d), indicate that the composite structures are ~7.5µm and ~6.6µm in height.

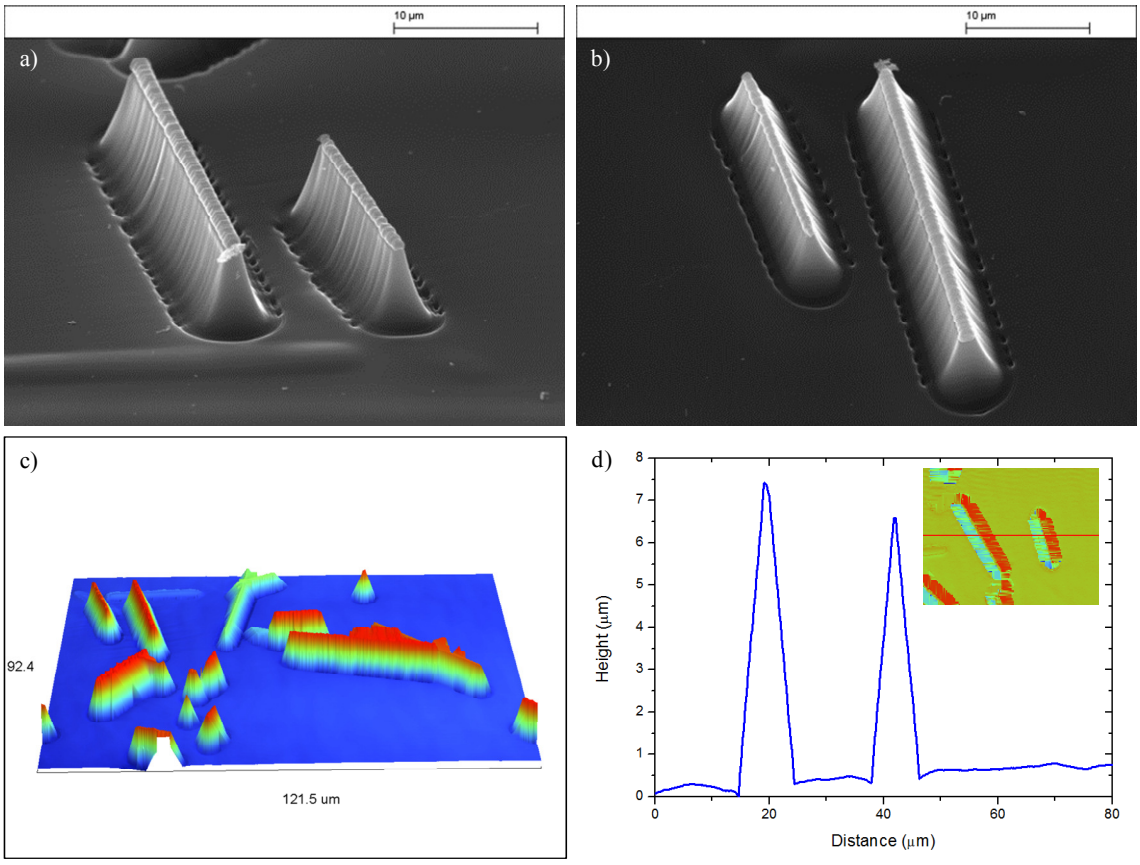

Figure 5.5: VUV 157nm F_2 laser irradiation of silicon carbide whiskers on CR-39 polymer substrate at laser fluence 145mJcm^{-2} with 100 laser pulses at 2Hz pulse repetition rate, whisker diameters ~890nm and ~710nm, whisker lengths ~15.2µm and ~9.6µm. SEMs viewed at a) 60° and b) 30°. c) and d) White light interferometry measurements of these two linear prismatic structures - site depth ~5.8µm, composite structure heights ~6.9µm and ~6.3µm.

The scanning electron micrographs shown in Figure 5.6 below show a single whisker that is protruding over the edge of one of the ablation sites. This result contributes to the evidence that the whiskers attach themselves firmly to both the CR-39 substrate and the prismatic structure. The prismatic structure has exceptionally smooth walls as the seeding whisker has a very smooth surface and is only ~670nm in diameter. This whisker, ~87.1µm in length, has been irradiated at a fluence of 145mJcm^{-2} with 1000 laser pulses at 10Hz pulse repetition rate, and as a result the ablation site is ~55µm deep. The micrographs, particularly Figure 5.6a), clearly show the very smooth walls of this structure which occur as a result of the small diameter and smooth surface structure

of the whisker. A top view of this structure, Figure 5.6b), shows how the linear prismatic structure formed from the CR-39 polymer substrate mimics the shape of the seeding whisker.

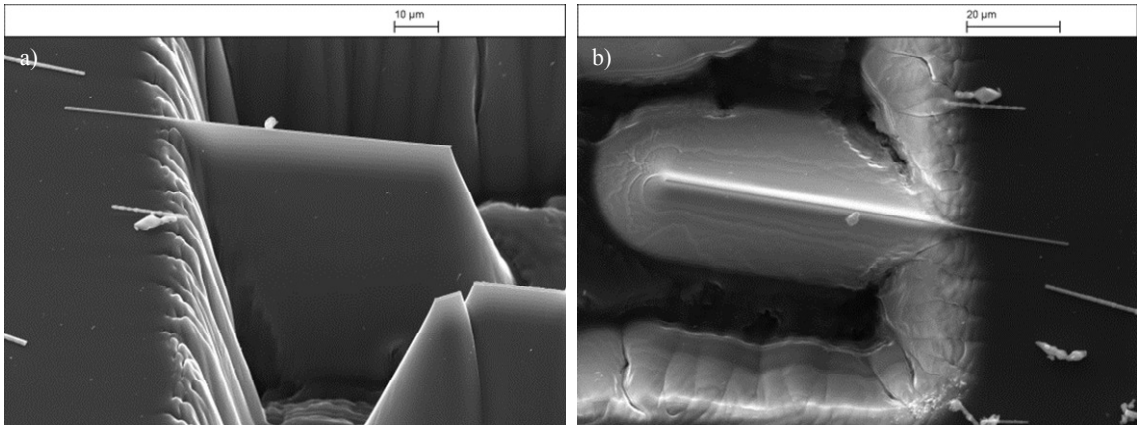

Figure 5.6: VUV 157nm F_2 laser irradiation of silicon carbide whisker on CR-39 polymer substrate at laser fluence 145mJcm^{-2} with 1000 laser pulses at 10Hz pulse repetition rate, whisker diameter ~670nm and length ~87.1µm. Site depth ~55µm, composite structure height ~56µm. SEMs viewed at a) 30° and b) top view.

The structure shown in Figure 5.7a) very strongly shows how the surface of the walls of the linear prismatic structure depends on the surface structure of the seeding particle.

The silicon carbide whisker is very rough (most likely as a result of the whisker fabrication process) and this has been resolved by the laser beam and has been replicated as undulations on the walls of the polymeric structure. In comparison with the whisker shown in Figure 5.6, which was very long with a small diameter, this whisker is shorter, with a much larger diameter, ~1.16µm. The smaller, smoother whisker seeds a linear prismatic structure with smooth walls, while the larger, more textured whisker seeds a linear prismatic structure with rougher walls.

Similarly to the previous micrographs, the images in Figure 5.7 show the interference fringe pattern surrounding the base of the structures. The interference fringes are more clearly seen close to the curved ends of the prismatic structure instead of the long sides, shown by Figure 5.7b), which show more scalloping due to the roughness of the whiskers surface. The structure in Figure 5.7b) has an apex half angle of ~15°.

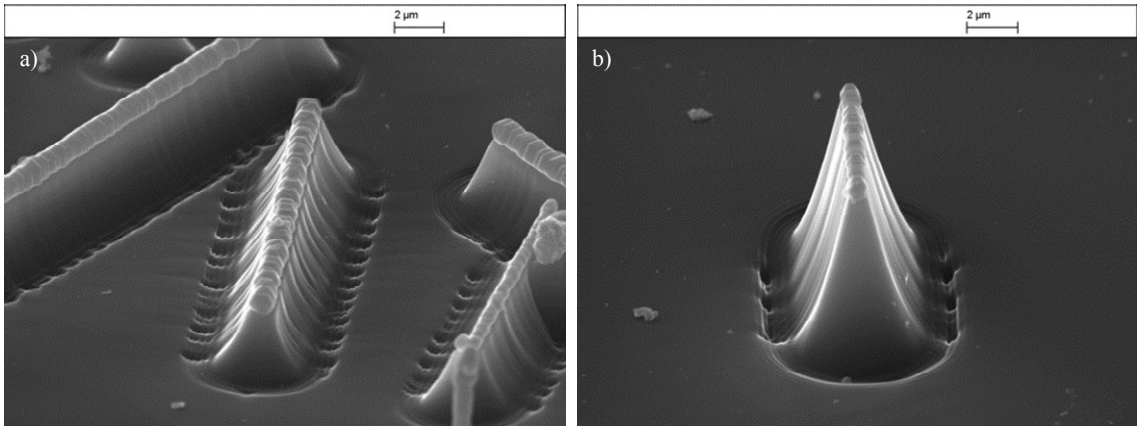

Figure 5.7: VUV 157nm F_2 laser irradiation of silicon carbide whiskers on CR-39 polymer substrate at a) laser fluence 115mJcm^{-2} with 100 laser pulses at 2Hz pulse repetition rate, whisker diameter ~1.16µm, site depth ~3.1µm, composite structure height ~4.3µm and b) laser fluence 145mJcm^{-2} with 100 laser pulses at 2Hz pulse repetition rate, whisker diameter ~846nm, site depth ~5.8µm, composite structure height ~6.7µm. SEMs viewed at a) 30° and b) 60°.

The SEMs presented previously of the irradiation of silicon carbide whiskers on polymeric substrates, and subsequent formation of linear prismatic composite structures, suggest that the seeding whisker remains attached to the top of the polymeric structure. Energy dispersive x-ray (EDX) analysis, shown in Figure 5.8, provides evidence that the seeding silicon carbide whisker remains attached to the top of the polymeric linear prismatic structure. The cross in Figure 5.8a) shows the position of the measurement, and the spectrum in Figure 5.8b) shows the EDX results. A sharp peak at ~1.7eV indicates high levels of silicon at this position, and hence confirms the presence of the seeding silicon carbide whisker at the apex of the linear prismatic structure.

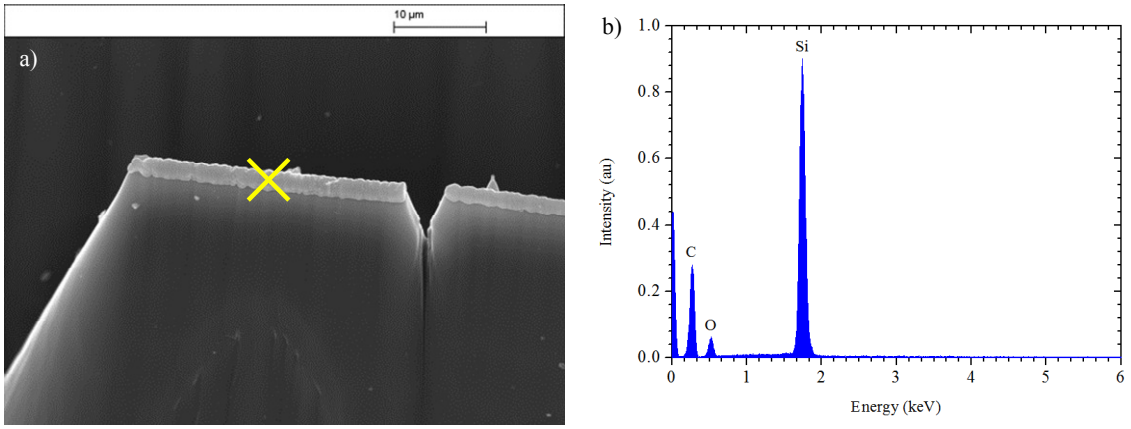

Figure 5.8: X-ray analysis of VUV 157nm F_2 laser irradiation of silicon carbide whiskers on CR-39 polymer substrate - a) SEM showing location of EDX measurement and b) x-ray analysis showing presence of SiC whisker on top of linear prismatic structure.

Section 5.2.3 - Irradiation of Silicon Carbide Whiskers at 45° to the Substrate

As seen previously in section 4.2.3, opaque spherical particles irradiated at an angle of 45° to the laser beam propagation direction seed the growth of oblique conical structures analogous to those fabricated when irradiated normal to the sample.

Similarly, irradiating opaque cylindrical particles at 45° to the laser beam direction fabricates oblique linear prismatic structures analogous to those presented in section 5.2.2. This type of structure can be seen in the SEMs presented below.

The silicon carbide whiskers shown in Figure 5.9 below have all been irradiated at 45° to the laser beam direction using 157nm laser radiation. The micrograph in Figure 5.9a) shows an entire ablation site, exhibiting the shape of the site that results from irradiation at an angle - the two longer sides of the site in fact form the top and bottom sides during irradiation, and hence the structures that are formed by the presence of the silicon carbide whiskers are orientated in this direction. This image also shows the ability of the F_2 laser to cleanly and sharply remove material from the polymer, to leave an ablation site with clean, sharp edges.

Figure 5.9b), c) and d) show a variety of structures that can be formed by the irradiation of isolated silicon carbide whiskers on a CR-39 polymer substrate.

Figure 5.9a) shows the ablation of silicon carbide whiskers that are randomly aligned during irradiation at a fluence of 140mJcm^{-2} with 500 laser pulses at a pulse repetition rate of 10Hz.

The silicon carbide whisker shown in Figure 5.9b) has a diameter of ~730nm and a length of ~11.1μm, and has been irradiated using the 157nm laser with 100 laser pulses at 5Hz pulse repetition rate at a fluence of 80mJcm^{-2}. The resulting composite structure is ~4.4μm in height.

The silicon carbide whisker shown in Figure 5.9c), of diameter ~740nm, was irradiated at 45° laser beam incidence at a fluence of 105mJcm^{-2} using 100 laser pulses at 5Hz pulse repetition rate. The composite structure has a height of ~6.5μm.

Figure 5.9d) shows a composite linear prismatic structure fabricated by the irradiation of a very small diameter, ~465nm, silicon carbide whisker irradiated at a fluence of 100mJcm^{-2} using 500 laser pulses at a pulse repetition rate of 10Hz. The composite structure is ~30.1μm in height and has a tip angle of ~13°.

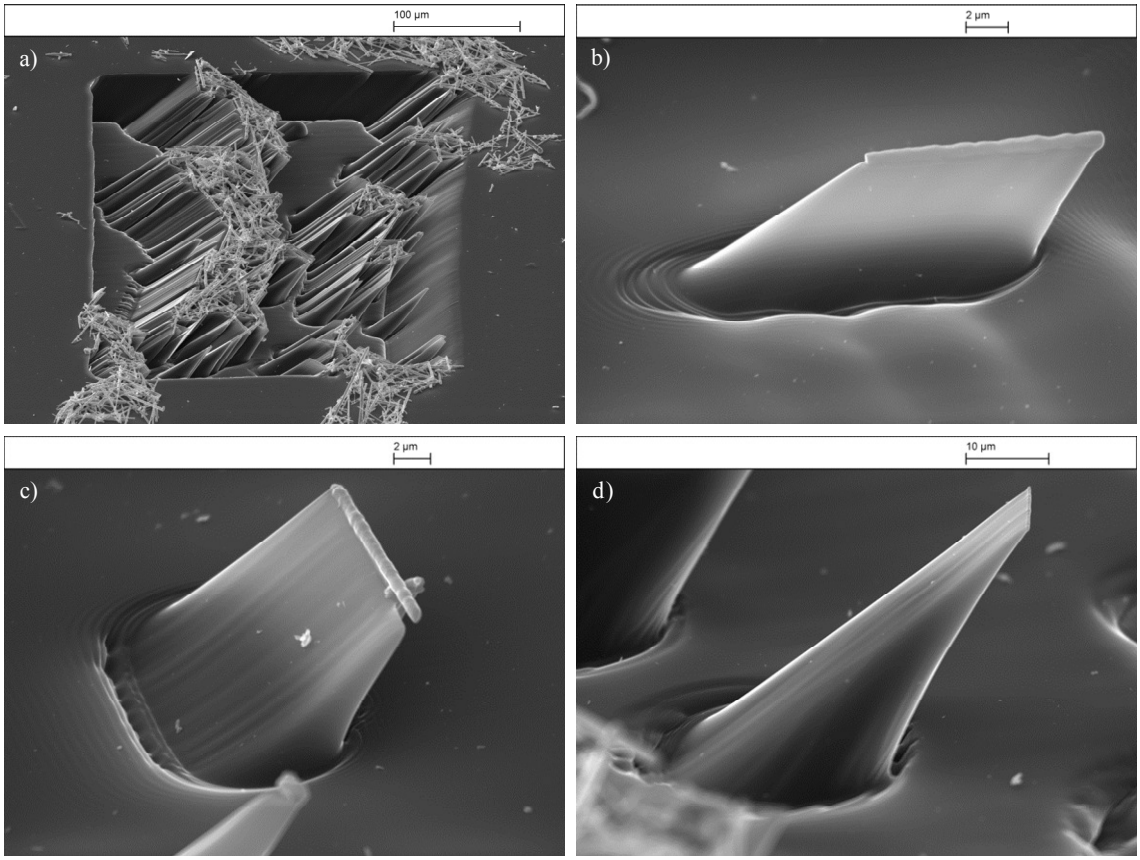

Figure 5.9: VUV 157nm F_2 laser irradiation at 45° of silicon carbide whiskers on CR-39 polymer substrate at a) laser fluence 140mJcm^{-2} with 500 laser pulses at 10Hz pulse repetition rate, site depth ~34.5µm, b) laser fluence 80mJcm^{-2} with 100 laser pulses at 5Hz pulse repetition rate, whisker diameter ~730nm and length ~11.1µm, site depth ~3.7µm, composite structure height ~4.4µm, c) laser fluence 105mJcm^{-2} with 100 laser pulses at 5Hz pulse repetition rate, whisker diameter ~740nm, site depth ~5.8µm, composite structure height ~6.5µm and d) laser fluence 100mJcm^{-2} with 500 laser pulses at 10Hz pulse repetition rate, whisker diameter ~465nm, site depth ~29.7µm, composite structure height ~30.1µm, tip angle ~13°. All SEMs viewed at 60°.

Similarly to the structures fabricated at normal incidence, the oblique structures exhibit an interference pattern around the base. However, the orientation of the seeding whisker with regards to the beam incidence direction appears to have an impact on the interference fringe pattern. When the whisker is aligned parallel to the laser beam direction, as in Figure 5.9b), the fringe pattern is more elongated behind the whisker compared with when the whisker is aligned perpendicular to the beam direction, as in Figure 5.9c) and d).

The spatial extent of the fringe pattern is related to the laser beam divergence in the two orthogonal directions, which are 8mrad and 3mrad in the high and low divergence directions respectively. The spatial coherence in each direction is given by [3]

$$\delta_h = \frac{\lambda}{\theta_h} M \qquad \text{and} \qquad \delta_l = \frac{\lambda}{\theta_l} M$$

Equation 5.1

where λ = 157nm is the wavelength of the laser and M = 1/10 is the magnification of the system.

Equation 5.1 gives spatial coherence lengths of ~ 2.0μm and 5.2μm in the high and low divergence directions respectively.

As with the linear prismatic structures produced under normal incidence laser irradiation, it can be seen that the silicon carbide whisker remains attached to the top of the structure.

Unlike the polystyrene particles that were irradiated using the F_2 laser in Chapter 4 which were seen to change shape and to melt as a result of the energy from the laser beam, the silicon carbide whiskers do not appear to change shape or melt as a result of the irradiation using the same laser. Investigations into both of these results are presented in Chapter 7.

Section 5.3 - Conclusions

In this chapter, opaque cylindrical particles have been irradiated using a VUV 157nm F_2 laser. Silicon carbide is opaque to the 157nm radiation, and hence particles, known as whiskers, of this material have been used.

A search of the available literature suggests that while spherical particles have frequently been used to seed the formation of micro- and nanoscale structures, cylindrical particles have not previously been utilised.

The process by which the whiskers seed the fabrication of the structures is the same as that shown by the spherical particles - the particle shields the polymeric substrate material underneath it while the material around it is removed by laser ablation. The presence of a cylindrical particle results in the formation of a linear prismatic structure, analogous to the growth of a conical structure by a spherical particle.

The silicon carbide whiskers were dispersed on polycarbonate and CR-39 polymer substrates by spin-coating and then irradiated using the VUV 157nm F_2 laser. The samples were irradiated normal to the laser beam direction to fabricate upright linear prismatic structures, and at 45° to the beam propagation direction to produce oblique linear prismatic structures. As before, the height of the linear prismatic structure can be altered by changing the laser fluence and/or the number of applied laser pulses, and can vary from a few tens of nanometres to several tens of microns. The polymeric substrate

materials are highly susceptible to the 157nm laser beam, hence resulting in very fine control over the depth of material removal and hence composite structure height.

These linear prismatic structures exhibit the same features as the conical structures. They have smooth, fairly straight walls, a fringe pattern surrounding the base of the structure, and the particle remains attached to the top of the composite structures. This has been confirmed using EDX measurements by a sharp peak in the spectrum at ~1.7eV, indicating high levels of silicon at the top of the structures.

Within the interference fringe pattern surrounding the base of the linear prismatic structures, there is enhanced scalloping along the length of the structure. This is a result of the higher surface roughness of the larger diameter whiskers. The smaller diameter whiskers do not appear to have this effect on the walls of the structure or the fringe pattern.

When the whiskers are irradiated at 45° to the direction of the laser beam propagation, the interference pattern varies with the orientation of the particle within the beam. If the particle is parallel with the beam direction the interference fringe pattern is elongated in the same direction compared with the fringe pattern formed by the irradiation of whiskers perpendicular to the beam direction.

During the spin-coating process, as shown in Figure 5.5, two whiskers have lined up almost parallel to each other. This opens up the potential for aligning these linear prismatic structures. The silicon carbide whiskers, in comparison with the polystyrene particles presented in Chapter 4, do not appear to change shape or melt as a result of the energy from the incident laser beam. This result is not unexpected, as silicon carbide is known to only melt at pressures above 35bar [104, 105], and sublimes at temperatures exceeding 2200°C [106].

So far, particles made from dielectric and semiconductor materials have been used to fabricate composite micro- and nanoscale structures. In the next chapter, metallic particles will be irradiated using the VUV 157nm F_2 laser in order to fabricate metallic-polymeric composite conical and linear prismatic micro- and nanoscale structures.

Chapter 6: VUV 157nm F_2 Laser Irradiation of Metallic Particles

Section 6.1 - Introduction

In this chapter, silver particles are irradiated at a wavelength of 157nm using the VUV F_2 laser. Similarly to both polystyrene and silicon carbide, silver can also be opaque to 157nm radiation. Therefore, irradiation of a silver particle on a polymeric substrate fabricates composite structures, the shapes of which are dependent on the geometry of the seeding particle.

Again, interactions between the laser beam and the particle, supporting structure and the substrate results in the appearance of an interference fringe pattern around the base of the composite structure.

Both quasi-spherical and cylindrical particles are used in these experiments to fabricate composite conical and linear prismatic structures. The particles are deposited on the polymeric substrate by spin-coating and irradiated with 157nm laser radiation normal to the direction of the laser beam propagation.

In the previous experiments, the dielectric (polystyrene) and ceramic (silicon carbide) seeding particles lend themselves mostly to structure fabrication only, although silicon carbide has demonstrated potential as a metamaterial [103]. The incorporation of the metallic particle to the fabrication process lends itself towards plasmonic applications.

Section 6.2 - Experimental Results & Discussion

Section 6.2.1 - Sample Preparation

Silver particles of various sizes were dispersed into deionised (DI) water to form solutions of ~2% particle concentration and sonicated to break up any agglomerated particles. The particles were then deposited onto CR-39 polymer substrates, which were first sonically cleaned in isopropanol and DI water and blown dry using nitrogen gas, N_2. The samples were then spun at 1000rpm for 30seconds to spread the particles across the substrate surface.

Using Equation 3.2, the attraction force between a silver spherical particle and polycarbonate substrate can be calculated using a combined Hamaker constant of

A = 1.56×10^{-19}J from Equation 3.7. The forces of attraction for different size silver particles are shown in Table 6.1 below.

Particle Diameter	Attraction Force (N)
10nm	8.15×10^{-10}
50nm	4.07×10^{-9}
350nm	2.85×10^{-8}
1.3μm	1.06×10^{-7}
7μm	5.70×10^{-7}

Table 6.1: Force of attraction between silver spherical particles of various sizes and a polycarbonate substrate.

The attraction forces between the particles and the substrate can sometimes be sufficient to visibly distort the substrate, as demonstrated by the silver nanoparticles in Figure 6.1. The silver particles are slightly embedded into the surface of the polymer substrate as shown by the ridge effect around the clusters of particles. This may also be due in part to the length of time between the deposition of the particles onto the substrate and the SEM imaging [101].

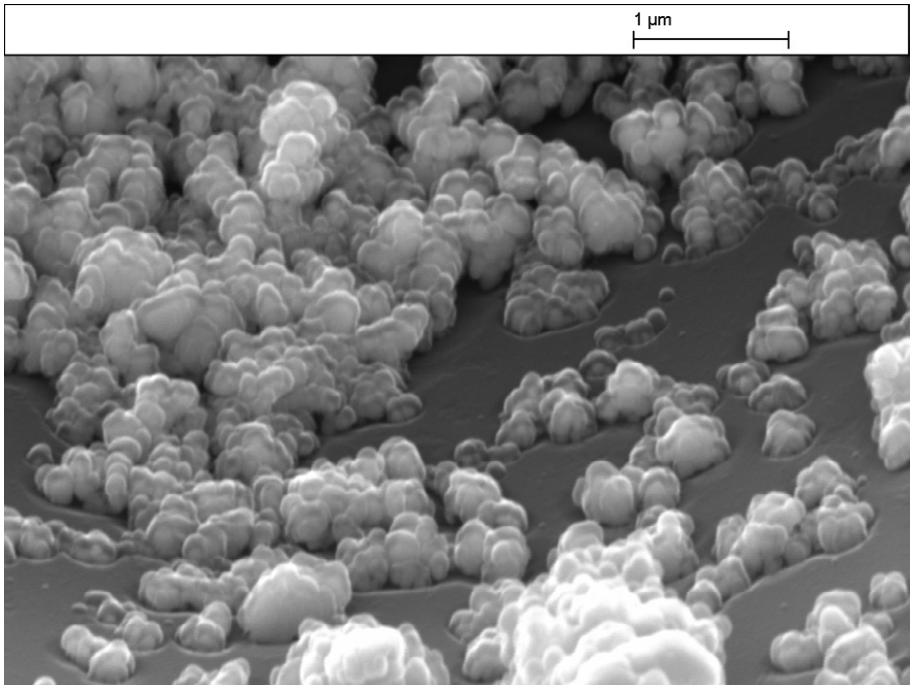

Figure 6.1: Silver nanoparticles on a polymeric substrate, showing substrate deformation arising from the attraction forces between the particles and the substrate.

The absorption spectra (Unicam 5625 UV/VIS Spectrometer) of 10nm diameter and 50nm diameter spherical silver particles are shown in Figure 6.2. The spectra show peaks around 395nm for the 10nm diameter particles and 418nm for the 50nm diameter particles. These peaks correspond to the plasmon resonance of silver, which varies depending on particle size.

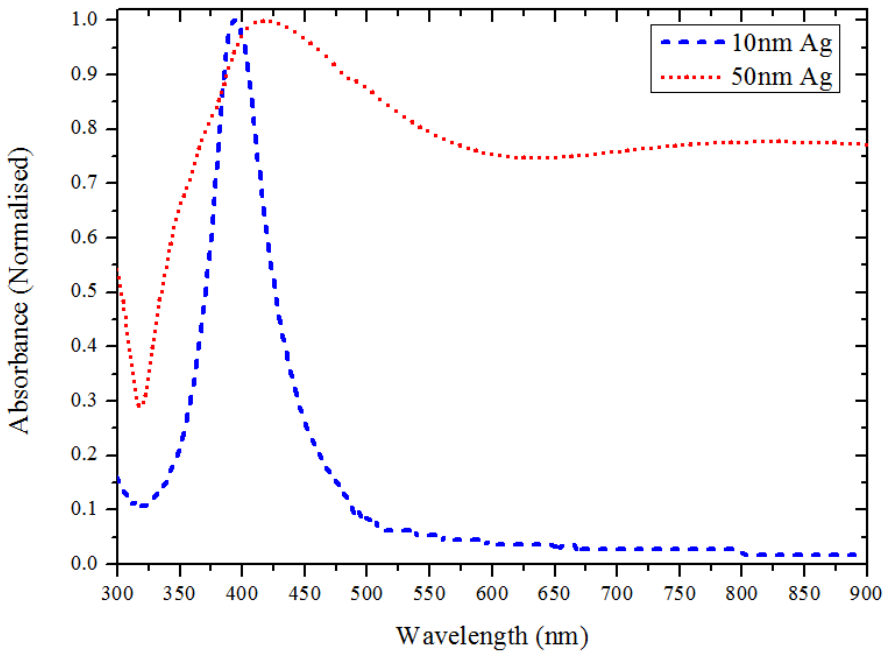

Figure 6.2: Absorption spectra of 10nm diameter (dashed blue line) and 50nm diameter (dotted red line) spherical silver particles.

Silver nanowires (Nanostructured and Amorphous Materials Inc., Houston, TX) were dispersed in either DI water or ethanol, and then sonicated to form a solution of ~10% particle concentration. Polycarbonate and CR-39 polymer substrates were cleaned by oxygen plasma treatment for 10minutes, then sonically cleaned in isopropanol and DI water and blown dry using N_2 gas. The silver nanowire solution was deposited onto the substrate, which was then spun at 500rpm for 60seconds to disperse the nanowires across the surface of the substrate, as shown in Figure 6.3.

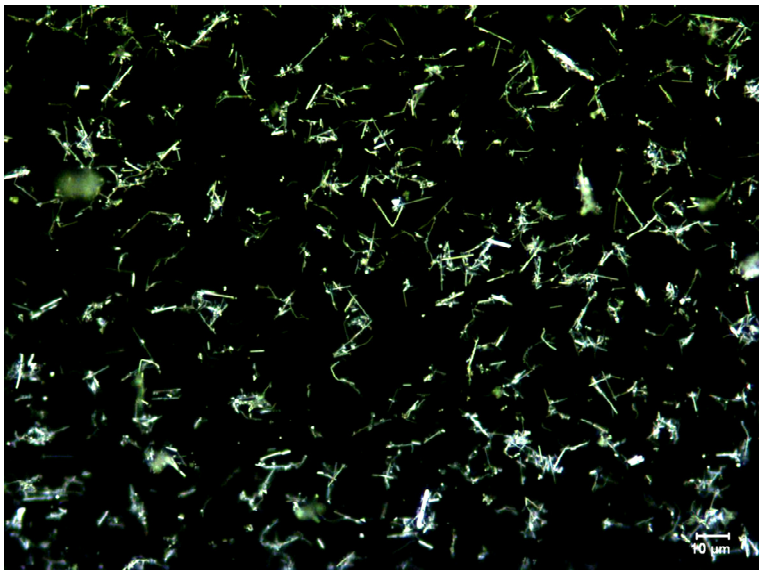

Figure 6.3: Optical micrograph of silver nanowires deposited on CR-39 polymer by dispersion in ethanol and spin coating at 500rpm for 60seconds.

The nanowire dimensions are specified by the manufacturer as diameter = 270-330nm and length = 20µm. However, a random sampling of the wires used for this experiment, before irradiation with the laser, showed an average diameter of ~420nm and an average length of ~6.9µm.

The absorption spectrum (Perkin Elmer UV/VIS Spectrometer Lambda Bio40) of the silver wires is shown in Figure 6.4. The spectrum shows peaks around 350nm (as a shoulder to the main peak) and 405nm. These wavelengths can be linked to the plasmon resonances of the wires – one for the transverse direction along the short axis of the wire (380nm), and the other for the longitudinal resonance along the long axis of the wire (405nm). The broadness of the peak can be attributed to the presence of particles with a range of sizes and shapes [49].

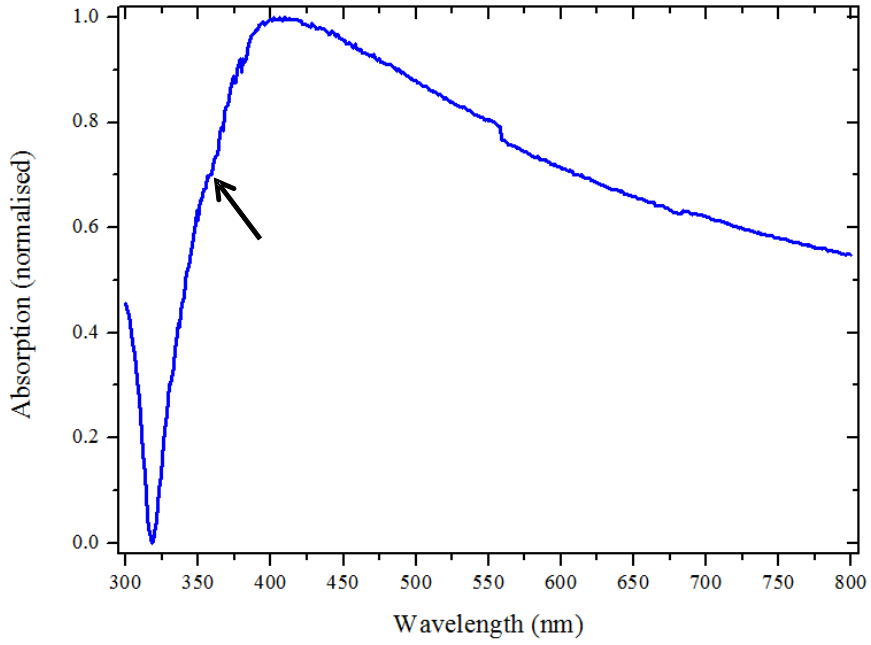

Figure 6.4: Absorption spectrum of silver nanowires. Arrow indicates peak at 380nm.

The seeded samples were then irradiated using a Lambda Physik LPF220 F_2 laser emitting at 157nm at a pulse energy of ≤50mJ per pulse at ≤200Hz with a pulse duration of ~26nm FWHM. The output laser beam was reduced in size by 1/25× magnification and passed through a flies eye homogeniser. The samples were irradiated at known fluences with 1-100 pulses per ablation site.

After irradiation, the samples were removed, and the ablation sites and fabricated structures characterised using an optical microscope (Leica DMLM), white light

interferometer (Veeco WYKO NT1100 Optical Profiling System) and a Scanning Electron Microscope (SEM, Carl Zeiss SMT Ltd, Model EVO 60).

Section 6.2.2 - Quasi-Spherical Particles

Silver particles, of diameter 250-350nm (Nanostructured & Amorphous Materials Inc., Houston TX, USA) were irradiated using the VUV 157nm F_2 laser.

The particles shown in Figure 6.5 are ~490nm and ~570nm in diameter. The silver-CR-39 polymer structure shown in Figure 6.5a) was fabricated by irradiation of the silver seeding particle with 10 laser pulses (1Hz pulse repetition rate) at a fluence of 260mJcm^{-2}. The resulting composite structure is ~1.4µm in height, and the smooth conical walls and interference fringe pattern are clearly evident. The silver seeding particle in Figure 6.5b) was irradiated at a laser fluence of 350mJcm^{-2} with 20 laser pulses (1Hz pulse repetition rate). This higher fluence and number of pulses has resulted in a composite structure height of ~2.9µm. The interference fringe pattern is again evident, although because of the slightly non-spherical shape of the silver particle the fringe pattern does not appear to be even around the base of the structure.

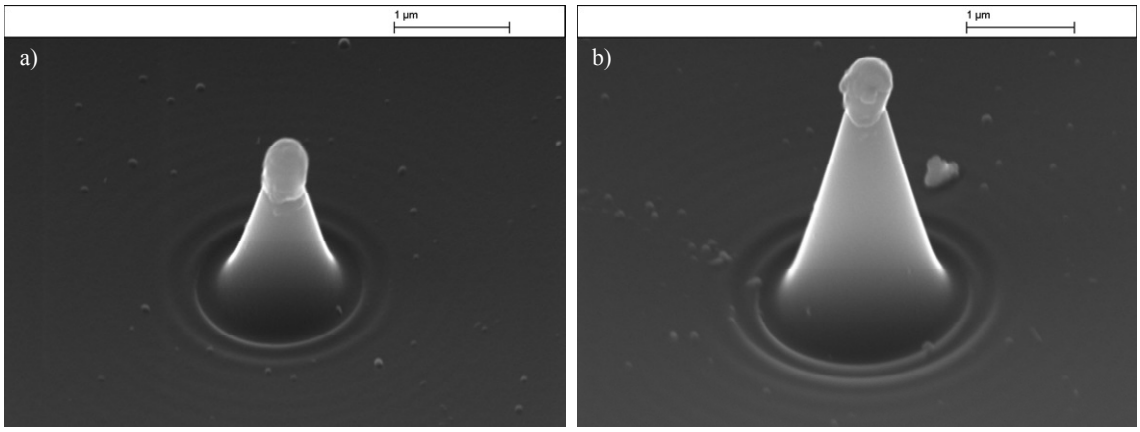

Figure 6.5: VUV 157nm F_2 laser ablation of silver particles on CR-39 polymer substrate - a) particle diameter 490nm, irradiated at laser fluence 260mJcm^{-2} with 10 laser pulses at a pulse repetition rate of 1Hz, composite structure height 1.43µm and b) particle diameter 570nm, irradiated at laser fluence 350mJcm^{-2} with 20 laser pulses at a pulse repetition rate of 1Hz, composite structure height 2.9µm. Both SEMs viewed at 45°.

Larger silver particles, of diameter 4-7µm (Alfa Aesar, UK), were also irradiated at a wavelength of 157nm using the VUV F_2 laser.

The scanning electron micrograph in Figure 6.6a) shows a selection of this sample of particles before irradiation with the laser. The average particle size is 9.6µm. The particles shown in Figure 6.6b) are ~500nm and ~480nm in diameter, and were irradiated at a laser fluence of 325mJcm^{-2} with 10 laser pulses (1Hz pulse repetition rate). As a result of the ablation of the surrounding polymeric substrate, the composite

conical structures are ~1.5µm in height. The ~1.2µm diameter silver particle shown in Figure 6.6c) was irradiated with 20 laser pulses (1Hz pulse repetition rate) at a fluence of 325mJcm^{-2}, resulting in a composite conical structure ~3.4µm in height. As the particles in Figure 6.6b) are slightly more spherical than the particle in Figure 6.6c), the interference fringe patterns are more even. The non-spherical shape of the particle in Figure 6.6c) has been translated into the shape of the polymeric support structure and the interference fringe pattern, which can be seen to replicate the shape of the particle.

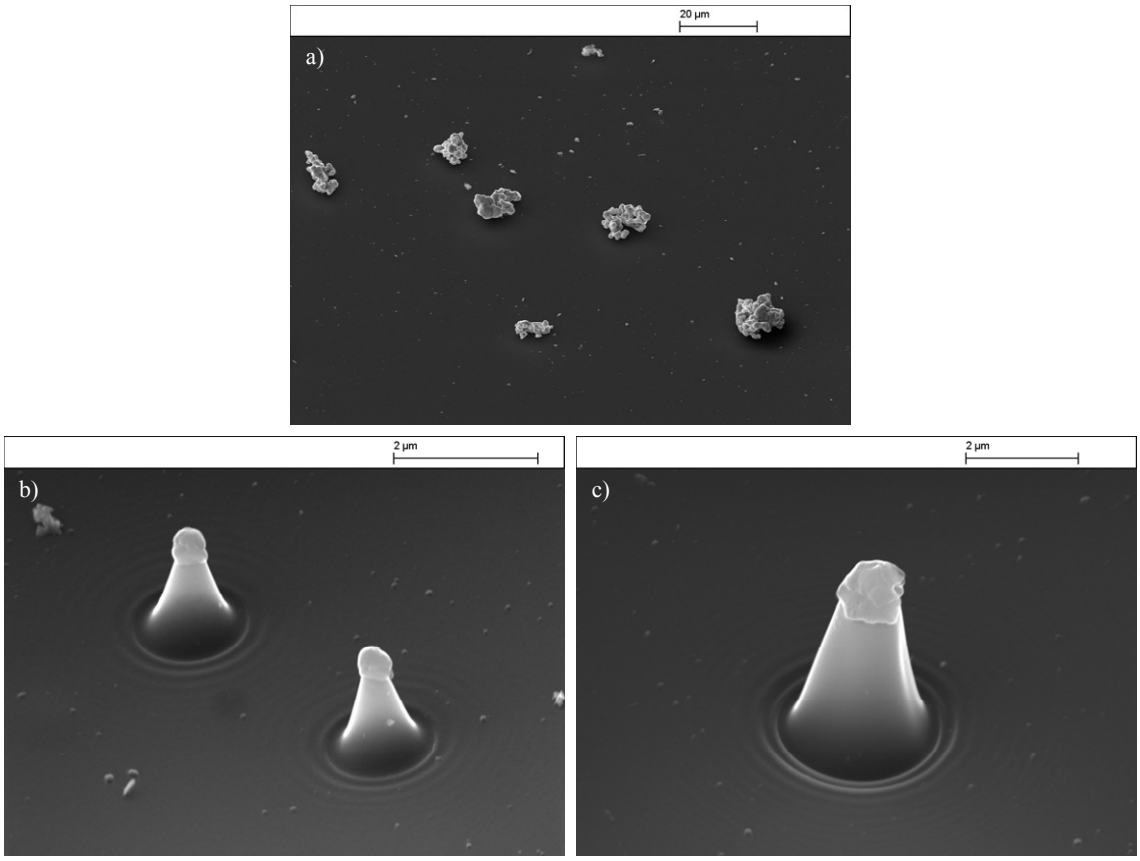

Figure 6.6: VUV 157nm F_2 laser ablation of silver particles on CR-39 polymer substrate - a) particles from the 4-7µm diameter sample, average diameter measured as 9.6 µm, b) particle diameters 500nm and 480nm, irradiated at laser fluence 325mJcm^{-2} with 10 laser pulses at a pulse repetition rate of 1Hz, composite structure heights ~1.5µm and c) particle diameter ~1.2µm, irradiated at laser fluence 325mJcm^{-2} with 20 laser pulses at a pulse repetition rate of 1Hz, composite structure height ~3.4µm. All SEMs viewed at 45°.

Section 6.2.3 - Cylindrical Particles (Wires)

Composite linear prismatic structures were formed by seeding polymeric substrates with silver nanowires and irradiating with the F_2 laser at a wavelength of 157nm. The laser fluence and number of applied laser pulses were varied to tailor the heights of the prismatic structures.

Shown in Figure 6.7 and Figure 6.8 are optical micrographs of the ablation sites in CR-39 polymer and polycarbonate respectively, corresponding to the Scanning Electron Micrographs used later.

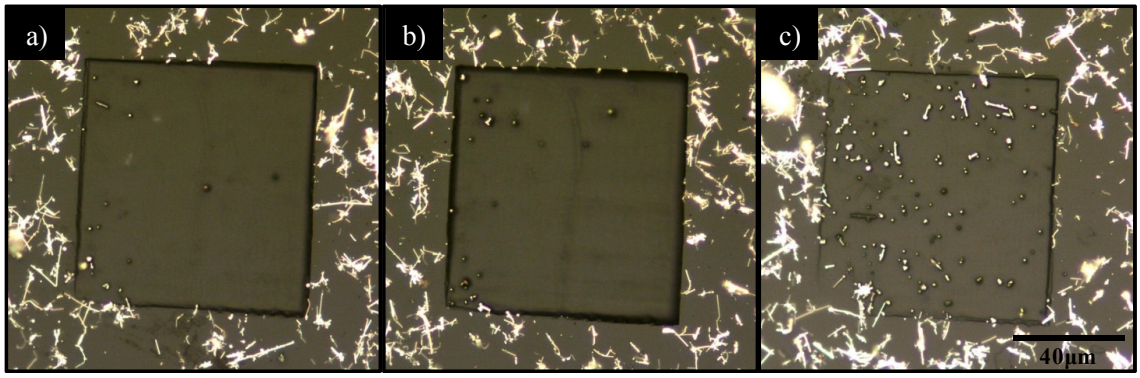

Figure 6.7: Optical micrographs of ablation sites in CR-39 polymer after irradiation with a 157nm laser at a pulse repetition rate of 10Hz at a) laser fluence 265mJcm^{-2} with 10 laser pulses, b) laser fluence 260mJcm^{-2} with 20 laser pulses and c) laser fluence 185mJcm^{-2} with 10 laser pulses. Scale bar in c) applies to all micrographs.

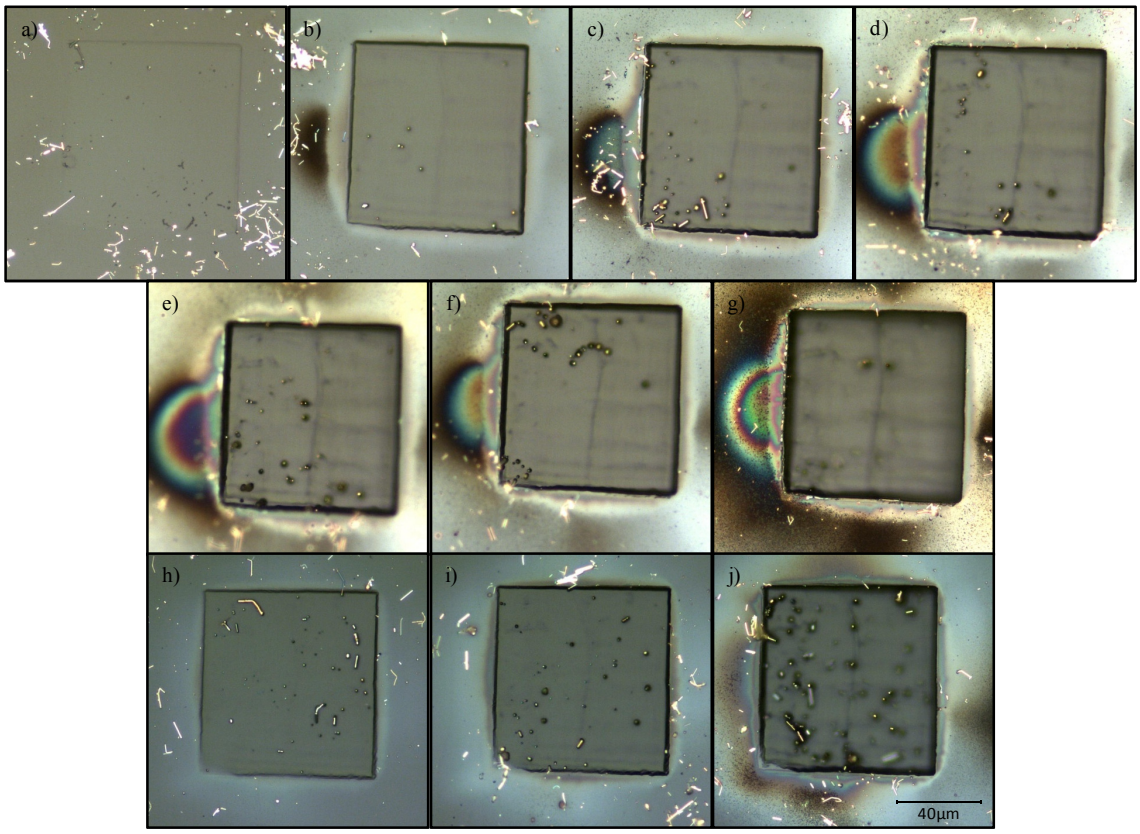

Figure 6.8: Optical micrographs of ablation sites in polycarbonate after irradiation with a 157nm laser at a pulse repetition rate of 10Hz with a) laser fluence 260mJcm^{-2} and 1 laser pulse, b) laser fluence 260mJcm^{-2} and 10 laser pulses, c) laser fluence 260mJcm^{-2} and 20 laser pulses, d) laser fluence 260mJcm^{-2} and 30 laser pulses, e) laser fluence 260mJcm^{-2} and 40 laser pulses, f) laser fluence 210mJcm^{-2} and 30 laser pulses, g) laser fluence 210mJcm^{-2} and 60 laser pulses, h) laser fluence 175mJcm^{-2} and 10 laser pulses, i) laser fluence 175mJcm^{-2} and 20 laser pulses and j) laser fluence 175mJcm^{-2} and 50 laser pulses. Scale bar in j) applies to all images.

The depths of the ablation sites, and hence the heights of the polymeric linear prismatic structures, were measured using a white light interferometer. As shown in the graphs in Figure 6.9, there is a linear increase in the polymeric linear prismatic structure height with the number of incident laser pulses, as well as an increase in height with laser fluence. To obtain the height of the full composite linear prismatic structure, the

diameter of the seeding silver nanowire should be added to the polymeric structure height.

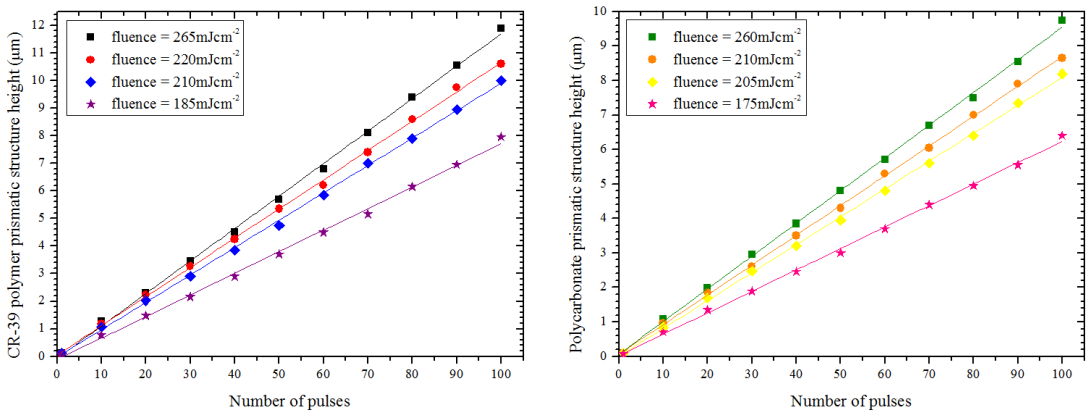

Figure 6.9: Graphs to show the polymer linear prismatic support structure heights for CR-39 polymer (left) and polycarbonate (right). The structure height is dependent on both the number of incident laser pulses and the fluence of the laser beam.

Figure 6.10 shows composite nanostructures formed by the ablation of a polycarbonate substrate that was seeded with silver nanowires. The sample was irradiated at a wavelength of 157nm with increasing pulse numbers at a laser fluence of 260mJcm^{-2}.

The wire shown in Figure 6.10a) has been irradiated with 1 laser pulse. This has fabricated a ~100nm high "plinth" for the seeding particle to sit on. This micrograph shows the initial development of a composite linear prismatic structure, which exhibits a small degree of deformation at the silver-polycarbonate interface. This wire has a diameter of ~560nm and length of ~3.3µm; the diameter is slightly larger than the average seen in non-irradiated wires.

Figure 6.10b) shows a silver wire that has been irradiated with 10 laser pulses at a pulse repetition rate of 10Hz. The wire overshoots the edge of the ablation site, and clearly shows the mechanism by which the linear prismatic structures (and analogous conical structures) are formed – the seeding particle, in this case a silver wire of diameter ~730nm and length ~4.1µm, shields the underlying polymer from the incident photons while the surrounding polymer is ablated. The degree of shielding is dependent on the effective cross-section of the shielding particle, meaning that the length and width of the final prismatic structure are defined by the length and diameter of the wire respectively. The height of the prismatic structure is mainly dependent on the number of laser pulses.

Figure 6.10c) shows a wire ~6.8µm in length with a diameter of ~780nm after irradiation with 20 laser pulses at a pulse repetition rate of 10Hz. The resulting silver-polycarbonate composite linear prismatic structure is ~2.8µm in height. While this wire

looks stable, it is surrounded by a number of composite conical structures, perhaps resulting from the transformation by laser heating from a wire to a spherical particle, a process which will be discussed later in Chapter 7.

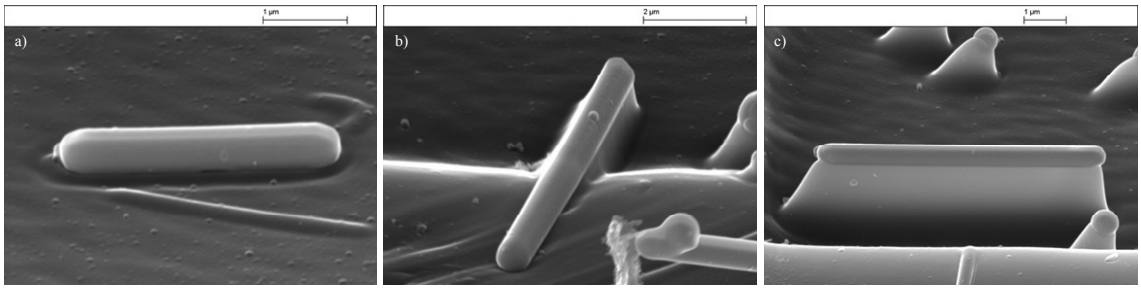

Figure 6.10: VUV 157nm F_2 laser irradiation of silver nanowires on polycarbonate substrate at laser fluence 260mJcm^{-2} with a) 1 laser pulse, b) 10 laser pulses and c) 20 laser pulses. SEMs viewed at 60°.

The composite structure shown in Figure 6.11a) was formed by the ablation of a CR-39 polymer substrate seeded with a silver nanowire at a wavelength of 157nm at a laser fluence of 265mJcm^{-2} with 10 laser pulses at a pulse repetition rate of 10Hz. The wire is ~610nm in diameter and ~4.5µm in length, and the composite linear prismatic structure is ~1.2µm in height.

Figure 6.11b) shows a composite linear prismatic structure formed by the ablation of CR-39 polymer seeded with silver nanowires at a fluence of 260mJcm^{-2} using 20 laser pulses at a pulse repetition rate of 10Hz. The seeding wire is ~460nm in diameter and ~7.8µm in length, and the fabricated composite linear prismatic structure is ~2.8µm in height. The micrograph also shows another linear prismatic structure, and a number of conical-type structures in the background.

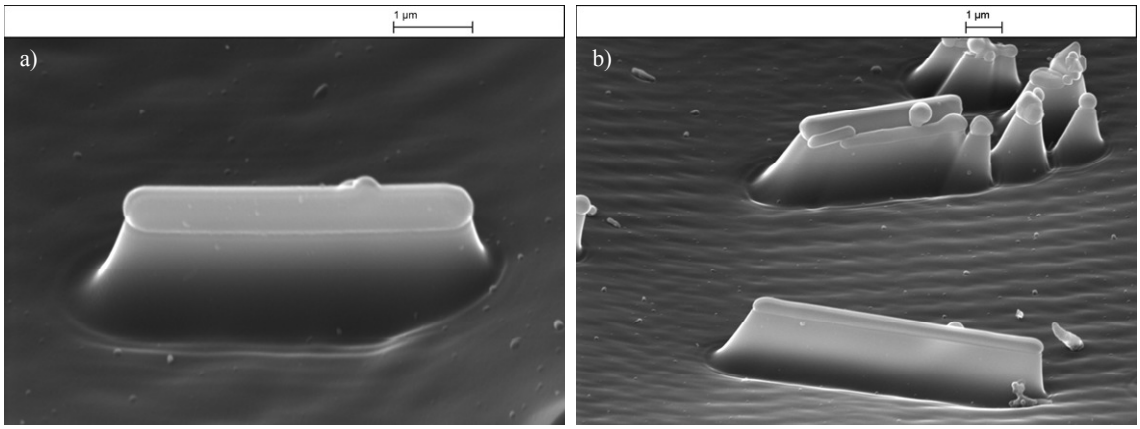

Figure 6.11: VUV 157nm F_2 laser irradiation of silver nanowires on CR-39 polymer substrate - a) laser fluence 265mJcm^{-2} with 10 laser pulses at a pulse repetition rate of 10Hz and b) laser fluence 260mJcm^{-2} with 20 laser pulses at a pulse repetition rate of 10Hz. SEMs viewed at a) 45° and b) 60°.

The silver wires shown in Figure 6.12 below were deposited on CR-39 polymer, and irradiated at a fluence of 185mJcm^{-2} using 10 laser pulses at a pulse repetition rate of

10Hz. The wires are on average ~370nm in diameter, and after irradiation, show some degree of melting. The inset to Figure 6.12a) appears to show that the wire begins to melt in the middle, and the length of the two halves recedes towards the ends of the wire. The diameter of the wire increases between 20-40% from the centre to the ends. As shown in Figure 6.12b), the wires also appear slightly more curved than before irradiation, perhaps suggesting some loss of structural rigidity due to the heating effects of the incident laser beam.

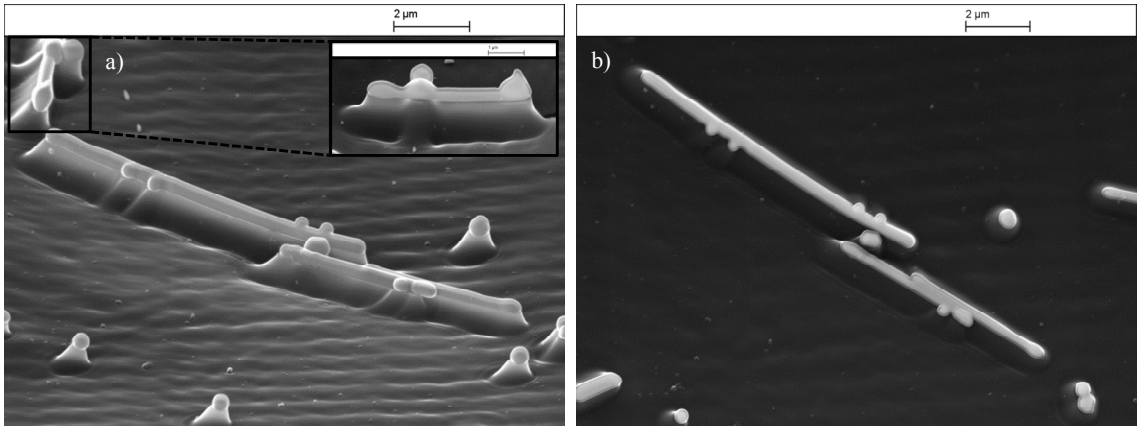

Figure 6.12: VUV 157nm F_2 laser irradiation of silver nanowires on CR-39 polymer substrate at laser fluence 185mJcm^{-2} with 10 laser pulses at a pulse repetition rate of 10Hz. SEMs viewed at a) 60°, inset 45° and b) 10°.

The SEMs in Figure 6.11b) and Figure 6.12 show a ripple-like pattern on the substrate. These *Laser-Induced Periodic Surface Structures*, or LIPSSs, develop as a result of polarised incident laser beams interfering with the scattered surface wave, which indicates that the alternative laser system used here has some degree of beam polarisation. It has been suggested that LIPSSs could be exploited for grating fabrication or surface microstructure modification [107, 108]. The periodicity of the ripples should be comparable to the wavelength of the laser radiation, in this case 157nm [107-109]. The periodicity has been measured to be ~230±83nm, which is in good agreement with the literature.

Figure 6.13 shows two composite structures, fabricated by irradiating a polycarbonate substrate seeded with silver nanowires with 157nm radiation at a laser fluence of 210mJcm^{-2}. The wire in Figure 6.13a) was irradiated with 30 laser pulses, and the wire in Figure 6.13b) with 60 laser pulses, both at a pulse repetition rate of 10Hz. The linear prismatic structure in Figure 6.13a) is ~2.6µm in height, including the wire of diameter ~890nm. The linear prismatic structure shown in Figure 6.13b) is ~5.3µm in height, including the wire diameter of ~1.1µm. While interference patterns surrounding the bases are not clearly evident, these prismatic structures exhibit similar features to the

polystyrene-seeded conical structures and the silicon carbide-seeded prismatic structures presented previously. However, due to the smoother surface structure of the silver wires, the walls of the silver-polycarbonate and silver-CR-39 polymer linear prismatic structures are smoother than the walls of the silicon carbide-seeded linear prismatic structures (the silicon carbide whiskers have a very rough surface structure, most likely due to the manufacturing process). The silver wire in Figure 6.13b) also shows some degree of surface melting.

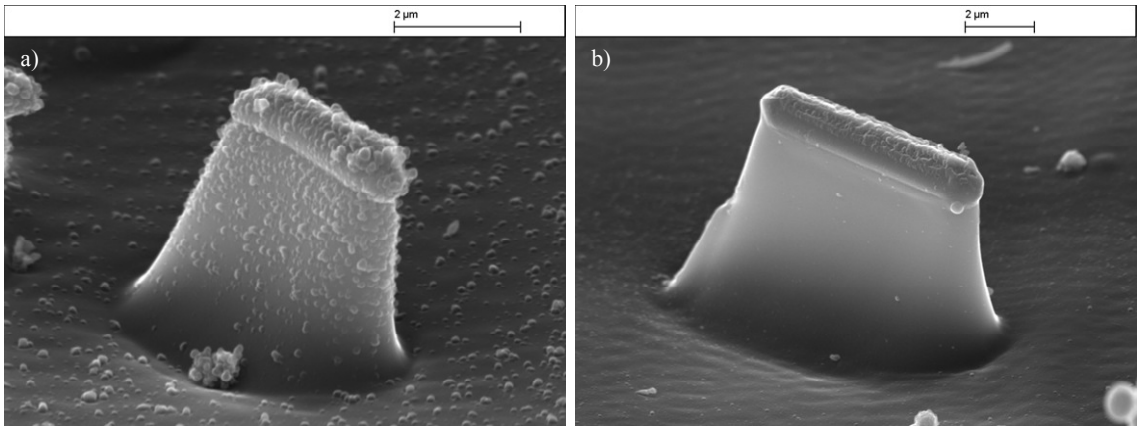

Figure 6.13: VUV 157nm F_2 laser irradiation of silver nanowires on polycarbonate substrate at laser fluence 210mJcm^{-2} at a pulse repetition rate of 10Hz with a) 30 laser pulses and b) 60 laser pulses. SEMs viewed at 60°. It is felt that the "beads" in a) are redeposited debris from subsequent laser pulses on the sample.

Figure 6.14 shows silver nanowires that were deposited on polycarbonate and irradiated at a fluence of 260mJcm^{-2} with increasing pulse numbers. The seeded polymer shown in Figure 6.14a) was ablated with 20 laser pulses, the sample in Figure 6.14b) with 30 laser pulses, and the structure in Figure 6.14c) with 40 laser pulses. The wire in Figure 6.14a) is narrower at one end, ~550nm, than at the other, ~1µm, perhaps suggesting that this is a portion of a longer wire that has broken apart, and this section has begun to recede into a spherical particle. This theory is also supported by the length of this wire, approximately 3µm – much shorter than that typically seen in non-irradiated samples.

The wire shown in Figure 6.14b) also supports a transformation from a wire to spherical particles. The wire is ~3.1µm in length, and ~620nm in diameter at the ends. The diameter is reduced to ~360nm in the centre, and the wire appears to be breaking apart at this point.

The wire shown in Figure 6.14c) can also be used to suggest a shape transformation. The diameter of the wire decreases towards the centre, reducing from ~1.1µm at the ends to ~810nm in the centre.

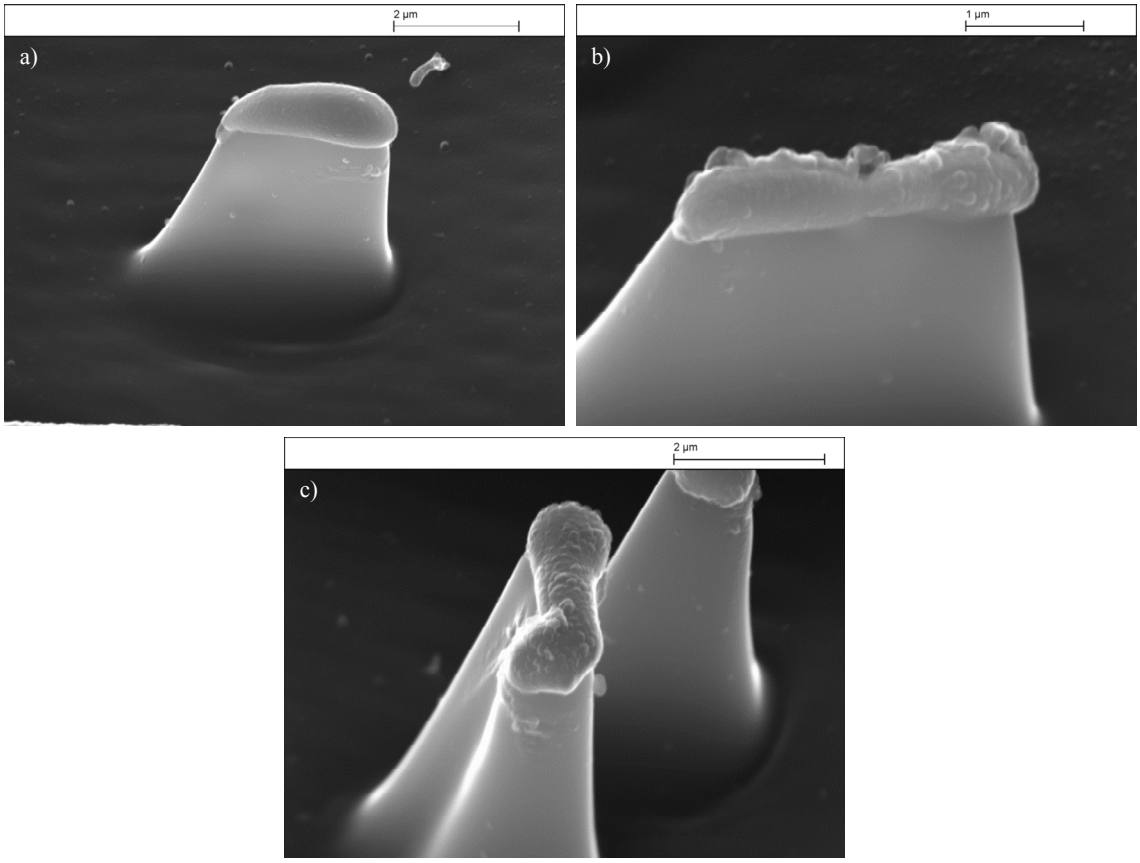

Figure 6.14: VUV 157nm F_2 laser irradiation of silver nanowires on polycarbonate substrate ate laser fluence 260mJcm^{-2} at a pulse repetition rate of 10Hz with a) 20 laser pulses, b) 30 laser pulses and c) 40 laser pulses. All SEMs viewed at 45°.

The particle sitting on top of the polycarbonate conical structure shown in Figure 6.15a) is ~790nm in diameter. The silver seeding particle, perhaps a nanowire, was irradiated at a fluence of 175mJcm^{-2} with 20 laser pulses at a pulse repetition rate of 10Hz. The diameter of this particle is much greater than that seen in non-irradiated wires, potentially suggesting that a longer nanowire has been heated sufficiently to induce melting, and a subsequent length contraction of a wire towards a spherical particle. Energy Dispersive X-Ray (EDX) analysis, shown in Figure 6.15b) confirms that the particle is silver, and this spectrum is typical of both the non-irradiated and laser irradiated particles. The spectrum was measured by positioning the x-ray beam normal to the apex of the silver-polycarbonate structure, as shown by the cross in Figure 6.15a). The numerous peaks present in the range 2.3eV to 3.5eV are evidence that the seeding particles are made from silver.

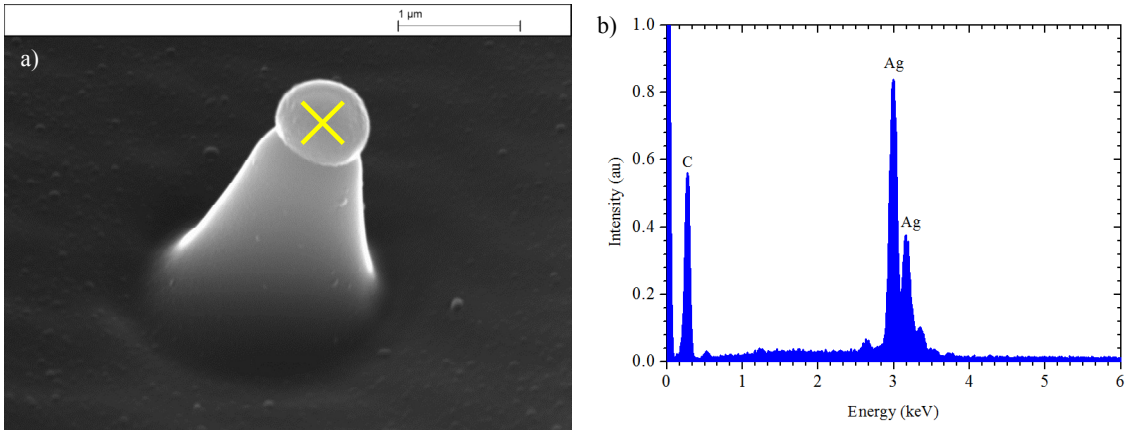

Figure 6.15: VUV 157nm F_2 laser ablation of silver particle on polycarbonate substrate at laser fluence 175mJcm^{-2} with 20 laser pulses at a pulse repetition rate of 10Hz, particle diameter 790nm - a) SEM viewed at 45° and b) Energy Dispersive X-Ray (EDX) analysis.

Calculations to determine the temperature of the nanoparticles during the laser irradiation, which are presented in Section 7.2.4, indicate that the laser fluences used in the experiments described here are sufficient to initiate melting of the silver quasi-spherical particles and wires.

Section 6.2.4 - Finite Element Method Modelling of Silver Particles

The Finite Element Method (FEM) software package COMSOL Multiphysics version 3.5a was used to model silver nanoparticles of various sizes, both free-standing and on substrates, irradiated at a variety of incident radiation wavelengths. Pairs of these spherical particles and individual silver nanowires as well as the composite conical and prismatic structures formed by laser ablation were also modelled. Polycarbonate was used as the substrate material for all models, where necessary.

The mesh size was varied depending on the geometry of the model, and continuity boundary conditions were used throughout.

The refractive index, n, and extinction coefficient, k of the silver and polycarbonate are dependent on the incident wavelength, and the values used are defined in Table 6.2. For polycarbonate irradiated at the wavelengths used here, $k \approx 0$.

All of the models described in this section were constructed by the same method. The models were drawn, and continuity boundary conditions applied. The subdomains were set with the appropriate optical properties, and an appropriate mesh size was applied to the model. The model was then solved by the software using Maxwell's equations. For all models, the light is incident from the left.

Wavelength / nm	Silver		Polycarbonate
	n	k	n
382.3	0.05	1.864	1.728
398.2	0.05	2.070	1.718
414.4	0.05	2.275	1.706
431.4	0.04	2.462	1.680
451.8	0.04	2.657	1.660
472.4	0.05	2.869	1.645
497	0.05	3.093	1.621
522	0.05	3.324	1.611
549.7	0.06	3.586	1.597
583.3	0.05	3.858	1.587
618.1	0.06	4.152	1.575
660.8	0.05	4.483	1.567

Table 6.2: Optical data for silver and polycarbonate - silver from [110], polycarbonate from [111].

Section 6.2.4.1 - Single Spherical Silver Particles - freestanding and supported on substrates

Finite element method software was used to model spherical silver particles comparable in size to those used experimentally to fabricate composite micro- and nanoscale structures. The particles are 500nm in diameter, and are shown in Figure 6.16. The optical coefficents used for these models were n = 1.16 and k = 0.75 (at 8eV) [112]. Both particles are irradiated with 157nm radiation; the particle in Figure 6.16a) is being irradiated with transverse electric (TE) polarised radiation, and the particle in Figure 6.16b) with transverse magnetic (TM) polarised radiation.

These models demonstrate the ability of the silver particles to shield the radiation and hence fabricate a structure when adjacent to a polymeric substrate. They also show that there is high EM field intensity at the top surface of the particle, which could also indicate a high temperature and hence the cause of the particle melting and shape transformation. This also applies to the other opaque seeding particles

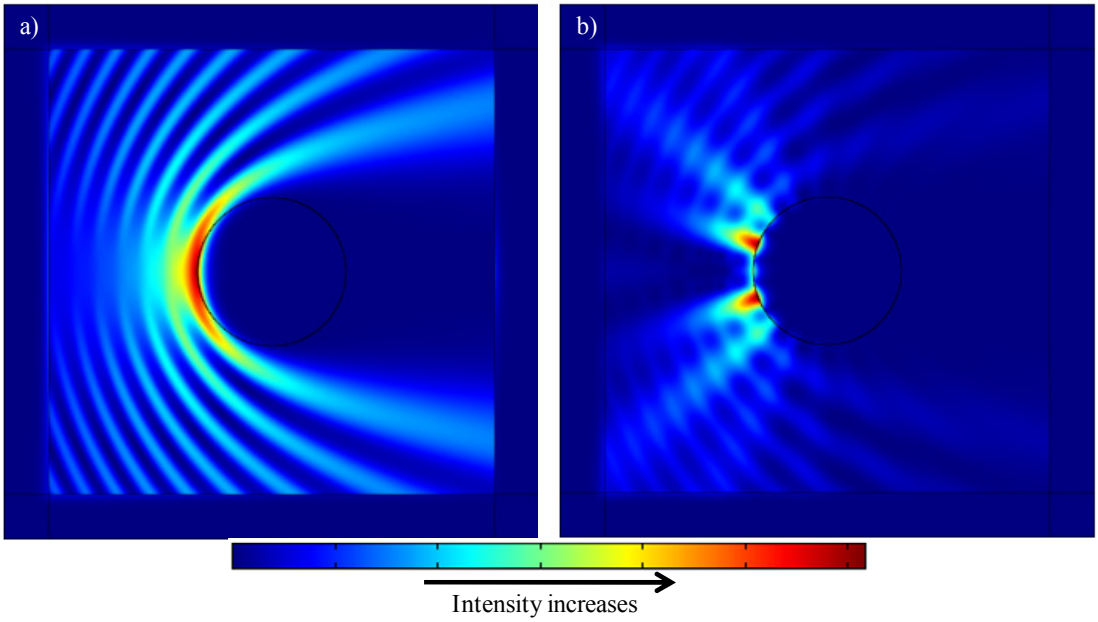

Figure 6.16: Two-dimensional FEM analysis of free-standing 500nm diameter silver particles irradiated at 157nm with a) TE polarised and b) TM polarised radiation.

One of the limitations of the FEM method is demonstrated in the models in Figure 6.16. The use of the two-dimensional model (through computational power limitations) means that the software "sees" the particle as a circle and not as a sphere. This causes the difference in the intensity distribution of the electromagnetic field when TE and TM polarised radiation are used, as seen in the models in Figure 6.16. If this investigation was carried out in three-dimensional space, the use of TE and TM radiation would result in identical intensity distributions.

The interaction between the electric field component and free-standing silver nanoparticles of different sizes can be seen in Figure 6.17. The diameter of the particle increases from 50nm in Figure 6.17a) to 100nm in Figure 6.17c) and to 500nm in Figure 6.17e). The meshes shown in Figure 6.17b), Figure 6.17d) and Figure 6.17f) relate to Figure 6.17a), Figure 6.17c) and Figure 6.17e) respectively. All of these particles are being irradiated at 451.8nm. The effect of the size of the particle on the electromagnetic field can be seen, and explained in terms of the field across the particle [113].

The field around the 50nm diameter particle shown in Figure 6.17a) is uniform on opposite sides. This is due to the particle being much smaller than the wavelength of the incident radiation. The electric field across the particle is uniform, causing the conduction electrons to move in-phase, producing dipole oscillations, as shown in Figure 6.18a).

As the size of the particle increases, as in Figure 6.17c) and Figure 6.17e), the field around the particle becomes distorted, with the degree of distortion dependent on the particle size. As the 100nm diameter particle is still smaller than the wavelength, the electric field across the particle is reasonably uniform, while the 500nm diameter particle is larger than the wavelength of the incident light. This results in the field across the particle becoming non-uniform, exciting multipole resonances, shown in Figure 6.18b) and Figure 6.18c).

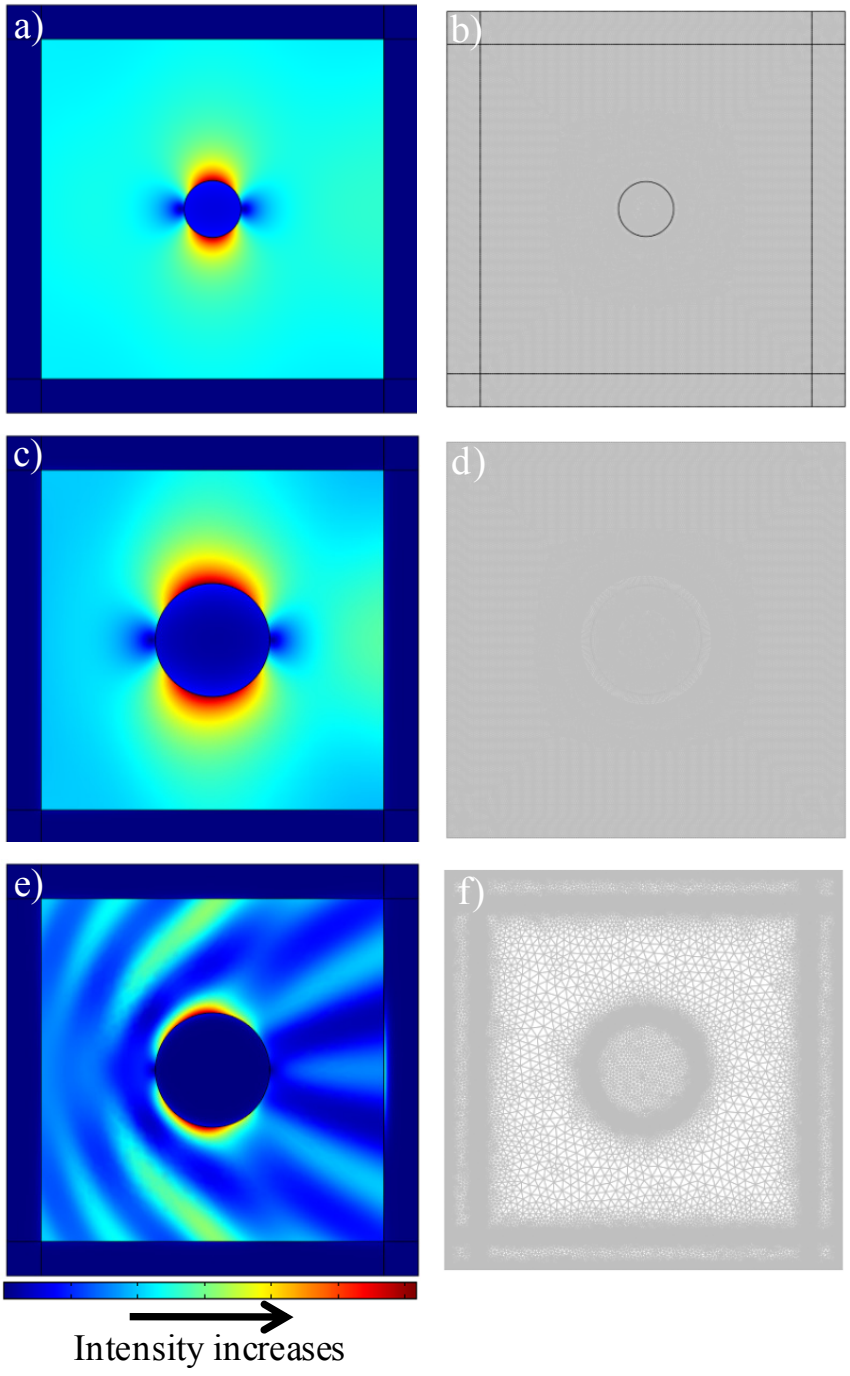

Figure 6.17: Two-dimensional FEM analysis of free-standing silver nanoparticles irradiated with TM polarised radiation at a wavelength of 451.8nm - a) 50nm diameter particle and b) model mesh, c) 100nm diameter particle and d) model mesh and e) 500nm diameter particle and f) model mesh.

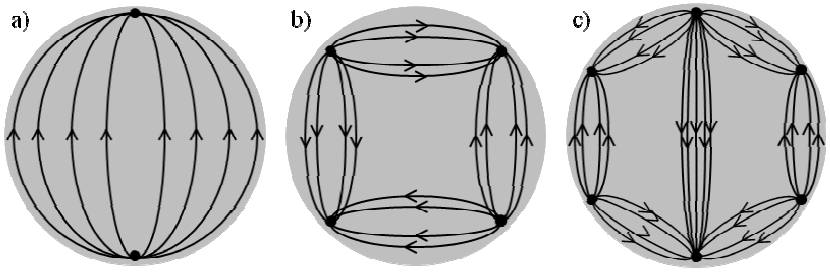

Figure 6.18: Diagrams of the electric field lines of a) dipoles in sub-wavelength nanoparticles, and b) quadrupoles and c) octupoles in increasing sized particles.

Shown in Figure 6.19 are 50nm diameter, 100nm diameter and 500nm diameter silver particles, as before, but in these models they are in contact with a polycarbonate substrate. Again, they are all irradiated at an incident wavelength of 451.8nm. Similarly to the free-standing particles, the field becomes more distorted as the particle size increases.

However, the presence of the substrate also distorts the electric field, with an increase in the field intensity at the interface between the silver particle and the polycarbonate substrate. Particularly with the 50nm diameter and 100nm diameter particles, the maximum of the intensity of the field appears to be "pulled around" the particle from the sides to the interface region due to the presence of the substrate. This would suggest increased energy incident on the polymer substrate surface around the base of the particle which would assist in the removal, or ablation, of the substrate material to initiate the fabrication of a conical structure. The higher intensity regions located on the sides of the larger particles in Figure 6.19c) and Figure 6.19e) would suggest that, under experimental conditions, these particles would suffer some degree of shape and/or size transformation due to a greater incident energy in these regions.

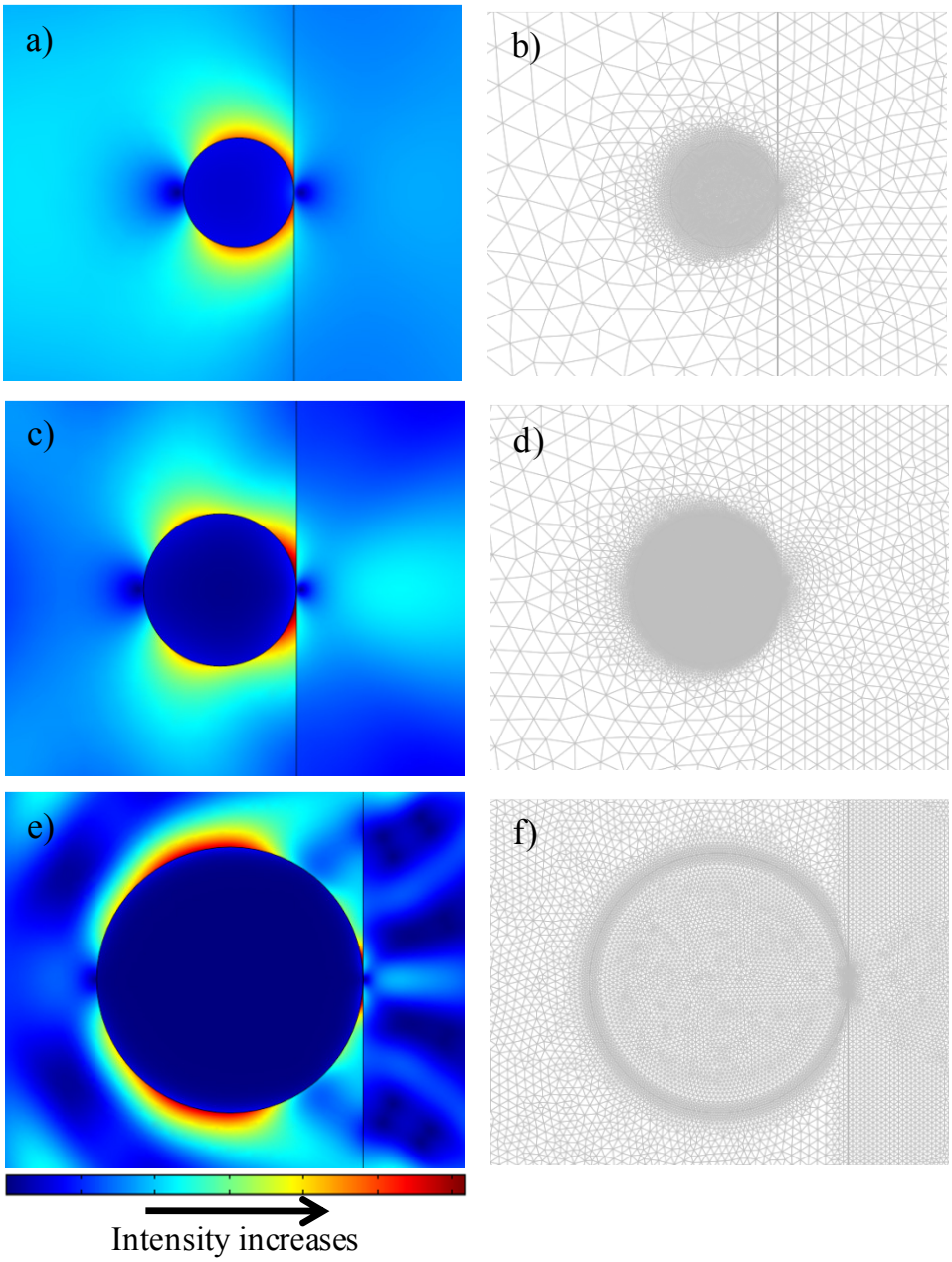

Figure 6.19: Two-dimensional FEM analysis of silver nanoparticles on polycarbonate substrate irradiated with TM polarised 451.8nm radiation - a) 50nm diameter particle and b) model mesh, c) 100nm diameter particle and d) model mesh and e) 500nm diameter particle and f) model mesh.

Section 6.2.4.2 - Pairs (Dimers) of Spherical Silver Particles - freestanding and supported on substrates

Two spherical silver nanoparticles in close proximity result in the coupling of the field enhancement around each individual particle. This is manifested as an intensity "hotspot" in the gap between the particles. Free-standing particle pairs and pairs of particles adjacent to a substrate exhibit the coupled field effect.

Two 50nm silver particles in close proximity, separated by a 5nm air gap, irradiated at different wavelengths are shown in Figure 6.20. A longer wavelength, such as 497nm

and 583.3nm, shown in Figure 6.20d) and Figure 6.20e) respectively, appears to excite a small degree of field enhancement on the outside of the particle pair that is not seen with shorter wavelength irradiation, such as 382.3nm and 451.8nm, as shown in Figure 6.20b) and Figure 6.20c) respectively. Figure 6.20f) shows the cross-section of the field intensity through the particle pair irradiated at 583.3nm, along the dotted line in Figure 6.20e). The intensity of the coupling in the gap between the particles is ~2.5× greater than the field enhancement around the outside of the pair, and ~5× greater than the background intensity.

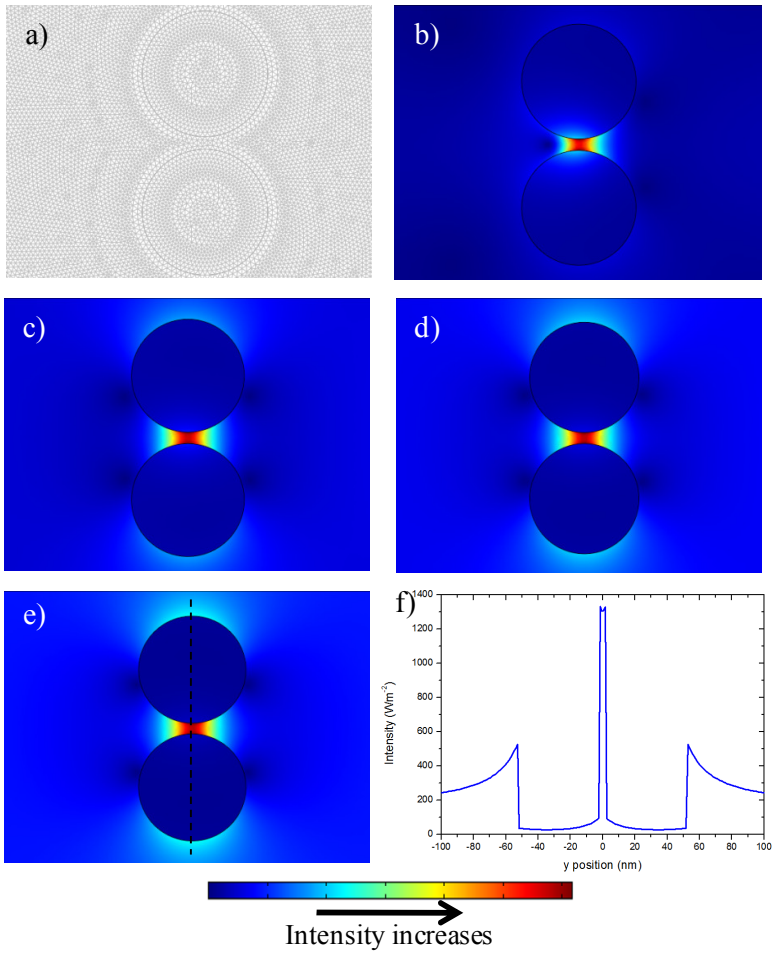

Figure 6.20: Two-dimensional FEM analysis of a pair of freestanding 50nm diameter silver nanoparticles separated by a 5nm air gap, irradiated with TM polarised radiation - a) model mesh, b) irradiated at 382.3nm, c) irradiated at 451.8nm, d) irradiated at 497nm, e) irradiated at 583.3nm and f) field intensity along the dotted line shown in e).

Similar features are seen when two free-standing 100nm diameter silver particles separated by a 5nm air gap are irradiated at different wavelengths, as shown in Figure 6.21. As an example, when the 100nm diameter particle pair is irradiated at 451.8nm, as shown in Figure 6.21c), the intensity of the electric field in the air gap is nearly 20× greater than the background field, as shown in the intensity profile in Figure 6.21d). Again, some field enhancement is seen around the outside of the particle pair at longer

wavelengths. This can be seen as a slight "halo" effect around the particles, for example when irradiated at 618.1nm as in Figure 6.21f).

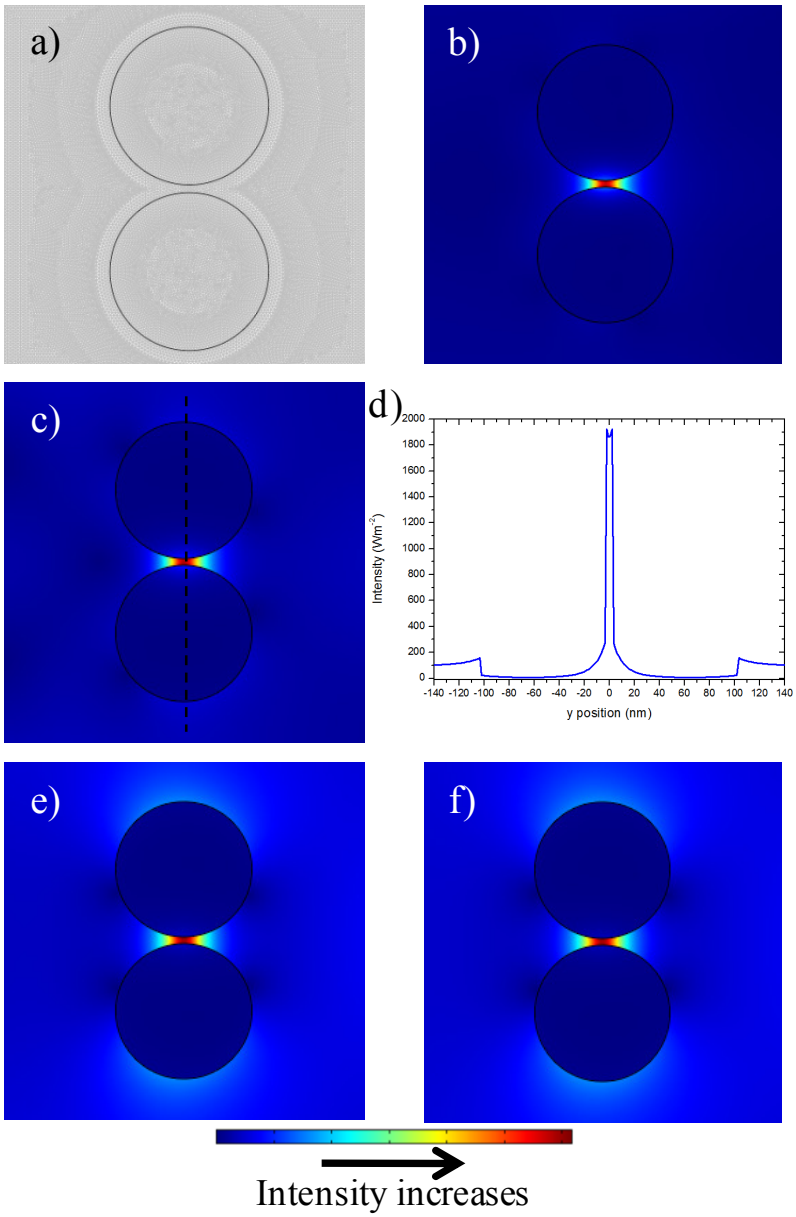

Figure 6.21: Two-dimensional FEM analysis of a pair of freestanding 100nm diameter silver nanoparticles separated by a 5nm air gap, irradiated with TM polarised radiation - a) model mesh, b) irradiated at 398.2nm, c) irradiated at 451.8nm, d) field intensity along the dotted line shown in c), e) irradiated at 583.3nm and f) irradiated at 618.1nm.

A pair of free-standing 500nm silver particles exhibits a slightly offset hotspot between the particles at shorter wavelengths, for example when irradiated at 382.3nm as shown in Figure 6.22b). These larger particles also exhibit a sharp increase in the field intensity in the gap between the particles, for example when the particle pair is irradiated at 431.4nm as shown in Figure 6.22c), the hotspot intensity is around 3× greater than the enhancement around the particle, and around 15× greater than the background, as

shown by the field intensity cross section (along the dotted line in Figure 6.22c) shown in Figure 6.22d).

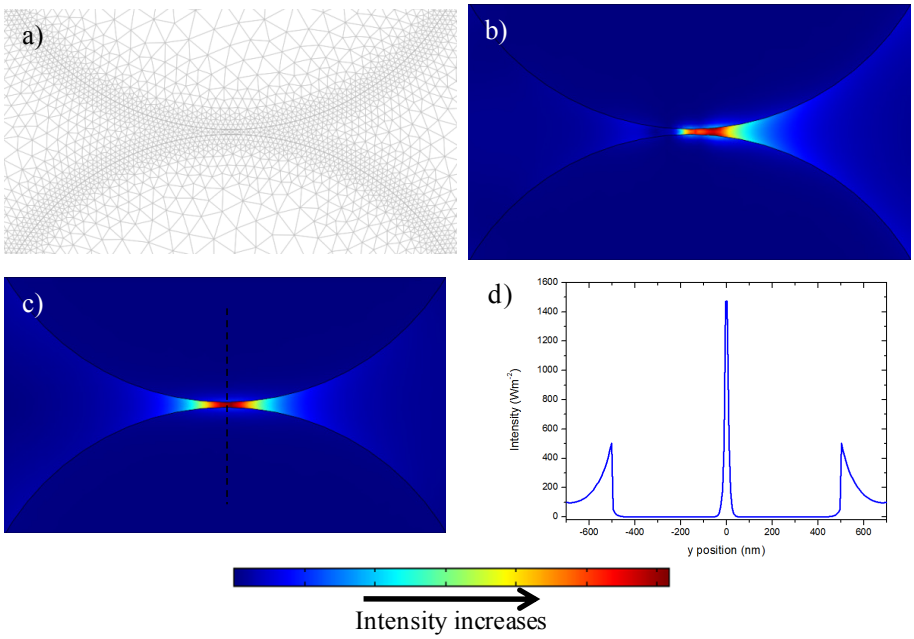

Figure 6.22: Two-dimensional FEM analysis of a pair of freestanding 500nm diameter silver nanoparticles separated by a 5nm air gap, irradiated with TM polarised radiation - a) model mesh, b) irradiated at 382.3nm, c) irradiated at 431.4nm and d) field intensity along the dotted line shown in c).

Pairs of silver nanoparticles adjacent to a polymeric substrate also exhibit this hotspot effect. However, as seen previously, the presence of the substrate also has an effect.

This effect can be seen in Figure 6.23 using a pair of 50nm diameter silver nanoparticles separated by a 5nm air gap. The intensity of the hotspot varies with wavelength, as shown in Figure 6.23a). There appears to be no relationship between wavelength and hotspot intensity, except for a general decrease in the hotspot intensity as wavelength increases. At an irradiation wavelength of 451.8nm, shown in Figure 6.23d), there is some field enhancement towards the "front" of the particle pair, possibly caused by a plasmon resonance effect. At an incident wavelength of 472.4nm, shown in Figure 6.23e), there is no intensity hotspot between the particles – the field enhancement appears at the interface between the nanoparticles and the substrate, on the "outside" of the particle pair. This effect is also seen at longer wavelengths, for example at 583.3nm, shown in Figure 6.23f), although a hotspot between the particles is seen at this wavelength.

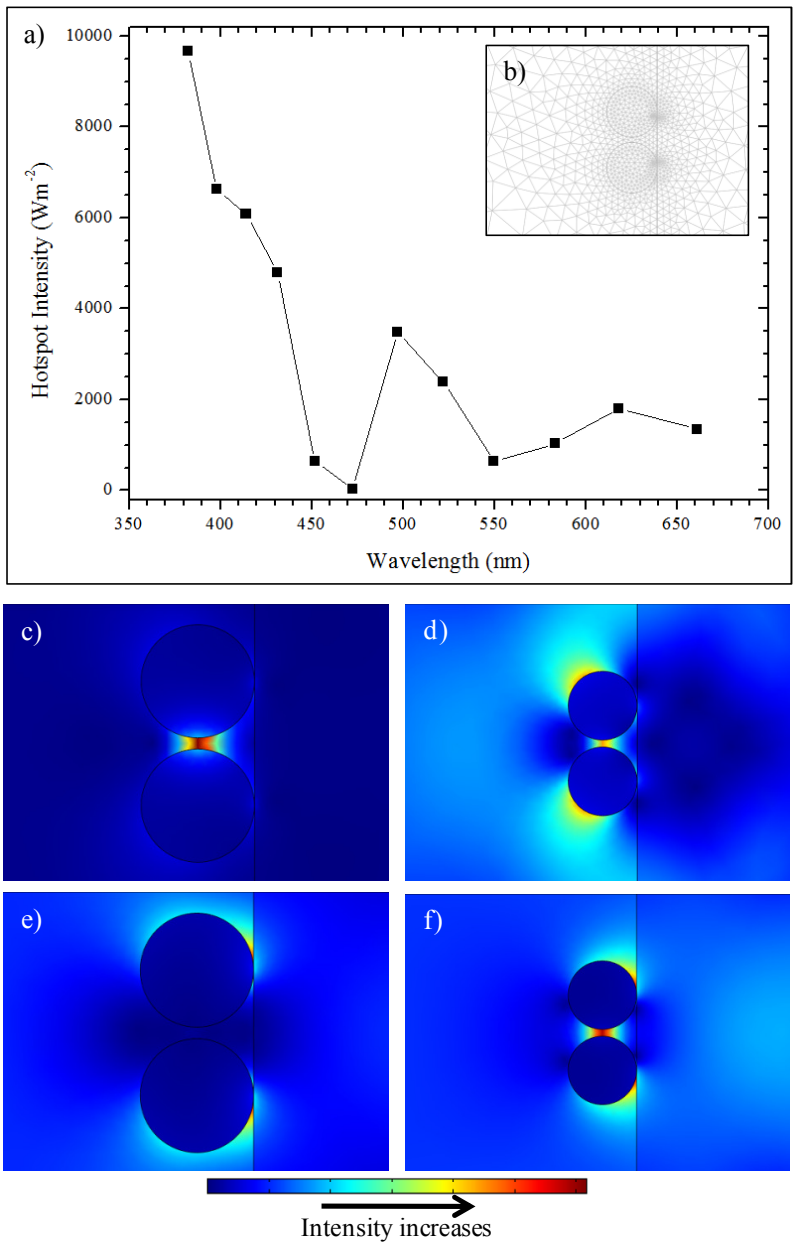

Figure 6.23: Two-dimensional FEM analysis of a pair of 50nm diameter silver nanoparticles, separated by a 5nm air gap, on polycarbonate substrate, irradiated with TM polarised radiation – a) graph of incident wavelength against hotspot region intensity, b) model mesh, c) irradiated at 382.3nm, d) irradiated at 451.8nm, e) irradiated at 472.4nm and f) irradiated at 583.3nm.

Similar effects can be seen using a 100nm diameter silver nanoparticle pair, also separated by a 5nm wide air gap, shown in Figure 6.24. As before, the graph in Figure 6.24a) shows no relation between the hotspot intensity and wavelength, except for a general decrease in intensity as wavelength increases. The peak intensity has shifted to a slightly longer wavelength than the smaller particles. The hotspot is also shifted slightly within the gap between the particles, more towards the substrate. The field enhancement on the outside of the pair at the particle-substrate interface can also been seen in these larger particles.

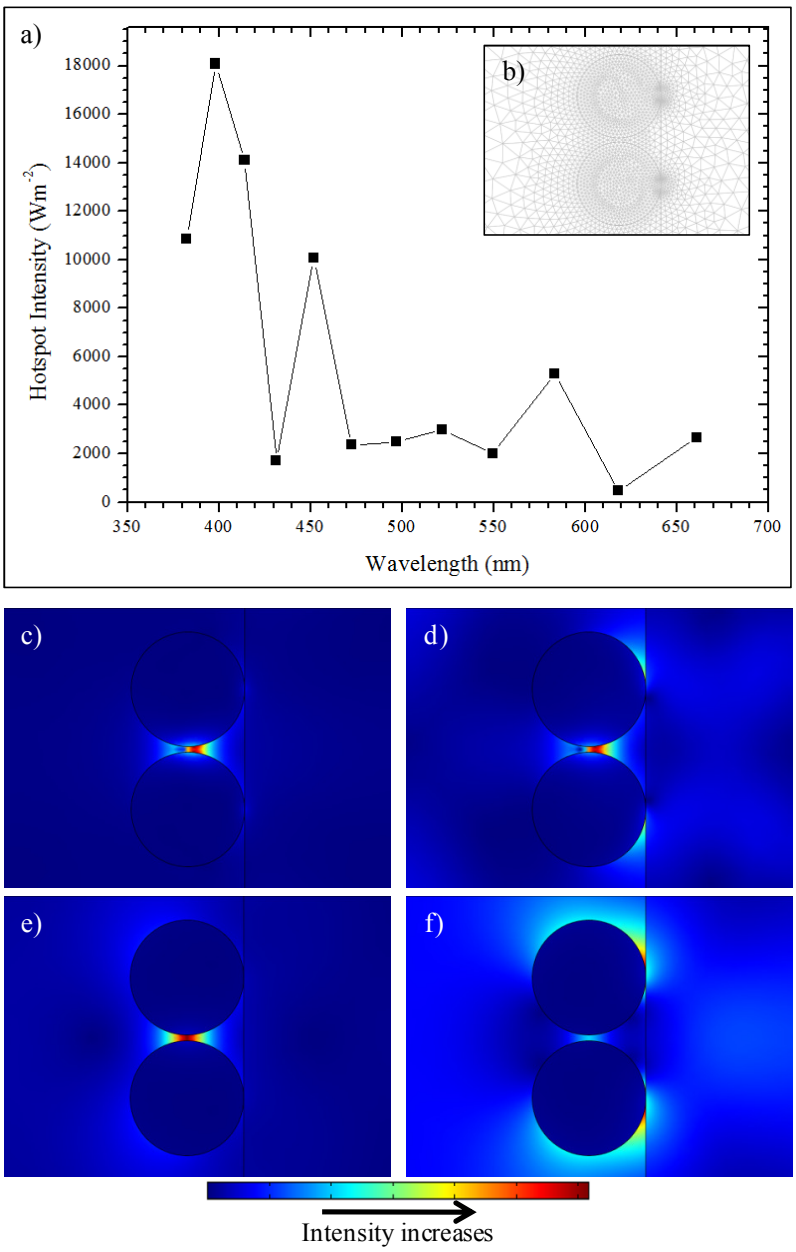

Figure 6.24: Two-dimensional FEM analysis of a pair of 100nm diameter silver nanoparticles, separated by a 5nm air gap, on polycarbonate substrate, irradiated with TM polarised radiation – a) graph of incident wavelength against hotspot region intensity, b) model mesh, c) irradiated at 398.2nm, d) irradiated at 431.4nm, e) irradiated at 583.3nm and f) irradiated at 618.1nm.

As the particle diameter increases to 500nm, still with a 5nm air gap, shown in Figure 6.25, the hotspot intensity is fairly consistent over the majority of the range of wavelengths studied, shown by the graph in Figure 6.25a). There is very little field enhancement at the particle-substrate interface, as shown in Figure 6.25c) and Figure 6.25d).

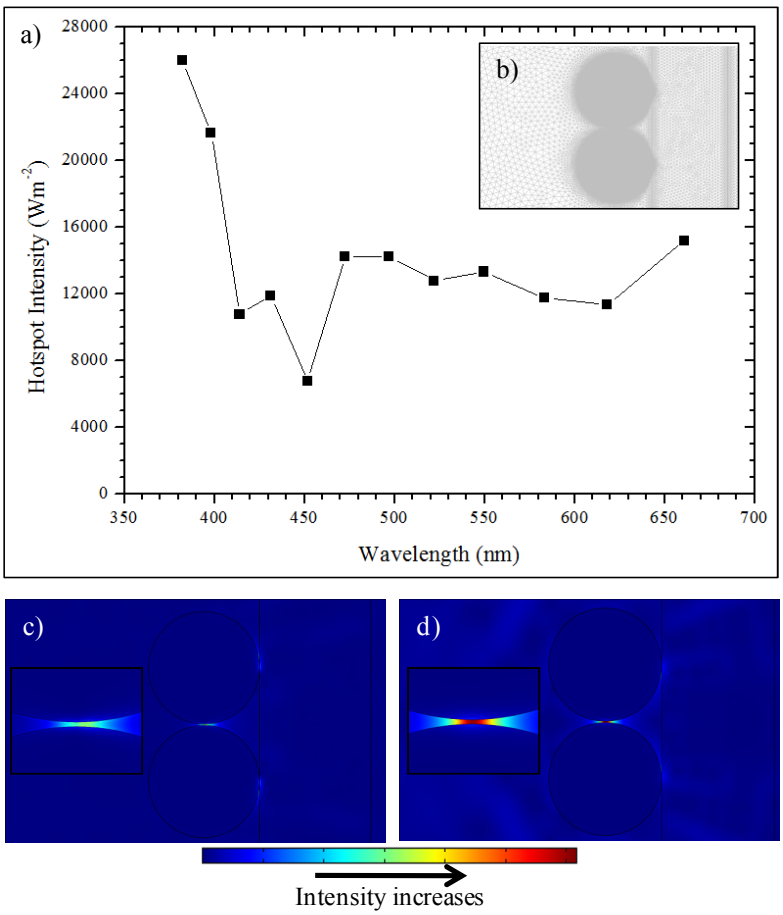

Figure 6.25: Two-dimensional FEM analysis of a pair of 500nm diameter silver nanoparticles, separated by a 5nm air gap, on polycarbonate substrate, irradiated with TM polarised radiation – a) graph of incident wavelength against hotspot region intensity, b) model mesh, c) irradiated at 382.3nm and d) irradiated at 451.8nm.

All of these models also show that the intensity of the hotspot increases as particle size increases.

Pairs of metallic particles in close proximity, such as those modelled in Figure 6.20-Figure 6.25, find application as optical antennas [114] and as SERS sensing platforms for chemical sensing, bioanalysis and biosensing [36, 37].

The separation distance between a pair of silver particles also has an effect on the hotspot intensity, as shown by the graph in Figure 6.26a). In the models previously presented, the separation distance was fixed at 5nm. Here, a pair of 500nm diameter spherical silver particles on a polycarbonate substrate is being irradiated at 420nm, with the spacing between the particles increasing. As the separation distance increases there is a general decrease in the hotspot field intensity. However, there are peaks in the hotspot intensity at separation distances of 2nm, shown in Figure 6.26b), and 5nm. There is then a sharp decrease in the hotspot intensity as the separation distance increases to 35nm, as shown in Figure 6.26c). At separation distances greater than

35nm, the field enhancement is seen on the outside of the particle pair at the particle-substrate interface. At separation distances around the irradiation wavelength, in this case 420nm, the intensity hotspot re-appears.

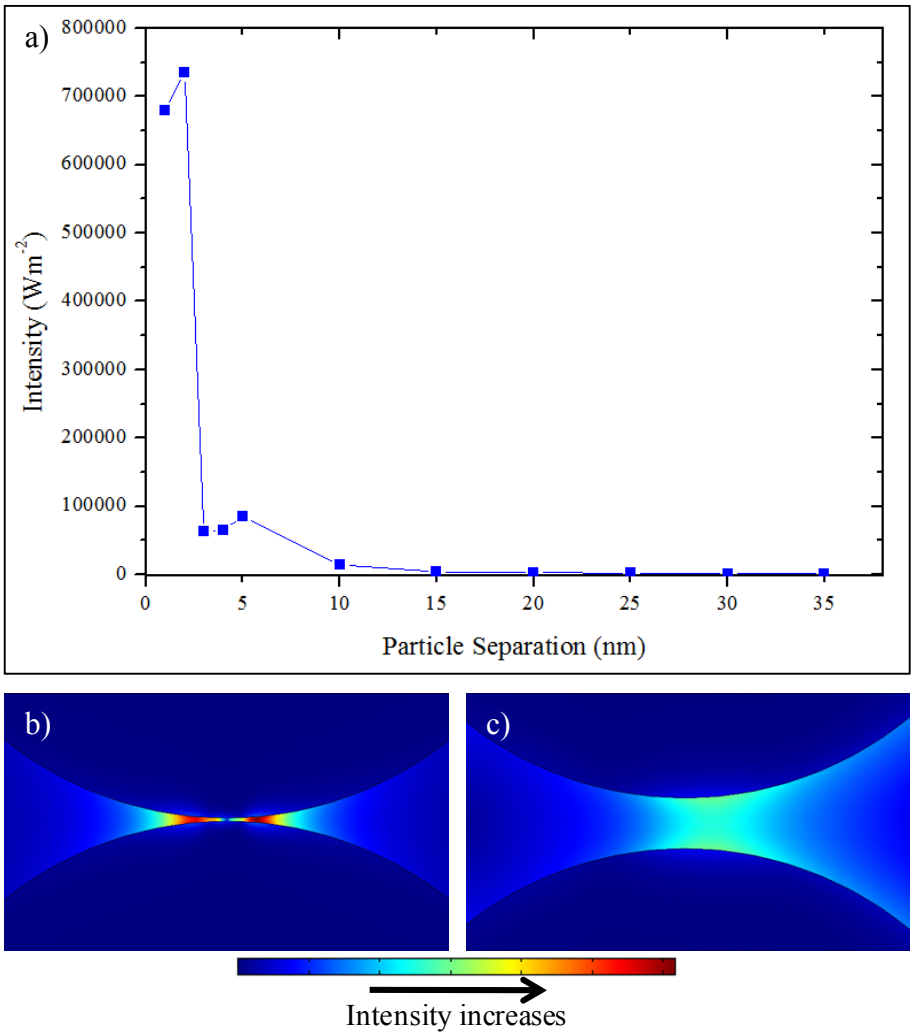

Figure 6.26: Two-dimensional FEM analysis of a pair of 500nm diameter silver nanoparticles on polycarbonate substrate, irradiated at 420nm with TM polarised radiation – a) graph of particle separation distance against hotspot intensity, b) 2nm separation and c) 35nm separation.

Changing the irradiation wavelength away from the plasmon resonance wavelength, there is a very sharp decrease in the hotspot intensity as the particle separation distance increases, as seen when the 500nm diameter particle pair is irradiated at 532nm as in Figure 6.27a). However, in this case there are no peaks in the hotspot intensity at other separation distances. The coupling of the electric field enhancement can clearly be seen at the smaller separation distances, such as 1nm and 10nm in Figure 6.27b) and Figure 6.27c) respectively. The breaking-apart of the coupled field occurs at larger separation distances; 55nm and 105nm separations are shown in Figure 6.27d) and Figure 6.27e) respectively.

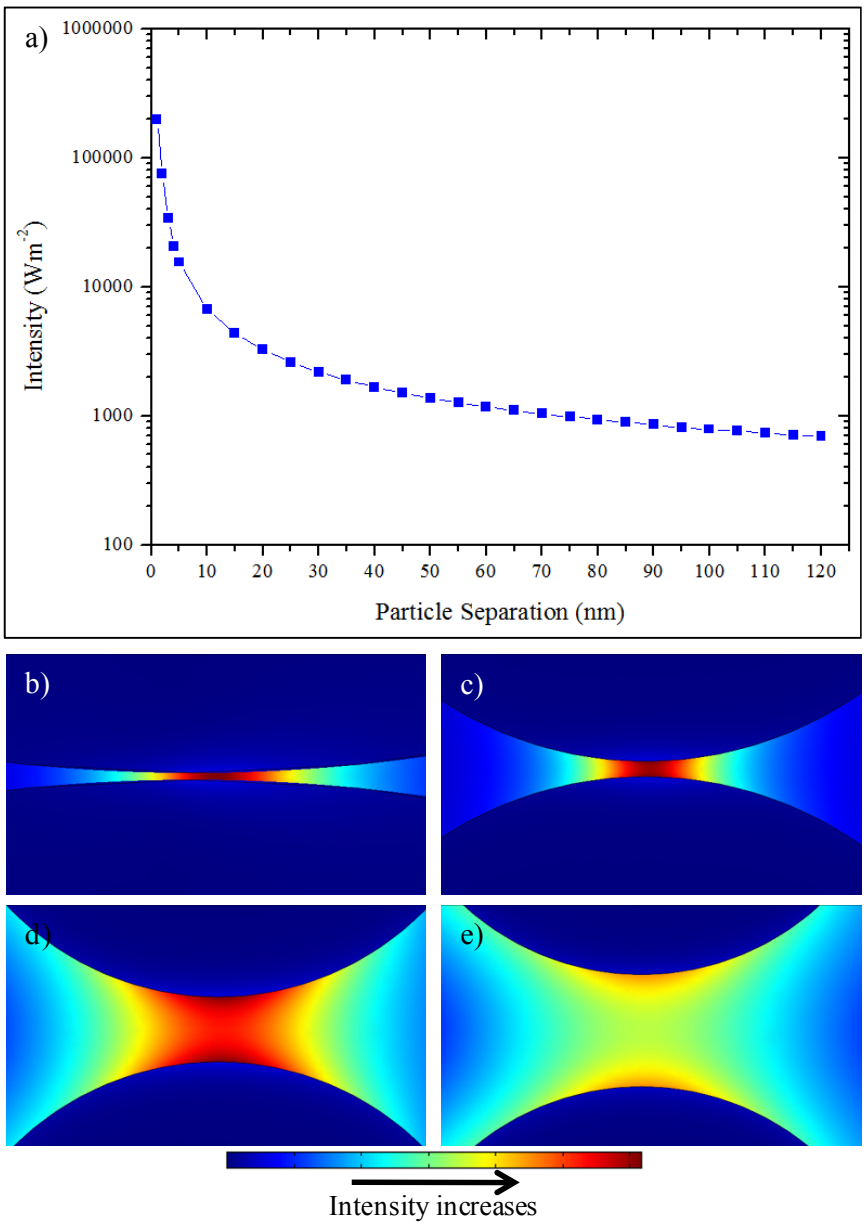

Figure 6.27: Two-dimensional FEM analysis of a pair of 500nm diameter silver nanoparticles on polycarbonate substrate, irradiated at 532nm with TM polarised radiation – a) graph of particle separation distance against hotspot intensity, b) 1nm separation, c) 10nm separation, d) 55nm separation and e) 105nm separation.

Section 6.2.4.3 - Cylindrical Silver Particles - Nanowires

Finite element method modelling can be used to support and give a deeper understanding of the processes involved in experimental work. For example, in the experimental work reported in section 6.2.3, silver nanowires were irradiated using a VUV F_2 laser emitting at 157nm.

FEM modelling was used to irradiate a silver nanowire, 10nm in diameter and 220nm long (much smaller than those used in the experiment) at 157nm, and the scattered electric field is shown in Figure 6.28a). A magnified view of one of the ends of the silver nanowire is shown in Figure 6.28b). This shows that when the wire is irradiated

with 157nm radiation, as in the experiments, the scattered electric field is more intense towards the centre of the wire and at the outside of the tips. For comparison, a similar effect is seen when the wire is irradiated at 530nm as shown in Figure 6.28c) and the magnified image in Figure 6.28d)). These observations can be used to support the theory, discussed later in Chapter 7, that the melting and subsequent shape change seen in the silver nanowires when irradiated with the VUV 157nm F_2 laser is initiated at the centre of the wire.

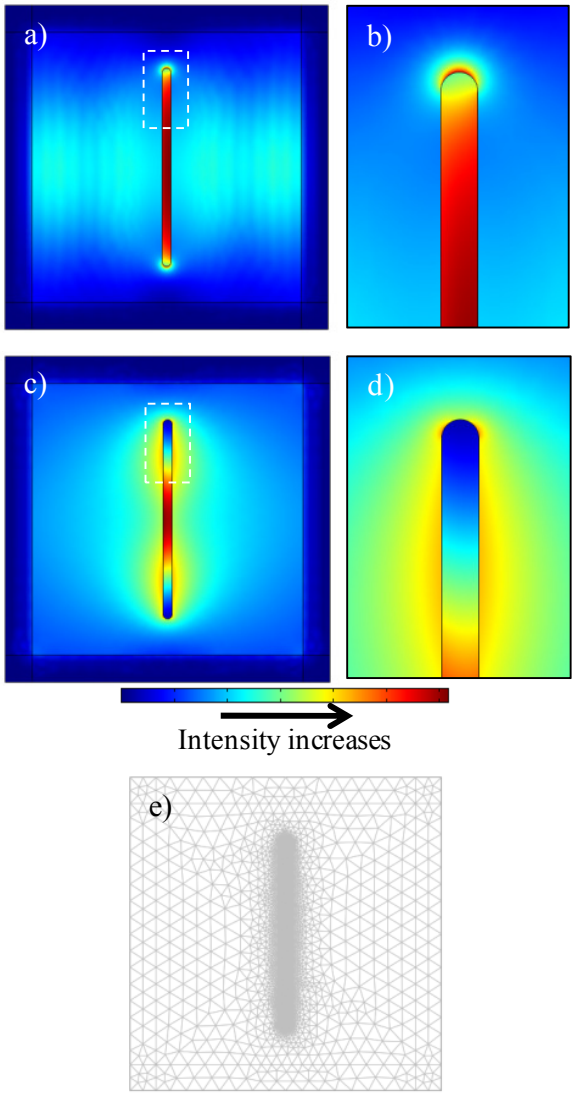

Figure 6.28: Two-dimensional FEM analysis of the scattered electric field around a free-standing silver nanowire, diameter = 10nm, length = 220nm, irradiated with TM polarised radiation at a) 157nm and c) 530nm. Magnified views of the end of the wire in b) and d) respectively and e) model mesh.

Section 6.2.4.4 - Composite Conical and Linear Prismatic Structures

Following experimental irradiation of silver nanowires on polymeric substrates, composite conical and linear prismatic structures were produced. An example of each of these types of laser ablated structures, shown in Figure 6.29, has been modelled using

finite element method software. The dimensions and geometry used in the models are based on these laser ablated composite structures.

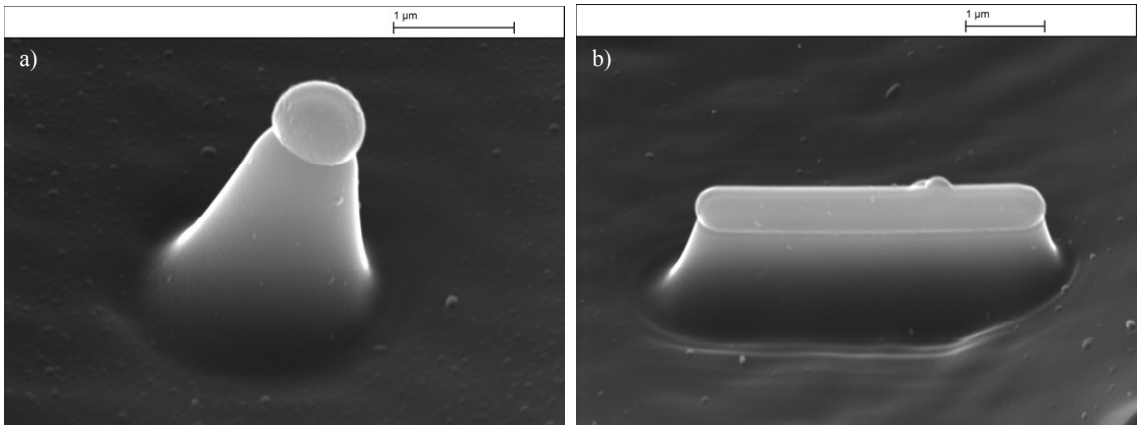

Figure 6.29: Laser fabricated silver-polymer composite a) conical and b) linear prismatic structures.

Figure 6.30 shows the model of the composite conical structure, irradiated at 549.7nm using both transverse electric (TE), in Figure 6.30a), and transverse magnetic (TM), in Figure 6.30c), polarised radiation. Figure 6.30b) and Figure 6.30d) are magnified images of the silver-polymer interface region from Figure 6.30a) and Figure 6.30c) respectively to see more clearly the interaction that occurs between the metallic seeding particle, the polymeric support structure and the composite structure itself with the incident electromagnetic field.

When irradiated with TE polarised radiation, as shown in Figure 6.30a) and Figure 6.30b), the incident field appears to be diffracted around the silver particle on the top of the conical polymeric structure, replicating the shielding action of the particle when irradiated with the 157nm laser beam, with some field enhancement at the sides of the top of the polymeric conical structure – this may be due however to the geometry of the model.

If TM polarised radiation is incident on the conical structure, the interaction between the composite structure occurs at the interface between the silver particle and the polymeric conical structure, as shown in Figure 6.30c) and Figure 6.30d). The field enhancement appears as a hotspot at the base of the spherical particle, in the interface region.

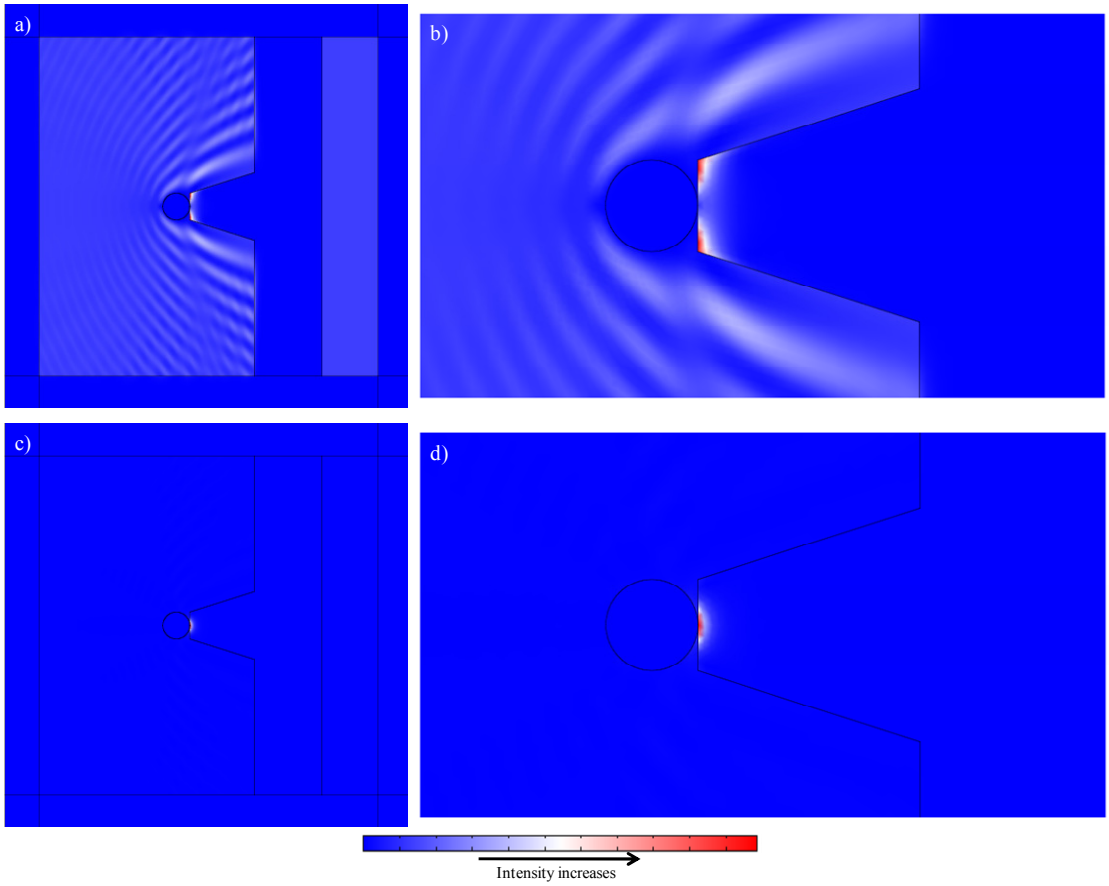

Figure 6.30: Two-dimensional FEM analysis of silver-polycarbonate composite conical structure, irradiated at 549.7nm - a) and b) TE polarised radiation, and c) and d) TM polarised radiation.

Figure 6.31 shows the model of the composite linear prismatic structure, irradiated at 497nm using both TE, in Figure 6.31a), and TM, in Figure 6.31c) polarised radiation. Figure 6.31b) and Figure 6.31d) are magnified images of the prismatic structures from Figure 6.31a) and Figure 6.31c) respectively, again to see the interaction between the silver wire, the polymeric support structure and the composite structure itself with the incident electromagnetic field.

When TE polarized radiation is incident on the composite prismatic structure, in this orientation, the prismatic structure exhibits a similar effect to the conical structure discussed above – the silver wire shields the polymer from the incident field, which diffracts around the particle. There is also field enhancement at the interface between the silver nanowire and the polymer.

When irradiated with TM polarized radiation, the interaction again appears along the interface between the silver wire and the polymeric prismatic support structure, this time as hotspots spaced at regular intervals along the interface region, as shown in Figure 6.31d).

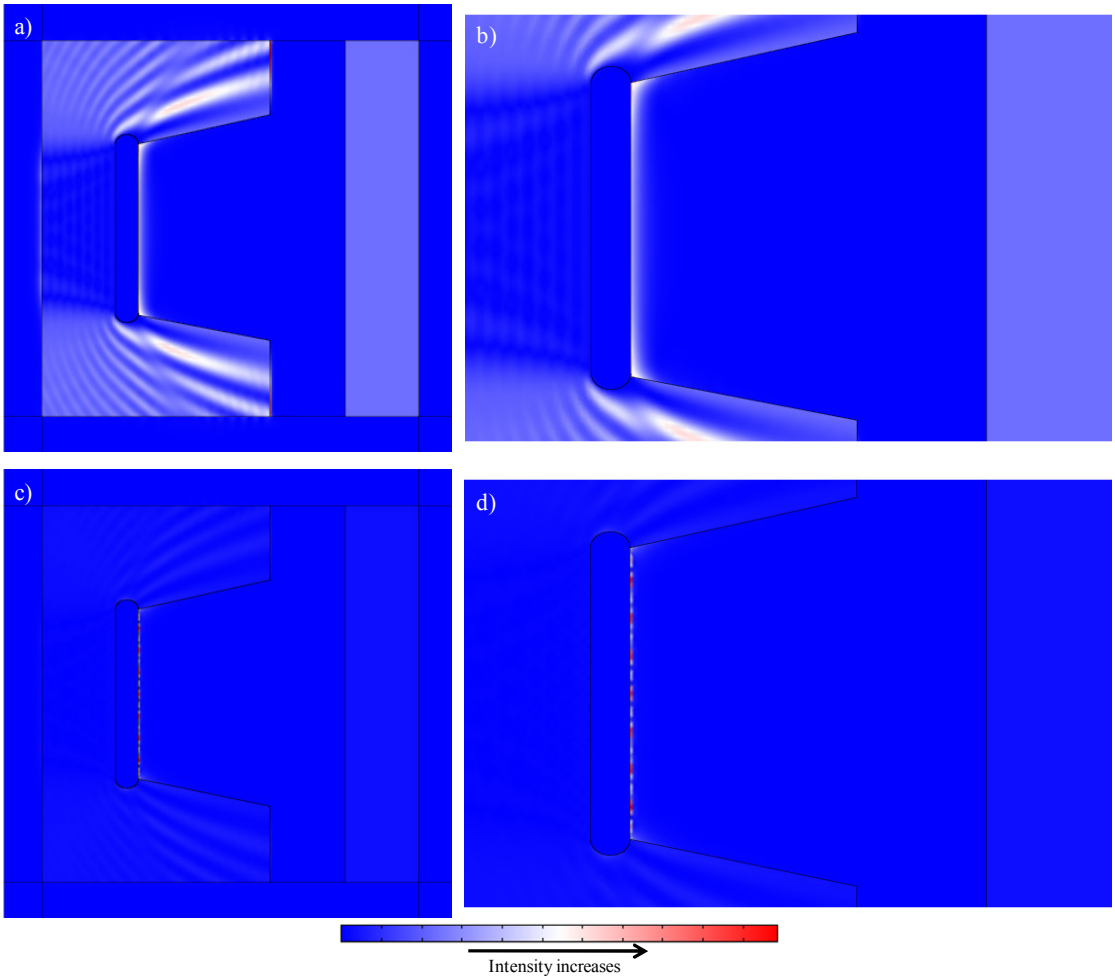

Figure 6.31: Two-dimensional FEM analysis of silver-polycarbonate composite linear prismatic structure, irradiated at 497nm - a) and b) TE polarised radiation, and c) and d) TM polarised radiation.

The models presented in Figure 6.30 and Figure 6.31 demonstrate clearly the shielding effect of the opaque particles during the laser irradiation experiments presented in Chapters 4, 5, 6, and 8. The EM field can be seen to "spread" around the tips of the seeding particle (in this two-dimensional model), with minimal interaction at the interface between the particle and the polymeric support structure. This spreading effect may account for the conical (with spherical seeding particles) or linear prismatic (with cylindrical seeding particles) shapes of the polmeric support structure.

Section 6.3 - Plasmonic Resonances in Metallic Particles and Potential for use in Sensing Devices

It is well known that small silver particles scatter green light and transmit red light, giving solutions containing small silver particles their characteristic yellow colour [113].

These effects are due to the plasmon resonances of the metallic nanoparticles. Plasmon resonances, or plasmons, arise from the interaction between incident electromagnetic

radiation and free charges, for example, the free electrons in a metal. Plasmons are an electromagnetic excitation, or resonance effect, at an interface between two media [115], usually a metal and a dielectric. Three factors contribute to this resonance effect. These are [113]

- the acceleration of the free electrons by the electric field component of the incident field,
- a restoring force resulting from the induced polarisation of the particle and surrounding medium,
- confinement of the electrons to an area smaller than the wavelength of the incident light.

Figure 6.32 demonstrates the plasmon resonance effect of a metallic nanoparticle. The electric field causes the free electrons to oscillate coherently and this electron cloud is displaced relative to the atomic nuclei. A restoring force arises between the electrons and their atomic nuclei, resulting in an oscillation of the electron cloud.

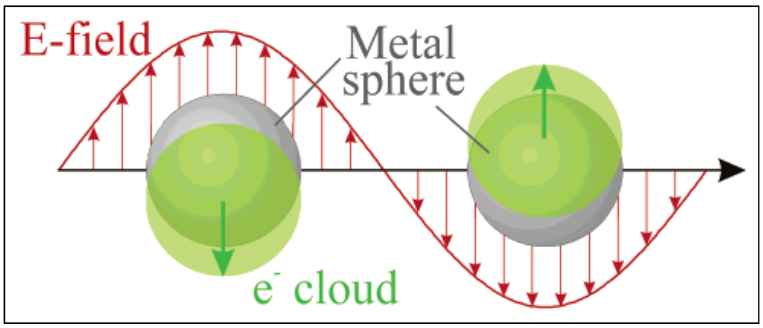

Figure 6.32: Schematic of plasmon resonance for a spherical metallic particle, from [116].

Light that is incident on a metal at a frequency below the plasma frequency induces motion in the free electrons, resulting in reflection of the incident field. The plasma frequency can be thought of as the natural frequency of the oscillation of the free electrons [117]. Above this plasma frequency, the plasmon resonances are transmitted. The plasmon resonance wave can be transmitted in many ways, two of the most useful being surface plasmon resonances (SPRs) and localised surface plasmon resonances (LSPRs). SPRs (also known as surface plasmon polaritons) propagate along the surface of the metal at the interface between the dielectric and the metal. LSPRs are contained within a small region of the surface of the metal. In the case of metal nanoparticles, the plasmons are localised [118].

Faraday, in a regularly cited 1857 paper, was the first to report that suspensions of metallic particles with dimensions many times smaller than the wavelength of visible light scatter and absorb light strongly, with even very dilute solutions exhibiting strong colours resulting from these plasmon resonances [119]. Mie was the first to calculate the extinction, scattering and absorption spectra of gold nanoparticles, and showed that the spectra are dependent on the size of the nanoparticle [113]. It has been known for around 100 years that the shape of a plasmonic nanoparticle also affects its interaction with incident light [49].

One nanoparticle geometry that is of particular interest is the nanowire, a cylindrical particle, which are also known as rods or whiskers, usually dependent on aspect ratio. For this particle geometry, the plasmon band splits into two regions, resulting in a transverse resonance perpendicular to the long axis of the particle and a longitudinal resonance parallel to the long axis of the particle [118]. The transverse plasmon resonance for nanowires is found around a similar wavelength of that of spherical particles, while the longitudinal plasmon resonance is red-shifted, the degree of which is dependent on the aspect ratio (length/diameter) of the nanowire.

The choice of material must also be taken into account. Gold, silver and copper all exhibit their plasmon resonances within the visible range of the electromagnetic spectrum, making them the materials of choice for most plasmonic applications [120, 121]. Most of the current research in this field appears to focus around the use of gold, although silver does hold many superior properties. For example, silver shows ~30% higher thermal and electrical conductivity than gold and the plasmon resonance lasts about 20% longer [122]. Silver also has a lower work function (4.3eV) than gold, meaning that a wider range of laser wavelengths can be used for laser-induced shape and size changes [123].

Section 6.4 - Conclusions

In this chapter, silver spherical and cylindrical particles of various sizes have been irradiated using a VUV 157nm F_2 laser.

Silver particles of these geometries are opaque to the 157nm laser radiation, and hence irradiation of these particles on a polymeric substrate results in the fabrication of composite micro- and nanoscale structures. As described previously, the particles shield the underlying polymer from the incident laser beam, while the substrate material surrounding the particles is removed by laser ablation. Spherical and quasi-spherical

particles seed the growth of conical structures, while cylindrical particles, known as wires, fabricate linear prismatic structures.

The seeding particle is clearly seen to remain attached to the tip of the polymeric support structure, and this has been confirmed using EDX measurements that exhibit sharp peaks around 2.3-3.5eV. The particles remain attached to the top of the support structure most likely by a combination of the attachment force between the particle and the substrate and by melting of the silver particle as a result of the energy absorbed from the laser beam.

The shape of the silver seeding particles is seen to be translated into the interference fringe pattern surrounding the base of the structure, for example the quasi-spherical particles result in an uneven fringe pattern.

Finite Element Method (FEM) modelling has been used to gain a better understanding of the interaction of the silver particles with electromagnetic radiation.

Individual silver spherical particles can be seen to enhance the electric field around them, when isolated and when in contact with a polymeric substrate. The size of the particle plays an important role in this - as the particle size becomes larger than the wavelength of the incident radiation, the field enhancement becomes distorted as multipole resonances develop and as Mie Scattering becomes the dominant regime. The presence of a substrate also has an effect on the field enhancement.

Pairs of silver spherical particles separated by a small air gap exhibit coupling of the electric field in the gap, creating an intensity "hotspot" which can be up to 20× greater than that of the background field in the models used here. While there is little dependence on the wavelength, the intensity of the hotspot is highly dependent on the distance between the two silver particles.

Silver nanowires modelled using the FEM software exhibit enhancement of the electric field within the nanowire, in the middle of the wire. There is also some field enhancement around the tips of the wire.

The types of structures fabricated by laser irradiation of silver spherical and cylindrical particles were also modelled using FEM software, and again, field enhancement is shown.

The use of metallic particles adds a different factor to these fabricated structures, compared to using dielectric and ceramic materials. Silver nanoparticles exhibit localised surface plasmon resonances (LSPRs) at a wavelength around 400nm. This has been confirmed by measuring the absorption spectra of small spherical particles and nanowires.

If these silver-polymer composite structures can be shown to exhibit plasmonic properties, these types of structures could be incorporated into various applications. Plasmonic particles have already found many applications in biological and chemical sensing devices [53, 54]. There has also been investigation into the effect of raising the plasmonic particle above the substrate in order to increase the sensitivity of the device [34], although this has not been investigated in this work.

The silver particles, similarly to the polystyrene particles presented in Chapter 4, and unlike the silicon carbide whiskers in Chapter 5, appear to experience a change in size and/or shape, potentially as a result of the energy generated by the incident laser beam. This will be discussed in the next chapter.

Chapter 7: Laser-Induced Shape Transformation of Small Particles

Section 7.1 - Introduction

The experiments carried out in the previous chapters show that the spherical, quasi-spherical and cylindrical particles used to seed the growth of composite conical and linear prismatic structures are not always the same shape and/or size after laser irradiation as they were before irradiation.

During the laser irradiation of the small particles, the energy of the laser beam is incident on the seeding particle and the polymeric substrate. The energy is absorbed in a short distance close to the surface of the materials. This is known as the optical absorption depth of the material.

In this chapter, the surface temperatures of the polystyrene, silicon carbide and silver particles as a result of irradiation with the VUV 157nm F_2 laser are calculated. The calculations are based on the fluence and pulse duration of the laser beam and the optical and thermal properties of the particles. The calculated temperatures are then used to postulate if the seeding particles have undergone the observed shape and/or size transformation as a result of mass transfer arising from melting and/or evaporation of the particle material.

Melting processes are discussed in relation to the seeding particle shape and in comparison to bulk materials and to planar surfaces.

The shape transformation seen when the silver nanowires are irradiated is discussed in more detail, as similar observations using other materials have been reported in the literature. The melting and shape transformation of gold nanoparticles and nanowires has been researched extensively recently (for a few examples, see [124-128] and references therein).

The majority of research into the interaction between plasmon resonances and shape changes seems to have been carried out using gold nanoparticles, while very little research using nanoparticles made of other noble metals, for example silver and copper (which are also known to exhibit plasmon resonances in the visible spectrum [120, 121]), has been carried out. As described earlier, the plasmon resonance of silver

nanostructures can be moved by altering the geometry of the particle [49], and the optical properties of silver nanoparticles and arrays have been investigated [113]. A reduction in size due to evaporation by direct heating has been observed and explained using the Kelvin equation [129], and a shape transformation from nanoprisms to spherical particles using femtosecond laser irradiation has been reported [130]. As yet, there appears to be no observation of a shape transformation from nanowire to spherical particle using silver particles.

Section 7.2 - Experimental Results & Discussion

Section 7.2.1 - Heating Models for Laser-Induced Particle Size and Shape Transformations

Takami et al. observed a laser-induced shape change and size reduction in gold nanoparticles in aqueous solution when irradiated with a pulsed Nd:YAG at 532nm. Before irradiation, the gold particles were ellipsoidal in shape with a size distribution between 19-47nm, while after irradiation the particles were spherical in shape with a size between 5-21nm, with a shift in the peak of the extinction spectrum from 531.5nm to 517nm [124]. They suggest that the mechanism of the size reduction is through heating of the nanoparticle. When the laser beam is incident on the gold particles, photons are absorbed and electrons are excited (creating a plasmon resonance) and the temperature of the gold particle is increased. If the temperature is elevated to above the melting point of the particle, the particle is liquefied, becoming spherical when the liquid particle cools. If the temperature of the particle is increased further, to above the boiling point, then atoms and/or small particles are ejected from the particle, resulting in a reduction in the size of the particle. When the laser irradiation ends, the particle cools and re-solidifies. Gold nanorods and wires are seen to transform from a wire to a sphere when heated by laser irradiation. A similar mechanism to that described above can be employed to explain this transformation.

It is well known that, due to size effects, the melting point for nanoparticles is greatly reduced compared to that of the bulk material. There is some debate over what this point actually is – experimental observations of gold suggest that the onset of significant melting for nanoparticles occurs at ~40% of the bulk temperature [128], while calculations for lead particles show that surface melting could occur at temperatures as low as 70% of the bulk melting point [125].

It has also been well established that the melting temperature of nanoparticles is dependent on particle size (see [131] and references therein). In 1909, Pawlow developed a Thermodynamic model that predicted a decrease in melting temperature that has a linear dependence on the inverse of the particle size. This decrease occurs for almost all free-standing nanoparticles [131].

The mass lost by the nanoparticle by melting and evaporation can be estimated using the Clausius-Clapeyron and Kelvin equations. The Clausius-Clapeyron equation is more accurate when calculating the mass loss from flat surfaces; however in 1870, Thomson (later Lord Kelvin) developed an equation for the vapour pressure over curved surfaces, stating that it is increased from that over a planar surface [132]. Thomson stated that the vapour pressure at different levels varies according to the curvature of the bounding liquid surface, being less when the liquid is concave and greater when it is convex [133]. This decrease in vapour pressure can also be used to account for a decrease in the temperature of the onset of evaporation and an increased rate of mass loss.

There is a general agreement in the literature [122, 123, 125, 127, 129, 131, 132] that there is a decrease in the melting temperature and onset of evaporation with decreasing particle size.

Investigations into the mass of material lost show the difficulties in obtaining consistent values for the melt temperature and temperature of the onset of evaporation, partly due to the different crystal facets of the material (defined by {hkl} in Equation 7.1). The driving force for surface melting is possibly due to a decrease in the total surface energy, $\Delta\gamma$, defined by [131]

$$\Delta\gamma^{\{hkl\}} = \gamma_{SV}^{\{hkl\}} - \gamma_{SL}^{\{hkl\}} - \gamma_{LV}$$

Equation 7.1

where the subscripts S, L and V define the solid, liquid and vapour phases respectively.

Assuming a temperature-independent enthalpy, the mass loss for a flat surface can be estimated using the Clausius-Clapeyron equation, adapted from [8]

$$P(T) = P_0 exp\left[\frac{\Delta H_{sub}}{R}\left(\frac{T - T_0}{T\,T_0}\right)\right]$$

Equation 7.2

where P_0 is the vapour pressure at initial temperature T_0, T is the temperature of the particle, R is the gas constant and ΔH_{sub} is the enthalpy of sublimation, where $\Delta H_{sub} = \Delta H_{fus} + \Delta H_{vap}$, where ΔH_{fus} and ΔH_{vap} are the enthalpies of fusion and vaporisation respectively.

Using this pressure, $P(T)$, the rate of evaporation (or mass removal rate), R_e, can be calculated using [129]

$$R_e = \frac{1}{4} \frac{P(T)}{kT} \sqrt{\frac{8kT}{\pi m}}$$

Equation 7.3

where k = 1.38×10^{-23}m^{2}kgs^{-2}K^{-1} is Boltzmann's constant [2] and m is the molecular weight of the particle material.

However, the Clausius-Clapeyron equation and this calculated mass removal rate do not take into account the fact that the silver particles have curved surfaces, which leads to an increase in the mass removal rate. The Kelvin equation can be used to account for the increase in the vapour pressure, and decrease in the melt temperature, of nanoparticles. The vapour pressure of a nanoparticle, P_{np}, can be defined by the Kelvin equation as [132]

$$P_{np} = P_0 exp\left(\frac{2\gamma m}{RT\rho_{np} r}\right)$$

Equation 7.4

where γ is the surface energy, ρ_{np} is the particle material density and r is the radius of the nanoparticle.

Taking into account the nanoparticle spherical geometry using the Kelvin equation shows that the mass removal rate is increased for curved surfaces and spherical particles. The Kelvin equation also suggests that, as the particle size decreases, there is a decrease in the nanoparticle melt temperature, T_{np}, and the temperature of the onset of evaporation.

It can be noted that a number of different melting processes exist which can be used to explain the shape transformation and size reduction seen in heated nanoparticles, including the liquid skin melting model and the liquid nucleation and growth model.

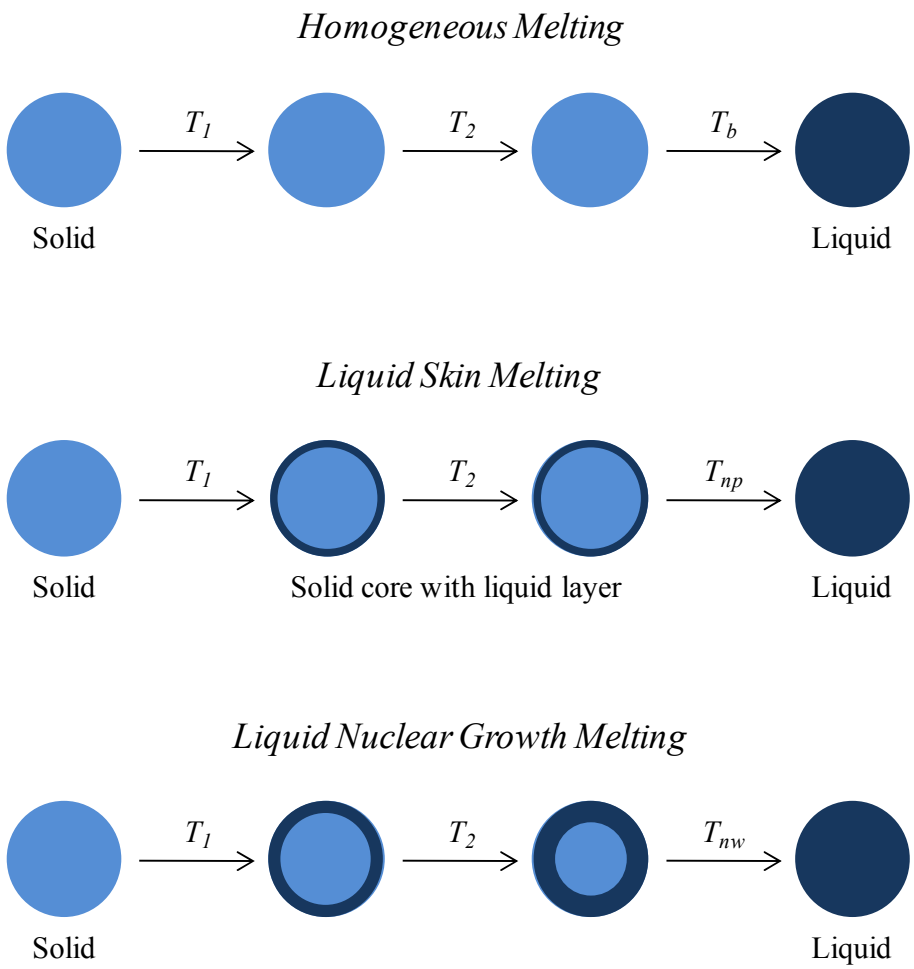

Figure 7.1: Melting models for bulk materials - homogenous melting, spherical particles - liquid skin melting and cylindrical particles - liquid nuclear growth melting.

Figure 7.1 describes the two mechanisms of the liquid skin and liquid nuclear growth models, and compares them with homogenous melting.

Bulk materials undergo homogeneous melting, as shown in Figure 7.1. This occurs when the material is heated, and as it reaches a certain temperature, denoted here as T_b, it transforms to a liquid state.

The liquid skin model assumes that as a spherical nanoparticle is heated through temperatures T_1 and T_2, the outer surface of the spherical particle forms a thin liquid layer, the thickness of which remains unchanged until the particle completely transforms to liquid at the melting temperature, T_{np}. The liquid skin melting, LSM,

model can be used to estimate the ratio between the silver spherical nanoparticle melting temperature, T_{np}, and the bulk silver melting temperature, T_b [131]

$$\frac{T_{np}}{T_b} = 1 - \frac{4\gamma_{SL}V}{\Delta H_{fus}(D - 2\delta)} = 1 - \frac{\beta}{D - 2\delta}$$

Equation 7.5

where V is the nanoparticle volume, D is the nanoparticle diameter, δ is the thickness of the liquid layer and $\beta = \frac{2V}{\Delta H_{fus}}(\gamma_{SV} - \gamma_{LV})$.

The liquid nuclear growth model applies to cylindrical nanoparticles (whiskers, wires and rods), and suggests that a liquid layer nucleates above a certain temperature T_1 and increases in thickness as the temperature increases through T_2 until the entire cylindrical nanoparticle is in a liquid state above the melt temperature T_{nw}. In all cases, T_1 and T_2 are arbitrary temperatures, where T_b, T_{np}, $T_{nw} > T_2 > T_1$.

A similar expression using a liquid nuclear growth, LNG, model can be used to estimate the temperature ratio T_{nw}/T_b for cylindrical particles (nanowires) [131]

$$\frac{T_{nw}}{T_b} = 1 - \left(\frac{4}{D} + \frac{2}{L}\right)\beta$$

Equation 7.6

where L is the length of the nanowire.

The effect of the optical absorption depth on temperature is a linear change with particle diameter, demonstrated for a silver spherical particle and a silver nanowire shown in Figure 7.2, using an optical absorption depth of ~17nm at a wavelength of 157nm. Taking a 500nm diameter silver particle as an example, the liquid skin model for spherical particles gives T_{np}/T_b ~0.77. For a nanowire, using the liquid nuclear growth model, there is a reduced normalised temperature; for example ~0.57 for a particle diameter of 500nm.

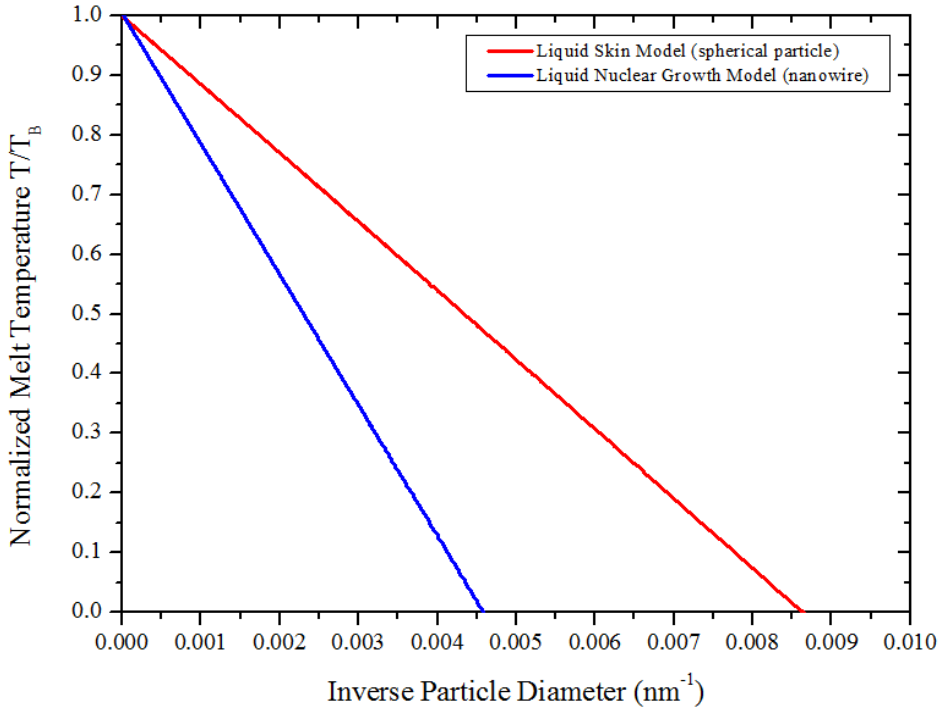

Figure 7.2: Normalised temperature against inverse particle diameter for a spherical silver nanoparticle using the liquid skin model (red line) and for a silver nanowire using the liquid nuclear growth model (blue line).

A surface heating model for the final surface temperature, T_s, of nanoparticles due to the incident VUV laser radiation was adapted from [8], where

$$T_s = T_0 + 2\frac{1-R}{K} I \left(\frac{D\tau}{\pi}\right)^{\frac{1}{2}}$$

Equation 7.7

where T_0 is the initial temperature of the sample, R is the reflectivity, K is the thermal conductivity, τ is the laser pulse duration at full width at half maximum (FWHM), I is the laser beam irradiance and D is the thermal diffusivity, given by [8]

$$I = \frac{laser\ beam\ fluence}{laser\ pulse\ duration\ at\ FWHM}$$

Equation 7.8

$$D = \frac{K}{\rho c}$$

Equation 7.9

where ρ is the density of the particle material, and c is the specific heat capacity.

The models and equations decribed in this section will now be used to investigate the heating effects of the 157nm wavelength laser radiation on the various seeding particles that were used in the composite structure fabrication experiments.

Section 7.2.2 - Polystyrene particles

Observation of polystyrene particles melting under laser irradiation has already been briefly mentioned in Chapter 4, and will be discussed in more detail here.

Under irradiation at a wavelength of 157nm, when the sample is mounted normal to the direction of the laser beam propagation, the spherical polystyrene particles undergo mass transfer, in some combination of melting and evaporation to become oblate spheres (disc shaped) or melted caps to the polymeric support structure, as shown in Figure 7.3.

The 1.58μm diameter polystyrene particles in Figure 7.3a) have not been irradiated, and exhibit a uniform spherical shape. In Figure 7.3b), these particles have been irradiated at a laser fluence of 380mJcm^{-2} with 10 laser pulses (1Hz pulse repetition rate). While the lateral diameter of the particles has decreased only slightly, to ~1.3μm, the spherical particles have been melted or ablated into a disc shape, with a height of ~640μm.

Figure 7.3c) and Figure 7.3d) show non-irradiated 1μm diameter polystyrene spherical particles and these particles irradiated at 430mJcm^{-2} with 5 laser pulses (2Hz pulse repetition rate) respectively. The relatively high laser fluence has caused the irradiated particles to reach a very high temperature and so they have melted. They have fused together as they will have been in contact with each other before irradiation, although the individual particles are still discernible from each other.

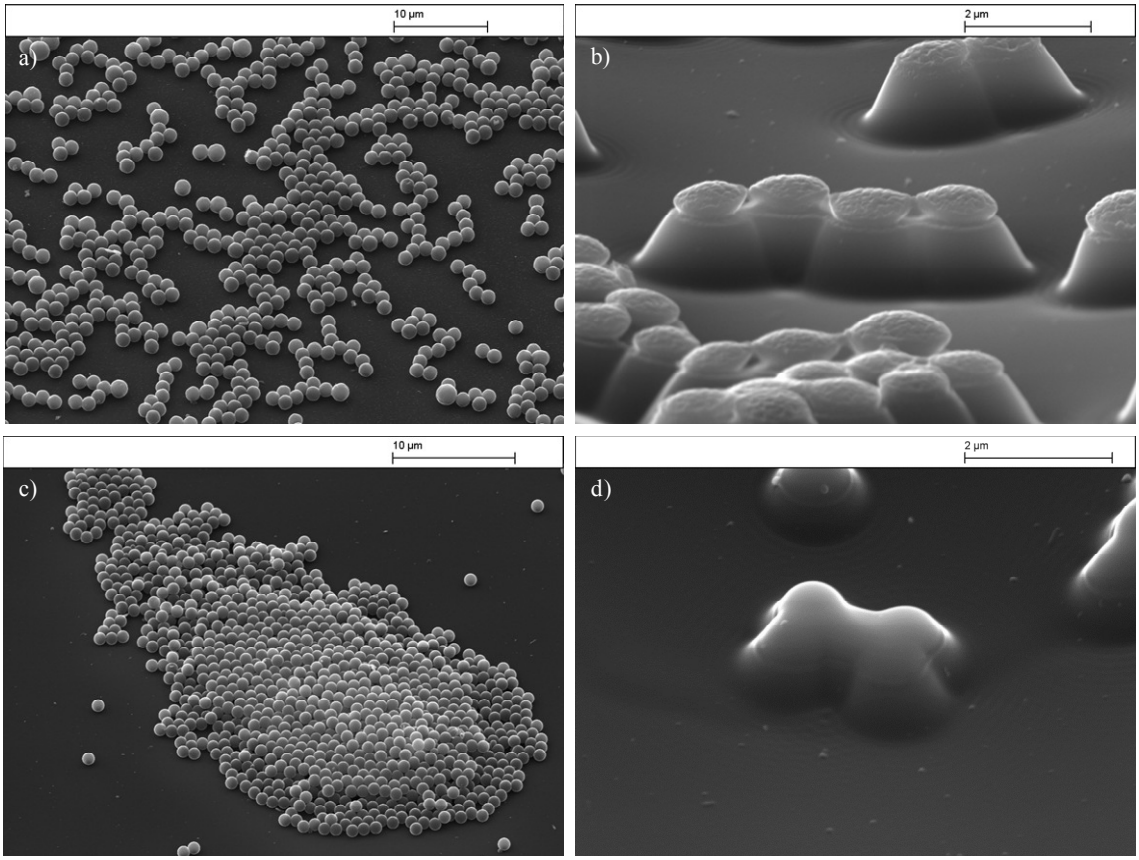

Figure 7.3: Polystyrene particles irradiated normal to the direction of the laser beam propagation undergo mass transfer to form oblate spheres (discs). SEMs viewed at b) 70° and a), c) and d) 45°.

When the polystyrene particles are irradiated at low fluence at an angle of 45° to the direction of the laser beam propagation, they seed the fabrication of oblique conical structures with a spherical particle at the top. When the laser fluence is sufficient to cause the particles to melt and material to evaporate, the particles change shape, becoming prolate spheres (resembling rugby balls), as shown in Figure 7.4. The particles in Figure 7.4a) and Figure 7.4b) were irradiated at 125mJcm^{-2} with 5 and 10 laser pulses (2Hz pulse repetition rate) respectively. As a result, they now have long axis diameters of ~1.59µm and ~1.54µm, and short axis diameters of ~1.4µm and ~920nm respectively. As shown by these measurements, the diameter perpendicular to the laser beam remains relatively unchanged with irradiation, the dimension along the laser beam propagation direction is drastically reduced as the number of laser pulses increases. The particle in Figure 7.4c) was irradiated at 160mJcm^{-2} with 5 laser pulses (2Hz pulse repetition rate) and has diameters of ~1.59µm and ~970nm. The particles in Figure 7.4d) are flatter and more disc-like than those seen in the other SEMs. They were irradiated with 1 laser pulse at a fluence of 180mJcm^{-2}.

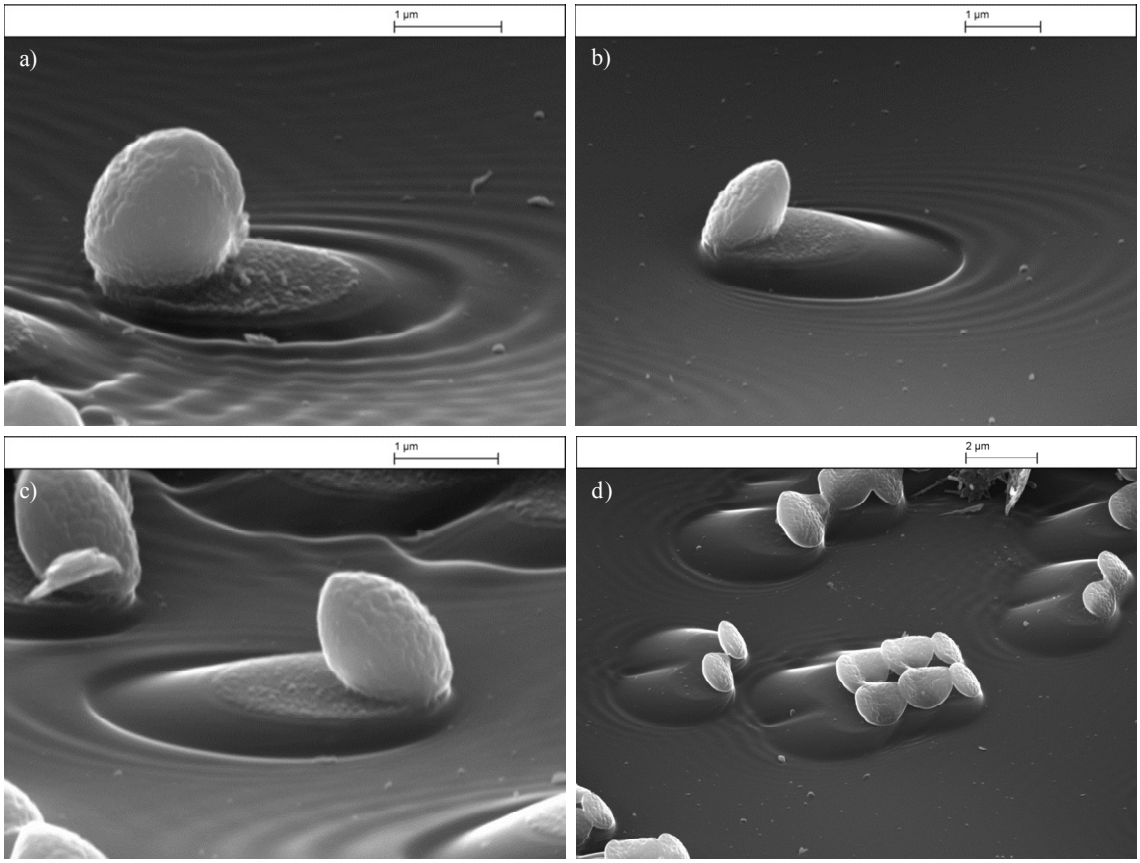

Figure 7.4: Polystyrene particles irradiated at 45° to the direction of the laser beam propagation undergo mass transfer to form prolate spheres (rugby balls). SEMs viewed at a), b) and c) 60° and d) 45°.

As the F_2 laser offers precise control over the laser beam properties, such as charging voltage and hence output energy, as well as the number of pulses, under the right conditions melting of the polystyrene particles can be finely controlled. In the SEMs shown in Figure 7.5, the polystyrene particles have been irradiated with the F_2 laser in such a way that only the top layer, or the top few layers, has been affected by the laser beam.

Figure 7.5a) and Figure 7.5b) show 490nm diameter spherical polystyrene particles that have been deposited into a Transmission Electron Microscope (TEM) square pattern grid before irradiation. The particles arranged themselves in the pattern of the grid, forming squares. The particles were then irradiated at a fluence of 110mJcm^{-2} with 10 laser pulses (2Hz pulse repetition rate) and the TEM grid was removed. As shown in Figure 7.5a), the exposed square block of particles has melted, but evidenced by the torn-away section in Figure 7.5b), it would appear that it is only the top layer of particles that has fused, leaving the particles below largely unaffected by the laser beam.

Figure 7.5c) shows the irradiation of 490nm diameter polystyrene particles at a fluence of 170mJcm^{-2} with only 10 laser pulses at a pulse frequency of 1Hz. The slow pulse

repetition rate appears to have allowed the heat energy generated by the laser pulse to dissipate before the next pulse hits the sample, resulting in the melting of the particles in the top few layers and subsequent fusing as the polystyrene cools down. The particle layer has also broken apart, resulting in "bricks" of polystyrene particles. A similar effect can be seen in Figure 7.5d). Again, the top few layers of particles have fused as a result of irradiation with 10 laser pulses (1Hz pulse repetition rate) at a fluence of 150mJcm^{-2}. These *photonic bricks*, a form of photonic crystal, may have applications in controlling, manipulating and confining light, for example as artificial opals and in bioinspiration.

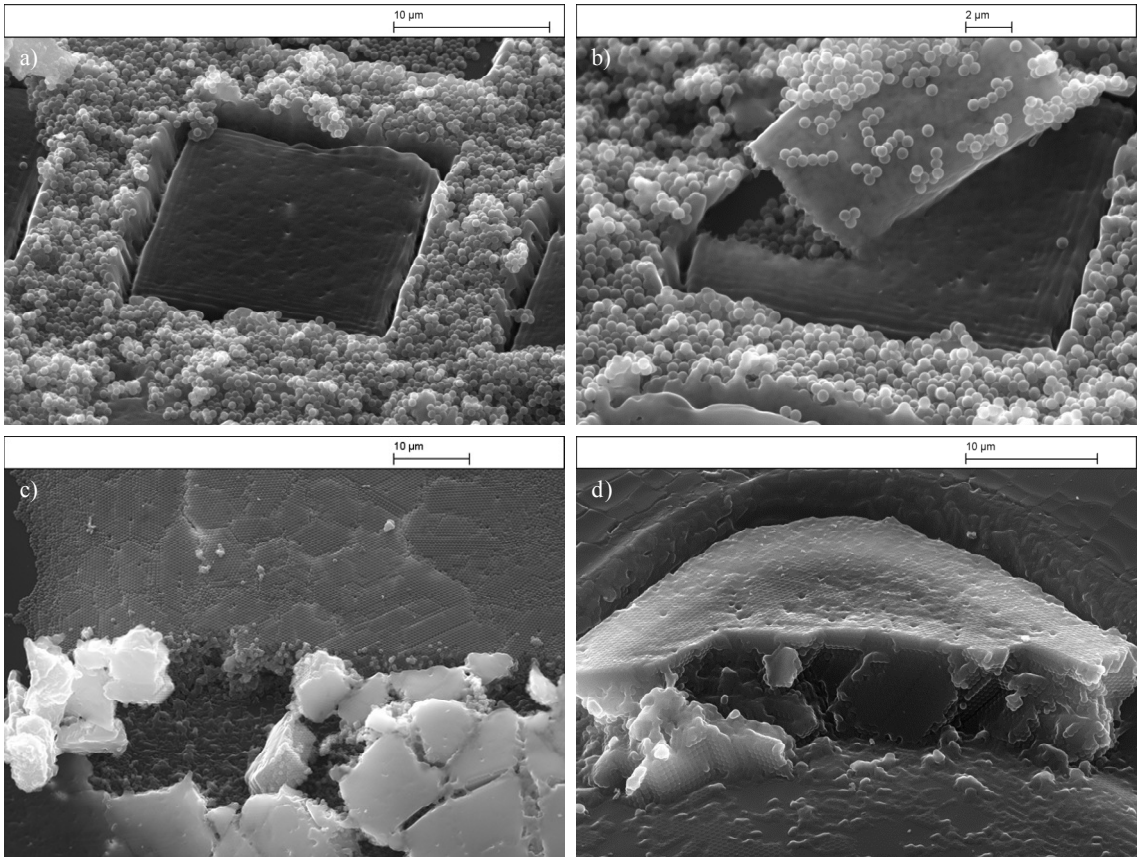

Figure 7.5: Polystyrene particles irradiated normal to the direction of the laser beam propagation undergo (surface) melting and fuse together to form "photonic bricks". SEMs viewed at a), b) and d) 45° and c) 30°.

The properties of polystyrene needed to calculate the surface temperature of the particles under laser irradiation are shown in Table 7.1.

Reflectivity, R	0.03 (based on n = 1.38) [100]
Thermal Conductivity, K	13Wcm^{-1}K^{-1} [98]
Density, ρ	1.05gcm^{-3} [2]
Specific Heat Capacity, c	1.3Jg^{-1}K^{-1} [2]

Table 7.1: Properties of polystyrene required for temperature calculations, where n is the real part of the refractive index at the appropriate wavelength.

Equation 7.7 can be used to calculate the surface temperature of the polystyrene particles to verify if the energy generated by the laser beam is sufficient to cause melting. The results of temperature calculations at the laser fluences used here are shown in Figure 7.6. The initial temperature of the particle is taken as T_0 = 300K, and a laser pulse duration at FWHM of τ = 11ns is used.

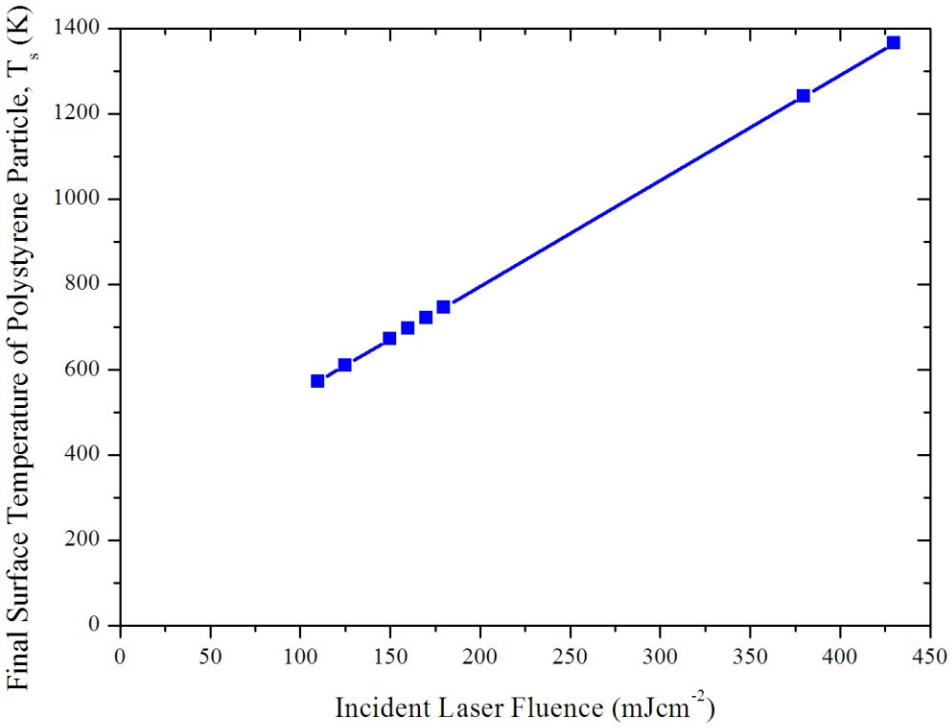

Figure 7.6: The final surface temperature of the polystyrene particles after irradiation at a wavelength of 157nm at various laser fluences.

Calculations for the optical absorption depth of polystyrene at 157nm indicate that the laser radiation is absorbed within ~73nm of the surface of the material (using k = 0.17 [100]). The heat dissipation depth, using Equation 7.11, was calculated to be ~3.2µm.

The melting point of bulk polystyrene is 510K [2], which corresponds to a laser melting fluence of ~85mJcm^{-2}. As shown here, the temperatures calculated to be reached by the polystyrene particles in these experiments are clearly sufficient to cause substantial melting of the particles, leading to a subsequent shape and size transformation.

Section 7.2.3 - Silicon Carbide Whiskers

Observation of the SEMs of the non-irradiated in comparison with the laser irradiated silicon carbide whiskers, shows very little change to the surface topology of the whiskers. This suggests that the whiskers do not melt as a result of absorbing the energy from the laser beam.

Calculations suggest that the laser energy is absorbed very close to the whisker surface. The optical absorption depth at 157nm is ~11nm (at 8eV [112]). The heat diffusion length was calculated using Equation 7.11 as ~1.3μm. As the specified average diameter of the silicon carbide whiskers is 1.5μm, the whiskers instead of the underlying polymer substrate will absorb the majority of the heat energy transferred from the laser beam. However, this still does not appear to be sufficient energy loading to melt the particles.

The melt temperature for bulk silicon carbide is 3103K [134]. Assuming that the melt temperature for nanoparticles is ~40% of that of bulk material, this suggests a whisker melt temperature of ~1241K.

Certain optical, thermal and physics properties of silicon carbide are required to calculate the temperature of the whiskers during laser irradiation, and these are shown below in Table 7.2.

Reflectivity, R	0.11 (based on n = 1.99)	[99]
Thermal Conductivity, K	$3.6 Wcm^{-1}K^{-1}$	[134]
Density, ρ	$3.2 gcm^{-3}$	[MSDS]
Specific Heat Capacity, c	$0.59 Jg^{-1}K^{-1}$	[135]

Table 7.2: Properties of silicon carbide required for temperature calculations, where n is the real part of the refractive index at the appropriate wavelength.

The temperature of the silicon carbide whiskers irradiated at the laser fluences used in Chapter 5 can be calculated using Equation 7.7, and are shown in Figure 7.7. The initial temperature of the particle is taken as T_0 = 300K, and a laser pulse duration at FWHM of τ = 11ns is used.

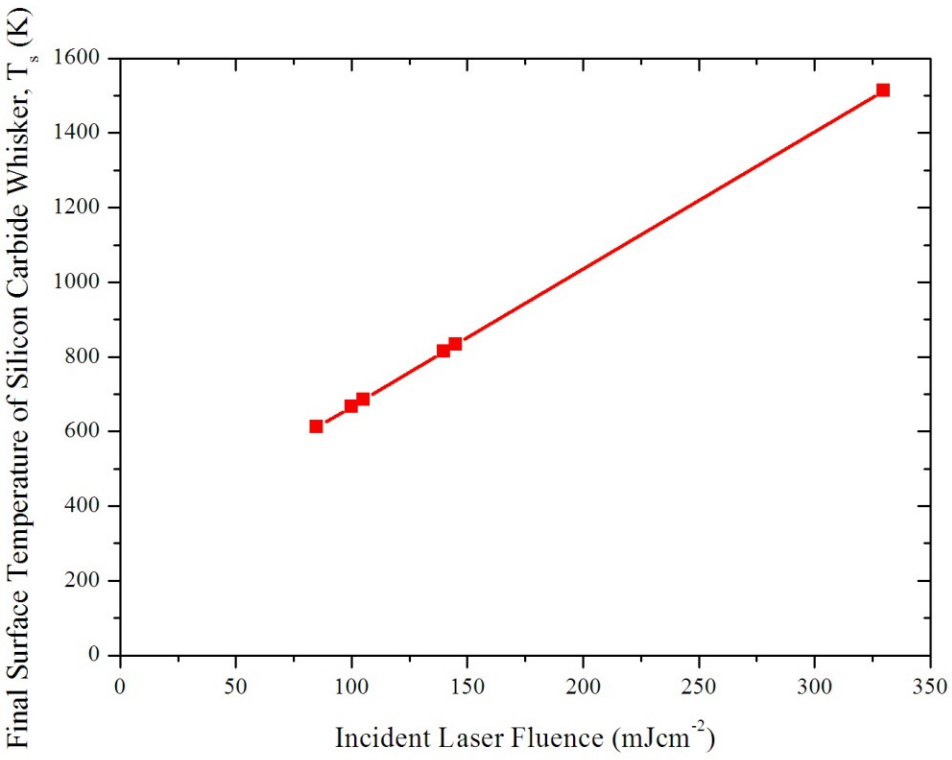

Figure 7.7: The final surface temperature of the silicon carbide whiskers after irradiation at a wavelength of 157nm at various laser fluences.

All of these calculated temperatures are well below the melt temperature for bulk silicon carbide. With the exception of the temperature calculated for a fluence of 330mJcm^{-2}, all of the other calculated temperatures are also below the theoretical particle melt temperature of 1241K. The silicon carbide whisker shown in Figure 5.3, which was irradiated at 330mJcm^{-2} shows little visible sign of melt reflow. The diameter of this irradiated whisker, ~1μm, does not deviate drastically from those of non-irradiated whiskers, so would also suggest little melting or shape and/size transformation.

Calculations indicate that the laser fluence under these experimental conditions required to initiate melting of a silicon carbide whisker is ~255mJcm^{-2}.

Section 7.2.4 - Silver particles

Calculations of the surface temperature for silver were carried out, to give an indication of whether or not the silver particles had melted.

Taking into account the wavelength of the incident radiation, λ, and the extinction coefficient, k, of silver, the absorption coefficient, α, and optical absorption depth of the incident radiation within the silver, α^{-1}, can be determined using [8]

$$\alpha = \frac{4\pi k}{\lambda}$$

Equation 7.10

where k = 0.75 at λ = 157nm [112]. Hence, the vacuum ultraviolet (VUV) radiation is absorbed in a shallow region of α^{-1} ≈ 17nm close to the silver particle surface. The optical absorption depth for silver over a range of wavelengths is shown in Figure 7.8 below.

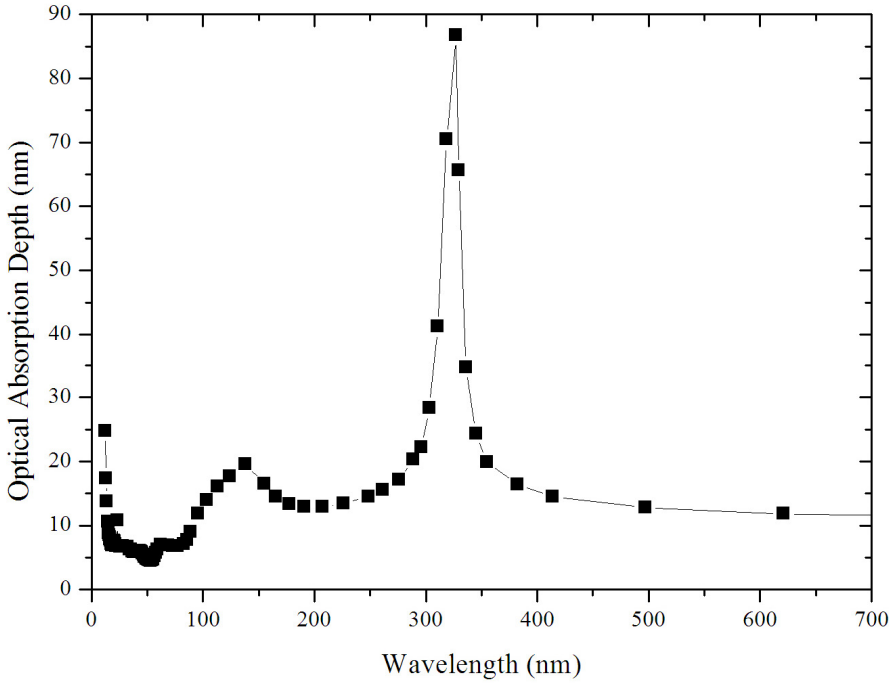

Figure 7.8: Optical absorption depth of silver. Data from [112].

During laser ablation, the optical absorption depth of a material plays an important role in estimating the energy loading and temperature increase in the material. It can also be used to suggest the presence of a near-surface modified layer that induces the structural and geometrical transformation of the particle.

A near-surface melting model (liquid skin model) can be adopted to explain the size transformation seen in the silver nanoparticles used in these experiments, and the liquid nuclear growth model to explain the shape change seen in the silver nanowires.

The Clausius-Clapeyron equation, shown in Equation 7.2, can be used to estimate the mass loss for a flat surface. Taking ΔH_{fus} = 11kJmol^{-1} and ΔH_{vap} = 258kJmol^{-1}, then ΔH_{sub} = 269kJmol^{-1} [122], R = 8.314JK^{-1}mol^{-1} [2], and P_0 = 1Pa at T_0 = 1230K [2]. As an example, under these experimental conditions, a laser fluence of 265mJcm^{-2}

corresponds to a surface temperature of 836K, therefore T = 836K. Therefore, $P(T)$ = 4.13×10^{-6}Pa.

Using the equation for the mass removal rate, Equation 7.3, where $m = 107.87/(1000 \times N_A)$, where N_A = 6.022×10^{23}mol^{-1} is Avogadro's Constant [2], under these example conditions, the mass removal rate for silver is ~36×10^{-3}atoms nm^{-2}s^{-1}.

However, the Clausius-Clapeyron equation and this calculated mass removal rate do not take into account the fact that the silver particles have curved surfaces, hence the Kelvin equation, shown in Equation 7.4, can be used. Taking the surface energy γ = 1.2Jm^{-2} [129] and ρ_{np} = 10.491gcm^{-3} (from MSDS), for particles at T = 836K, a 5nm radius silver particle has a mass removal rate of ~17.8×10^{7}atoms nm^{-2}s^{-1}. In comparison, the mass removal rate for a particle with r = 500nm is ~8.8×10^{7}atoms nm^{-2}s^{-1}, supporting an increased mass removal rate at smaller particle sizes.

In order to calculate the temperature increase of silver spherical and cylindrical nanoparticles using Equation 7.7, various optical, thermal and physical properties need to be defined. These are shown in Table 7.3.

Reflectivity, R	0.114	[112]
Thermal Conductivity, K	4.29Wcm^{-1}K^{-1}	[112]
Density, ρ	10.491gcm^{-3}	[MSDS]
Specific Heat Capacity, c	0.235Jg^{-1}K^{-1}	[2]

Table 7.3: Properties of silver required for temperature calculations.

The melting point of bulk silver is ~1230K [2], However, it has been suggested that the temperature at which significant surface melting of metallic nanoparticles occurs is ~40% of that of the bulk material [128]. Assuming that this is correct, then surface melting of the silver spherical particles and nanowires should be seen to initiate at around 495K, corresponding to an incident laser fluence of ~100mJcm^{-2} under the experimental conditions used here.

Section 7.2.4.1 - Spherical Particles

One example of the shape and size transformation seen in these experiments was during the irradiation of the ~7μm quasi-spherical silver particles seen previously in Figure 6.6, and described again here in Figure 7.9. Before laser irradiation, the average particle diameter seen in Figure 7.9a) is ~9.6μm, and the particles appear more like clusters of

silver rather than regularly shaped. After laser irradiation at a fluence of 325mJcm^{-2} with 10 laser pulses (1Hz pulse repetition rate), shown in Figure 7.9b), the particles at the apex of the composite conical structures are much more spherical than those not irradiated, and are also much smaller. These two are ~500nm and ~480nm in diameter. As the particles are irradiated, they begin to melt and hence form more spherical shapes as this is a more thermodynamically stable shape.

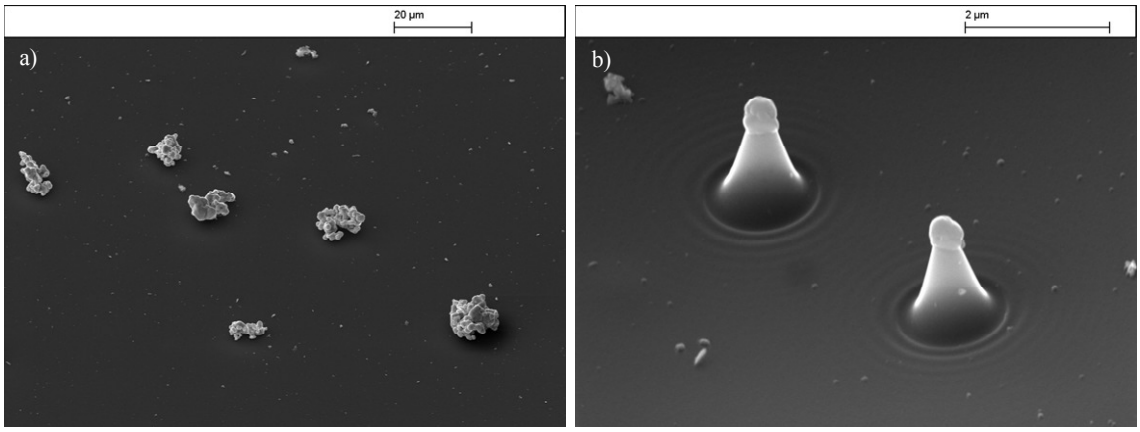

Figure 7.9: Silver particles a) before and b) after irradiation with the VUV 157nm F_2 laser at fluence 325mJcm^{-2} with 10 laser pulses at a pulse repetition rate of 1Hz. Average particle diameter before irradiation ~9.6µm, particle diameters after irradiation ~500nm and ~480nm. Both SEMs viewed at 45°.

Calculations for the temperature of the particles, using Equation 7.7, at this laser fluence with a laser pulse duration of τ = 11ns indicate a surface temperature of 1253K. This temperature is much higher than the estimated nanoparticle melt temperature of 495K, and is also greater than the melting temperature of bulk silver, 1230K [2]. This indicates that the primary cause of the shape and size transformation seen in the silver particles is mass loss through melting.

Section 7.2.4.2 - Cylindrical Particles - Nanowires

As seen in the experimental results shown in section 6.2.3, there is a tendency for silver nanowires to undergo a shape transformation during laser irradiation. Laser ablation of a polymeric substrate seeded with silver nanowires results in the formation of composite linear prismatic structures, as well as a large number of composite conical structures in close proximity to each other. At much higher laser fluences and greater pulse numbers, there is a lack of silver wires, silver spherical particles or other structures in the ablation sites, suggesting that ablative cleaning of the polymer substrate becomes the dominant process.

Due to the lack of complete nanowires and high density of modified nanowires and spherical particles, it can be suggested that the silver nanowires melt as a result of

absorption of the energy from the laser beam increasing the temperature of the nanowire. The nanowire then begins to melt, most likely in the centre of its length, and as the rest of of the wire melts, the length of the nanowire receeds to the ends, which become spherical particles. This process has been demonstrated using the structures shown in Figure 7.10. The nanowires become spherical particles as this is the most thermodynamically stable shape. Evaporation of the nanowire material is also a possible factor in the material removal, provided the temperature increase is sufficient for this to occur.

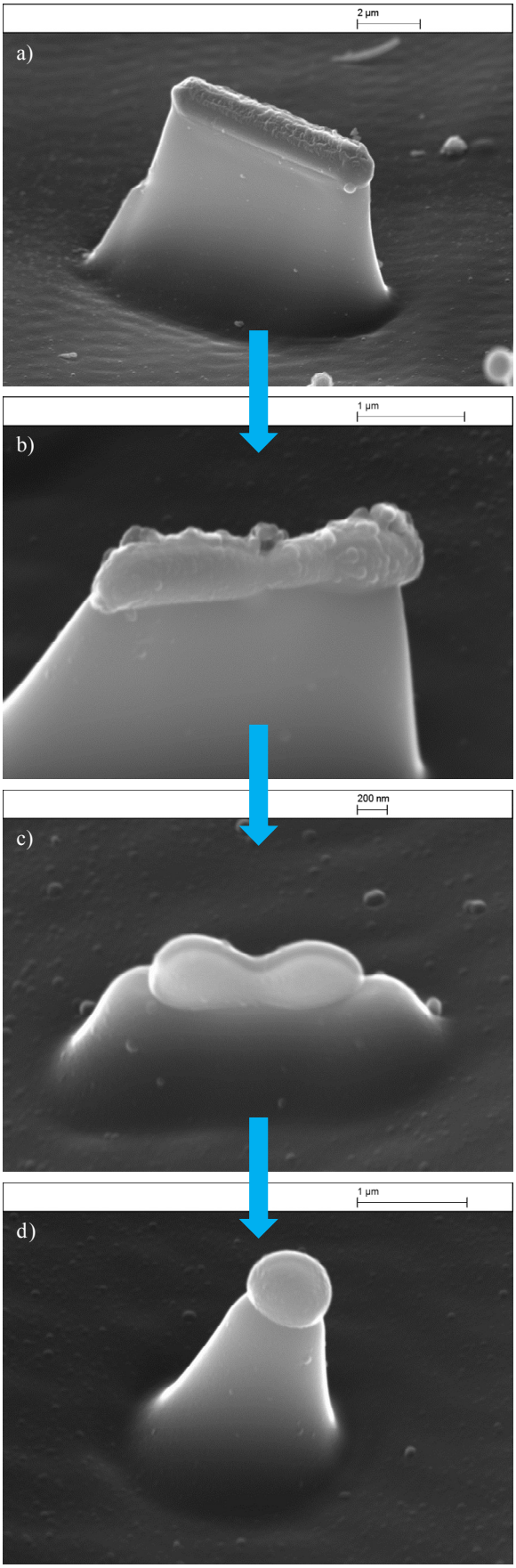

Figure 7.10: Examples of the stages of the shape transformation seen in silver nanowires from wire to sphere. Silver wires irradiated with a VUV 157nm F_2 laser at a) laser fluence 210mJcm^{-2} with 30 laser pulses at 10Hz pulse repetition rate, b) laser fluence 260mJcm^{-2} with 30 laser pulses at 10Hz pulse repetition rate, c) laser fluence 175mJcm^{-2} with 10 laser pulses at 10Hz pulse repetition rate and d) laser fluence 175mJcm^{-2} with 20 laser pulses at 10Hz pulse repetition rate. SEMs viewed at a) 60° and b), c) and d) at 45°.

The silver wire shown in Figure 7.11 was irradiated at a laser fluence of 175mJcm^{-2} using 50 laser pulses at a pulse repetition rate of 10Hz. The micrograph shows perhaps the initiation of a transformation from a wire to a spherical particle. The main length of the wire, ~720nm in diameter, is intact while one end, shown in the magnified image, has started to elongate and form a spherical particle of diameter ~540nm. This spherical particle appears to be breaking away from the main length of the wire.

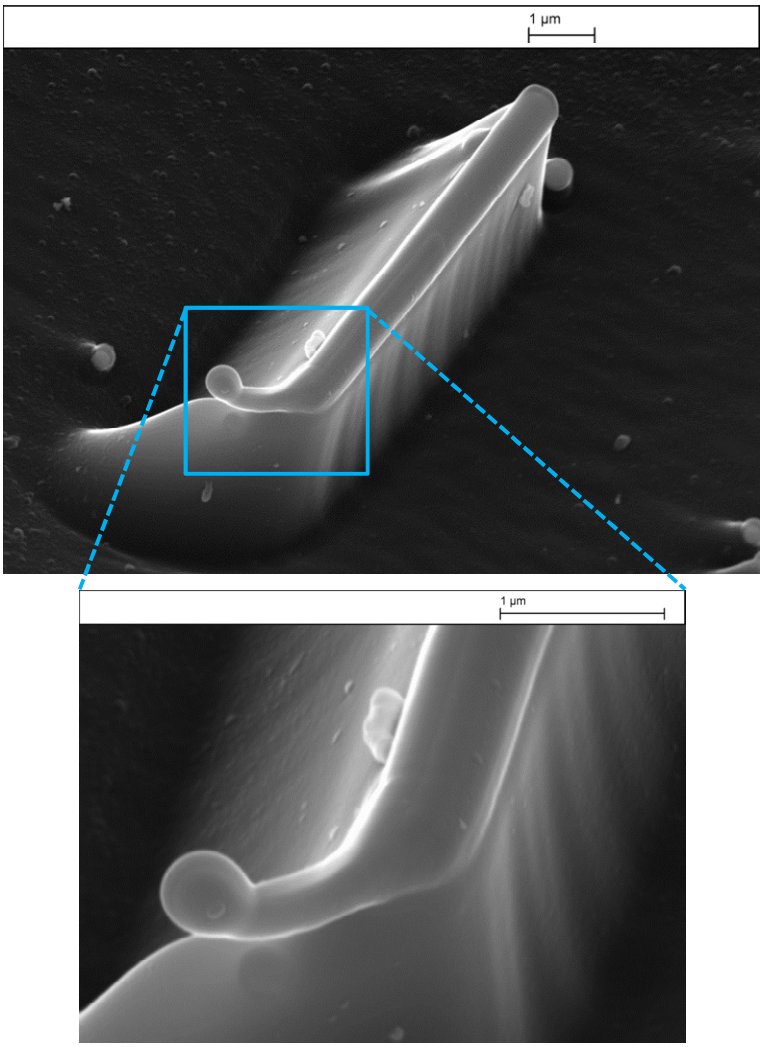

Figure 7.11: VUV 157nm F_2 laser irradiation of a silver nanowire on polycarbonate substrate at laser fluence of 175mJcm^{-2} with 50 laser pulses at a pulse repetition rate of 10Hz. Wire diameter ~720nm, ball diameter ~540nm. SEMs viewed at 45°.

The scanning electron micrograph shown in Figure 7.12 provides strong evidence for a shape transformation from wire to sphere during laser irradiation at 157nm. The composite structure with a seeding particle that most resembles a nanowire (at the top of the micrograph) is very short and the ends are very smooth and rounded, unlike those seen in non-irradiated wires. The rest of the structures are conical - seeded by spherical particles. It is the two pairs of conical structures that are highlighted and magnified that are of the most interest. As the particles are in close proximity to each other, their

polymeric supporting structures are overlapping. However, it is the shape of these connecting support structures that indicates that at some time during the laser irradiation, each pair of particles was connected, most likely by a nanowire that has subsequently melted and/or evaporated. The polymer that was underneath the nanowire would have been ablated away by subsequent laser pulses as the nanowire melted and receded or evaporated, leaving behind the connecting polymer structure that can be seen in the micrograph. The pairs of particles left behind are separated by <300nm and <350nm gaps.

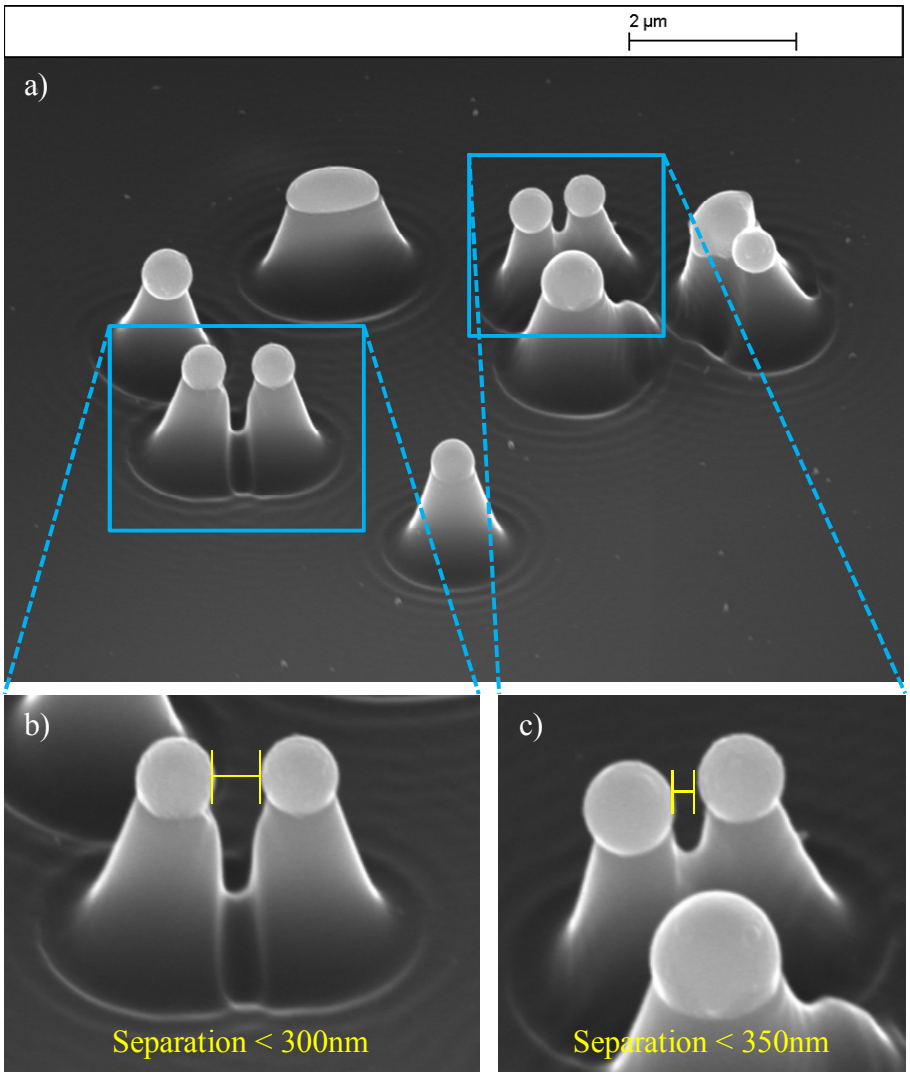

Figure 7.12: VUV 157nm F_2 laser irradiation of silver nanowires on CR-39 polymer substrate at laser fluence 285mJcm^{-2} with 10 laser pulses at a pulse repetition rate of 2Hz. SEMs viewed at 45°.

The shape transformation from nanowire to spherical particle is believed to be due to mass transfer arising from a combination of melting and evaporation. Understanding the shape transformation process is important in being able to control the inter-particle separation distance. The main control parameters include the initial size of the nanowire, the number of laser pulses, the laser fluence and the thermal properties of

both the particle and the substrate. An ability to control the inter-particle spacing would be useful for reproducing the intense coupling effect seen in the silver dimers in Figure 6.26 and Figure 6.27 for applications such as sensing platforms.

Using Equation 7.4 for the vapour pressure of the nanoparticle and Equation 7.7 with the properties of silver shown in Table 7.3, the final surface temperature, T_s, of the silver nanowires during irradiation can be determined for the incident laser fluences used in the experiments in Chapter 6. These calculated temperatures are shown in Figure 7.13. The initial temperature of the particle is assumed to be T_0 = 300K, and a laser pulse duration at FWHM of τ = 26ns is used.

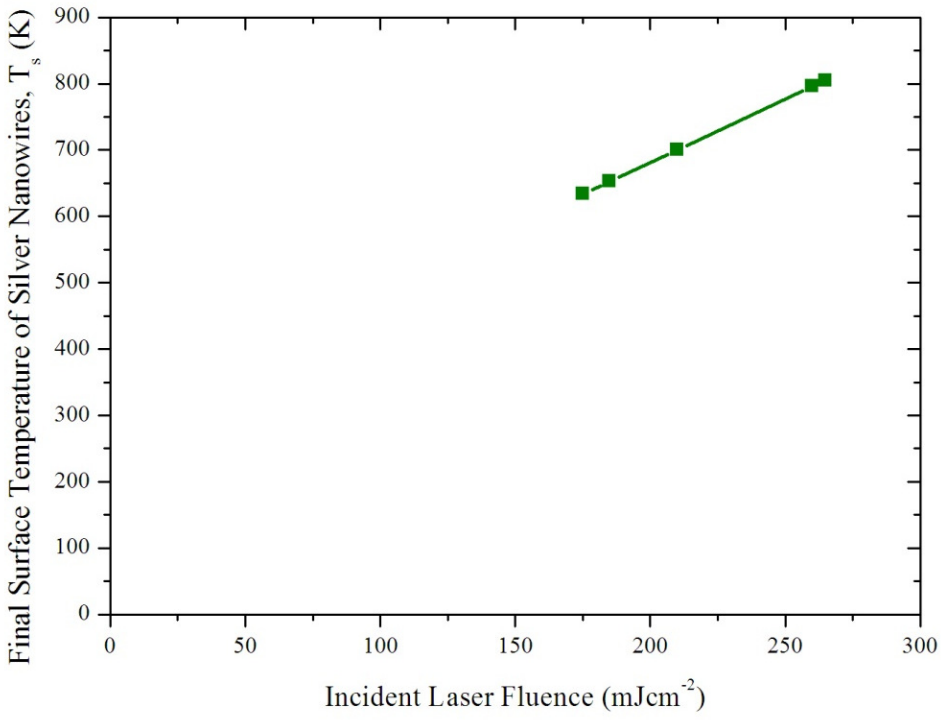

Figure 7.13: The final surface temperature of the silver nanowires after irradiation at a wavelength of 157nm at various laser fluences.

Geometrical effects and excitation of plasmonic modes have been reported to affect the melting of nanowires and particles [124, 126, 127, 136], but this has not been taken into account in these calculations.

The heat diffusion length, d, of silver can be determined using [137]

$$d = \sqrt{(D\tau)}$$

Equation 7.11

resulting in $d \approx 2.3\mu m$. As the average diameter of the non-irradiated wires is only ~420nm, the majority of the heat from the laser beam will be diffused into the polymer substrate and dissipated.

Section 7.3 - Conclusions

Experimental results of near field laser ablation at an irradiation wavelength of 157nm of seeded polymers suggest a size and/or shape transformation of the seeding particle under certain incident laser conditions.

The spherical polystyrene particles are seen to become oblate and prolate spheres after irradiation normal to the laser beam direction and at an angle to the laser beam direction respectively. The calculations to determine the surface temperature of the polystyrene particles show that the laser beam energy is sufficient to raise the temperature of the particles to a level melting of the particle is initiated.

The silicon carbide whiskers used to seed the growth of linear prismatic structures do not appear to undergo a shape or size change as a result of the laser irradiation. The calculations to determine the temperature of the silicon carbide whiskers suggest that the laser fluences used in these experiments in general may not have been sufficient to cause melting.

Quasi-spherical silver particles before irradiation are seen to become much more spherical after laser irradiation. They are also smaller in size than before irradiation. Surface temperature calculations indicate that the laser fluences used in the experiments presented here are sufficient to cause both the silver quasi-spherical and cylindrical particles to melt.

When the silver nanowires were irradiated, there were a large number of spherical silver particles seen at the apex of the supporting polymeric structures. This suggests that there is the potential for the cylindrical particle to undergo a shape transformation and become spherical. It would appear that the wire loses structural stability and breaks down in a particular location along the wire, and the length of the wire recedes into spherical droplets at the ends of the wire. The point along the wire length where it begins to melt and break apart may depend on the length of the wire [138].

Mass loss due to melting and evaporation are suggested to be the main mechanisms involved in causing the observed size and shape transformations. The Clausius-Clapeyron and Kelvin equations can be used to estimate the mass loss from flat and

curved surfaces respectively, and the liquid skin and liquid nuclear growth models have been used to suggest a near-surface modified layer that induces the shape transformation. This layer may exist as a result of the optical properties, notably the optical absorption depth, of the small particles. The surface tension of the liquid layer may also affect the shape transformation into a spherical particle.

The increase in mass removal rate due to size dependent effects (such as particle geometry, particle diameter etc) goes some way in explaining the shape transformation seen in the laser irradiated silver nanowires used in the experiments described here.

Due to the (relatively) large heat penetration depth in silver at 157nm, ~2.3μm, the majority of the heat from the incident laser beam will be dissipated into the supporting polymeric substrate. However this effect has not been investigated here. It has been suggested [139] that the interaction between the substrate and the nanoparticle also plays a significant role in the melting of nanoparticles. The melting temperature of a supported nanoparticle, i.e. adjacent to a substrate, has been shown to be equal to the melting temperature of a free nanoparticle with the same surface curvature [140], while the thermodynamic model predicts there is a difference, with a dependence on the contact angle between the nanoparticle and the supporting substrate [131].

In addition to thermal effects, nanowires exhibit plasmonic effects when they are excited by laser radiation, which causes electron pile up and regions of localised charge [126, 127, 136]. Under appropriate conditions, this will cause localised enhancement of the electromagnetic field and induce an elevated nanowire temperature which will influence mass transport and mass removal rates. This has been supported by FEM modelling carried out in Chapter 6, but has not been involved in the calculations carried out here.

Chapter 8: Use of Fluorescent Particles for the Fabrication of Active Composite Structures

Section 8.1 - Introduction

Nanoparticles and core-shell particles have many potential applications in modern technology, particularly in sensing applications.

Silver polystyrene core-shell particles will be fabricated by the addition of polyelectrolyte layers to plain silver nanoparticles. The core-shell particles will be characterised using Tunnelling Electron Microscopy to ensure that the added layers are of reasonably uniform thickness. Increasing thickness shells will be added to the silver nanoparticles.

These core-shell particles will be incorporated into an active medium of Rhodamine 6G dye in deionised water in order to investigate the effect of the presence of the particles on the emission properties of the dye. Finite Element Method (FEM) modelling will be used to explore the interaction between silver-polystyrene core-shell particles and the electric field component of an incident electromagnetic wave.

Plain polystyrene particles will be doped with Coumarin 7 dye using a liquid two-phase system. These doped particles will be characterised using a fluorescence microscope to ensure that the fluorescent dye has been absorbed into the particles, and photoluminescence measurements will be used to measure the intensity of the emission from the doped particles.

Fluorescent polystyrene particles will be deposited onto CR-39 polymer substrates for irradiation with the VUV 157nm F_2 laser in order to fabricate composite spherical capped fluorescent structures. These structures will be investigated in order to determine the effect of the laser irradiation on the emission properties of the fluorescent particles.

Section 8.2 - Experimental Results & Discussion

Section 8.2.1 - Silver-Polystyrene Core-Shell Particles

Section 8.2.1.1 - Fabrication & Characterisation of Silver-Polystyrene Core-Shell Particles

In order to fabricate core-shell particles comprised of a silver core and a polystyrene shell, plain silver nanoparticles, 30-50nm in diameter (Nanostructured and Amorphous Materials Inc., Houston, TX) were selected to be coated using poly (allyl amine hydrochloride), PAH, and poly(sodium 4-styrene-sulfonate), PSS.

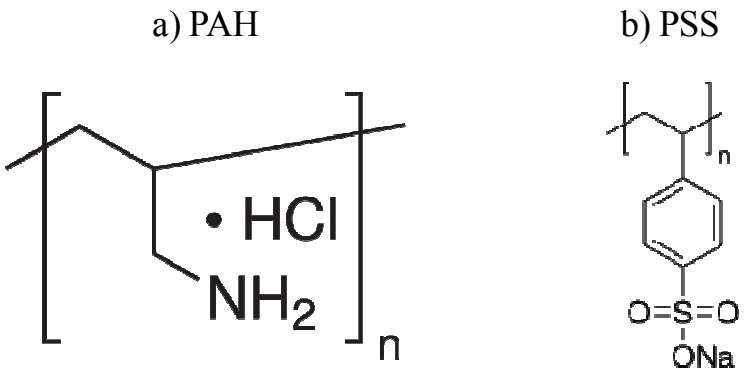

Figure 8.1: Chemical structures of a) PAH and b) PSS. From [141] and [142].

The size of the silver particles was measured (Malvern Instruments Zetasizer 3000), and the results are shown below in Figure 8.2. The silver particles were also measured to have a negative surface charge with a magnitude of -27mV.

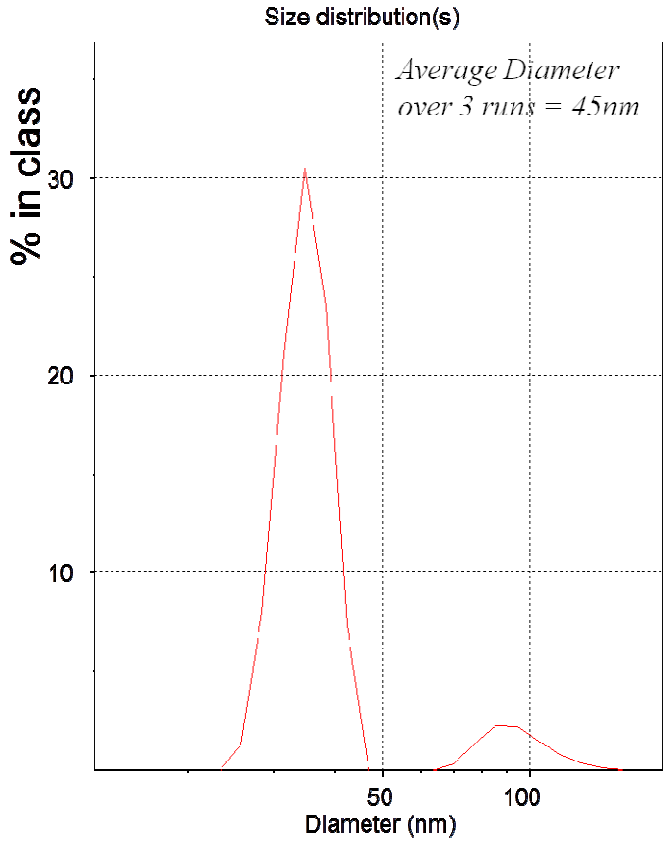

Figure 8.2: Size measurements for silver nanoparticles, diameter specified as 30-50nm. Measurements averaged over 3 runs, average diameter 45nm.

To coat the silver particles with a polystyrene shell, alternating layers of PAH and PSS were added around the silver particles. PAH was added as the initial layer as it has a positive charge, opposing the negative surface charge of the silver particle; PSS was added as the second layer as it too has a negative charge.

First, the silver particles were cleaned in MilliQ water by shaking (IKA MS3 sonicator basic), and were then separated from the water by centrifuge, which was then discarded. This was repeated three times. PAH, which had previously been dissolved in MilliQ water, was added to the precipitated silver particles, and the solution was shaken for 20minutes to allow the PAH to form a layer around the silver particles. This solution was then centrifuged to remove any remaining PAH solution and the particles were cleaned. The PSS, also dissolved in MilliQ water, was added in the same manner to form a layer on the outside of the PAH layer. This method adds ~2nm with each pair of PAH+PSS layers added.

Alternating layers of PAH and PSS were built up in pairs using this method, thereby increasing the thickness of the shell around the silver particle in 2nm increments up to ~10nm.

A Tunnelling Electron Microscope (TEM) was used to characterise the fabricated silver-polystyrene core-shell particles. The TEM micrographs in Figure 8.3a) and Figure 8.3b) show examples of the silver particles with one PAH+PSS layer. EDX measurements were used to verify that these are the coated silver particles, and the spectrum shown in Figure 8.3c) supports this with a sharp peak around 2.8-3.5keV. The peaks in the spectrum attributed to copper arise due to the presence of the TEM grid used to support the particles.

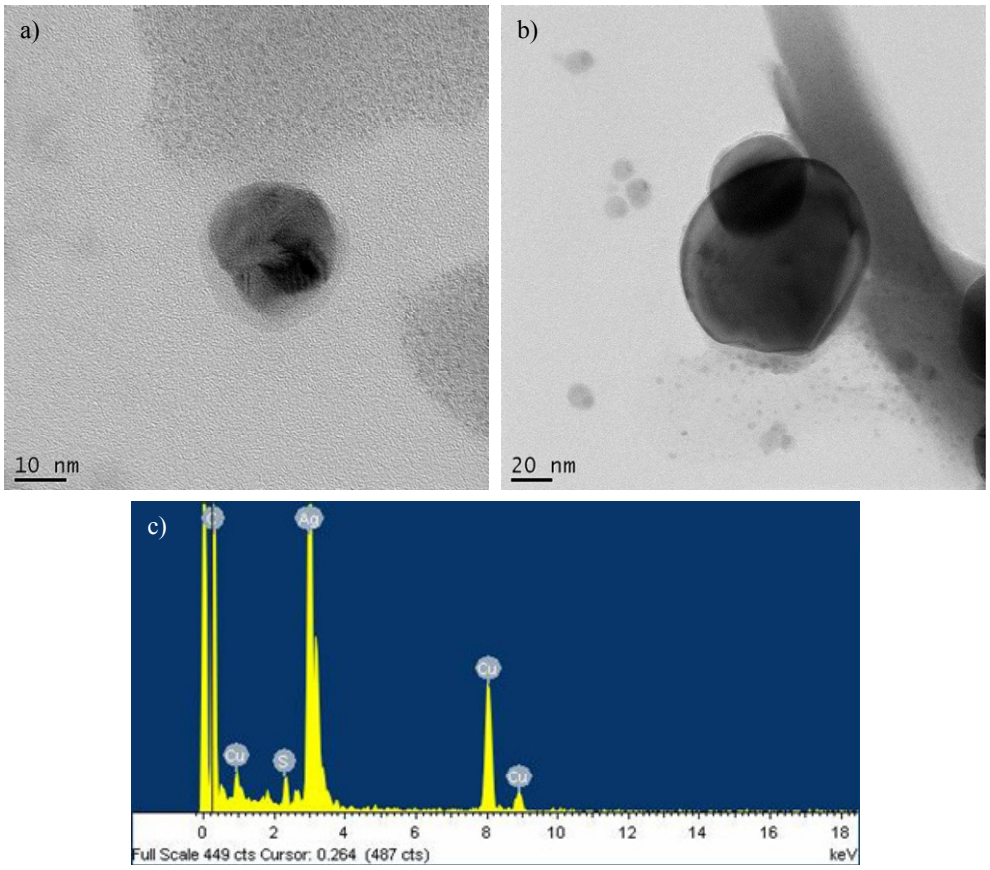

Figure 8.3: Silver-polystyrene core-shell particles fabricated using one PAH+PSS layer coating - a) and b) TEM micrographs and c) EDX measurements (copper line from use of copper TEM grid).

The effect of adding the further pairs of PAH and PSS layers can be seen in Figure 8.4. Measurements for the thickness of the coatings are consistent with those expected from the coating process. The shell thicknesses are reasonably uniform around the silver core particles, and measure ~ 2nm, 5nm and 10nm for Figure 8.4a), Figure 8.4b) and Figure 8.4c) respectively.

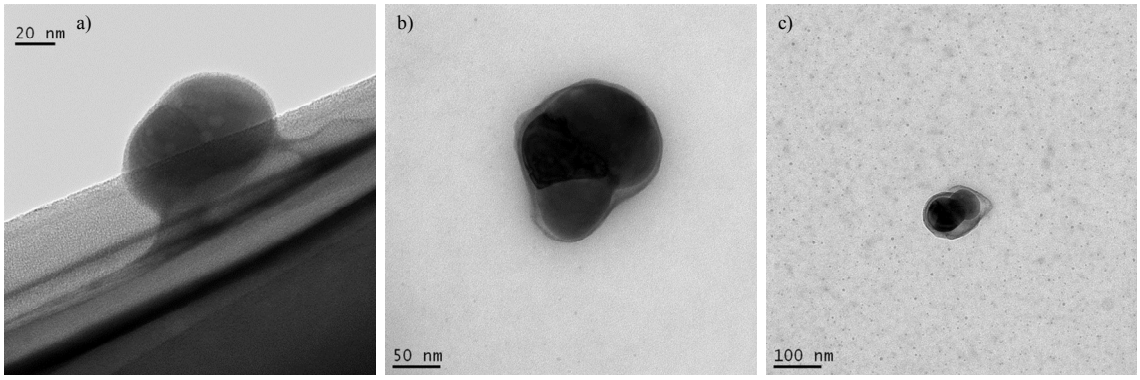

Figure 8.4: TEM micrographs of silver-polystyrene core-shell particles fabricated using pairs of PAH and PSS layers - a) 1 pair, b) 3 pairs and c) 5 pairs of layers.

The absorption spectra for plain silver particles and the silver-polystyrene core-shell particles are shown in Figure 8.5. In all of these spectra, there is a strong peak around a wavelength of 410-420nm, in line with the plasmon resonance wavelength of silver.

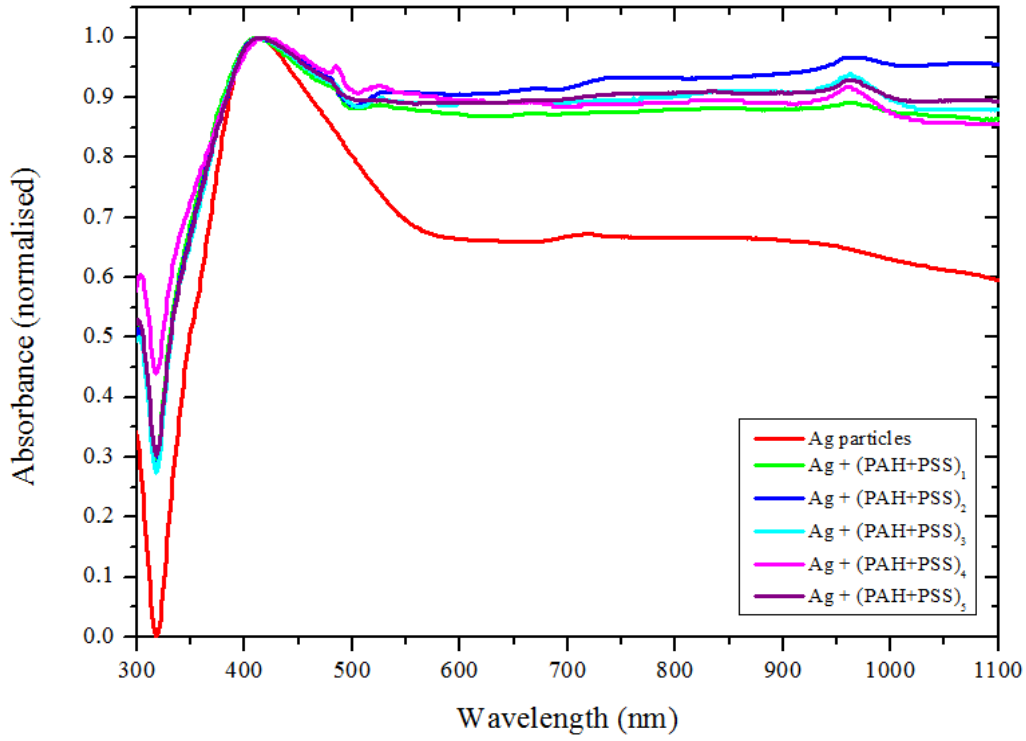

Figure 8.5: Absorption spectra for plain silver particles and the silver-polystyrene core-shell particles of increasing shell thickness - plasmon resonance peaks at - plain silver 412.5nm (red line), 1 PAH+PSS layer 411nm (green line), 2 PAH+PSS layers 414.5nm (blue line), 3 PAH+PSS layers 413nm (turquoise line), 4 PAH+PSS layers 419.5nm (pink line) and 5 PAH+PSS layers 414.5nm (purple line).

Section 8.2.1.2 - Use of Core-Shell Particles in an Active Medium

The silver-polystyrene core-shell particles were added to an active medium in order to examine the effect of the presence of the particles on the emission of the active substance.

Rhodamine 6G is a commonly used dye, and was chosen as the active medium for these experiments.

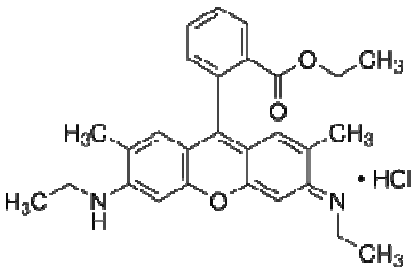

Figure 8.6: Chemical structure of Rhodamine 6G. From[143].

Absorption and emission spectra are shown in Figure 8.7, with peak absorption at a wavelength of ~537nm and peak emission at ~570nm. In accordance with the literature [60], the absorption and emission spectra are roughly symmetrical around a wavelength of ~554nm.

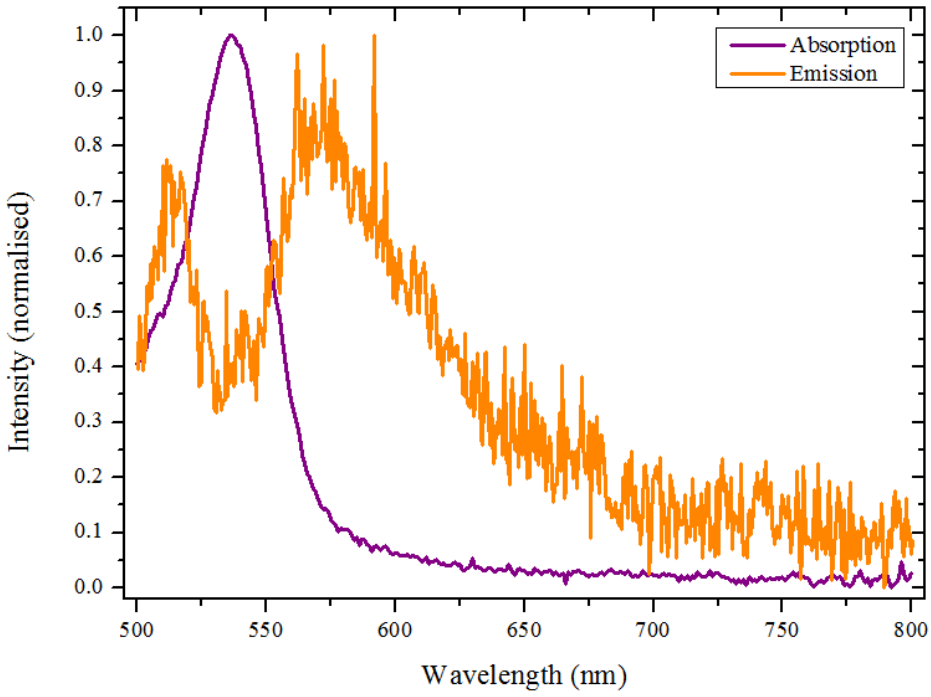

Figure 8.7: Rhodamine 6G absorption (purple line) and emission when excited at 465nm (orange line).

Rhodamine 6G is highly emissive, and only a small quantity of dye is required in order to emit light. Prior to the core-shell particle experiment, the emission of different quantities of Rhodamine 6G dye in deionised (DI) water was measured. The emission spectra for 1%, 2%, 5% and 10% concentration of Rhodamine 6G in DI water are shown in Figure 8.8. These spectra show that as the concentration increases, the emission intensity of the dye decreases. This is due to the dye molecules quenching

each other as they emit. Quenching processes require contact between the fluorescent molecule and the quenching molecule [144] - in this case another fluorescent molecule - causing the fluorescent molecule to return to the ground state without emission of a photon, thereby reducing the intensity of the emission from the sample. Therefore it is obvious that increasing the concentration of the fluorophore within the water medium will result in an increased probability of contact between the individual fluorophores. Oxygen is also a well-known fluorophore quencher [144], which is in good supply when the Rhodamine 6G is dissolved in water.

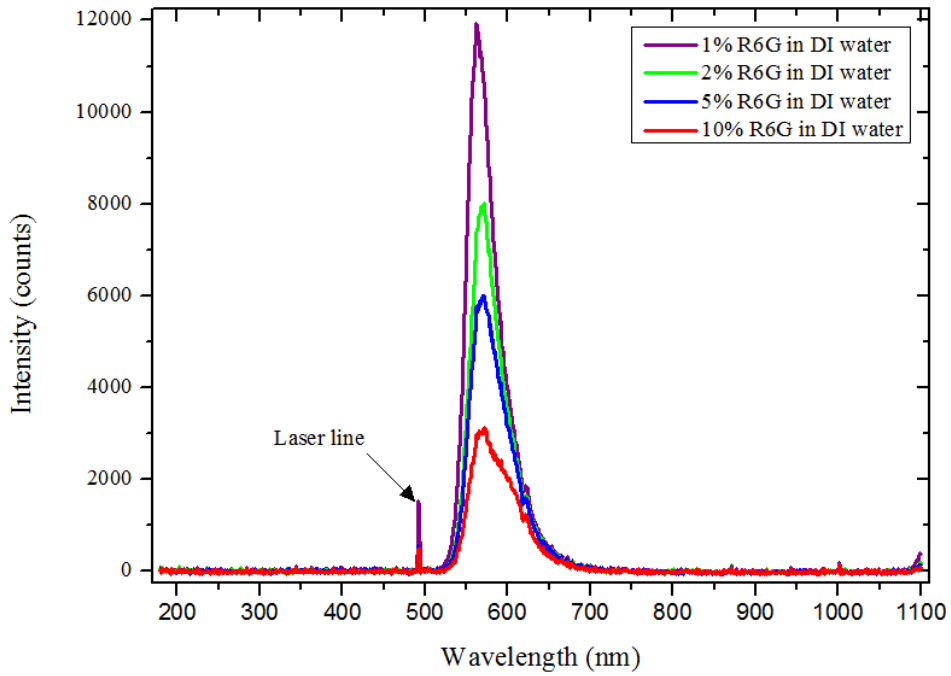

Figure 8.8: Emission spectra of increasing concentrations of Rhodamine 6G in DI water excited at 496nm - 1% (purple line), 2% (green line), 5% (blue line) and 10% (red line).

For the experiments with the silver-polystyrene core-shell particles, a dye concentration of 1% Rhodamine 6G in DI water was chosen because, as shown by the spectra in Figure 8.8, the emission of the dye is relatively very strong at this concentration.

The increasing thickness silver-polystyrene core-shell particles were added to a 1% Rhodamine 6G in DI water solution to a particle concentration of 0.25%. Plain silver particles and 50nm diameter plain polystyrene particles (Bangs Laboratories Inc, Fishers IN, USA) were also added to individual Rhodamine 6G-DI water solutions, and a Rhodamine 6G-DI water solution was used as a control sample.

The photograph in Figure 8.9a) shows the particle solutions under white light. The cuvette on the left contains the 30-50nm plain silver particles in a Rhodamine 6G-DI

water mixture, and the cuvette on the right contains the 50nm plain polystyrene particles in a Rhodamine 6G-DI water mixture. The presence of the silver particles gives the Rhodamine 6G-DI water solution a darker appearance than usual, and the presence of the polystyrene gives the Rhodamine 6G-DI water mixture a lighter, pearlescent appearance.

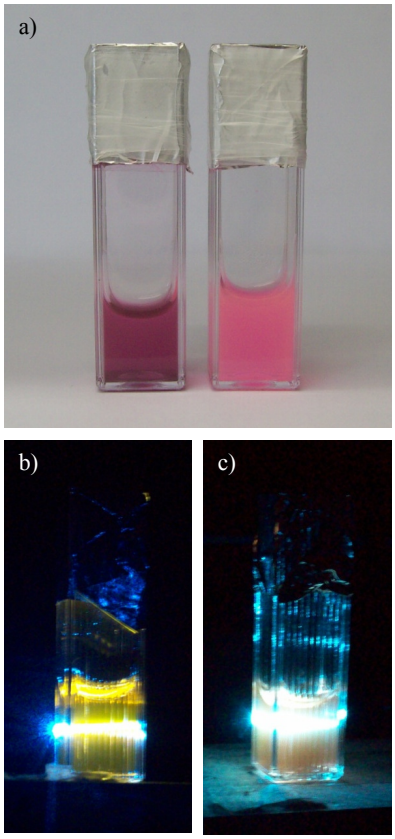

Figure 8.9: Particle-R6G-DI water solutions - a) 30-50nm diameter silver particles in R6G and DI water (left) and 50nm diameter polystyrene particles in R6G and DI water (right) under white light, b) 30-50nm diameter silver particles in R6G and DI water excited at 496nm and c) 50nm diameter polystyrene particles in R6G and DI water excited at 496nm.

Photoluminescence measurements of the different particle solutions were then carried out. The solutions were excited at a wavelength of 496nm (Melles Griot 43 Series Ion Laser), and the intensity of the emission measured (Avantes AvaSpec-2048).The plain silver and polystyrene particle solutions during irradiation are shown in Figure 8.9b) and Figure 8.9c) respectively. The spectra of the emission of each plain and core-shell particle solution, as well as the control sample, are shown in Figure 8.10 below. Figure 8.10a) shows the emission spectra for all of the samples, and shows that the emission of the sample containing the plain polystyrene particles is much greater (~3.3×) than that of the other particle solutions, and even the control sample of only Rhodamine 6G in DI water. Figure 8.10b) shows the emission spectra of the plain silver particles and the

silver-polystyrene core-shell particles in comparison with the Rhodamine 6G-DI water control sample.

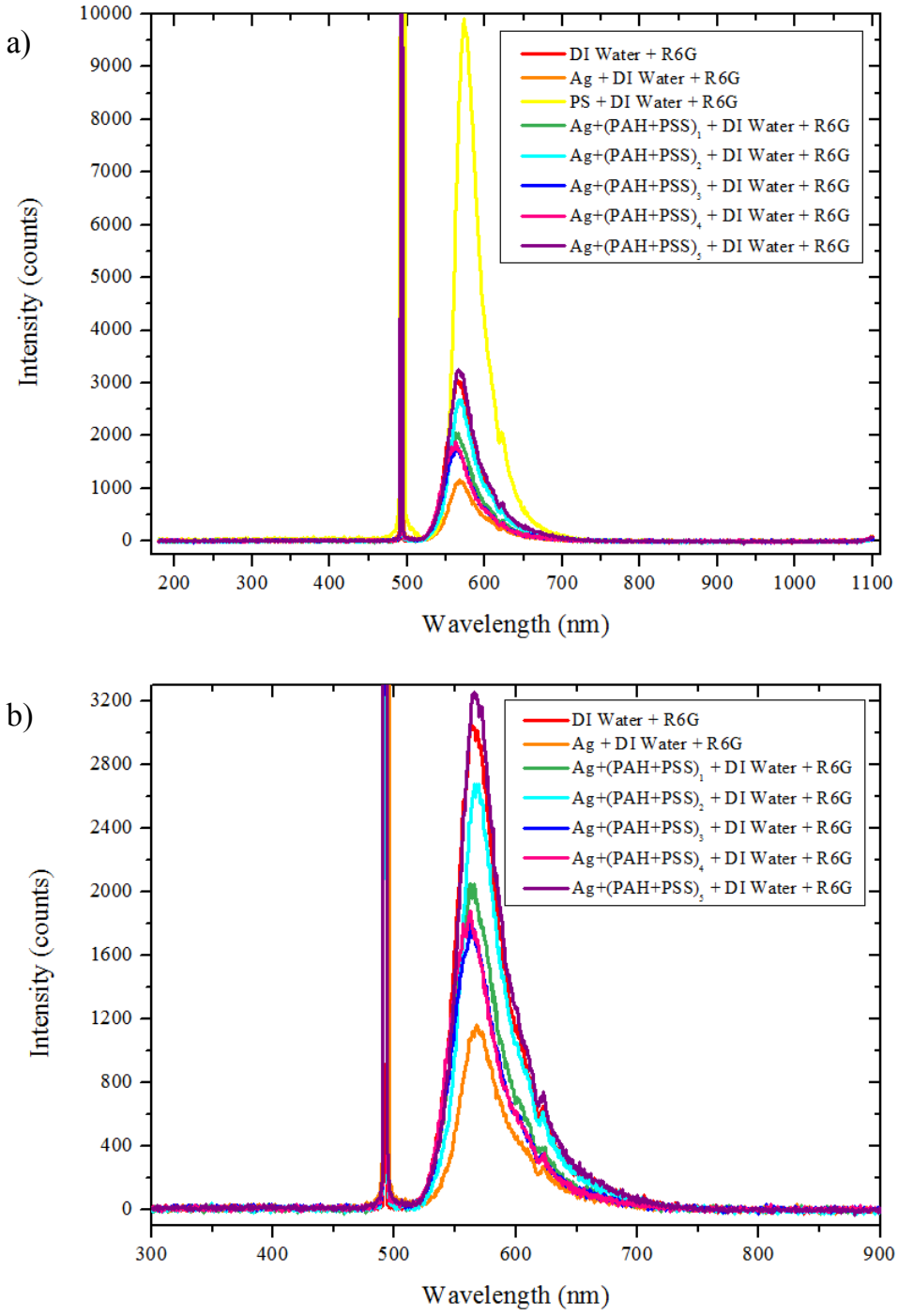

Figure 8.10: Photoluminescence measurements of the emission of the silver-polystyrene core-shell particles, plain silver particles and polystyrene particles in a Rhodamine 6G-DI water solution. $(PAH+PSS)_n$, where "n" denotes the number of layer pairs surrounding the silver core particle. A measurement integration time of 10msec was used.

The emission of the Rhodamine 6G-DI water solution is greatly reduced by the presence of the plain silver particles, from ~3050 counts to ~1160 counts. Silver is a well-known quencher of some fluorophores, and this may be the cause of this drastic reduction in

intensity. Silver particles smaller than the wavelength of the incident light are also proficient scatterers, which may result in light being scattered away from the fluorescent Rhodamine 6G molecules before they can be excited. However, the presence of the polystyrene shell around the silver core reduces this quenching effect, and in general, as the shell thickness increases the intensity increases, as shown in Figure 8.11, until the thickest shell thickness slightly enhances the emission from the Rhodamine 6G, although not to the same extent as the plain polystyrene particles.

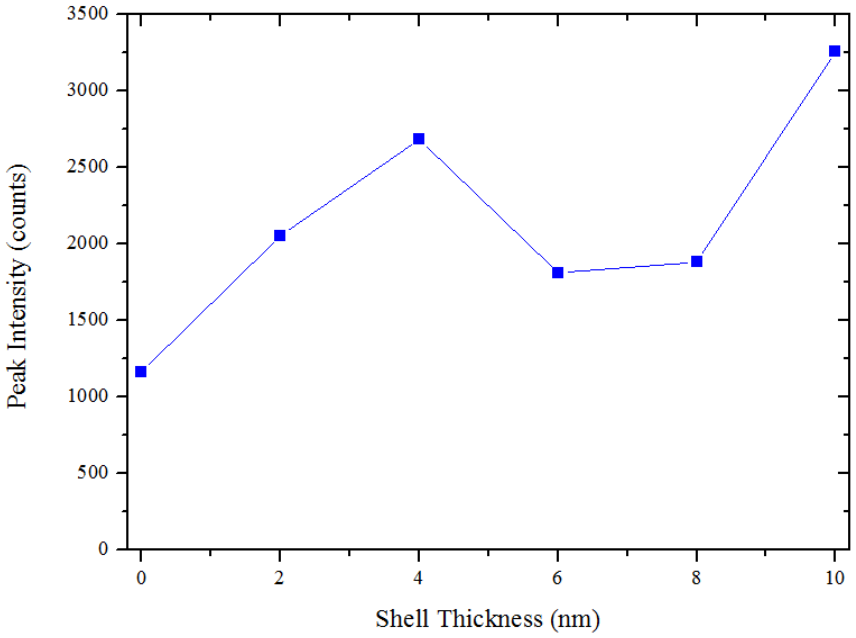

Figure 8.11: Emission peak intensity dependence on silver-polystyrene core-shell shell thickness (based on number of PAH+PSS layer pairs).

This pattern may arise from the plain silver particles scattering the incident laser light before it can stimulate emission from the Rhodamine 6G molecules. The presence of the thinner polystyrene shells may reduce this effect until the thickest shell is reached and the scattering effect is nullified. The irregularity in the general trend of the graph may be as a result of inconsistencies in the thicknesses of the shell layers in the samples.

Section 8.2.1.3 - FEM Modelling of Silver-Polystyrene Core-Shell Particles

For the purposes of modelling the silver-polystyrene core-shell particles in COMSOL Multiphysics version 3.5a, an irradiation wavelength of 451.8nm with TM polarisation was chosen though a few trials, as at this wavelength the silver particles demonstrate excellent field enhancement.

For the model, the refractive index of both silver and polystyrene at this wavelength were required. The values used for silver were n = 0.04 and k = 2.657 (at 2.75eV) [110]. For polystyrene, values of n = 1.611 and k ≈ 0 [145] were used.

Section 8.2.1.3.1 - Single free-standing silver-polystyrene core-shell particles

In a similar manner to the plain silver particles modelled in section 6.2.4.1, free-standing isolated silver-polystyrene core-shell particles exhibit enhancement of the electric field in the surrounding area, particularly when irradiated at wavelengths comparable to the plasmon resonance wavelength. For example, the silver-polystyrene core-shell particle modelled in Figure 8.12 has a core particle diameter of 50nm and a shell thickness of 5nm - similar to the particles fabricated in the experiments previously presented. The intensity cross-section graphs in Figure 8.12c) and Figure 8.12d) represent the intensity across the core-shell particle in the horizontal and vertical directions as denoted by the dashed lines "h" and "v" in Figure 8.12b) respectively. This particle, shown irradiated at a wavelength of 451.8nm (from the left), exhibits enhancement of the electric field intensity at the top and bottom of the particle, ~2.2×, and a reduction in the intensity, ~98%, at the front and back of the particle.

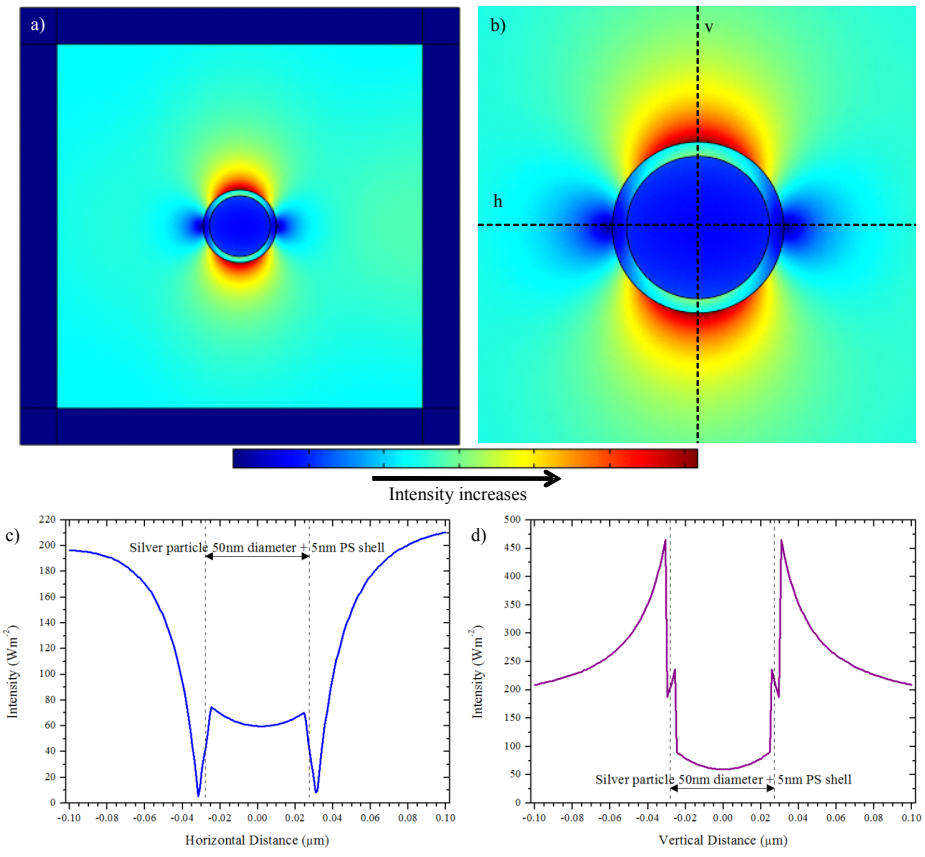

Figure 8.12: Two-dimensional FEM analysis of a single free-standing silver-polystyrene core-shell particle irradiated at 451.8nm with TM polarised radiation, core diameter 50nm, shell thickness 5nm - a) intensity plot, b) magnified view of intensity plot with c) intensity cross-section along dashed line marked "h" and d) intensity cross-section along dashed line marked "v".

Section 8.2.1.3.2 - Pairs of free-standing silver-polystyrene core-shell particles

Similarly to the pairs of plain silver particles, free-standing pairs of the silver-polystyrene core-shell particles also exhibit coupling of the electric field in the gap between the particles when they are separated by a small distance.

This effect is demonstrated in the graph in Figure 8.13a). At small separation distances, the electric field intensity at the middle of the air gap can be up to ~12× greater than when the particles are separated by a much larger air gap. At small separation distances, for example 1nm as shown in Figure 8.13b), the hotspot is very intense in the small gap, and there is little field intensity enhancement around the rest of the particle. As the separation distance increases, for example to 10nm shown in Figure 8.13c), the intense hotspot begins to break apart, although there is still coupling between the particles and little enhancement around each individual particle.

As the separation distance increases even more, to 40nm and then to 90nm as depicted in Figure 8.13d) and Figure 8.13e) respectively, the coupling between the particles begins to break apart and the particles begin to act more like individual particles rather than a coupled pair, and the intensity of the field in the middle of the air gap begins to equalise with the background intensity.

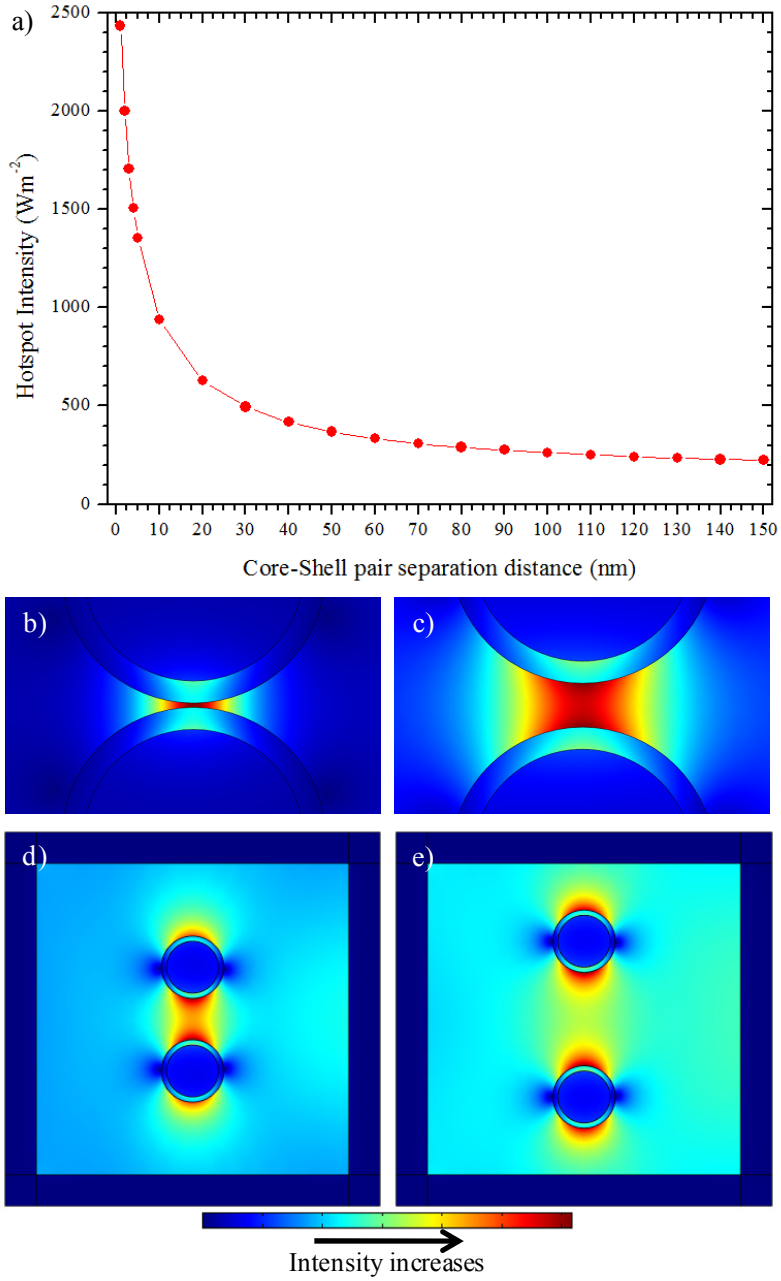

Figure 8.13: Two-dimensional FEM analysis of a free-standing pair of silver-polystyrene core-shell particles irradiated at 451.8nm with TM polarised radiation, core diameters 50nm, shell thicknesses 5nm - a) hotspot intensity dependence on particle pair separation distance, b) pair separation 1nm, c) pair separation 10nm, d) pair separation 40nm and e) pair separation 90nm.

If the silver-polystyrene core-shell particles are placed adjacent to each other, the effect of the thickness of the polystyrene shell on the coupling of the electric field by the particle pair can be determined. As the shell thickness increases the intensity of the electric field decreases, as shown in the graph in Figure 8.14a). The intensity when there is no polystyrene shell, i.e. when the two silver core particles are in contact, is greatly reduced when a polystyrene shell is incorporated. It would appear that the polystyrene dampens the field enhancing effects of the two silver particles. This can be seen when

there is no polystyrene shell, and when the shell has a thickness of 1nm, 3nm and 5nm as shown in Figure 8.14b), Figure 8.14c), Figure 8.14d) and Figure 8.14e) respectively.

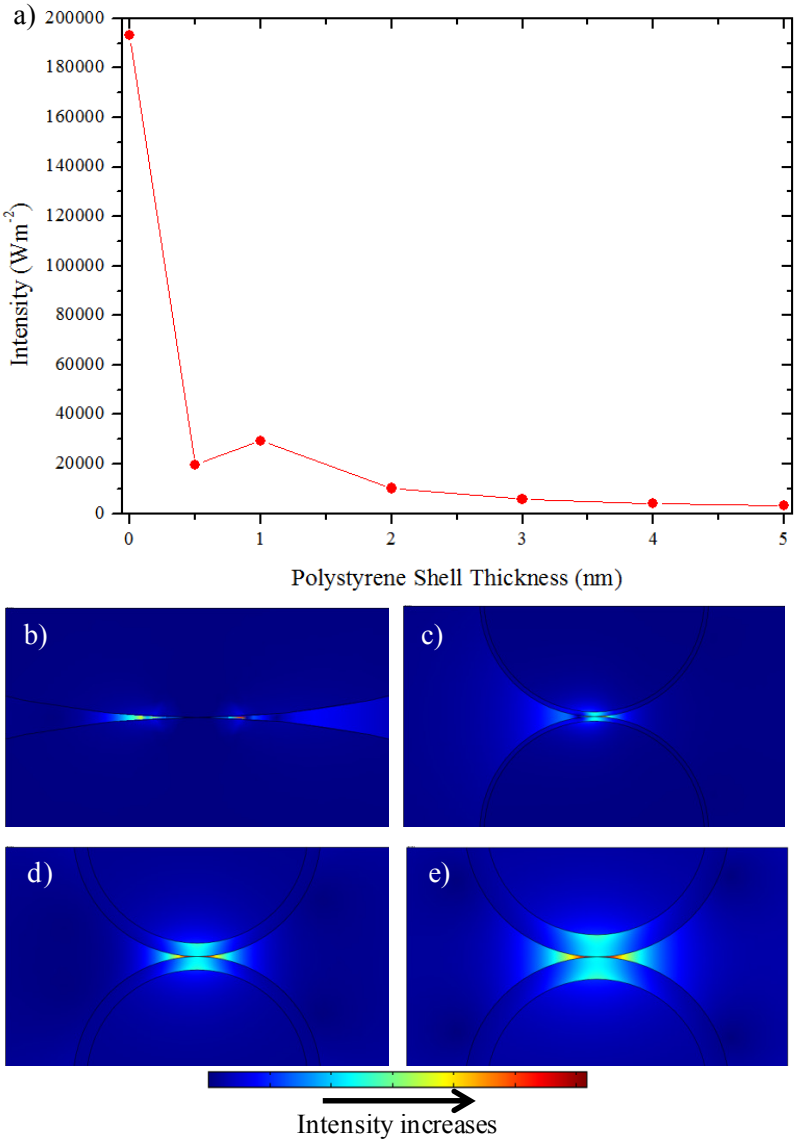

Figure 8.14: Two-dimensional FEM analysis of a free-standing pair of silver-polystyrene core-shell particles irradiated at 451.8nm with TM polarised radiation, core diameters 50nm - a) hotspot intensity dependence on polystyrene shell thickness, b) no polystyrene shell, c) polystyrene shell thickness 1nm, d) polystyrene shell thickness 3nm and e) polystyrene shell thickness 5nm.

Section 8.2.2 - Fluorescent Polystyrene Particles

Section 8.2.2.1 - Fabrication & Characterisation of Fluorescent 490nm Diameter Polystyrene Particles

Plain polystyrene particles with a diameter of 490nm (Bangs Laboratories Inc, Fishers IN, USA) were infused with Coumarin 7, a fluorescent dye.

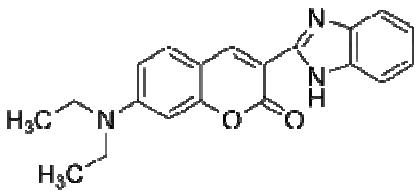

Figure 8.15: Chemical structure of Coumarin 7. From [146].

A liquid two-phase system was used to dye the polystyrene particles, which was adapted from the literature [147-149]. The polystyrene particles were dispersed by sonication in deionised water to a concentration of 0.1%. Coumarin 7 dye was added to xylene to a concentration of 10mg/ml and sonicated. A small quantity, 500µl, of the Coumarin 7 and xylene solution was added to 8ml of the polystyrene particle in water solution. As xylene and DI water are immiscible, the dye-xylene solution sat on top of the polystyrene-water solution. This was then shaken for two hours to allow the xylene to evaporate. As the xylene evaporated, the Coumarin 7 dye transferred to the polystyrene-water mixture and was absorbed into the polystyrene particles. After all of the xylene had evaporated, the particle-dye-water solution was centrifuged to separate the dyed particles, which were then washed and re-dispersed back to the original concentration of 0.1% in DI water.

The particles were deposited on a clean microscope slide by drop-casting, and a fluorescence microscope (Olympus IX71) was used to image the particles to determine whether the fluorescent dye had in fact been absorbed into the polystyrene particles. The fluorescence micrographs are shown in Figure 8.16. These results confirm that the polystyrene particles were infused with the Coumarin 7 dye.

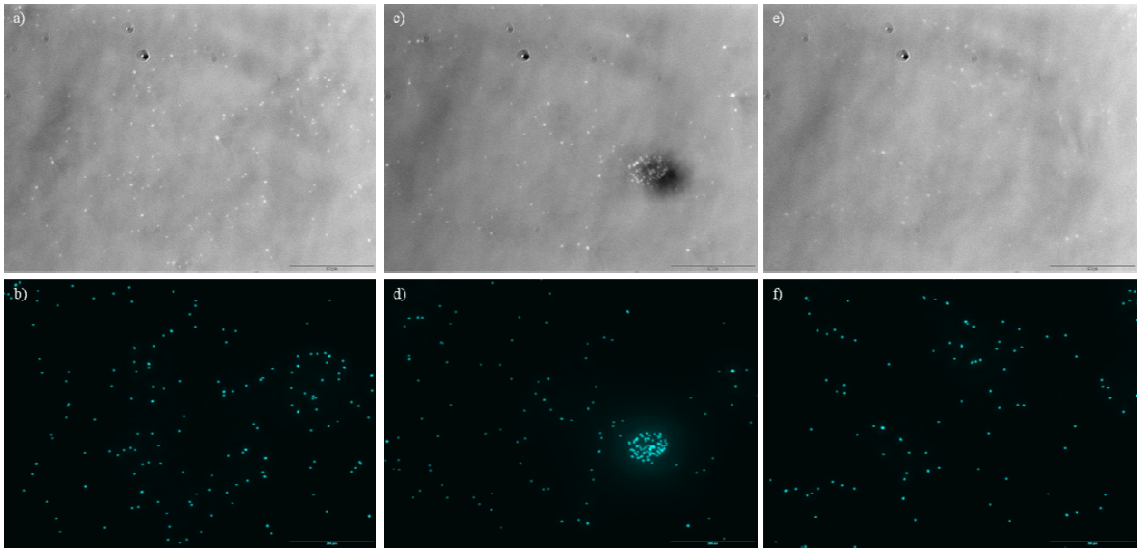

Figure 8.16: 490nm diameter polystyrene particles doped with Coumarin 7, magnification 40×. a), c) and e) white light and fluorescence micrographs b), d) and f) with 434nm light. Images are false-coloured to correspond with experimental observations. 1second exposure time.

The absorption spectrum of Coumarin 7 is shown in Figure 8.17 below. It has an absorption peak of ~440nm.

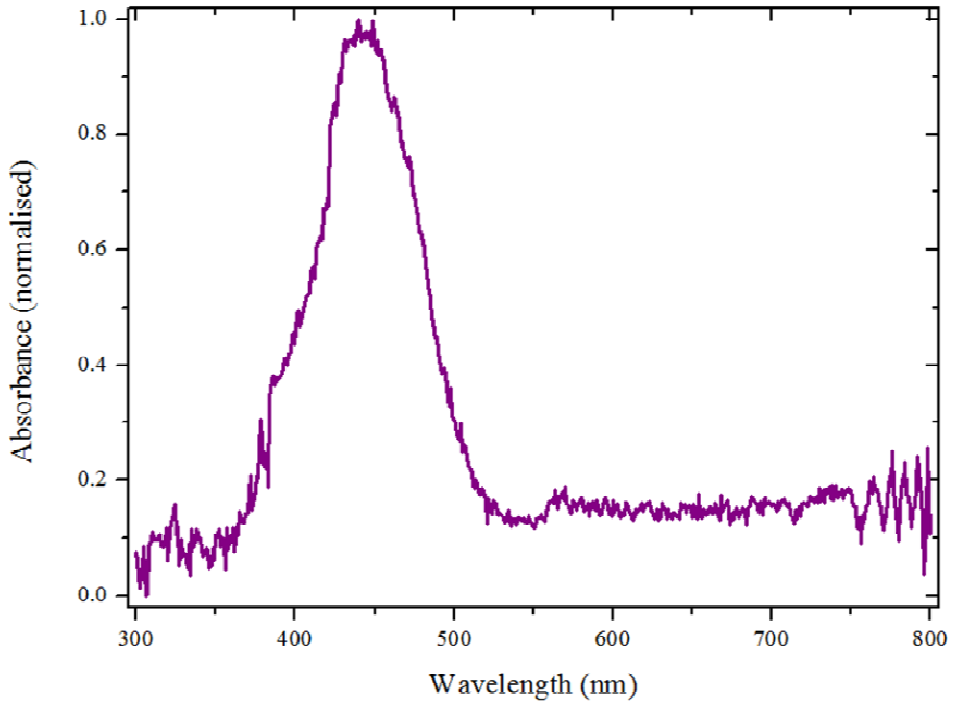

Figure 8.17: Absorption spectrum of Coumarin 7.

The emission (Horiba Jobin Yvon iHR320) of the doped polystyrene particles, irradiated at a wavelength of 405nm (Surelite OPO Plus Continuum), is shown below in Figure 8.18. The laser wavelength of 405nm is well within the absorption band of Coumarin 7, shown in Figure 8.17 and so stimulates emission from the dye within the

particles. The emission shows a double peak, at wavelengths of approximately 514nm and 535nm.

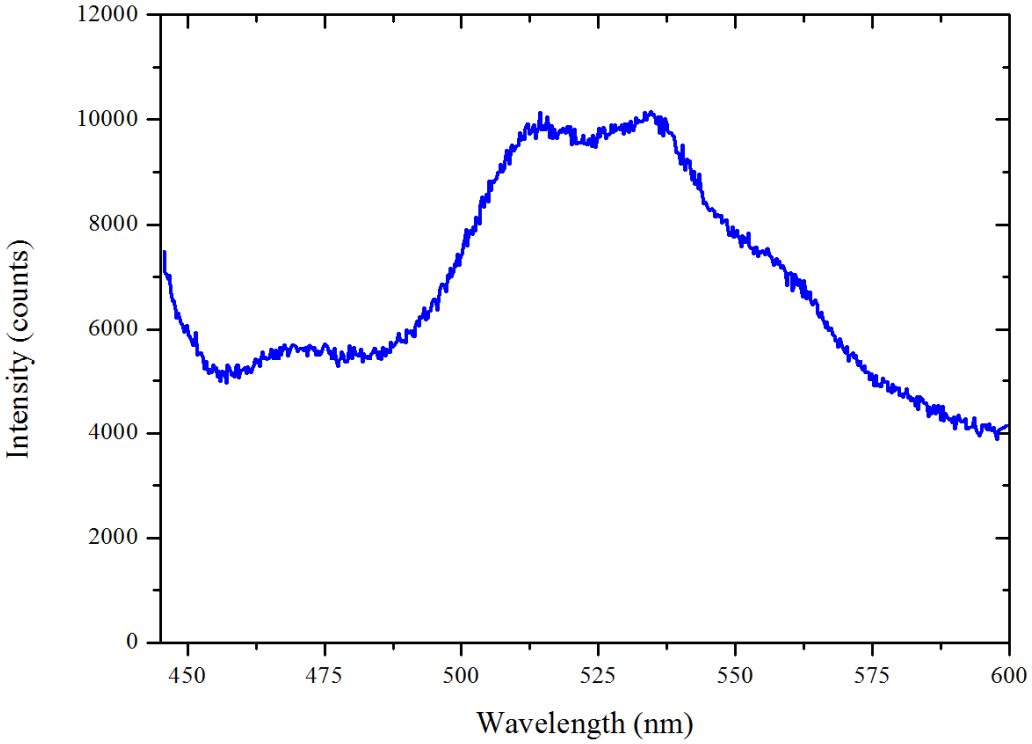

Figure 8.18: Emission of 490nm diameter doped polystyrene particles when excited at a wavelength of 405nm.

The fabrication of these doped polystyrene particles by this method shows that it is quick and straightforward to create fluorescent particles.

While the liquid two-phase system was used to dope the plain polystyrene particles and can be used for silica particles, other methods are available which are just as quick and simple for both particle types. These include the gradual solvent evaporation method [150] which is similar to the liquid two-phase system but involves swelling the polystyrene particles prior to the addition of the fluorescent dye. Doping polystyrene and silica particles with quantum dots instead of a dye is also possible [69, 70].

Section 8.2.2.2 - VUV 157nm F_2 Laser Irradiation of Fluorescent Polystyrene Particles

For the laser irradiation experiments, larger diameter fluorescent polystyrene particles were used.

Fluorescent polystyrene particles of diameters 960nm and 44.2µm (Bangs Laboratories Inc, Fishers IN, USA) were deposited onto CR-39 polymer substrates by spin-coating at 500rpm for two minutes and 250rpm for five minutes respectively.

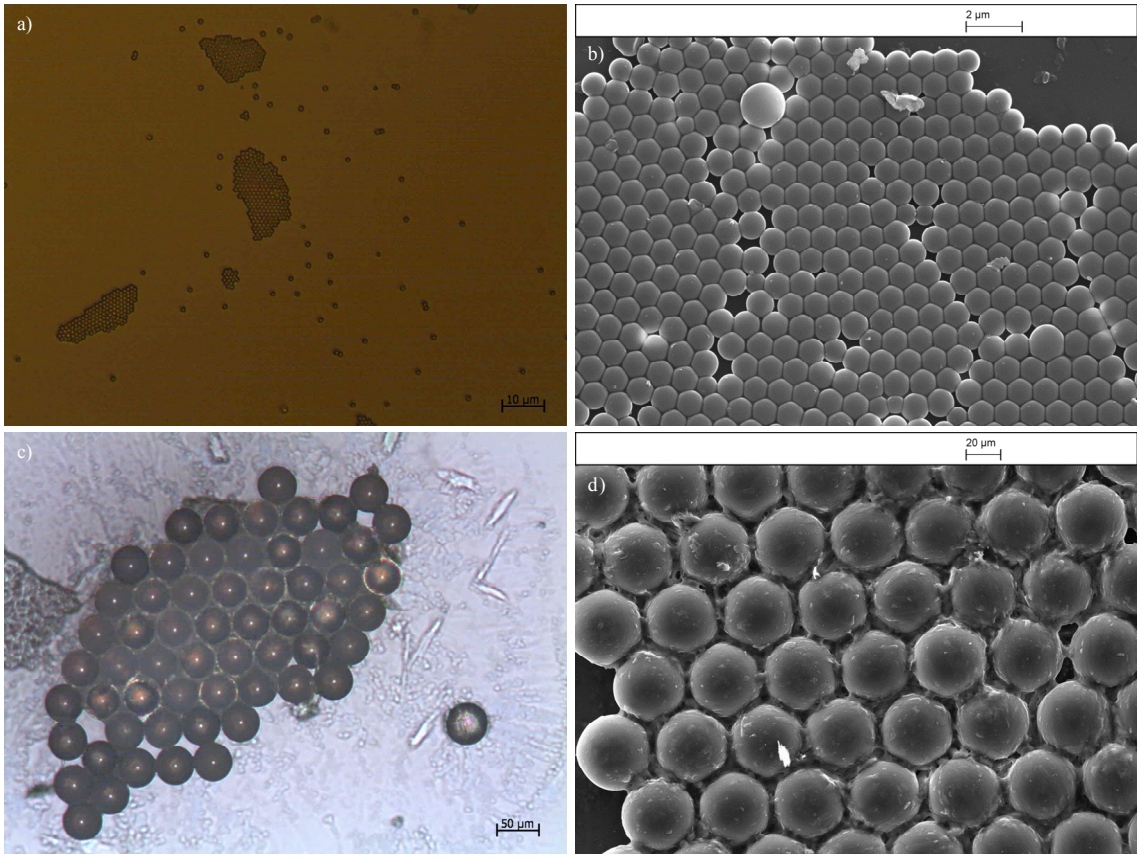

Figure 8.19: Non-irradiated fluorescent polystyrene particles on CR-39 polymer substrates, diameters – 960nm a) optical micrograph and b) SEM, and 44.2µm c) optical micrograph and d) SEM.

The emission spectra for the two sets of fluorescent polystyrene particles when excited at a wavelength of 405nm are shown in Figure 8.20 below. The particles show peak emission at wavelengths of 560nm and 510nm for the 960nm diameter and 44.2µm diameter particles respectively.

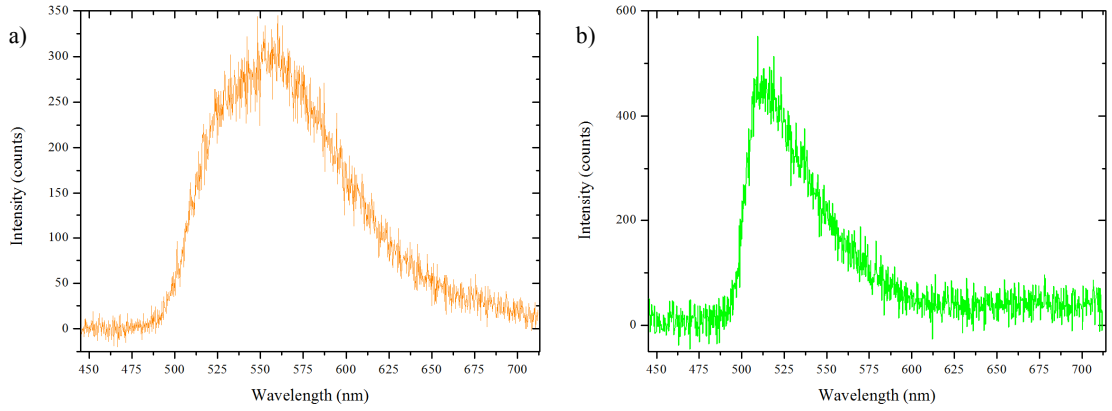

Figure 8.20: Emission spectra for a) 960nm diameter fluorescent polystyrene particles and b) 44.2µm diameter fluorescent polystyrene particles, both excited at a wavelength of 405nm.

The fluorescent particles on CR-39 polymer substrates were then irradiated using the VUV 157nm F_2 laser, with the substrate oriented normal to and angled at 45° to the laser beam propagation direction, using the experimental set-ups shown in Figure 4.3

and Figure 4.7 respectively. The particles were irradiated at reasonably low laser fluences and pulse numbers in order to attempt to prevent significant damage to both the particle and the fluorescent dye molecules.

Prior to laser irradiation, using optical microscopy it was noted that while the particles on one of the samples were relatively monodisperse, with a particle diameter of 960nm, there were a number of large particles mixed in with these smaller particles. EDX measurements gave confidence that these larger particles were of the same composition as the 960nm diameter particles, so the ablation results of these larger particles were included in the analysis.

The 960nm diameter fluorescent polystyrene particles were irradiated normal to the laser beam direction at a laser fluence of 170mJcm^{-2} with different numbers of pulses.

The ablation site shown in Figure 8.21 was irradiated with 10 laser pulses (2Hz pulse repetition rate), resulting in an ablation site depth of ~630nm. The ablation site was imaged using a Fluorescence Microscope (Olympus IX71). The phase contrast image shown in Figure 8.21b) shows the location of some of the features inside the ablation site. The fluorescence micrograph shown in Figure 8.21c) corresponds to the phase contrast image, and shows that the features inside the ablation site are fluorescent even after laser irradiation under these conditions. The feature indicated in the fluorescence micrograph is discussed later in section 8.2.2.3.

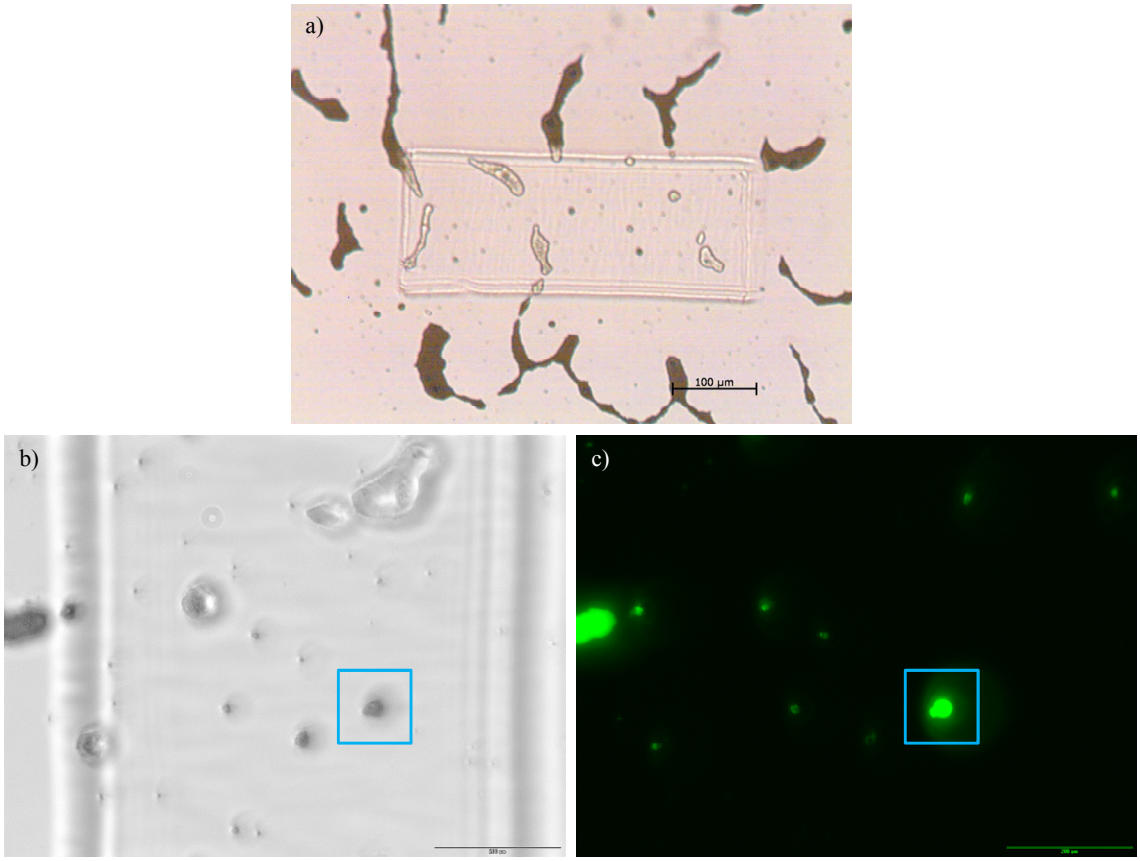

Figure 8.21: VUV 157nm F_2 laser irradiation of small fluorescent polystyrene particles at a laser fluence of 170mJcm^{-2} with 10 laser pulses at a pulse repetition rate of 2Hz - a) optical micrograph of ablation site, site depth ~630nm, b) phase contrast image using white light, integration time 5ms and c) fluorescence micrograph using 490nm radiation, integration time 200ms. Fluorescence micrograph is false-coloured to correspond with experimental observations.

The composite structure shown in Figure 8.22 was also found within this ablation site, having been irradiated with 10 laser pulses (2Hz pulse repetition rate). In this instance, as is usually the case when working with different sized particles, several smaller particles have grouped around the larger particles, as shown in Figure 8.22b). The emission spectrum for this group of particles when excited at 405nm, focussed on the largest particle of diameter ~2.8µm, is shown in Figure 8.22a), and the inset shows the optical micrograph of the particles. The emission peak is at a wavelength of 554nm, and the intensity is much higher than non-irradiated particles. The smaller of the two main particles has a diameter of ~2µm, and the smaller melted particles surrounding the larger particles appear to have originated from the 960nm diameter particles. The larger particles here appear to be aspheric, as shown in the higher viewing angle SEMs in Figure 8.22c) (45°) and Figure 8.22d) (70°). The two large particles, from left to right, have heights of ~ 1.55µm and 2.18µm, and the diameter of the bottom hemisphere is roughly double that of the top hemisphere.

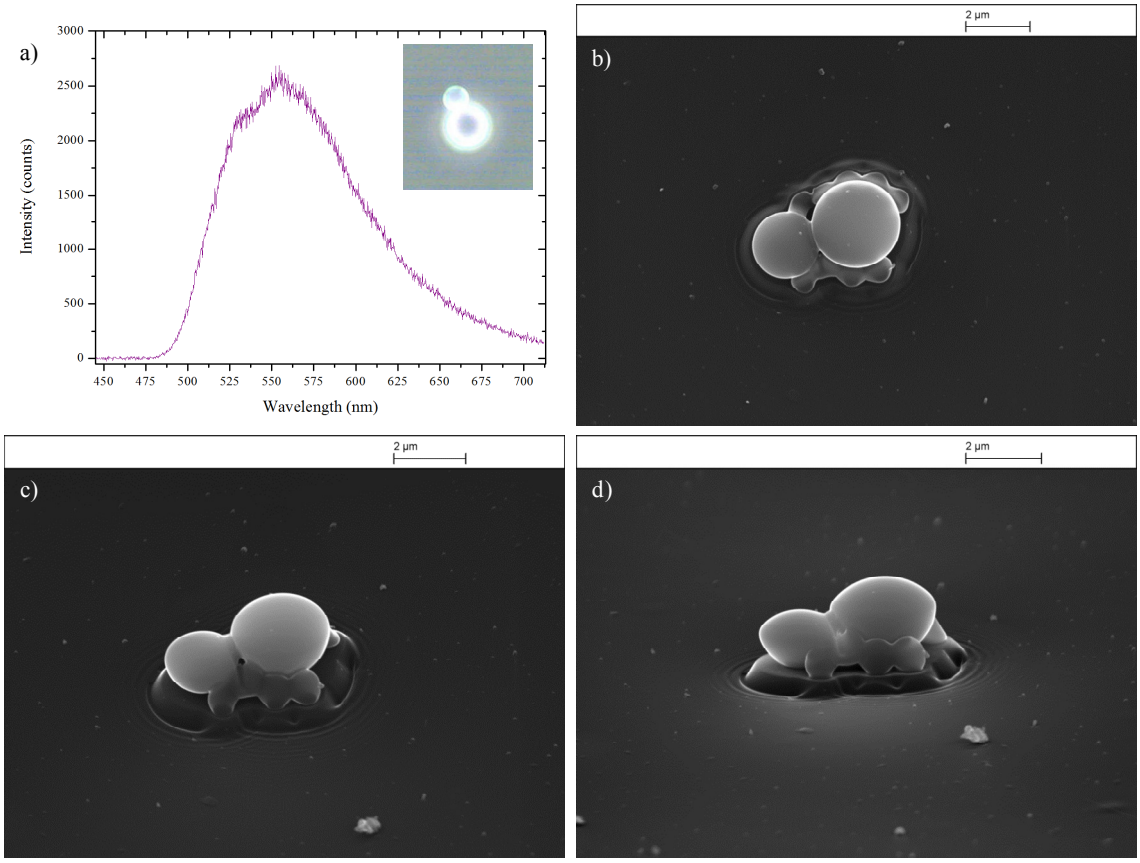

Figure 8.22: VUV 157nm F_2 laser irradiation of small fluorescent polystyrene particles at a laser fluence of 170mJcm^{-2} with 10 laser pulses at a pulse repetition rate of 2Hz - a) emission of composite structure excited at 405nm, inset - OM of structure, SEMs of structure viewed at b) 0°, c) 45° and d) 70°.

The effect of increasing the number of applied laser pulses can be seen in Figure 8.23. The ablation site shown in Figure 8.23a) was irradiated with 20 laser pulses (2Hz pulse repetition rate), and is ~930nm deep. The phase contrast image in Figure 8.23c) and the fluorescence micrograph in Figure 8.23d) are both views of inside the ablation site and show that even at this higher number of laser pulses, the polystyrene particles at the apex of the fabricated composite structures are fluorescent.

As mentioned previously, the smaller particles in this sample tend to collect around the larger particles, and this is the case with the structure in Figure 8.23. This structure is fluorescent, and the emission when excited at a wavelength of 405nm is shown in the spectrum in Figure 8.23b), where the emission peaks at a wavelength of 550nm. The inset shows the structure using an optical microscope, and the smaller particles surrounding the larger one can be seen in this image.

The SEM, viewed from the top, in Figure 8.23e) shows that the smaller particles have been resolved by the laser beam, and the composite structure shape takes these into account. The diameter of the large particle is ~5.3µm. This particle has also undergone a shape transformation from spherical particle to aspherical particle as a result of the laser

irradiation, and this can be seen as the SEM viewing angle increases as shown by Figure 8.23f). The particle height is ~3.75µm, but the radii of the two hemispheres are more equal than seen in the previous examples. This is most likely due to increased mass loss as a result of the increased number of applied laser pulses. The smaller particles around the outside of the large particle have also melted quite considerably, becoming flattened discs ~750nm in height, and these have bridged to the larger particle.

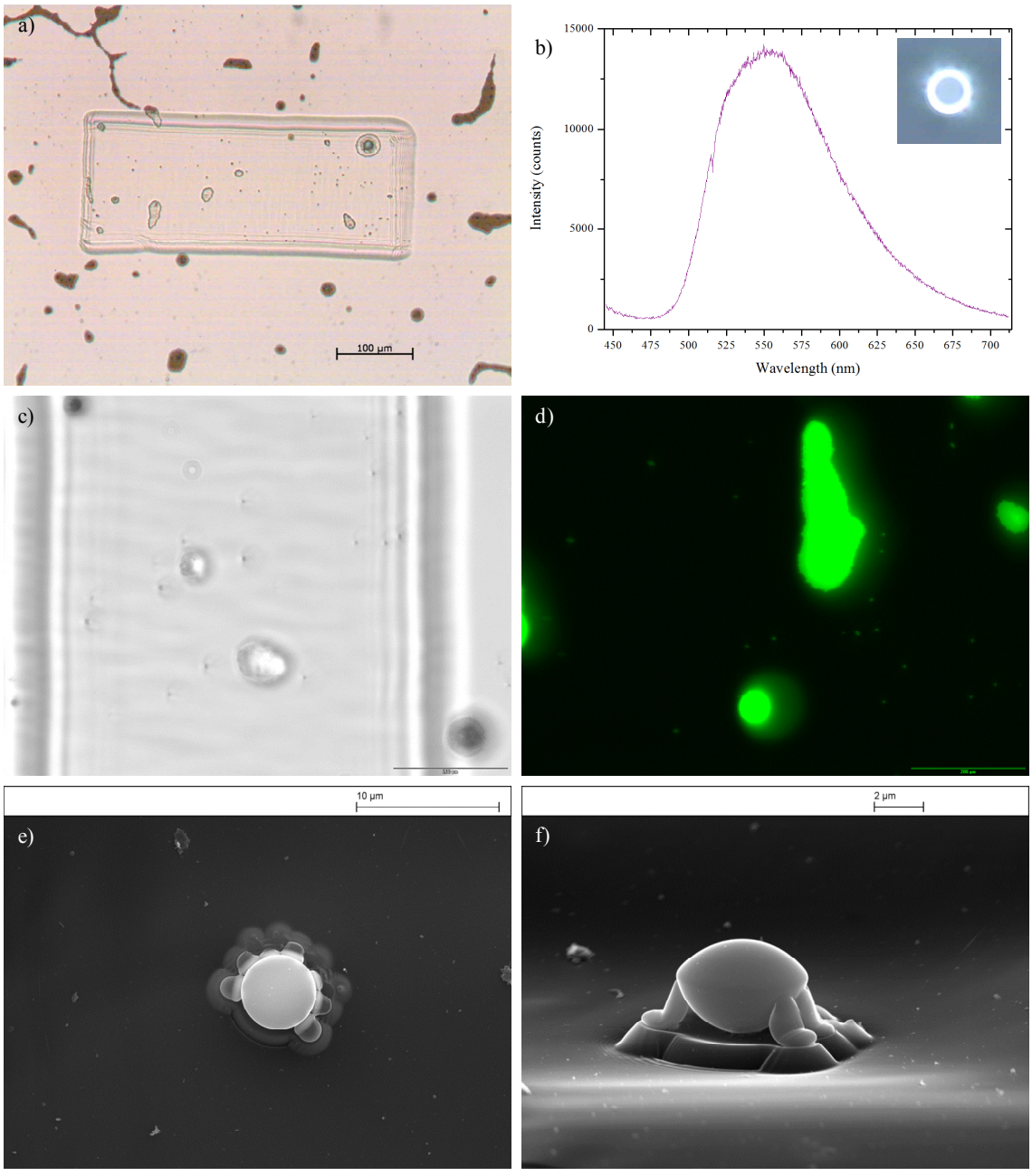

Figure 8.23: VUV 157nm F_2 laser irradiation of small fluorescent polystyrene particles at a laser fluence of 170mJcm^{-2} with 20 laser pulses at a pulse repetition rate of 2Hz - a) optical micrograph of ablation site, site depth ~930nm, b) emission of composite structure excited at 405nm, inset - OM of structure, c) phase contrast image using white light, integration time 5ms, d) fluorescence micrograph using 490nm radiation, integration time 200ms and SEMs of structure viewed at e) 0° and f) 70°. Fluorescence micrograph is false-coloured to correspond with experimental observations.

The ablation site shown in Figure 8.24a) was also irradiated with 20 laser pulses at a laser fluence of 170mJcm^{-2}, resulting in an ablation site depth of ~920nm. The particle indicated in Figure 8.24a) was shown to be fluorescent when irradiated at a wavelength of 490nm using the phase contrast image and the fluorescence micrograph in Figure 8.24c) and Figure 8.24d) respectively (the particle is at the bottom edge of the images). The emission spectrum when excited at a wavelength of 405nm is shown in Figure 8.24b), and the emission peak is at a wavelength of 563nm.

The SEMs at viewing angles of 0° and 70° in Figure 8.24e) and Figure 8.24f) respectively, show that this composite structure is comprised of a pair of polystyrene particles, of diameters ~4.8μm and ~1.7μm. The higher angle SEM shows that the spherical particles have become aspheric as a result of the laser irradiation, and the two particles have heights of ~ 3.6μm and 930nm. This combination of measurements for the smaller particle, which has bridged to the larger particle, suggests two possible shape changes - either a 960nm diameter particle has spread in lateral diameter but has not lost vertical height, or a larger lateral diameter particle has lost vertical height as a result of the laser beam energy.

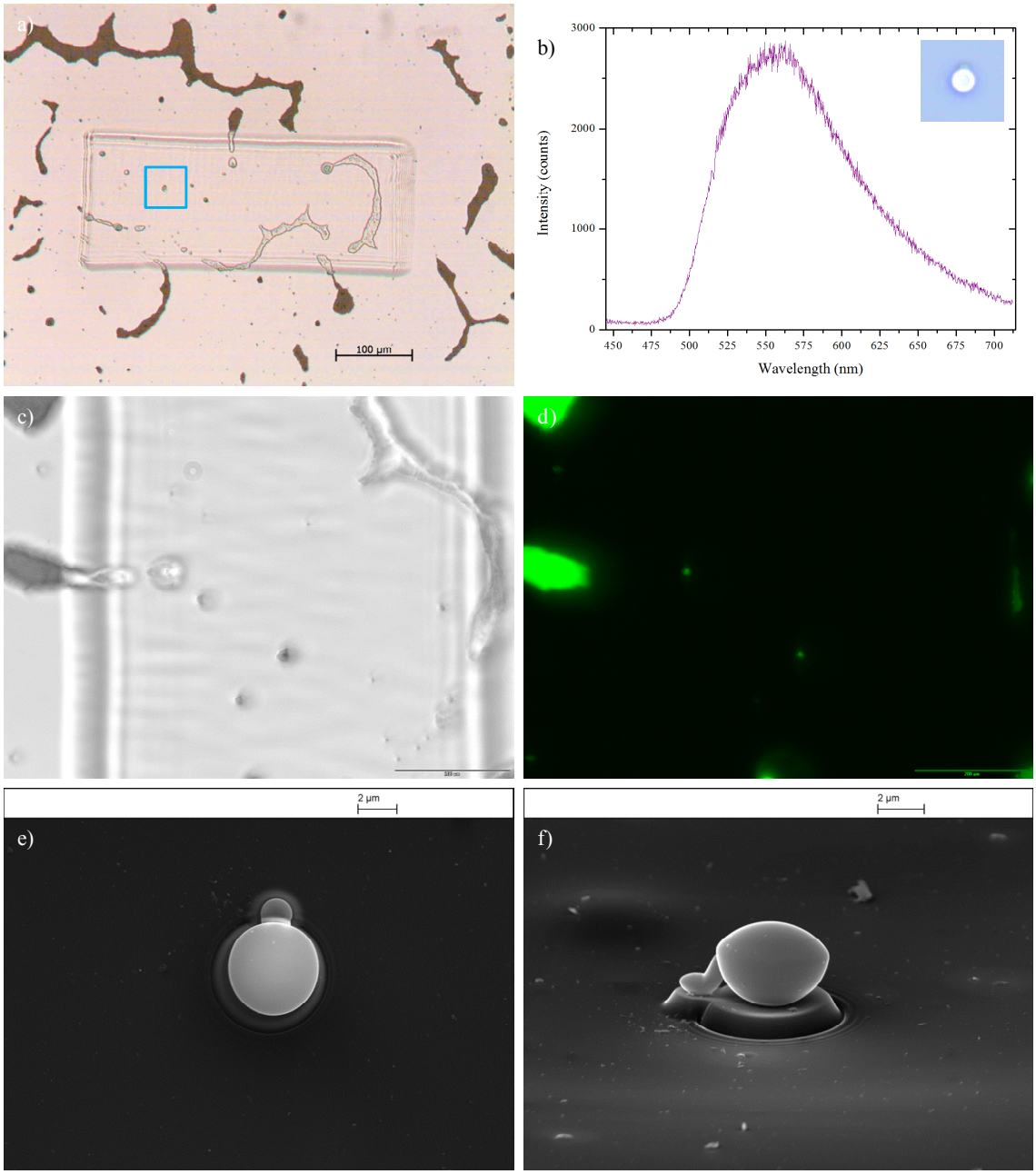

Figure 8.24: VUV 157nm F_2 laser irradiation of small fluorescent polystyrene particles at a laser fluence of 170mJcm^{-2} with 20 laser pulses at a pulse repetition rate of 2Hz - a) optical micrograph of ablation site, site depth ~920nm, b) emission of composite structure excited at 405nm, inset - OM of structure, c) phase contrast image using white light, integration time 5ms, d) fluorescence micrograph using 490nm radiation, integration time 200ms, SEMs viewed at e) 0° and f) 70°. Fluorescence micrograph is false-coloured to correspond with experimental observations.

It is of interest to note that at incident laser pulse numbers of 50 pulses and above, the remaining structures are no longer fluorescent. This may be due to laser-induced damage to the fluorophore used to dope the particles, or sufficient damage to or a shape change of the polystyrene particles.

The experimental arrangement depicted in Figure 4.7 was used to irradiate the 960nm diameter polystyrene particle sample at a 45° angle to the incident laser beam to fabricate fluorescent oblique conical structures.

The composite structure described in Figure 8.25 was irradiated with 100 laser pulses (2Hz pulse repetition rate) at a fluence of 75mJcm^{-2}. Figure 8.25a) shows an optical micrograph of the ablation site, with the feature of interest indicted. This feature is also shown in the phase contrast image in Figure 8.25c) and the fluorescence micrograph irradiated at a wavelength of 490nm in Figure 8.25d). This image shows that the feature is fluorescent even after 100 laser pulses, and the emission spectrum when the feature is excited at 405nm is shown in Figure 8.25b). At this wavelength, the emission peak is at a wavelength of 550nm. The SEMs viewed at 0° in Figure 8.25e) and at 70° in Figure 8.25f) show that this fluorescent feature is in fact made up of a few 960nm diameter particles sitting on top of a larger particle. After laser irradiation, the original large spherical particle has become a flat disc ~2.4μm in diameter. The disc is oriented perpendicular to the direction of the laser beam, and the pedestal follows the shape of both the disc and the (still largely spherical) smaller particles.

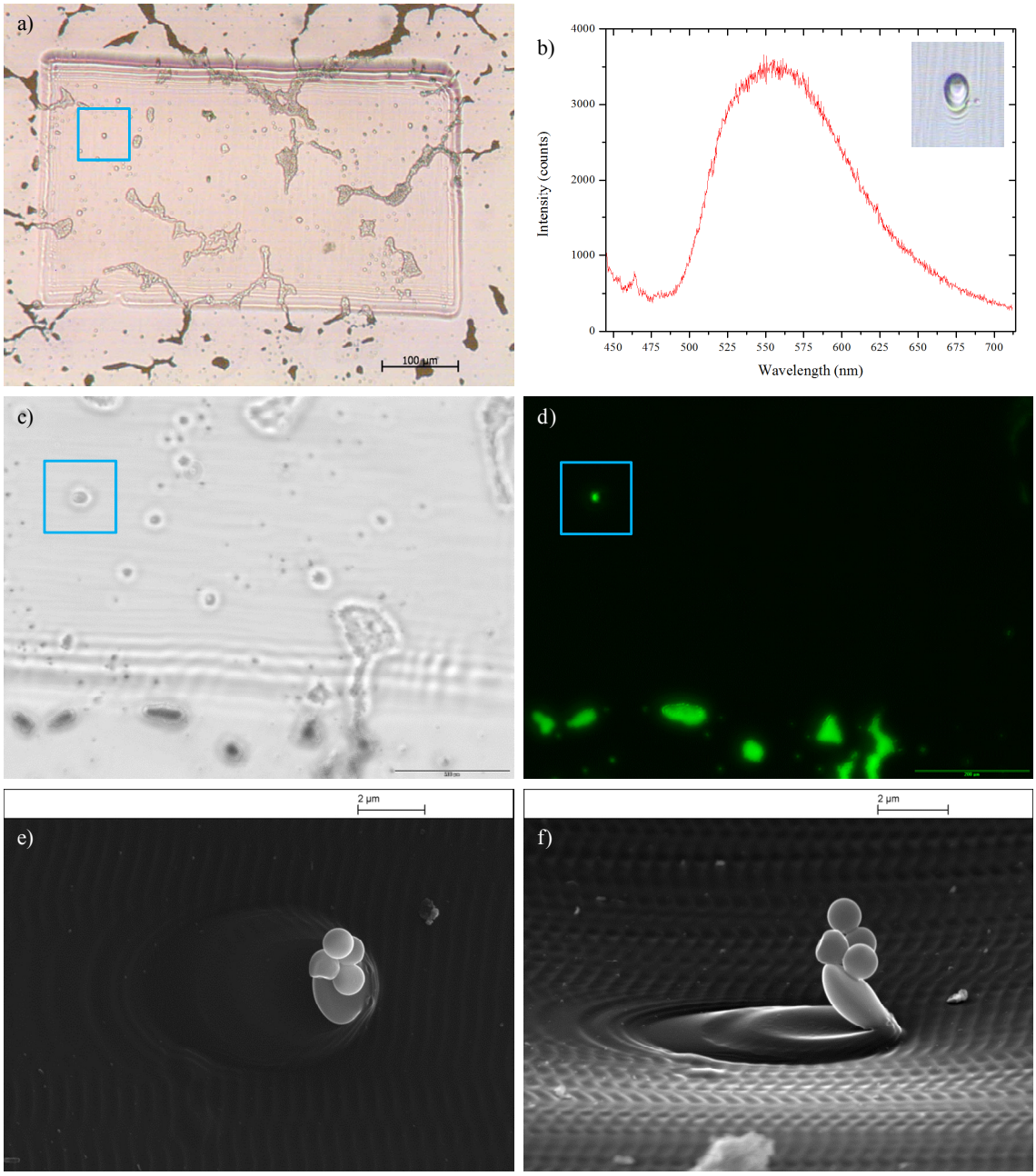

Figure 8.25: VUV 157nm F_2 laser angled irradiation of small fluorescent polystyrene particles at a laser fluence of 75mJcm^{-2} with 100 laser pulses at a pulse repetition rate of 2Hz - a) optical micrograph of ablation site, site depth 676nm, b) emission of composite structure excited at 405nm, inset - OM of structure, c) phase contrast image using white light, integration time 5ms, d) fluorescence micrograph using 490nm radiation, integration time 200ms, SEMs viewed at e) 0° and f) 70°. Fluorescence micrograph is false-coloured to correspond with experimental observations.

The 44.2µm diameter fluorescent polystyrene particles, although much larger than previously irradiated particles present no problem in the fabrication of composite structures. It was observed that these large particles tend to clump together, even during spin coating.

First, these large particles were irradiated normal to the direction of laser beam propagation.

The ablation site shown below in Figure 8.26a) partly covers the clump of 44.2µm diameter fluorescent polystyrene particles. These particles were irradiated at a laser fluence of 220mJcm^{-2} with 50 laser pulses (2Hz pulse repetition rate), resulting in a polymeric support structure height of 4.4µm. Even when irradiated at this fluence with multiple laser pulses, the polystyrene particles have not drastically changed shape or size. Excitation at a wavelength of 490nm causes the irradiated particles to fluoresce, as shown in Figure 8.26d), and the emission spectrum when excited at a wavelength of 405nm is shown in Figure 8.26b), where the emission peak is at a wavelength of ~525nm. The SEM viewed at 70°, Figure 8.26f), shows that conical structures have formed on the surfaces of the large polystyrene particles. These are most likely due to the deposition of debris from the earlier laser pulses on top of the polystyrene particles, which is then irradiated by the latter laser pulses, forming conical structures.

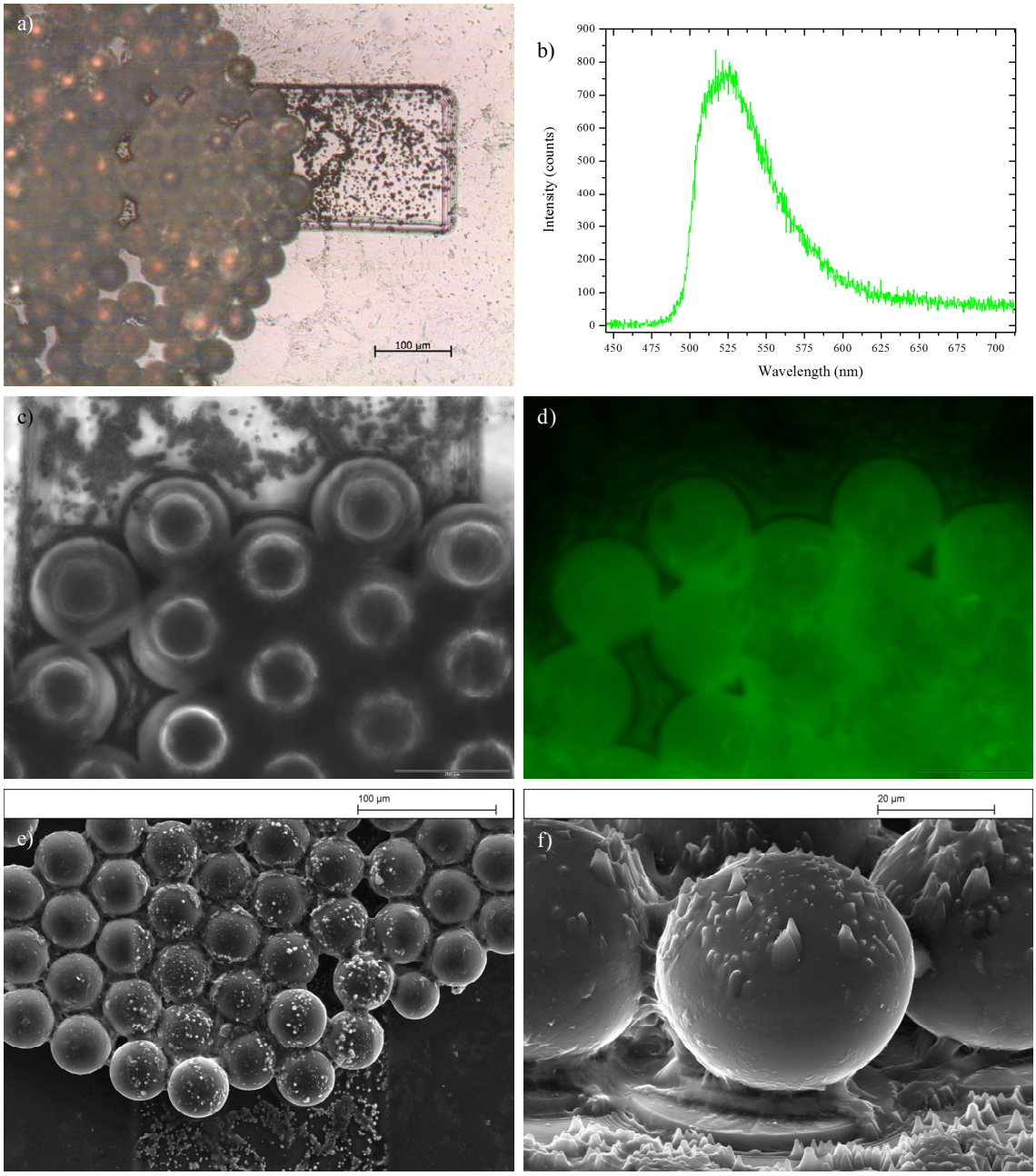

Figure 8.26: VUV 157nm F_2 laser irradiation of 44.2µm diameter fluorescent polystyrene particles at a laser fluence of 220mJcm^{-2} with 50 laser pulses at a pulse repetition rate of 2Hz - a) optical micrograph of ablation site, site depth 4.4µm, b) emission of composite structure excited at 405nm, c) phase contrast image using white light, integration time 5ms, d) fluorescence micrograph using 490nm radiation, integration time 10ms, SEMs viewed at e) 0° and f) 70°. Fluorescence micrograph is false-coloured to correspond with experimental observations.

The 44.2µm diameter polystyrene particles were also irradiated at an angle of 45° to the laser beam propagation direction. This results in the fabrication of oblique composite structures, such as those shown in Figure 8.27 and Figure 8.28.

The single polystyrene particle shown in Figure 8.27 was irradiated at a laser fluence of 160mJcm^{-2} with only 25 laser pulses (5Hz pulse repetition rate), resulting in an ablation site depth, and hence particle support pedestal of only 700nm. The emission spectrum for this composite structure is shown in Figure 8.27b) when excited at a wavelength of

405nm, and the peak emission is at a wavelength of 510nm. Using the fluorescence microscope, the particle was also shown to be fluorescent when excited at a wavelength of 490nm, as shown in the fluorescence micrograph in Figure 8.27d). The diameter of the particle is slightly larger than the specified dimensions, indicating that perhaps the heat generated by the incident laser beam has caused the particle to swell slightly. As shown by the SEM in Figure 8.27a), the particle appears relatively spherical, suggesting that the relatively low number of applied laser pulses has not affected the particle to such an extent as to cause a change in shape.

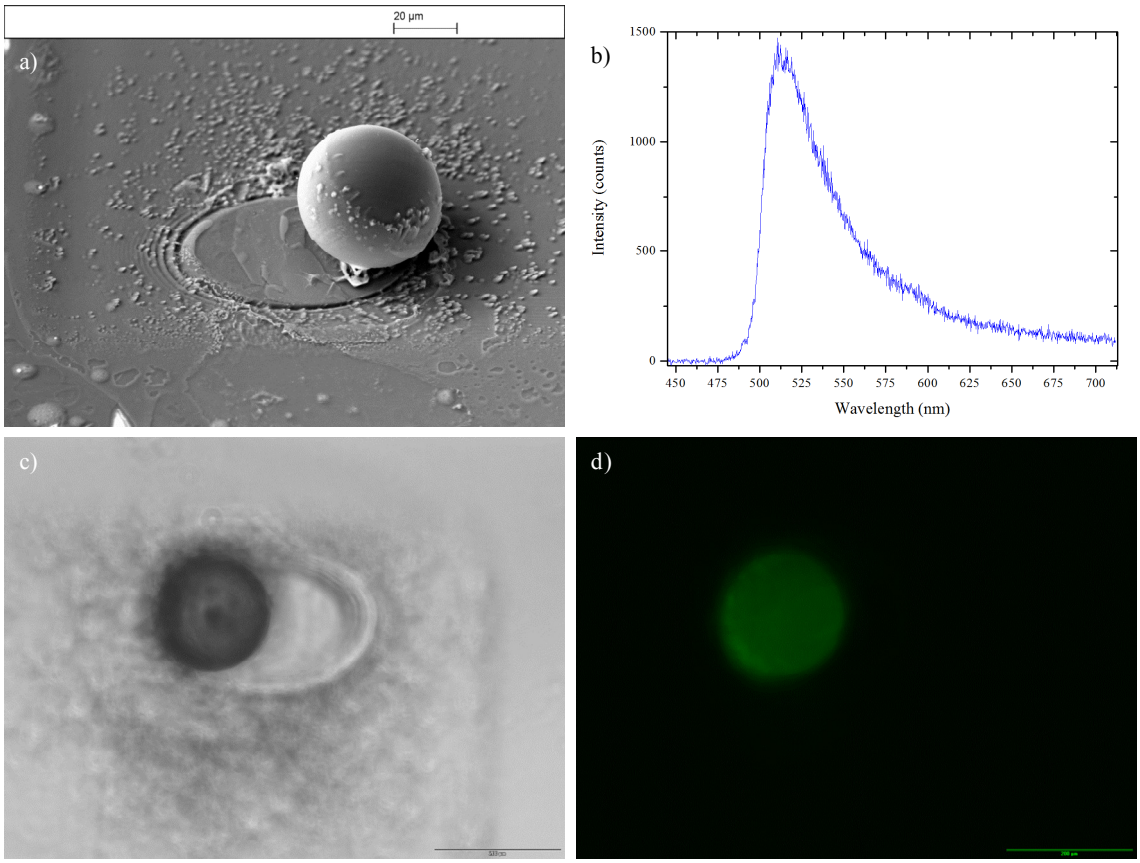

Figure 8.27: VUV 157nm F_2 laser angled irradiation of 44.2µm diameter fluorescent polystyrene particles at a laser fluence of 160mJcm^{-2} with 25 laser pulses at a pulse repetition rate of 5Hz - a) SEM of composite structure viewed at 45°, site depth 700nm, b) emission of composite structure excited at 405nm, c) phase contrast image using white light, integration time 5ms, d) fluorescence micrograph using 490nm radiation, integration time 10ms. Fluorescence micrograph is false-coloured to correspond with experimental observations.

This, however, is not the case for the irradiated particles shown in Figure 8.28. The particles have also been irradiated at a laser fluence of 160mJcm^{-2}, however in this case 200 laser pulses have been applied to the sample. This has resulted in a similar shape change to those seen in the irradiated 960nm diameter polystyrene particles - the side of the particle facing the incident laser beam appears to have flattened compared with the non-irradiated side. The full extent of this shape transformation can be seen in the SEMs viewed at 0° in Figure 8.28e) and particularly clearly at 70° in Figure 8.28f). While the

diameter of the particle facing the incident laser beam has not changed much, the particles have lost about a third of their depth. Despite this mass loss and shape change, the irradiated particles are still fluorescent, as shown by the emission spectrum at 405nm, where the emission peak is at a wavelength of 515nm. The particles are also fluorescent when excited at a wavelength of 490nm as shown in the fluorescence micrograph in Figure 8.28d).

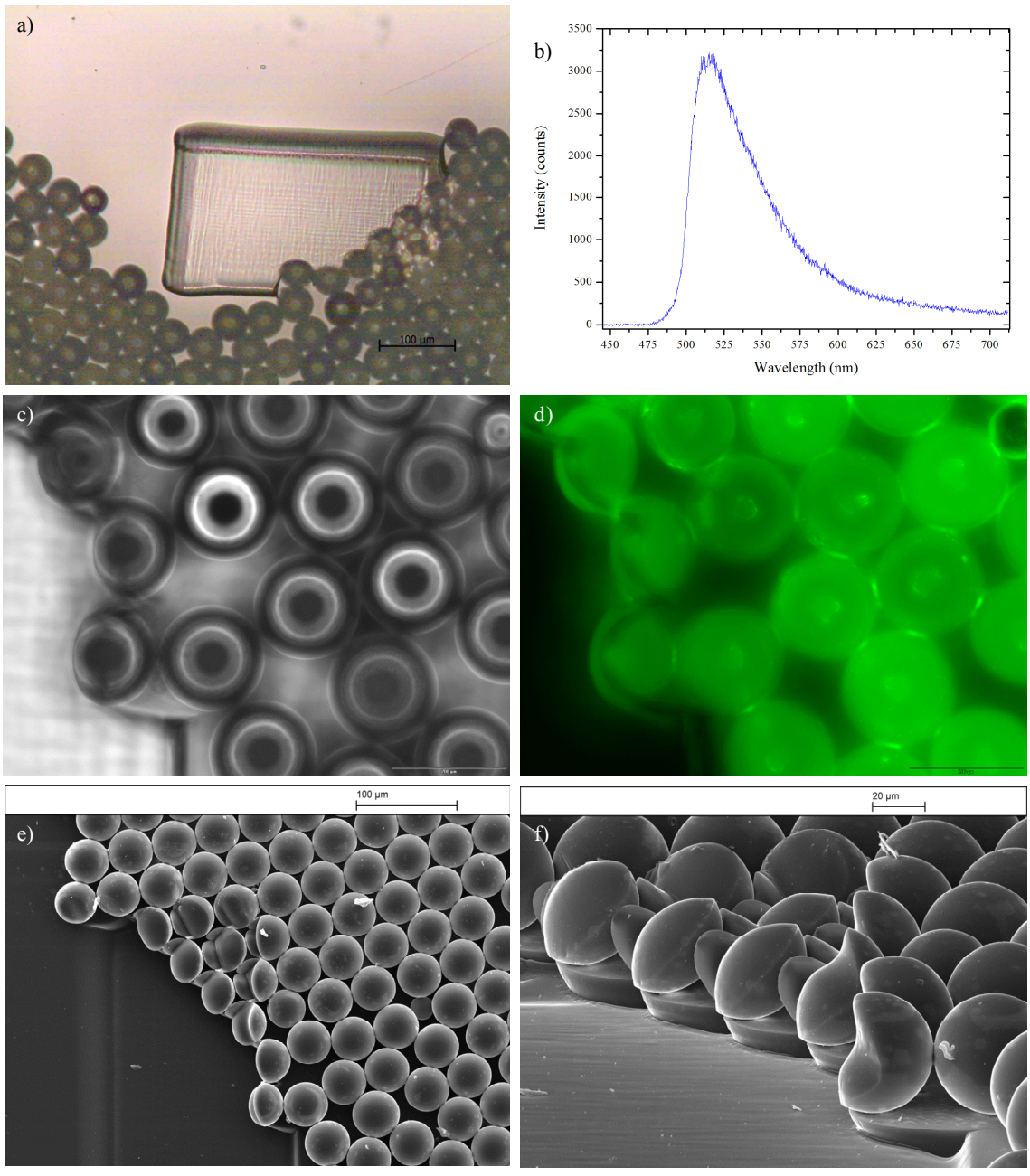

Figure 8.28: VUV 157nm F_2 laser angled irradiation of 44.2µm diameter fluorescent polystyrene particles at a laser fluence of 160mJcm^{-2} with 200 laser pulses at a pulse repetition rate of 5Hz - a) optical micrograph of ablation site, site depth 7.8µm, b) emission of composite structure excited at 405nm, c) phase contrast image using white light, integration time 5ms, d) fluorescence micrograph using 490nm radiation, integration time 10ms, SEMs viewed at e) 0° and f) 70°. Fluorescence micrograph is false-coloured to correspond with experimental observations.

These results are highly promising as they show that under certain laser conditions, the fluorescent polystyrene particles retain their emission properties when laser irradiated and sitting on a polymeric support structure.

It is also of interest to note that the emission intensity of the laser irradiated particles, of both the 960nm diameter and 44.2μm diameter samples, is much greater than that of the non-irradiated samples, shown in Figure 8.20. While size discrepancies, particularly in the 960nm diameter particles sample, may have an effect on this, it is possible that raising the fluorescent particle above the main substrate on a polymeric support structure helps to enhance the emission from the particles by reducing absorption by the substrate. The shape change may also have helped to expose the dye moleules contained within the particle and increase the emission.

Section 8.2.2.3 - Supported Fluorescent Polystyrene Particles Displaying Whispering Gallery Modes

Whispering Gallery Modes were first described acoustically by Lord Rayleigh in 1912, who demonstrated that a whisper in the dome of St. Paul's Cathedral in London, could be heard 100 feet away [151]. This was made possible by the acoustic wave travelling around the inside of the dome wall. Whispering Gallery Modes are also known as *Morphology Dependent Resonances*.

An analogous process occurs optically in dielectric spherical particles, where the spherical particle acts as a cavity. When the angle of light incidence at the particle-air boundary exceeds the critical angle, the light is trapped by total internal reflection. The trapped light then reflects around the inner edge of the particle, and returns in phase after single or, usually, multiple trips around the sphere. The light typically makes a large number of round trips, well in excess of 10^6 [152], and the propagating beams of light interfere with each other before being absorbed. The number of resonant modes per spectrum, an integer, decreases as the diameter of the resonant particle decreases [147].

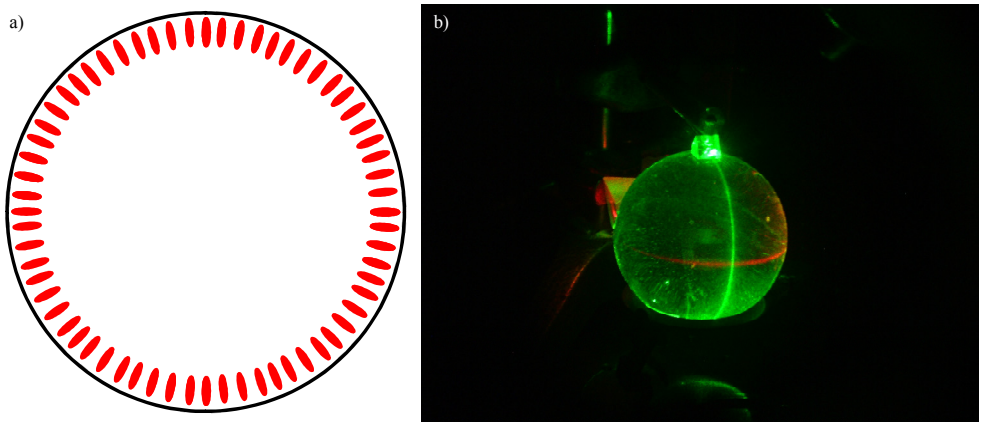

Figure 8.29: Whispering Gallery Mode propagating around the inside boundary of a spherical dielectric cavity - a) schematic showing modes and b) WGMs inside a large glass ball. Photograph courtesy of John Metheringham.

An important element is the method of inputting the light into the particle (cavity). For larger spheres, coupling arrangements such as prisms and tapered optical fibres are typically utilised [148], as demonstrated in Figure 8.29b).

The principal aim of micro- and nano-laser research is to achieve highly directional emission (as demonstrated by traditional, large-scale lasers), as well as high Quality Factors (Q Factors). Whispering Gallery Modes, due to their low losses and typically high Q Factors, may be the extra feature that nanolaser devices require. However, in spherical cavities WGMs can only be weakly coupled out through scattering of the evanescent wave arising from the particle surface roughness.

A number of WGM micro- and nanolasers based on spherical particles have emerged, including rhodamine-doped ethanol droplets, rhodamine-coated polystyrene spherical particles and neodymium-doped silica microspheres – see [153] and references therein for details.

Notched elliptical resonators offer a solution to the problems presented by spherical particles. Spherical microcavity lasers do not produce directional emission due to their radial symmetry, however elliptical devices break this symmetry. Elliptical resonators with a notch located at the intersection between the boundary and the short axis of the ellipse have demonstrated collimated laser emission at a wavelength of 10μm, with a beam divergence of 6° [154]. This Quantum Cascade laser is made of a material described in [155] and is electrically pumped, much like a conventional laser. The notch is comparable in size to the wavelength, and acts as a scatterer - as the WGM resonance propagates around the boundary of the ellipse, when it interacts with the notch it is reflected to the opposite side of the ellipse where it escapes as a parallel beam of light,

as shown in Figure 8.30. Q Factors of ~1,260 have been achieved by this device [154], which is tuneable to near-infrared and visible wavelengths.

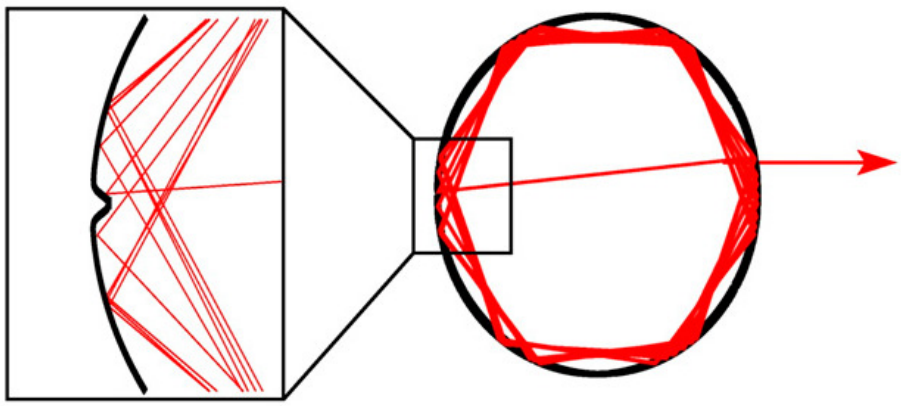

Figure 8.30: Ray simulation of the WGM resonance in a notched elliptical resonator. From [154].

Biosensors that are capable of detecting single molecules are becoming highly sought after, particularly those that are small in size and label-free. Label-free detection means that measurements can be done quickly on-site, taking advantage of new *point-of-care* testing apparatus, such as *Lab-on-a-Chip* microreactors. *Lab-on-a-Chip* devices have so far shown potential in diagnostic applications, blood screening and environmental monitoring, as well as for the separation of multiphase flow streams [156]. Biosensors displaying WGMs made from silica micro-toroids [157] and silica spherical particles [158] have recently been presented that are able to detect single molecules. This enhanced sensitivity arises from an increase in the WGM resonance wavelength shift that results from a molecule binding event through a *thermo-optic boost*. This thermo-optic boost changes the refractive index of the resonator particle, which, in turn, creates an additional wavelength shift, enhancing the shift that occurs from the binding event. The refractive index changes as, if there is sufficient energy in the evanescent field, the temperature of the bound molecule increases, which then transfers heat energy to the resonant particle. These WGM sensors have many potential applications in biological and chemical sensors, for example, multiple resonant cavities could be integrated into *Lab-on-a-Chip* devices for providing information on the composition of a blood sample [158]. It has also been proposed that WGM resonant cavities could also be used *in vivo*, for example they could be incorporated into empty red blood cells and circulate around the cardiovascular system, monitoring for toxins or disease markers, while being excited and monitored from outside the body [158].

Low Q value spherical hollow nanoshells exhibiting WGMs are being investigated for broadband light absorption for use in high-performance solar cells. Nanoshells 50nm in

diameter have demonstrated enhanced optical absorption compared to micron-thickness standard solar cells of the same material, particularly in the near-infrared region [159]. The incident light is confined within the nanoshell and propagates by WGM resonance. These resonant modes not only enhance the light trapping and absorption capabilities of the nanoshells, due to their low Q values (20-100) they also broaden the absorption region [159]. The nanoshells also suffer no change in absorption characteristics when applied to flexible substrates.

Fluorescent microparticles displaying WGM resonances have recently been introduced for use as optical sensors for remote refractive index sensing and biosensing [147]. For some sensing applications it is of interest to know that for surface-adhered particles the influence of the substrate is negligible. This is particularly useful for sensing in small environments such as micro-fluidic and Lab-on-a-Chip devices [147]. Whispering gallery mode resonances are highly sensitive to many factors, including resonant cavity geometry and optical properties, as well as the refractive index of the surrounding environment, which makes them ideal for biosensing.

The excitation of fluorescence is a convenient and versatile way of analysing WGMs over a wide wavelength range [147]. The WGM resonances typically modulate the emission spectrum of the fluorescent medium, appearing as sharp peaks on the spectrum.

A few of the composite conical structures fabricated through the course of these experiments exhibit the WGM effect.

The ablation site shown in Figure 8.31a) was irradiated at a laser fluence of 170mJcm^{-2} with 5 laser pulses (2Hz pulse repetition rate), resulting in an ablation site depth of ~210nm. The features inside the ablation site are fluorescent when excited at a wavelength of 490nm, as confirmed in the fluorescence micrograph in Figure 8.31c).

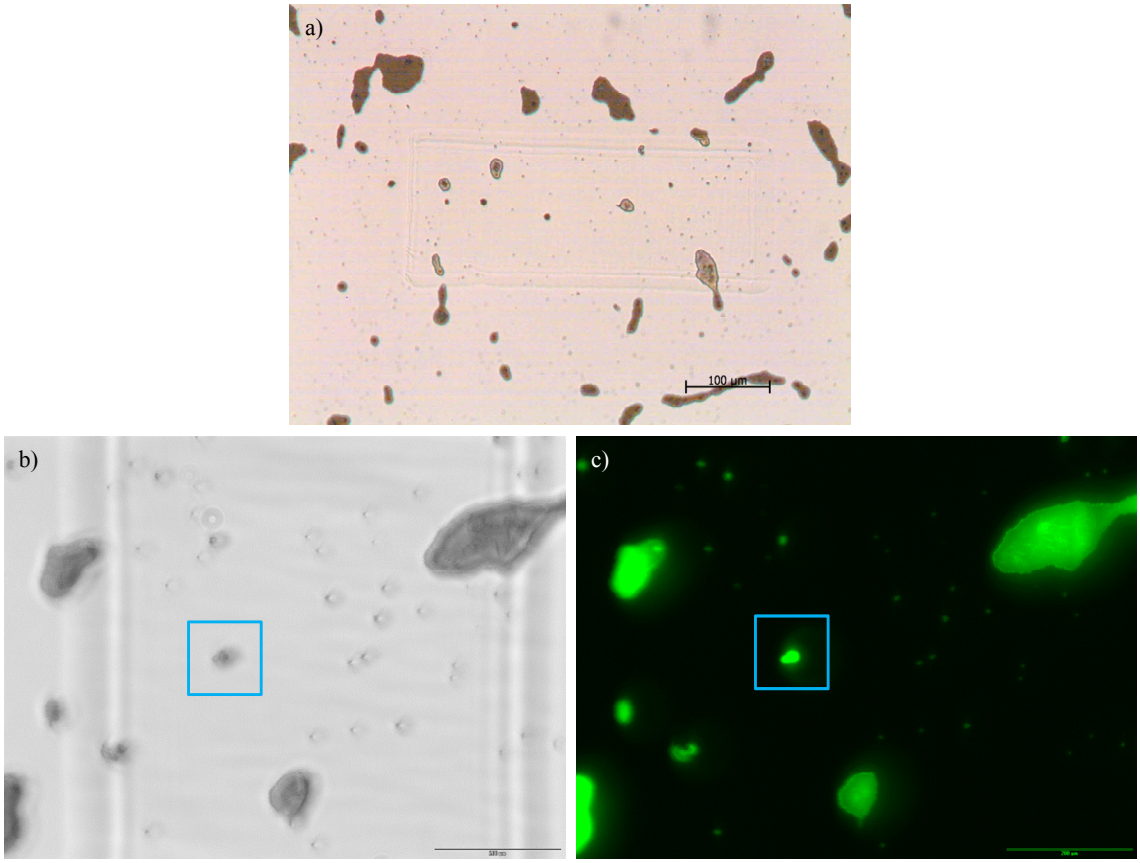

Figure 8.31: VUV 157nm F_2 laser irradiation of 960nm diameter fluorescent polystyrene particles at a laser fluence of 170mJcm^{-2} with 5 laser pulses at a pulse repetition rate of 2Hz - a) optical micrograph of ablation site, site depth ~210nm, b) phase contrast image using white light, integration time 5ms and c) fluorescence micrograph using 490nm radiation, integration time 200ms. Fluorescence micrograph is false-coloured to correspond with experimental observations.

Some of the composite structures exhibiting WGM resonances were found within this ablation site, and these are described in Figure 8.32, Figure 8.33 and Figure 8.34.

The pair of particles shown in Figure 8.32 are indicated in the phase contrast image and the fluorescence micrograph in Figure 8.31b) and Figure 8.31c). This pair of fluorescent polystyrene particles have diameters of ~ 2.5µm and 3.4µm respectively. The emission of the larger particle, when excited at a wavelength of 405nm is shown in Figure 8.32a), and the peak is centred around a wavelength of 560nm. The peaks on the spectrum caused by the WGM resonances are evident. As shown by the high angle SEM in Figure 8.32d), the top halves of these particles have reduced as a result of the laser irradiation, and the particles have heights of ~ 2.2µm and 3.1µm. Combined with the polymeric support structure, this composite structure has a maximum height of ~ 3.3µm.

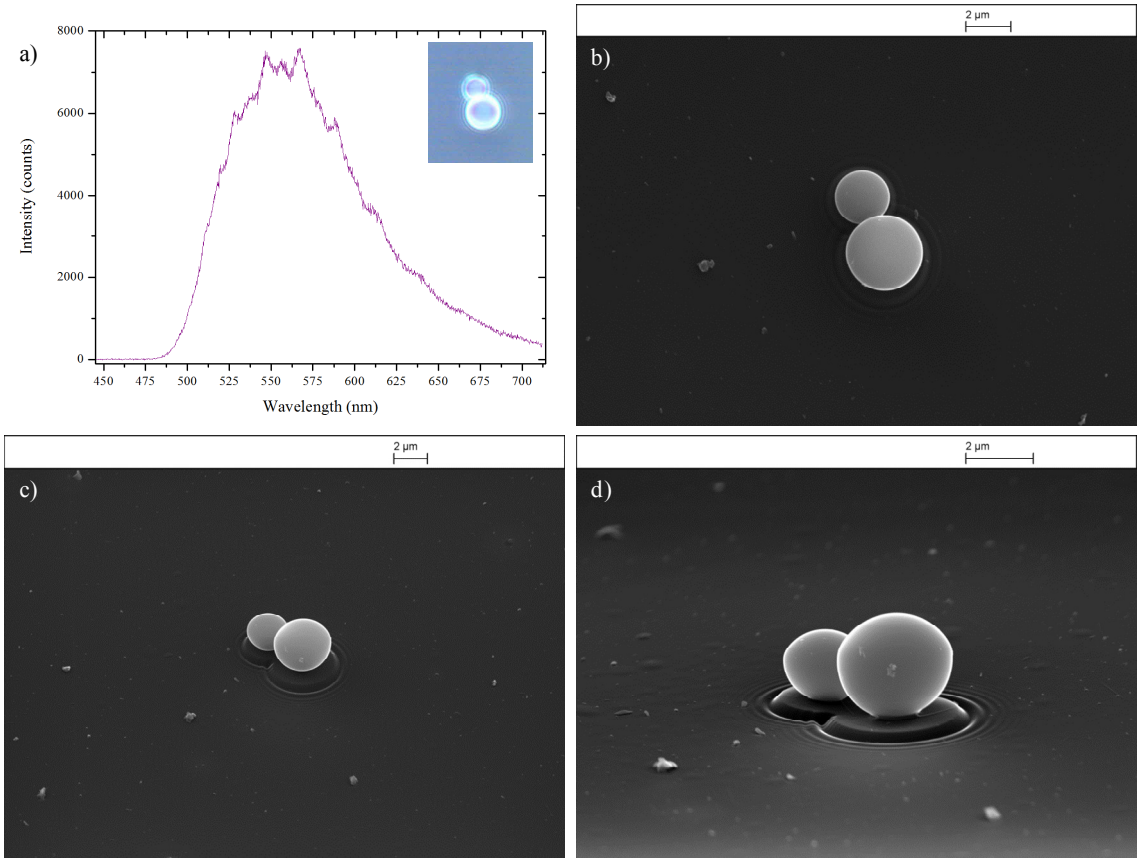

Figure 8.32: VUV 157nm F_2 laser irradiation of small fluorescent polystyrene particles at a laser fluence of 170mJcm^{-2} with 5 laser pulses at a pulse repetition rate of 2Hz - a) emission of composite structure excited at 405nm, inset - OM of structure, SEMs of structure viewed at b) 0°, c) 45° and d) 70°.

The structure shown in Figure 8.33 also exhibits a WGM effect on the emission spectrum, which is shown in Figure 8.33a). The structure was excited at a wavelength of 405nm, and the emission is centred around a wavelength of 563nm. The WGM peaks in fact show a double peak effect, which may be due to the splitting of the transverse electric (TE) and the transverse magnetic (TM) modes, with $\lambda_{TM} < \lambda_{TE}$ [147]. This resonant structure is different from the one discussed previously. That was comprised of a pair of similarly sized particles. This structure however is made of a large particle, diameter ~4.6µm, surrounded by a number of smaller particles of diameters ~1.1-1.9µm. The larger particle has reduced in vertical diameter slightly under the effect of the laser beam, with a total height of ~4.4µm as shown in the high angle SEMs in Figure 8.33c) and Figure 8.33d), which also show that the smaller particles have also been affected by the laser beam.

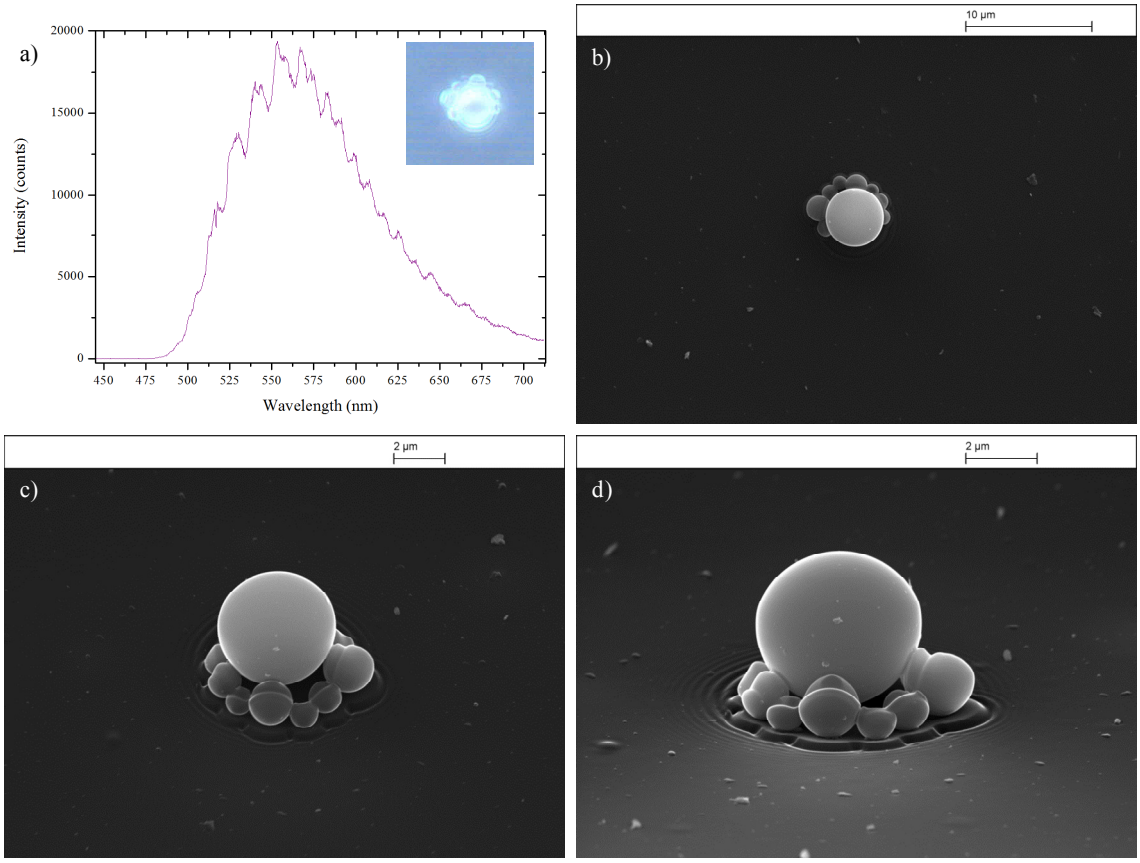

Figure 8.33: VUV 157nm F_2 laser irradiation of small fluorescent polystyrene particles at a laser fluence of 170mJcm^{-2} with 5 laser pulses at a pulse repetition rate of 2Hz - a) emission of composite structure excited at 405nm, inset - OM of structure, SEMs of structure viewed at b) 0°, c) 45° and d) 70°.

The resonant structure shown in Figure 8.34 is similar to that shown in Figure 8.33 - it is comprised of a larger particle of diameter ~4.6µm surrounded by smaller particles with diameters in the range ~1.4-2.4µm. These particles have also changed shape as a result of the heat generated from the incident laser beam. However, they are still fluorescent as demonstrated by the emission spectrum shown in Figure 8.34a). When excited at a wavelength of 405nm, the emission peak is centred around a wavelength of 553nm. The peaks caused by WGM resonances can be clearly seen on this spectrum, indicating that the large particle acts as a resonant cavity.

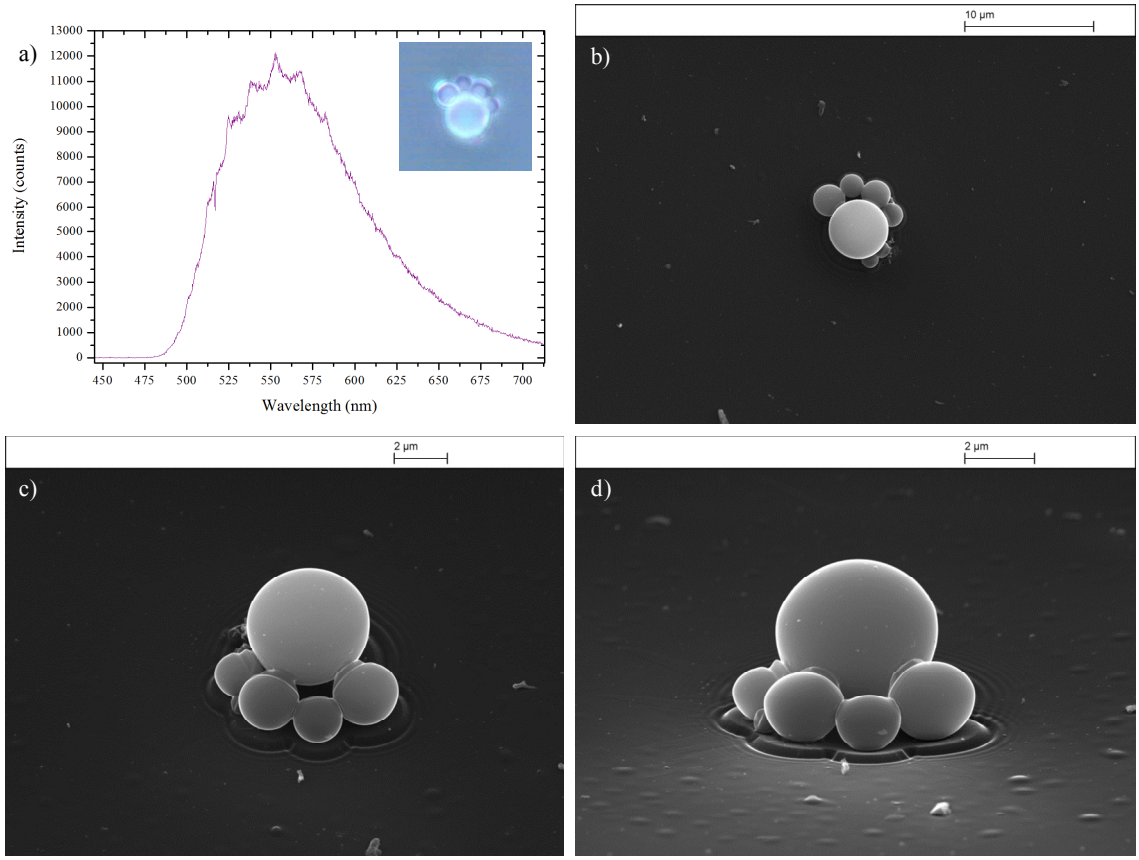

Figure 8.34: VUV 157nm F_2 laser irradiation of small fluorescent polystyrene particles at a laser fluence of 170mJcm^{-2} with 5 laser pulses at a pulse repetition rate of 2Hz - a) emission of composite structure excited at 405nm, inset - OM of structure, SEMs of structure viewed at b) 0°, c) 45° and d) 70°.

The larger polystyrene particle supported structure shown in Figure 8.35 exhibits a WGM effect, as shown by the peaks in the emission spectrum in Figure 8.35a). These supported particles have diameters of ~ 2.3µm and 5.2µm, and hence a size ratio of ~1:2.3. These particles are fluorescent, as indicated in Figure 8.21c). Similarly to previously discussed structures, as shown in the higher viewing angle SEM in Figure 8.35d) the smaller particle appears to have melted slightly and formed a bridge to the larger particle. The two particles have heights of ~ 2µm and 4.7µm respectively. The inset to Figure 8.35b) shows the confinement of the light around the inside edge of the larger fluorescent polystyrene particle - this is the Whispering Gallery Mode effect.

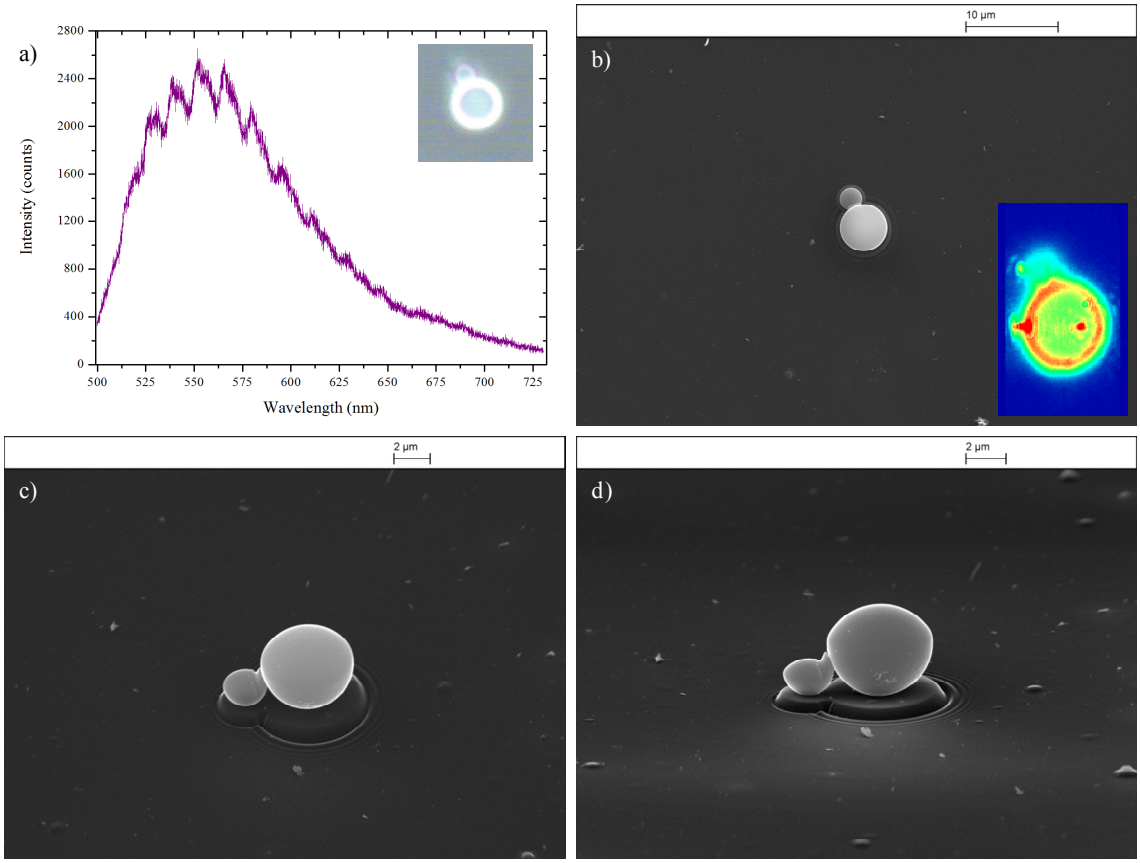

Figure 8.35: VUV 157nm F_2 laser irradiation of small fluorescent polystyrene particles at a laser fluence of 170mJcm^{-2} with 10 laser pulses at a pulse repetition rate of 2Hz - a) emission of composite structure excited at 405nm, inset - OM of structure, SEMs of structure viewed at b) 0°, c) 45° and d) 70°. Inset to b) shows the confinement of the light inside the large particle.

The ablation site shown in Figure 8.36a) was irradiated using 50 laser pulses (2Hz pulse repetition rate) at a laser fluence of 170mJcm^{-2}, resulting in a site depth of ~2µm. The feature indicated in the optical micrograph was investigated further using fluorescence microscopy and excited at a wavelength of 490nm, shown in Figure 8.36d). The emission from this feature was analysed when excited at a wavelength of 405nm, and the spectrum is shown in Figure 8.36b). The characteristic WGM peaks can be seen on this spectrum, although they are not as clearly defined as in the previous example. A possible reason for this can be seen in the SEMs in Figure 8.36e) and Figure 8.36f) - the large particle, diameter 10µm and height ~8.1µm, is both surrounded and supported by a collection of smaller particles. Most of these can be seen to have suffered a high degree of melting as a result of the laser beam which may have affected the interaction between the incident laser beam, the emitted fluorescence and hence the WGM capability of the large particle.

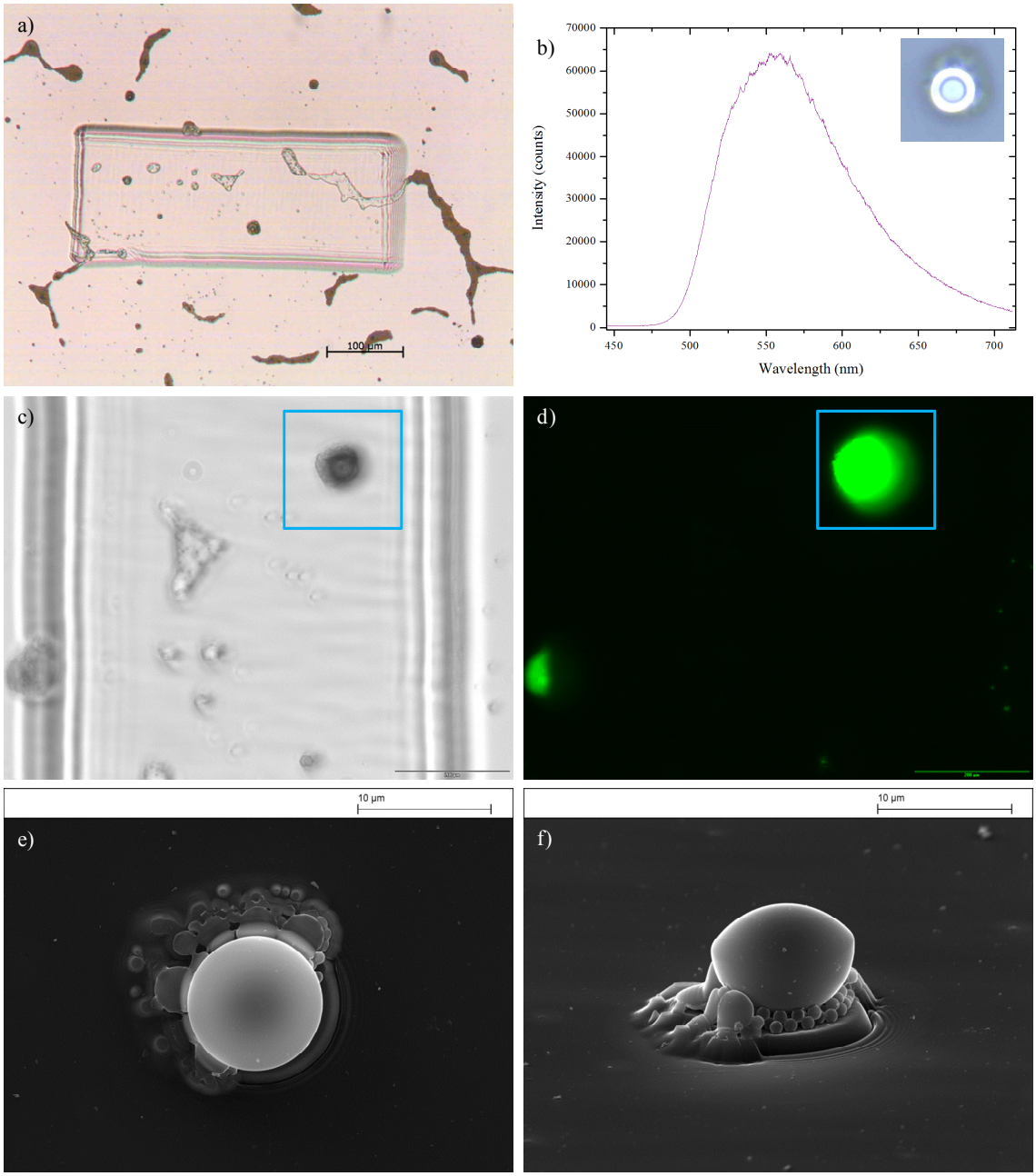

Figure 8.36: VUV 157nm F_2 laser irradiation of small fluorescent polystyrene particles at a laser fluence of 170mJcm^{-2} with 50 laser pulses at a pulse repetition rate of 2Hz - a) optical micrograph of ablation site, site depth ~2µm, b) emission of composite structure excited at 405nm, inset - OM of structure, c) phase contrast image using white light, integration time 5ms, d) fluorescence micrograph using 490nm radiation, integration time 200ms, SEMs viewed at e) 0° and f) 70°. Fluorescence micrograph is false-coloured to correspond with experimental observations.

The particles shown in Figure 8.37 were irradiated at an angle of 45° to the laser beam propagation direction, at a laser fluence of 75mJcm^{-2} with 20 laser pulses (2Hz pulse repetition rate). As a result, the site depth, and therefore particle support structure height is only ~230nm. The particles of interest are indicated in the optical micrograph, and also in the phase contrast image in Figure 8.37c) and the fluorescence micrograph in Figure 8.37d). In the fluorescence micrograph the sample is excited at a wavelength of 490nm. The emission spectrum shown in Figure 8.37b) shows the fluorescence when

the particles are excited at a wavelength of 405nm. The characteristic WGM resonances are fairly clear on this spectrum, and the SEMs shown in Figure 8.37e) and Figure 8.37f) support the WGM supported structure shown in Figure 8.35 - a pair of particles, one larger than the other. Using the top-view SEM in Figure 8.37e), the diameters of the laser-incident particle faces are ~ 7.4µm and 5.5µm. In the laser beam propagation direction the particles are aspherical, with heights of ~ 6.7µm and 4.7µm.

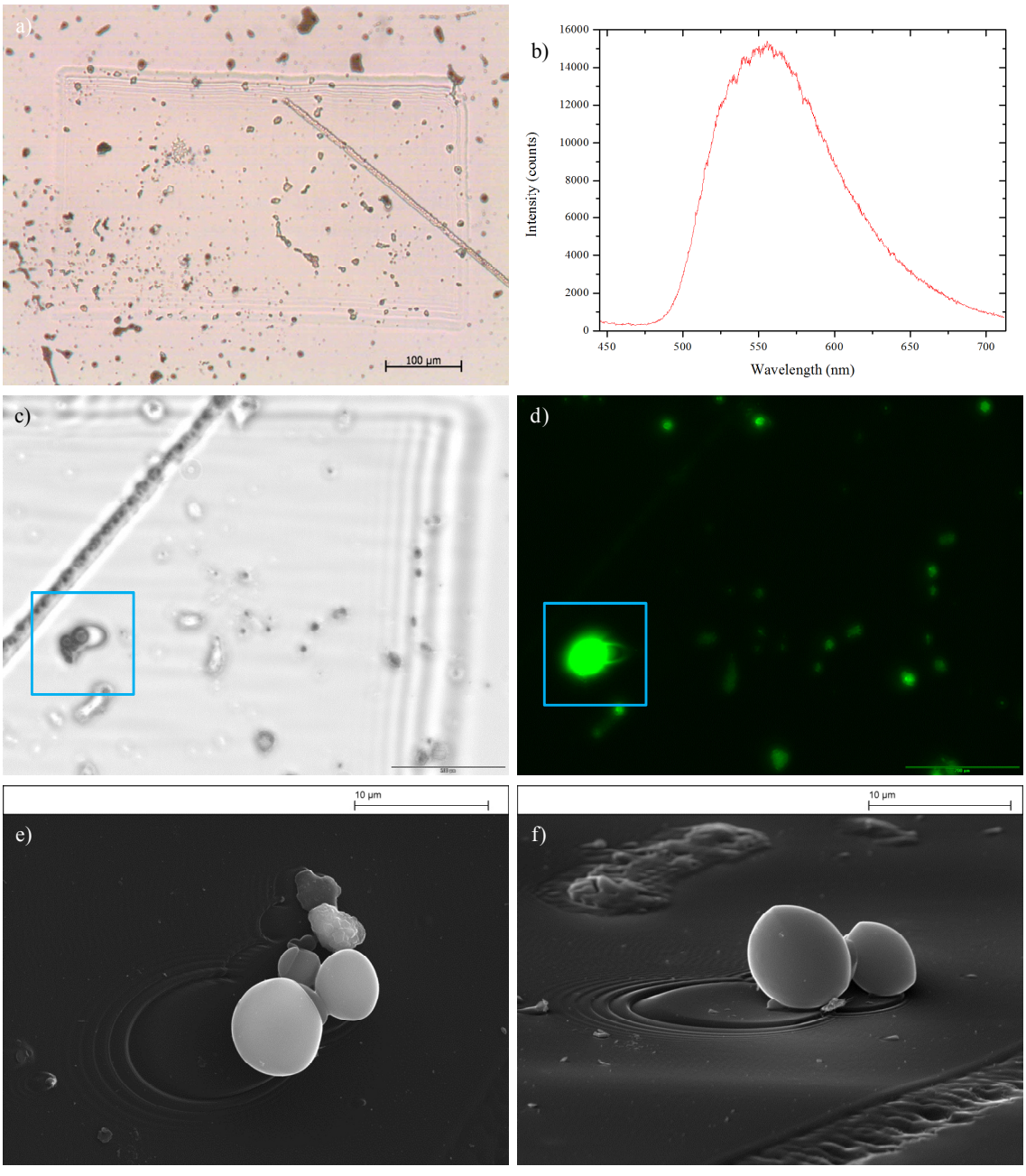

Figure 8.37: VUV 157nm F_2 laser angled irradiation of small fluorescent polystyrene particles at a laser fluence of 75mJcm^{-2} with 20 laser pulses at a pulse repetition rate of 2Hz - a) optical micrograph of ablation site, site depth ~230nm, b) emission of composite structure excited at 405nm, inset - OM of structure, c) phase contrast image using white light, integration time 5ms, d) fluorescence micrograph using 490nm radiation, integration time 200ms, SEMs viewed at e) 0° and f) 70°. Fluorescence micrograph is false-coloured to correspond with experimental observations.

The fluorescent polystyrene particles act as optical resonators, or cavities, and this is shown by the resonance peaks on the emission spectra of the supported particles. The wavelength spacing of these resonances is known as the *Free Spectral Range*, FSR, which can be used to estimate the radius, and hence diameter of the resonant cavity, or the particle using [77]

$$R = \frac{\lambda^2}{2\,\pi\,n\,F}$$

Equation 8.1

where R is the radius of the particle, λ is the wavelength of the light contained within the resonant cavity, n is the refractive index of the particle and F is the Free Spectral Range.

The Quality Factor, or Q Factor, describes the damping of a resonant system - a higher Q factor indicates that the resonance lasts for a longer period of time. With regards to WGM resonant cavities, the Q Factor effectively describes the number of times a photon passes around the cavity before it is lost by scattering or absorption. The Q Factor of a resonant cavity can be determined using the WGM peaks on the emission spectra shown here using [148, 158]

$$Q = \frac{\lambda}{\Delta\lambda}$$

Equation 8.2

where λ is the wavelength at which the resonance peak occurs and $\Delta\lambda$ is the bandwidth, or wavelength range, over which the resonance peak occurs. In the determination of the Q Factor here, the bandwidth at the resonance peak half maximum (FWHM) was used.

A narrower bandwidth, and hence a sharper resonance peak, are conducive to a higher Q Factor. However, for some applications a lower Q Factor is preferable as it leads to increased sensitivity to the WGMs. The sensitivity also increases as the radius of the resonator decreases.

The FSR and predicted particle diameter using Equation 8.1 where a value of n = 1.596 (at 555nm) [145] is used, for each of the resonant structures is shown in Table 8.1, along with the measurement of the particle diameter using the SEMs for each structure for comparison.

	FSR (nm)	Particle Diameter (μm) (to 1.d.p)		Q Factor (average)
		Predicted by FSR	Measured from SEM	
Figure 8.32	9.6	6.5	3.4	409
Figure 8.33	10.3	6.1	4.6	300
Figure 8.34	14.4	4.2	4.6	524
Figure 8.35	14.3	4.3	5.2	180
Figure 8.36	6.3	9.8	10	377

Table 8.1: Determination of the Free Spectral Range (FSR) using the emission spectra, estimated particle diameter compared with the measured value and Quality Factor (Q Factor) for the supported particles exhibiting Whispering Gallery Modes (WGMs).

For the angled structure shown in Figure 8.37, the peaks on the emission spectrum are not clear enough to measure the Quality Factor (Q Factor) of the resonances, however the FSR is ~7.5nm, which predicts a particle diameter of 8.2μm.

The observation that as the particle diameter increases the FSR increases corresponds to the literature [147].

The question arises of why only certain particles, and hence composite structures, exhibit Whispering Gallery Modes. Using the results presented for both categories of "emissive" and "WGM" structures, it is theorised that it is the combination of a larger fluorescent particle with one or more smaller particles that exhibit WGMs. It is suggested that the smaller particle(s) enable the incident exciting light to couple into the larger particle, exciting emission from the fluorescent dye, which the larger particle then confines, acting as a resonant cavity. The smaller particle offers guidance of the incident light within a small region, providing strong light confinement into the larger, resonant, particle. Whispering Gallery Modes can only be observed when the shape of the cavity is distorted slightly from the spherical; both the contact from the smaller particle(s) and the shape transformation by laser ablation may be the reason for the observation of the WGMs.

The ratio between the sizes of the smaller and the larger particle in the pair may also play a role in the ability of the larger particle to exhibit a WGM. For the examples shown here in Figure 8.32-Figure 8.37, the ratio between the particles sizes are between 1:1.9 and 1:2.3, suggesting that there may be a limiting region of particle size combinations that cause WGM resonances. The only other pair of particles shown here,

in Figure 8.24, has a pair size ratio of 1:2.8, and does not exhibit Whispering Gallery Mode resonances.

Section 8.3 - Conclusions

Silver-polystyrene core-shell particles have been fabricated by coating plain silver nanoparticles with alternating layers of PAH and PSS polyelectrolytes. Layers of different thicknesses were created by altering the number of pairs of polyelectrolyte layers added to the silver core particle. These silver-polystyrene core-shell particles were characterised by Transmission Electron Microscopy to confirm that the shells were of reasonably uniform thickness and that the shell thickness increased as expected from the method of fabrication. Measurement of the absorption of the core-shell particles showed that the plasmon resonance effect of the silver particle was still evident even with the presence of a dielectric outer layer.

These core-shell particles, with increasing shell thickness, were added to an active medium in order to investigate the effect of the particle on the emission of the medium. Rhodamine 6G was dissolved in DI water to a low concentration to allow for high fluorescent emission - this was determined experimentally using different concentrations of Rhodamine 6G in water and measuring the emission. Control samples of Rhodamine 6G in DI water, plain silver particles in Rhodamine 6G in DI water and plain polystyrene particles Rhodamine 6G in DI water were used for comparison. It was found that the plain polystyrene particles (of the same size as the plain silver particles) actually enhanced the emission of the Rhodamine 6G dye by ~3.3×. It was also found that the presence of plain silver particles reduces the emission of the Rhodamine 6G, most likely by scattering the incident exciting light before it can stimulate emission from the dye molecules or by quenching the emission from the dye molecules. However, this quenching effect is reduced by the presence of the increasing thickness polystyrene layers around the silver core particle.

Finite element method modelling was used to investigate the interaction of the silver-polystyrene core-shell particles with electromagnetic radiation. Similarly to plain silver particles, these core-shell particles enhance the electric field around them. When pairs of these core-shell particles are in close proximity the electric field enhancement couples and is exhibited as an intensity hotspot in the air gap between the particle pair. The intensity of this hotspot decreases as the separation distance between the particle pair increases. When the core-shell particle pair are in contact, increasing the shell thickness reduces the hotspot intensity.

Fluorescent polystyrene particles were fabricated *in-house* by doping plain polystyrene particles with Coumarin 7 dye. A liquid two-phase system was used in order for the dye to be absorbed into the particles. Fluorescence microscopy and photoluminescence measurements were used to confirm that the doped particles were in fact fluorescent.

For the laser ablation experiments, larger diameter fluorescent particles were purchased rather than being fabricated *in-house*. These particles were dispersed onto CR-39 polymer substrates and irradiated at a wavelength of 157nm using a VUV F_2 molecular gas laser. The fluorescent polystyrene particles shield the underlying polymeric substrate, resulting in the fabrication of composite structures. As low incident laser fluences and pulse numbers were used in an attempt to minimise damage to the structure of the particles and the fluorescent molecules, the polymeric structures were not very high and acted more as support structures to raise the fluorescent particle slightly above the main substrate surface. Fluorescence microscopy was used to confirm that the laser irradiated particles were still fluorescent, although there was found to be a laser pulse number threshold limit for this.

The polystyrene particles were found to undergo a shape transformation as a result of mass transfer from the increase in particle temperature due to the energy from the incident laser beam.

The emission of the laser irradiated supported fluorescent particles was measured, and it was observed that the emission of the fluorescent particles after laser irradiation was greater than before irradiation. This may be due to decreased absorption of the emitted light as the distance from the substrate increases, and the removal of particle material may expose more of the contained fluorescent dye.

The laser irradiated fluorescent polystyrene particles seem to emit their excited radiation in all directions, making them potentially useful for miniature multi-directional light sources as well as WGM sensor devices. Optical cavities have already found applications as microscopic laser sources [149]. For usable light sources and optical antennas the emitter/detector needs to be similar in size or preferably smaller than the device it is to be used upon. Small scale supported fluorescent resonant cavities could be easily fabricated using the VUV 157nm F_2 laser due to its proven excellent resolution.

Some of the laser irradiated supported fluorescent particles exhibited Whispering Gallery Mode resonances. It is suggested that a number of factors contribute to this

effect - the shape change of the particles due to laser irradiation and the combination of a larger and a smaller particle of a particular size ratio. Pairs of spherical polystyrene particles have already been demonstrated to exhibit WGMs [160]. Measurements of the FSR of the WGM resonances were used to predict the diameter of the resonant particle (cavity) and these corresponded well with those measured experimentally.

Calculations of the Q Factors for the laser fabricated resonant cavities gave values in the range 180-524. Q Factors have been demonstrated to exceed 10^8 for sub-millimeter silica spheres and toroids [148], and 10^{10} for quartz spheres with diameters of several tens of microns [160], however a high Q value results in low sensitivity in applications. Polymeric particles with low Q values (typically $\leq$ 10,000), and hence higher sensitivity are being investigated as a substitute to glass particles [148].

Deviations have been observed in the WGM features in particles smaller than 7.6μm, and at present the particle size limit for use in WGM devices appears to be around 8μm. To date the smallest particles for which the excitation of WGMs has been reported are dye-doped polystyrene particles with a diameter of 2μm [149, 160].

Polystyrene particles of diameter 10μm doped with Nile Red have demonstrated Q Factors in the range 500-1000, which is typical for particles of this size [148]. The Q factors determined from the experiments presented here are comparable to these reported values, showing that there seems to be little effect on emission, resonances and hence sensitivity when the fluorescent particles are irradiated with a VUV F_2 laser emitting at 157nm and raised above the main substrate on a supporting polymeric structure.

Chapter 9: Directions for Future Work

The results presented here have many potential applications. The main challenge facing the usability of the composite conical and linear prismatic structures, seeded both by dielectric materials and metals, is the ability to control the position of the seeding particle and hence the structure itself.

There are many methods that are potentially capable of leading to this, for example Dielectrophoresis and Dip-Pen Nanolithography, DPN.

Dielectrophoresis enables cylindrical particles, such as the silicon carbide whiskers and the silver nanowires to be arranged parallel to each other by the application of an electric field.

Preliminary experiments, shown in Figure 9.1, using silicon carbide whiskers show that this method, with some optimisation, could be used effectively to fabricate aligned arrays of whiskers and nanowires. A CR-39 polymer slide was coated with a gold layer ~30nm thick before a channel was laser ablated through the gold and electrodes connected on each side of the slide. The silicon carbide whiskers were dispersed in deionised water and deposited onto the channel, and an electric field was applied. This caused the silicon carbide whiskers to line up perpendicular to the channel, bridging the gap between the two gold-plated sides.

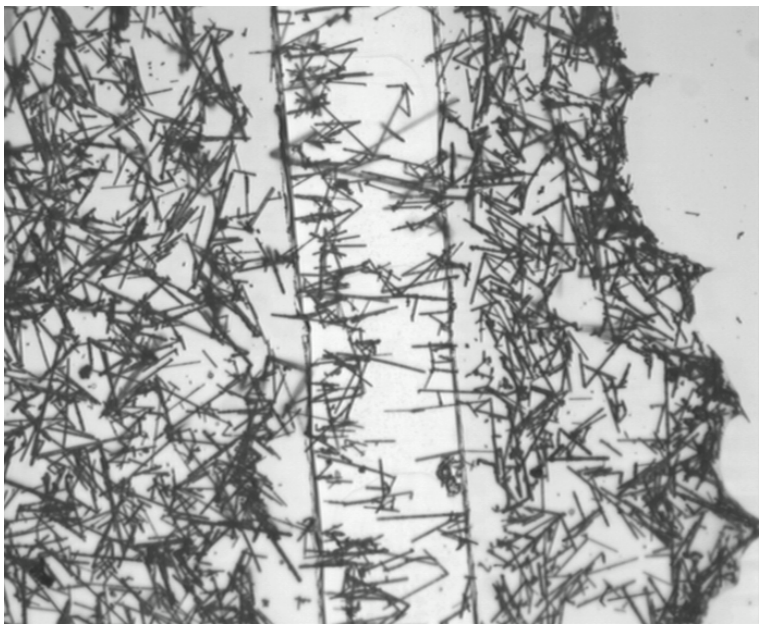

Figure 9.1: Methods for arranging nanoparticles - Dielectrophoretic alignment of silicon carbide whiskers.

The Dip-Pen Nanolithography Technique uses a modified AFM tip to deposit an "ink" onto a substrate – this ink is typically made up of nanoparticles dispersed in solution.

This method has a high level of control over the position of the droplets of the nanoparticle solution over a wide area. Examples of dot and line arrays of silver particles deposited on a glass substrate are shown in Figure 9.2a) and Figure 9.2b).

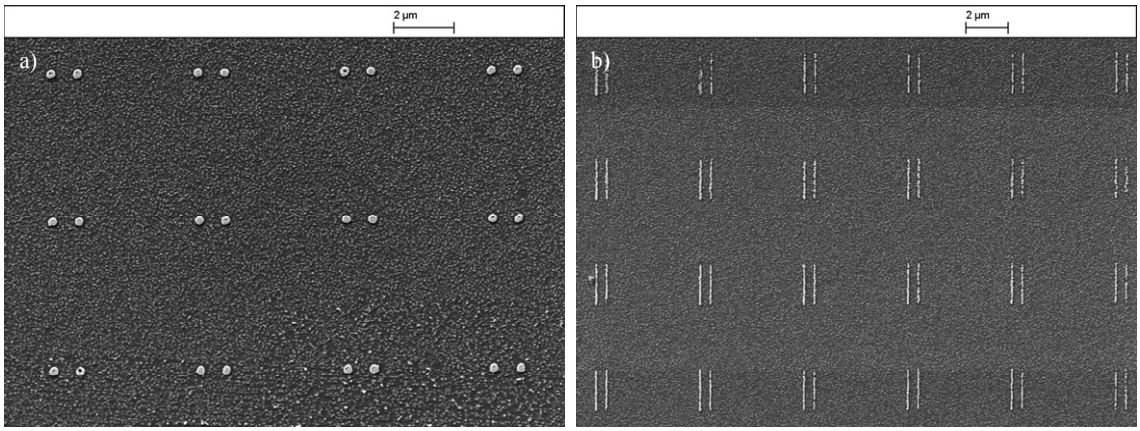

Figure 9.2: Methods for arranging nanoparticles - DPN arrangement of pairs of a) silver dots and b) lines of silver particles. DPN samples courtesy of NanoInk Inc. Skokie IL, USA.

Plasmonic particles and sensor devices have many applications in biological, chemical and medical sensing – indeed many examples have already proven effective in cancer detection and treatment. If the silver-polymer conical and linear prismatic structures can be shown to exhibit plasmonic effects, and their spatial positioning can be controlled, they could very easily be incorporated into sensor devices for use in these fields.

The shape transformation demonstrated by the silver nanowires in Chapter 7 is dependent on many factors, including the initial size of the nanowire, the laser fluence and number of applied laser pulses, and the thermal properties of the particle and the substrate. The irradiating wavelength could be altered to determine the role that wavelength plays, for example in plasmon excitation. Different length wires could be used to investigate if the location of the initial melt point is affected by wire length. When these factors are fully understood, it would be possible to control the melting of the nanowires into spherical particles, or to a point in between the two states.

Fluorescent nanoparticles, particularly those displaying Whispering Gallery Mode resonances also have many applications, for example as miniature light sources, nanolasers and biological and chemical sensors. While the fluorescent polystyrene particles, after they have been irradiated with the VUV F_2 laser emitting at a wavelength of 157nm and are supported by a polymeric plinth structure, are still capable of

fluorescent emission and exhibiting WGM resonances, the particle itself is greatly affected by the incident laser beam.

Silica particles are much more resilient to the heating effects of the 157nm laser radiation and do not suffer the same shape transformation that the polystyrene particles demonstrated in Chapters 7 and 8, as shown by the silica-CR-39 polymer composite structure in Figure 9.3.

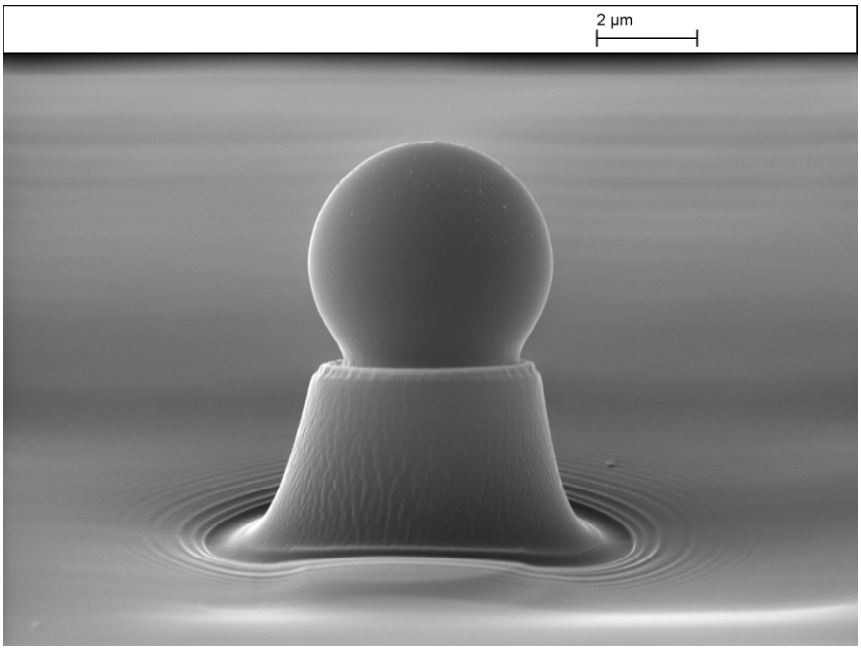

Figure 9.3: Silica particle on CR-39 polymer substrate irradiated with the VUV F_2 laser at a wavelength of 157nm at a laser fluence of 155mJcm^{-2} with 50 laser pulses at a pulse repetition rate of 2Hz.

While measurements presented in Chapter 8 suggest that the emission of the fluorescent polystyrene particles may increase after laser irradiation, the effect of the presence of both the polymeric substrate and the particle support structure could be investigated in order to optimise the emission from the supported fluorescent particles.

Thesis Conclusions

The results presented in this thesis are concerned with the interaction between small particles and 157nm radiation. The particles were supported on polymeric substrates and were made of a variety of materials, of different shapes and sizes, in order to cover a wide range of interaction effects.

Firstly, the VUV 157nm F_2 laser system that was used in these experiments was introduced. The polymer substrate materials were investigated and their relevant properties determined, including laser ablation threshold fluence, optical absorption coefficient and optical absorption depth.

Then, silica spherical particles were irradiated using the F_2 laser. As these particles are transparent to the 157nm laser radiation, they acted as lenses and focussed the incident laser radiation into a hotspot located at the base of the particle, towards the boundary with the polymeric substrate. Finite Element Method (FEM) modelling was used for numerical investigation into this hotspot effect for silica particles of 500nm and 1µm diameters. Calculations estimated that the focussing effect enhanced the intensity of the electric field by a factor of ~126. When irradiated with only one laser pulse, the lens effect resulted in the fabrication of a small dimple on the surface of the polymer substrate. The dimples were ~150-220nm in diameter, depending on the size of the silica particle, and had depths of ~80nm which was determined by inverse moulding the dimples using PDMS. When irradiated with higher laser pulse numbers, the dimple effect is seen to be smoothed out until a flat surface remains. When irradiated with one laser pulse the silica particle was ejected from the substrate surface. This suggested that the force induced by the laser beam on the particle and substrate was sufficient to overcome the attraction force between the particle and the substrate, which was calculated for a range of particle sizes and materials. Futher FEM modelling was carried out to determine the dependence of the focussing effect of the small particle on both the incident wavelength and the particle material. To the author's knowledge, this is the first time dimple structures have been fabricated by the irradiation of transparent particles at a wavelength of 157nm.

Next, polystyrene spherical particles that were opaque to the 157nm laser radiation were investigated. In contrast to the transparent particles, these opaque particles shielded the

underlying substrate material while the material around the particle was ablated away. This process resulted in the fabrication of a polymeric conical support structure with the original seeding particle sitting at the apex. A fringe pattern was formed around the base of the composite conical structure which arose from the interaction between the incident laser radiation, the particle, the substrate and the support structure wall. The polystyrene particles were irradiated normal to and at 45° to the direction of laser beam propagation to fabricate both upright and oblique composite conical structures. The resolution capabilities of the laser photons to fabricate smaller structures was tested, and it was found that particles of a diameter of ~100nm were easily resolved by the incident radiation. The height of the composite conical structures can be finely controlled by varying the laser fluence and the number of applied laser pulses.

The shape of the polymeric support structure is dependent on the shape of the initial seeding particle. Previously, opaque spherical particles were shown to fabricate conical structures, and so opaque cylindrical particles (known as wires, whiskers and rods) made from silicon carbide were then irradiated in order to form analogous linear prismatic structures. Similarly to the conical structures, the seeding whisker remained attached to the top of the polymeric support structure, which was confirmed using EDX measurements, and an interference fringe pattern was formed around the base. Many of the SiC whiskers had rough surface topography, and this was translated into the walls of the polymer support structure as undulations.

Silver particles that were also opaque to the 157nm laser radiation were irradiated. Both quasi-spherical and cylindrical particles were irradiated to form composite conical and linear prismatic structures. The fringe pattern around the base of the structures was again evident and shown to be highly dependent on the seeding particle shape. EDX measurements were used to confirm that the silver particles remained attached to the apex of the polymeric support structure. Finite Element Method modelling was used to investigate the field enhancing effects of single particles and dimers both isolated and supported by a polymeric substrate. Dimers, or pairs of particles, exhibit coupling of the electric field as a high intensity hotspot in the gap between the two particles. Silver nanowires, composite conical structures and composite linear prismatic structures were also modelled. Experimentally, the silver particles themselves exhibited plasmon resonances. If the composite conical and linear prismatic structures could be shown to also exhibit a plasmonic effect, these types of structures could find use in biological and chemical sensor devices.

During the laser irradiation experiments, the polystyrene spherical particles and the silver spherical and cylindrical particles were seen to undergo shape and size transformations as a result of the interaction with the laser radiation. However, the silicon carbide whiskers did not visibly appear to undergo these transformations. It was postulated that these transformations occurred as a result of the particles absorbing energy from the laser photons, which in turn caused a heating effect in the particles. Heating and melting models were discussed in relation to the different particles, and calculations of the temperatures of the particles during laser irradiation were carried out. It was determined that the incident laser energy was sufficient to cause significant melting and/or evaporation of the polystyrene and silver particles, and result in the observed shape and size transformations.

Silver-polystyrene core-shell particles were fabricated *in house* and incorporated into an active medium to investigate the effect of the presence of the particles on the emission properties of the active medium. Small fluorescent polystyrene particles were also fabricated *in house* by doping plain particles with Coumarin 7 dye.

Larger fluorescent polystyrene particles were irradiated with the F_2 laser to fabricate active composite supported structures. The particles were shown to be fluorescent even after irradiation and a shape change that was dependent on the laser irradiation orientation. Some of the irradiated particles exhibited a Whispering Gallery Mode effect, shown by a characteristic “spiking” effect on the emission spectrum of the fluorescent particle. These WGM structures were determined to have low Quality Factors (Q Factors), which potentially makes them ideal for WGM sensing applications. To the author's knowledge, this is the first time WGM supported structures have been fabricated by laser irradiation of spherical fluorescent particles at a wavelength of 157nm.

To continue the work presented in this thesis, the areas to focus on in more detail include the challenges faced in arranging the different particles into ordered arrays, and preliminary experiments utilising the methods with potential, i.e. Dielectrophoresis and Dip-Pen Nanolithography have already taken place. This is particularly important for investigating the potential plasmonic properties of the composite conical and linear prismatic metal-polymer structures and their use in wide-ranging sensing and detection applications.

As the method of fabrication for the composite conical and linear prismatic structures using opaque spherical and cylindrical particles is well established, the main focus for any subsequent research following on from this thesis should clearly be the application of this production method to the fabrication of light-emitting structures using fluorescent seeding particles. While the influence of the laser irradiation and the effect of raising the fluorescent particle above the main substrate on a polymeric support structure does require further nvestigation, the potential applications from the work presented in Chapter 8 here are clear. These types of structures, particularly those exhibiting Whispering Gallery Modes, have already shown potential in high-sensitivity detection applications.

Conferences

- CLEO 2009, Munich - poster presentation - *Ablation of pristine and radiation exposed CR-39 polymer using a 157nm laser*, S. Cockcroft, P.E. Dyer, C. Moore, C.D. Walton & R. Zakaria.

- COLA 2009, Singapore - poster presentation - *VUV 157nm Laser Ablation of Nano-Composite Structures*, S. Cockcroft, C.D. Walton & R. Zakaria.

- HPLA 2012, Santa Fe - poster presentation - *VUV 157nm Laser Ablation of Spherical Particles and the Realisation of Whispering Gallery Mode Optical Antenna Structures*, S. Cockcroft, W.J. Metheringham & C.D. Walton.

Publications

- S. Cockcroft, C.D. Walton and R. Zakaria, *VUV 157nm laser ablation of composite* structures, Applied Physics A: Materials Science & Processing, Volume 101, pages 379-383, 2010.

- C.D. Walton and S. Cockcroft, *Formation of Micro and Nano Structures Using VUV 157nm Laser Radiation*, International Symposium on High Power Laser Ablation 2010, AIP Conference Proceedings, Volume 1278, pages 262-270, 2010.

- C.D. Walton, S. Cockcroft and W.J. Metheringham, *VUV 157nm Laser Ablation of Spherical Particles and Modelling of Whispering Gallery Mode Optical Antenna Structures*, International Symposium on High Power Laser Ablation 2012, AIP Conference Proceedings, Volume 1464, pages 200-208, 2012.

References

[1] D. Basting, G. Marowsky, Excimer Laser Technology, Springer, Berlin, 2005.

[2] R.M. Tennent, Science Data Book, Oliver & Boyd, Harlow, 2004.

[3] W.T. Silfvast, Laser Fundamentals, Second Edition ed., Cambridge University Press, Cambridge, 2004.

[4] R. Srinivasan, W.J. Leigh, Ablative Photodecomposition: Action of Far-Ultraviolet (193nm) Laser Radiation on Poly(ethylene terephthalate) Films, Journal of the American Chemical Society, 104 (1982).

[5] R. Srinivasan, V. Mayne-Banton, Self-developing photoetching of poly(ethylene terephthalate) films by far-ultraviolet excimer laser radiation, Applied Physics Letters, 41 (1982) 576.

[6] P.E. Dyer, Excimer laser polymer ablation: twenty years on, Applied Physics A: Materials Science & Processing, 77 (2003) 167-173.

[7] P.E. Dyer, Laser Ablation of Polymers, in: I.W. Boyd, R.B. Jackman (Eds.) Photochemical Processing of Electronic Materials, Academic Press, London, 1992.

[8] W.W. Duley, UV Lasers: effects and applications in materials science, Cambridge University Press, Cambridge, 1996.

[9] P.E. Dyer, J. Sidhu, Direct-etching studies of polymer films using a 157-nm F_2 laser, Journal of the Optical Society of America B, 3 (1986) 792-795.

[10] P.E. Dyer, C.D. Walton, R. Zakaria, Interference effects in 157nm laser ablated cones in polycarbonate and application to spatial coherence measurement, Applied Physics A: Materials Science & Processing, 95 (2009) 319-323.

[11] S. Küper, J. Brannon, K. Brannon, Threshold Behaviour in Polyimide Photoablation: Single-Shot Rate Measurements and Surface-Temperature Modeling, Applied Physics A: Solids and Surfaces, 56 (1993) 43-50.

[12] P. Gruenewald, J. Cashmore, J. Fieret, M. Gower, High-resolution 157nm laser micromachining of polymers, Proceedings of SPIE, 4274 (2001) 158.

[13] F. Haehnel, R. Bertam, G. Reisse, R. Boettcher, S. Weissmantel, Production of microstructures in wide-band-gap and organic materials using pulsed laser ablation at 157nm wavelength, Applied Physics A: Materials Science & Processing, 101 (2010) 491-495.

[14] G. Lalev, P. Petkov, N. Sykes, H. Hirshy, V. Velkova, S. Dimov, D.A. Barrow, Fabrication and validation of fused silica NIL templates incorporating different length scale features, Microelectronic Engineering, 86 (2009) 705-708.

[15] S. Lazare, P.D. Hoh, J.M. Baker, R. Srinivasan, Controlled Modification of Organic Polymer Surfaces by Continuous Wave Far-Ultraviolet (185nm) and Pulsed-Laser (193nm) Radiation: XPS Studies, Journal of the American Chemical Society, 106 (1984) 4288-4290.

[16] S. Lazare, R. Srinivasan, Surface Properties of Poly(ethylene terephthalate) Films Modified by Far-Ultraviolet Radiation at 193nm (Laser) and 185nm (Low Intensity), Journal of Physical Chemistry, 90 (1986) 2124-2131.

[17] P.E. Dyer, S.D. Jenkins, J. Sidhu, Development and origin of conical structures on XeCl laser ablated polyimide, Applied Physics Letters, 49 (1986) 453-455.

[18] P.E. Dyer, S.D. Jenkins, J. Sidhu, Novel method for measuring excimer laser ablation thresholds of polymers, Applied Physics Letters, 52 (1988) 1800-1882.

[19] D.J. Krajnovich, J.E. Vázquez, Formation of "intrinsic" surface defects during 248nm photoablation of polyimide, Journal of Applied Physics, 73 (1993) 3001-3008.

[20] J.-F. Silvain, H. Niino, S. Ono, S. Nakaoka, A. Yabe, Surface modification of elastomer/carbon composite by Nd^{+}:YAG laser and KrF eximer laser ablation, Applied Surface Science, 141 (1999) 25-34.

[21] R. Zakaria, P.E. Dyer, Cone evolution on VUV laser ablated polymers, Applied Physics A: Materials Science & Processing, 101 (2010) 13-18.

[22] S.D. Jenkins, Modification of polymer surfaces using excimer lasers, in, University of Hull, 1989.

[23] M.H. Hong, S.M. Huang, B.S. Luk'yanchuk, T.C. Chong, Laser assisted surface nanopatterning, Sensors and Actuators A, 108 (2003) 69-74.

[24] U.C. Fischer, H.P. Zingsheim, Submicroscopic pattern replication with visible light, Journal of Vacuum Science and Technology, 19 (1981) 881.

[25] C.L. Haynes, R.P. Van Duyne, Nanosphere Lithography: A Versatile Nanofabrication Tool for Studies of Size-Dependent Nanoparticle Optics, Journal of Physical Chemistry B, 105 (2001) 5599-5611.

[26] Y. Zhou, M.-H. Hong, Y.-H.J. Fuh, L. Lu, L.S. Tan, B.S. Luk'yanchuk, Light Irradiation through Small Particles and Its Applications for Surface Nanostructuring in Near Field, Chinese Physics Letters, 24 (2007) 2947-2950.

[27] Z.B. Wang, W. Guo, A. Pena, D.J. Whitehead, B.S. Luk'yanchuk, L. Li, Z. Liu, Y. Zhou, M.H. Hong, Laser micro/nano fabrication in glass with tunable-focus particle lens array, Optics Express, 16 (2008) 19706-19711.

[28] T. Sakai, T. Miyanishi, N. Nedyalkov, Y. Nishizawa, M. Obara, Nano-dimple processing of silicon surfaces by femtosecond laser irradiation with dielectric particle templates in the Mie scattering domain, Journal of Physics D: Applied Physics, 42 (2009) 025502.

[29] C.F. Bohren, D.R. Huffman, Absorption and Scattering of Light by Small Particles, Wiley-VCH, Weinheim, Germany, 2004.

[30] B.S. Luk'yanchuk, Y.W. Zheng, Y.F. Lu, Basic physical problems related to dry laser cleaning, RIKEN Review No. 43: Focused on 2nd International Symposium on Laser Precision Microfabrication, (2002) 28-34.

[31] M.J. Fagan, Finite Element Analysis: Theory and Practice, Pearson Education, Harlow, Essex, 1992.

[32] COMSOL, RF Module User's Guide, COMSOL, Burlington, MA, 2008.

[33] M.W. Knight, Y. Wu, J.B. Lassiter, P. Nordlander, N.J. Halas, Substrates Matter: Influence of an Adjacent Dielectric on an Individual Plasmonic Nanoparticle, Nanoletters, 9 (2009) 2188-2192.

[34] A. Dmitriev, C. Hägglund, S. Chen, H. Fredriksson, T. Pakizeh, M. Käll, D.S. Sutherland, Enhanced Nanoplasmonic Optical Sensors with Reduced Substrate Effect, Nanoletters, 8 (2008) 3893-3898.

[35] Z. Jian, Z. Jun-Wu, L. Jian-Jun, Location-Dependent Local Field Enhancement Along the Surface of the Metal-Dielectric Core-Shell Nanostructure, Plasmonics, 5 (2010) 311-318.

[36] T. Vo-Dinh, A. Dhawan, S.J. Norton, C.G. Khoury, H.-N. Wang, V. Misra, M.D. Gerhold, Plasmonic Nanoparticles and Nanowires: Design, Fabrication and Application in Sensing, Journal of Physical Chemistry C, 114 (2010) 7480-7488.

[37] C.G. Khoury, S.J. Norton, T. Vo-Dinh, Plasmonics of 3-D Nanoshell Dimers Using Multipole Expansion and Finite Element Method, ACSNano, 3 (2009) 2776-2788.

[38] C.G. Khoury, S.J. Norton, T. Vo-Dinh, Investigating the plasmonics of a dipole-excited silver nanoshell: Mie theory versus finite element method, Nanotechnology, 21 (2010) 315203.

[39] H.A. Pohl, The Motion and Precipitation of Suspensoids in Divergent Electric Fields, Journal of Applied Physics, 22 (1915) 869-871.

[40] S.-Y. Lee, T.-H. Kim, D.-I. Suh, N.-K. Cho, H.-K. Seong, S.-W. Jung, H.-J. Choi, S.-K. Lee, A study of dielectrically aligned gallium nitride nanowires in metal electrodes and their electrical properties, Chemical Physics Letters, 427 (2006) 107-112.

[41] A.D. Wissner-Gross, Dielectrophoretic reconfiguration of nanowire interconnects, Nanotechnology, 17 (2006) 4986-4990.

[42] J. Suehiro, Application of dielectrophoresis to fabrication of nanomaterial-based sensors, in: IMEKO International Measurement Confederation 15th Symposium on Novelties in Electrical Measurements and Instrumentation, Iasi, Romania, 2007.

[43] A. Ashkin, J.M. Dziedzic, J.E. Bjorkholm, S. Chu, Observation of a single-beam gradient force optical trap for dielectric particles, Optics Letters, 11 (1986) 288-290.

[44] K. Sendur, W. Challener, O. Mryasov, Interaction of spherical nanoparticles with a highly focused beam of light, Optics Express, 16 (2008) 2874-2886.

[45] R. Fardel, E. McLeod, Y.-C. Tsai, C.B. Arnold, Nanoscale ablation through optically trapped microspheres, Applied Physics A: Materials Science & Processing, 101 (2010) 41-46.

[46] H. Zhang, DPN-Generated Nanostructures Made of Gold, Silver, and Palladium, Chemistry of Materials, 16 (2004) 1480-1484.

[47] H.-T. Wang, O.A. Nafday, J.R. Haaheim, E. Tavaarwerk, N.A. Amro, R.G. Sanedrin, C.-Y. Chang, F. Ren, S.J. Pearton, Toward conductive traces: Dip Pen Nanolithography of silver nanoparticle-based inks, Applied Physics Letters, 93 (2008) 143105.

[48] M. Ranjan, T.W.H. Oates, S. Facsko, W. Möller, Optical properties of silver nanowire arrays with 35nm periodicity, Optics Letters, 35 (2010) 2576-2578.

[49] B.J. Wiley, S.H. Im, Z.-Y. Li, J. McLellan, A. Siekkinen, Y. Xia, Maneuvering the Surface Plasmon Resonance of Silver Nanostructures through Shape-Controlled Synthesis, Journal of Physical Chemistry B, 110 (2006) 15666-15675.

[50] S. Ye, Y. Lu, Optical Properties of Ag@Polypyrrole Nanoparticles Calculated by Mie Theory, Journal of Physical Chemistry C, 112 (2008) 8767-8772.

[51] V.V. Hardikar, E. Matijević, Coating of Nanosize Silver Particles with Silica, Journal of Colloid and Interface Science, 221 (2000) 133-136.

[52] M.W. Knight, N.J. Halas, Nanoshells to nanoeggs to nanocups: optical properties of reduced symmetry core-shell nanoparticles beyond the quasistatic limit, New Journal of Physics, 10 (2008) 105006.105001-105006.105010.

[53] G. Peng, U. Tisch, O. Adams, M. Hakin, N. Shehada, Y.Y. Broza, S. Billan, R. Abdah-Bortnyak, A. Kuten, H. Haick, Diagnosing lung cancer in exhaled breath using gold nanoparticles, Nature Nanotechnology, 4 (2009) 669-673.

[54] A.J. Haes, L. Chang, W.L. Klein, R.P. Van Duyne, Detection of a Biomarker for Alzheimer's Disease from Synthetic and CLinical Samples Using a Nanoscale Optical Biosensor, Journal of the American Chemical Society, 127 (2005) 2264-2271.

[55] P.K. Jain, I.H. El-Sayed, M.A. El-Sayed, Au nanoparticles target cancer, nanotoday, 2 (2007) 18-29.

[56] A. Burns, H. Ow, U. Wiesner, Fluorescent core-shell silica nanoparticles: towards "Lab on a Particle" architectures for nanobiotechnology, Chemical Society Reviews, 35 (2006) 1028-1042.

[57] C. Loo, A. Lin, L.R. Hirsch, M.-H. Lee, J. Barton, N.J. Halas, J.L. West, R. Drezek, Nanoshell-Enabled Photonics-Based Imaging and Therapy of Cancer, Technology in Cancer Research & Treatment, 3 (2004) 33-40.

[58] L.R. Hirsch, R.J. Stafford, J.A. Bankson, S.R. Sershen, B. Rivera, R.E. Price, J.D. Hazle, N.J. Halas, J.L. West, Nanoshell-mediated near-infrared thermal therapy of tumors under magnetic resonance guidance, PNAS, 100 (2003) 13549-13554.

[59] M.W. Knight, N.K. Grady, R. Bardhan, F. Hao, P. Nordlander, N.J. Halas, Nanoparticle-Mediated Coupling of Light into a Nanowire, Nanoletters, 7 (2007) 2346-2350.

[60] M.A. Noginov, G. Zhu, A.M. Belgrave, R. Bakker, V.M. Shalaev, E.E. Narimanov, S. Stout, E. Herz, T. Suteewong, U. Wiesner, Demonstration of a spaser-based nanolaser, Nature, 460 (2009) 1110-1112.

[61] J.A. Schuller, T. Taubner, M.L. Brongersma, Optical antenna thermal emitters, Nature Photonics, 3 (2009) 658-661.

[62] J.A. Schuller, R. Zia, T. Taubner, M.L. Brongersma, Dielectric Metamaterials Based On Electric and Magnetic Resonances of Silicon Carbide Particles, Physical Review Letters, 99 (2007) 107401.107401-107401.107404.

[63] M.H. Huang, S. Mao, H. Feick, H. Yan, Y. Wu, H. Kind, E. Weber, R. Russo, P. Yang, Room-Temperature Ultraviolet Nanowire Nanolasers, Science, 292 (2001) 1897-1899.

[64] J.C. Johnson, H.-J. Choi, K.P. Knutsen, R.D. Schaller, P. Yang, R.J. Saykally, Single gallium nitride nanowire lasers, Nature Materials, 1 (2002) 106-110.

[65] M.P. Nezhad, A. Simic, O. Bondarenko, B. Slutsky, A. Mizrahi, L. Feng, V. Lomakin, Y. Fainman, Room-temperature subwavelength metallo-dielectric lasers, Nature Photonics, 4 (2010) 395-399.

[66] R. Chen, T.-T.D. Tran, K.W. Ng, W.S. Ko, L.C. Chuang, F.G. Sedgwick, C. Chang-Hasnain, Nanolasers grown on silicon, Nature Photonics, 5 (2011).

[67] R.F. Oulton, V.J. Sorger, T. Zentgraf, R.-M. Ma, C. Gladden, L. Dai, G. Bartal, X. Zhang, Plasmon lasers at deep subwavelength scale, Nature, 461 (2009) 629-632.

[68] T. Yamasaki, T. Tsutsui, Spontaneous emission from fluorescent molecules embedded in photonic crystals consisting of polystyrene microspheres, Applied Physics Letters, 72 (1998) 1957-1959.

[69] X. Gao, S. Nie, Doping Mesoporous Materials with Multicolor Quantum Dots, Journal of Physical Chemistry B, 107 (2003) 11575-11578.

[70] X. Gao, S. Nie, Quantum Dot-Encoded Mesoporous Beads with High Brightness and Uniformity: Rapid Readout Using Flow Cytometry, Analytical Chemistry, 76 (2004) 2406-2410.

[71] J. Enderlein, Theoretical study of single molecule fluorescence in a metallic nanocavity, Applied Physics Letters, 80 (2002) 315-317.

[72] I.G. Koprinkov, K.V. Stamenov, K.A. Stankov, Intense Laser Generation from an Atomic-Fluorine Laser, Applied Physics B: Photophysics and Laser Chemistry, 33 (1984) 235-238.

[73] V.V. Datsyuk, K. Vogler, I. Bragin, Spectral-kinetic characteristics of the F_2 laser transition, Applied Physics B: Lasers and Optics, 78 (2004) 425-432.

[74] P. Misra, M.A. Dubinskii, Ultraviolet Spectroscopy and UV Lasers, CRC Press, 2002.

[75] Lambda Physik GmbH, Lambda Physik User Manual LPF200, 04/00, Göttingen, Germany.

[76] E.D. Palik, Handbook of Optical Constants of Solids Volume 2, Academic Press, 1991.

[77] E. Hecht, Optics, 4th Edition ed., Addison Wesley, San Francisco, CA, 2002.

[78] B. Jaleh, P. Parvin, K. Mirabaszadeh, M. Katouzi, KrF laser irradiation effects on nuclear track recording properties of polycarbonate, Radiation Measurements, 38 (2004) 176-183.

[79] S. Shahid, M.S. Rafique, M. Khaleeq-ur-Rahman, I.M. Ghauri, Faizan-ul-Haq, Effect of CO_2 laser irradiation on the track registration properties of CR-39, in: 31st EPS Conference on Plasma Physics, London, 2004, pp. P-5.045.

[80] P. Parvin, B. Jaleh, N. Sheikh, N. Amiri, Surface effect of KrF laser exposure on ECE of alpha particle tracks in polycarbonate polymer, Radiation Measurements, 40 (2005) 775-779.

[81] D. Nikezic, K.N. Yu, Analyses of light scattered from etched alpha-particle tracks in PADC, Radiation Measurements, 43 (2008) 1417-1422.

[82] N. Dwaikat, T. Iida, F. Sato, Y. Kato, I. Ishikawa, W. Kada, A. Kishi, M. Sakai, Y. Ihara, Study etching characteristics of a track detector CR-39 with ultraviolet laser irradiation, Nuclear Instruments and Methods in Physics Research A, 572 (2007) 826-830.

[83] Nidhi, R. Gupta, T. Sharma, S. Aggarwal, S. Kumar, Effect of thermal annealing on optical properties of CR-39 polymeric track detector, Indian Journal of Physics, 83 (2009) 921-926.

[84] R. Kelly, A. Miotello, B. Braren, C.E. Otis, On the debris phenomenon with laser-sputtered polymers, Applied Physics Letters, 60 (1992) 2980-2982.

[85] E.D. Palik, Handbook of Optical Constants of Solids Volume 1, Academic Press, 1985.

[86] Y.W. Zheng, B.S. Luk'yanchuk, Y.F. Lu, W.D. Song, Z.H. Mai, Dry laser cleaning of particles from solid substrates: Experiments and theory, Journal of Applied Physics, 90 (2001) 2135-2142.

[87] B.S. Luk'yanchuk, N. Arnold, S.M. Huang, Z.B. Wang, M.H. Hong, Three-dimensional effects in dry laser cleaning, Applied Physics A: Materials Science & Processing, 77 (2003) 209-215.

[88] W.D. Callister, Materials Science and Engineering: An Introduction, 4th Edition, John Wiley & Sons, New York, 1997.

[89] P.E. Dyer, S.M. Maswadi, C.D. Walton, M. Ersoz, P.D.I. Fletcher, V.N. Paunov, 157-nm laser micromachining of N-BK7 glass and replication for microcontact printing, Applied Physics A: Materials Science & Processing, 77 (2003) 391-394.

[90] S.I. Kudryashov, S.D. Allen, Removal versus ablation in KrF dry laser cleaning of polystyrene particles from silicon, Journal of Applied Physics, 92 (2002) 5159-5162.

[91] X. Wu, E. Sacher, M. Meunier, The modelling of excimer laser particle removal from hydrophilic silicon surfaces, Journal of Applied Physics, 87 (2000) 3618-3627.

[92] H.C. Hamaker, The London-van der Waals Attraction Between Spherical Particles, Physica IV, 10 (1937) I058-1070.

[93] B.S. Luk'yanchuk, Laser Cleaning, World Scientific Publishing, Singapore, 2002.

[94] M. Sitti, R.S. Fearing, Nanomolding Based Fabrication of Synthetic Gecko Foot-Hairs, in: IEEE-Nano2002, 2002, pp. 137-140.

[95] J. Shao, R.E. Baltus, Hindered Diffusion of Dextran and Polyethylene Glycol in Porous Membranes, AIChE Journal, 46 (2000) 1149-1156.

[96] M.D. Croucher, M.L. Hair, Hamaker Constants and the Principle of Corresponding States, The Journal of Physical Chemistry, 81 (1977) 1631-1636.

[97] S.R. Saunders, M. Anand, S.-S. You, C.B. Roberts, Total Interaction Energy Model to Predict Nanoparticle Dispersibility in CO_2-Expanded Solvents, Computer Aided Chemical Engineering, 28 (2010) 1651-1656.

[98] J.E. Mark, Polymer Data Handbook, Oxford University Press, Oxford, 1999.

[99] E.D. Palik, Handbook of Optical Constants of Solids Volume 3, Academic Press, 1998.

[100] J.G. Carter, T.M. Jelinek, R.N. Hamm, R.D. Birkoff, Optical Properties of Polystyrene in the Vacuum Ultraviolet, The Journal of Chemical Physics, 44 (1966) 2266-2269.

[101] G. Schrems, M.P. Delamare, N. Arnold, P. Leiderer, D. Bäuerle, Influence of storage time on laser cleaning of SiO_2 on Si, Applied Physics A: Materials Science & Processing, 76 (2003) 847-849.

[102] B.S. Luk'yanchuk, Z.B. Wang, M.H. Hong, T.C. Chong, N. Arnold, Optical Resonance and Near-Field Effects: Applications for Nanopatterning, Proceedings of SPIE, 5448 (2004) 37.

[103] D. Korobkin, Y.A. Urzhumov, B. Neuner III, C. Zorman, Z. Zhang, I.D. Mayergoyz, G. Shvets, Mid-infrared metamaterial based on perforated SiC membrane: engineering optical response using surface phonon polaritons, Applied Physics A: Materials Science & Processing, 88 (2007) 605-609.

[104] R.I. Scace, G.A. Slack, Solubility of Carbon in Silicon and Germanium, Journal of Chemical Physics, 30 (1959) 1551.

[105] P.H. Key, D. Sands, M. Schlaf, C.D. Walton, C.J. Anthony, K.M. Brunson, M.J. Uren, Infra-red reflectivity of ion-implanted and pulsed excimer laser irradiated 4H-SiC, Thin Solid Films, 364 (2000) 200-203.

[106] P. Friedrichs, T. Kimoto, L. Ley, G. Pensl, Silicon Carbide - Volume 1: Growth, Defects and Novel Applications, Wiley-VCH, Weinheim, 2010.

[107] P.E. Dyer, R.J. Farley, Periodic surface structures in the excimer laser ablative etching of polymers, Applied Physics Letters, 57 (1990) 765-767.

[108] P.E. Dyer, R.J. Farley, Dynamics of laser-induced periodic surface structures in excimer laser ablation of polymers, Journal of Applied Physics, 74 (1993) 1442-1444.

[109] M. Li, Q.H. Lu, J. Yin, Y. Sui, G. Li, Y. Qian, Z.G. Wang, Periodic microstructure induced by 532nm polarized laser illumination on poly(urethane-imide) film: orientation of the azobenzene chromophore, Applied Surface Science, 193 (2002) 46-51.

[110] P.B. Johnson, R.W. Christy, Optical Constants of the Noble Metals, Physical Review B, 6 (1972) 4370-4379.

[111] S.E. Caudill, W.T. Grubbs, Interferometric Measurements of Refractive Index Dispersion in Polymers over the Visible and Near-Infrared Spectral Range, Journal of Applied Polymer Science, 100 (2006) 65-72.

[112] Chemical Rubber Company, CRC Handbook of Chemistry and Physics, 83rd edition, Chemical Rubber Company, Cleveland, Ohio, 2002.

[113] D.D. Evanoff Jr., G. Chumanov, Synthesis and Optical Properties of Silver Nanoparticles and Arrays, ChemPhysChem, 6 (2005) 1221-1231.

[114] J. Smajic, C. Hafner, L. Raguin, K. Tavzarashvili, M. Mishrikey, Comparison of Numerical Methods for the Analysis of Plasmonic Structures, Journal of Computational and Theoretical Nanoscience, 6 (2009) 763-774.

[115] S.A. Ramakrishna, T.M. Grzegorczyk, Physics and Applications of Negative Refractive Index Materials, CRC Press, Boca Raton, FL, 2009.

[116] K.L. Kelly, E. Coronado, L.L. Zhao, G.C. Schatz, The Optical Properties of Metal Nanoparticles: The Influence of Size, Shape and Dielectric Environment, Journal of Physical Chemistry B, 107 (2003) 668-677.

[117] S.A. Maier, Plasmonics: Fundamentals and Applications, Springer, New York, 2007.

[118] P.N. Prasad, Nanophotonics, John Wiley & Sons, New Jersey, 2004.

[119] M. Faraday, The Bakerian Lecture: Experimental Relations of Gold and Other Metals to Light, Philosophical Transactions of the Royal Society A, 147 (1857) 145-181.

[120] J.B. Pendry, Negative Refraction Makes a Perfect Lens, Physical Review Letters, 85 (2000) 3966-3969.

[121] P.K. Jain, X. Huang, I.H. El-Sayed, M.A. El-Sayed, Review of Some Interesting Surface Plasmon Resonance-enhanced Properties of Noble Metal Nanoparticles and their Applications to Biosystems, Plasmonics, 2 (2007) 107-118.

[122] Y. Khalavka, C. Ohm, L. Sun, F. Banhart, C. Sönnichsen, Enhanced Thermal Stability of Gold and Silver Nanorods by Thin Surface Layers, The Journal of Physical Chemistry C: Letters, 111 (2007) 12886-12889.

[123] S.J. Kim, C.S. Ah, D.-J. Jang, Laser-induced growth and reformation of gold and silver nanoparticles, Journal of Nanoparticle Research, 11 (2009) 2023-2030.

[124] A. Takami, H. Kurita, S. Koda, Laser-Induced Size Reduction of Noble Metal Particles, Journal of Physical Chemistry B, 103 (1999) 1226-1232.

[125] A. Plech, V. Kotaidis, S. Grésillon, C. Dahmen, G. von Plessen, Laser-induced heating and melting of gold nanoparticles studied by time-resolved x-ray scattering, Physical Review B, 70 (2004) 195423.

[126] S.-S. Chang, C.-W. Shih, C.-D. Chen, W.-C. Lai, C.R.C. Wang, The Shape Transition of Gold Nanorods, Langmuir, 15 (1999) 701-709.

[127] S. Link, C. Burda, M.B. Mohamed, B. Nikoobakht, M.A. El-Sayed, Laser Photothermal Melting and Fragmentation of Gold Nanorods: Energy and Laser Pulse-Width Dependence, The Journal of Physical Chemistry A, 103 (1999) 1165-1170.

[128] H. Petrova, J.P. Juste, I. Pastoriza-Santos, G.V. Hartland, L.M. Liz-Marzán, P. Mulvaney, On the temperature stability of gold nanorods: comparison between thermal and ultrafast laser-induced heating, Physical Chemistry Chemical Physics, 8 (2006) 814-821.

[129] J.R. Sambles, L.M. Skinner, N.D. Lisgarten, An Electron Microscope Study of Evaporating Small Particles: The Kelvin Equation for Liquid Lead and the Mean Surface Energy of Solid Silver, Proceedings of The Royal Society A: Mathematical, Physical & Engineering Sciences, 318 (1970) 507-522.

[130] Q. Zhao, L. Hou, C. Zhao, S. Gu, R. Huang, S. Ren, Conversion of silver nanoprisms into colloidal nanoparticles induced by femtosecond laser pulses, Laser Physics Letters, 1 (2004) 115-117.

[131] K.K. Nanda, Size-dependent melting of nanoparticles: Hundred years of thermodynamic model, Pramana - journal of physics, 72 (2009) 617-628.

[132] L.M. Skinner, J.R. Sambles, The Kelvin Equation - A Review, Aerosol Science, 3 (1972) 199-210.

[133] W. Thomson (Kelvin), On The Equilibrium of Vapour at a Curved Surface of Liquid, Philosophy Magazine Series 4, 42 (1871) 448-452.

[134] G.L. Harris, Properties of Silicon Carbide, INSPEC, London, 1995.

[135] R.W. Waynant, M.N. Ediger, Electro-Optics Handbook, Second Edition, McGraw-Hull, New York, 200.

[136] H. Staleva, S.E. Skrabalak, C.R. Carey, T. Kosel, Y. Xia, G.V. Hartland, Coupling to light, and transport and dissipation of energy in silver nanowires, Physical Chemistry Chemical Physics, 11 (2009) 5889-5896.

[137] D. Bäuerle, Laser Processing and Chemistry, Springer, Berlin, 1996.

[138] H. Yao, Z. Li, Q. Gong, Coupling-induced excitation of a forbidden surface plasmon mode of a gold nanorod, Science in China Series G: Physics, Mechanics & Astronomy, 52 (2009) 1129-1138.

[139] M. Dippel, A. Maier, V. Gimple, H. Wider, W.E. Evenson, R.L. Rasera, G. Schatz, Size-Dependent Melting of Self-Assembled Indium Nanostructures, Physical Review Letters, 87 (2001) 095505.

[140] F. Ding, A. Rosén, S. Curtarolo, K. Bolton, Modeling the melting of supported clusters, Applied Physics Letters, 88 (2006) 133110.

[141] Poly(allylamine hydrochloride) average Mw ~58,000 - Sigma-Aldrich, in.

[142] Poly(sodium 4-styrenesulfonate) average Mw ~70,000, powder - Sigma-Aldrich, in.

[143] Rhodamine 6G Dye content 99% - Sigma-Aldrich, in.

[144] J.R. Lakowicz, Principles of Fluorescence Spectroscopy: Third Edition, Springer, 2006.

[145] S.N. Kasarova, N.G. Sultanova, C.D. Ivanov, I.D. Nikolov, Analysis of the dispersion of optical plastic materials, Optical Materials, 29 (2007) 1481-1490.

[146] Coumarin 7 98% - Sigma-Aldrich, in.

[147] A. Francois, M. Himmelhaus, Optical Sensors Based on Whispering Gallery Modes in Fluorescent Microbeads: Size Dependence and Influence of Substrate, Sensors, 9 (2009) 6836-6852.

[148] A. Francois, K.J. Rowland, T.M. Monro, Highly efficient excitation and detection of whispering gallery modes in a dye-doped microsphere using a microstructured optical fibre, Applied Physics Letters, 99 (2011) 141111.

[149] A. Weller, F.C. Liu, R. Dahint, M. Himmelhaus, Whispering gallery mode biosensors in the low-Q limit, Applied Physics B: Lasers and Optics, 90 (2008) 561-567.

[150] Q. Zhang, Y. Han, W.-C. Wang, L. Zhang, J. Chang, Preparation of fluorescent polystyrene microspheres by gradual solvent evaporation method, European Polymer Journal, 45 (2009) 550-556.

[151] The Chapter of St Paul's Cathedral, Visits & Events - St Paul's Cathedral, London, UK, in, 2012.

[152] M.O. Scully, Collimated unidirectional laser beams from notched elliptical resonators, PNAS, 107 (2010) 22367-22368.

[153] V. Sandoghdar, F. Treussart, J. Hare, V. Lefèvre-Seguin, J.-M. Raimond, S. Haroche, Very low threshold whispering-gallery-mode microsphere laser, Physical Review A, 54 (1996) R1777-R1780.

[154] Q.J. Wang, C. Yan, N. Yu, J. Unterhinninghofen, J. Wiersig, C. Pflügl, L. Diehl, T. Edamura, M. Yamanishi, H. Kan, F. Capasso, Whispering-gallery mode resonators for highly unidirectional laser action, PNAS, 107 (2010) 22407-22412.

[155] Q.J. Wang, C. Yan, L. Diehl, M. Hentschel, J. Wiersig, N. Yu, C. Plügl, M.A. Belkin, T. Edamura, M. Yamanishi, H. Kan, F. Capasso, Deformed microcavity quantum cascade lasers with directional emission, New Journal of Physics, 11 (2009) 125018.

[156] O.K. Castell, C.J. Allender, D.A. Barrow, Liquid-liquid phase separation: characterisation of a novel device capable of separating particle carrying multiphase flows, Lab on a Chip, 9 (2009) 388-396.

[157] A.M. Armani, R.P. Kulkarni, S.E. Fraser, R.C. Flagan, K.J. Vahala, Label-Free, Single-Molecule Detection with Optical Microcavities, Science, 317 (2007) 783-787.

[158] F. Vollmer, S. Arnold, Whispering-gallery-mode biosensing: label-free detection down to single molecule, Nature Methods, 5 (2008) 591-595.

[159] Y. Yao, J. Yao, V.K. Narasimhan, Z. Ruan, C. Xie, S. Fan, Y. Cui, Broadband light management using low-Q whispering gallery modes in spherical nanoshells, Nature Communications, 3 (2012) 664.

[160] T. Mukaiyama, K. Takeda, H. Miyazaki, Y. Jimba, M. Kuwata-Gonokami, Tight-Binding Photonic Molecule Modes of Resonant Bispheres, Physical Review Letters, 82 (1999) 4623-4626.